Study of the Aggregation Behaviour of Egg Yolk Lecithin/Bile Salt Mixtures by Increasing the Ionic Strength

Dilek Madenci

A thesis submitted in fulfilment of the requirements
for the degree of Doctor of Philosophy
to the
University of Edinburgh May 2009

Dedicated to my parents
with love

Hüseyin and Güler Madenci

Kaderimin Oyunu - Orhan Gencebay

Çilesiz günüm yok dert ararsan çok
Öyle dertliyim ki,
Bana kaderimin bir oyunumu bu
Aldı sevdiğimi verdi zulumu
Dünyaya doymadan geçip gideceğim
Yoksa yaşamanın kanunumu bu
Bıktım artık yaşamaktan
Çekmekle bitermi bu hayat yolu

Abstract

This thesis describes a study of the aggregational behaviour of egg yolk lecithin (EYL), a natural lecithin, and bile salt mixtures especially with respect to an increase of the ionic strength of the solvent.

Mixtures of two amphiphiles with very different spontaneous curvature as EYL lecithin and bile salt form mixed micelles and vesicles in aqueous solution. Their properties have been well-studied under physiological conditions, i.e. 150 mM electrolyte concentration and pH 7-8, while other conditions are still hardly explored. Upon increasing ionic strength the formed structures and the transitional pathways (micelles, coexistence of micelles and vesicles, and vesicles) change the generated structures completely from those observed under physiological conditions. We quantitatively determined these structures formed in a broad range of electrolyte concentrations with various scattering techniques, x-ray, light and neutron scattering and calorimetry. With calorimetry, phase diagrams in the EYL and bile salt concentration phase plane were determined at various ionic strength ranging from physiological salt concentration to up to 1000 mM.

Additionally a new electrochemical approach using functionalised electrodes, i.e. sensitive and selective to bile salt, and thus to control the bile salt concentration in solution (concentrations below the critical micellar concentration (*cmc*) was attempted, since bile salt removal or injection drives the micelle-to-vesicle or the vesicle-to-micelle transition, respectively, of the mixed aggregational system of EYL/bile salt. Although this control was not achieved within the framework of this thesis, promising results show directions for future experiments.

Declaration

I do hereby declare that this thesis was composed by myself and that the work described within is my own, except where explicitly stated otherwise.

Dilek Madenci
May 2009

Acknowledgements

Looking back there are a huge number of people, who helped me go my way until eventually finishing this PhD. They accompanied me in various steps of my life, and encouraged me to do the next step. During my undergraduate studies, I would like to thank Prof. emer. Friedrich Hehl, Prof. emer. Janos Hajdu and Dr. Dmitry Luchinsky, who motivated me to pursue research.

But for my PhD, I would like to thank first of all Prof. Stefan U. Egelhaaf and Dr. Andrew R. Mount, for the opportunity to perform this PhD work. I would especially like to thank both for their support and their encouragement and enthusiasm, that they gave and give me.

Actually Stefans enthusiasm was the trigger to start this PhD. And whenever, I step from his office, even now, I gain somehow this energy to go on.

I have enjoyed both working in the chemistry and physics department in Edinburgh and in the soft matter section in Düsseldorf. I would like to thank various people. Especially, Dr. Nhan Pham for allowing me to use his EQCM. Iris Coe, Julia Drewer, Nhan Pham and Helen Hermes, thanks for the nice atmosphere and discussions in our various offices.
The electrochemistry group of Dr. Andy Mount, especially John Bruce Henry, for mutual aid and support.
The soft condensed matter group of Prof. Dr. Stefan U. Egelhaaf in Düsseldorf. Dr. Marco Laurati, Dr. Frederic Cardinaux and Dr. Helen Hermes for my various discussions. I especially thank Beate Moser. She "translated" my pen and paper drawings as the schemes used in chapter 2 into nice digital versions.

Special thanks to Dr. Nadine van Os, from the former Zoophysiology group of Prof. Grieshaber in Düsseldorf, who introduced me plus allowed me to use the ITC equipment, also Dr. Mina Tabatabai in the organic chemistry group of Prof. Ritter for allowing to use the ITC equipment at higher temperatures and Klaus Kowski at the Univeristy of Duisburg-Essen for using the ITC equipment in his group at lower temperatures.

I am very grateful to Prof. Jan Skov Pedersen, Dr. D. G. Roshan and Dr. Christiano Olivera from the University of Århus for the a lot of things: Using the instrument, for all their time invested to help me in this week, while I was there, for the help afterwards.
I would like to thank the Marie-Curie program not only for funding, but most of all to see science performed in a network of groups and universities with so different ideas and research fields.

Most importantly, I thank my family for their love, care, patience, encouragement, help and support.

List of Abbreviations

α ..... ratio between lipid in micellar form and total lipid concentration
β ..... number of bound ions to the aggregate
χ^2 ..... least square
ΔG_d ..... Gibbs energy of demicellisation
ΔH_d ..... demicellisation enthalphy
$\Delta H_{d_{mic}}$ ..... enthalphy of the dilution of micelles
$\Delta H_{d_{mon}}$ ..... enthalphy of the dilution of monomers
ΔS_d ..... entropy of demicellisation
Δ f ..... change in frequency, Hz
Δ m ..... change in mass, μg
ϵ ..... detector efficiency
η ..... viscosity of the liquid
η_1 ..... Cailleé parameter
Γ ..... relaxation rate
γ ..... Eulers constant
λ ..... wavelength
ν ..... sweep rate of the potential in a electrochemical experiment
Ω_0 ..... solid angle element in scattering experiments
ρ ..... scattering length density
ρ_d ..... mass density
ρ_z ..... electron density profile
σ ..... cross section
σ^{sat} ..... surface potential density at the saturation line
σ^{sol} ..... surface potential density at the solubilisation line
σ_i ..... FWHM of the headgroup
σ_{coh} ..... coherent part of the scattering cross section
σ_{mic} ..... polydispersity of the length of the micelles
σ_{ves} ..... polydispersity of the vesicle radii
τ_t ..... relaxation time

θ ..... scattering angle
$\vec{k_i}$ ..... wave vector of the incoming beam
$\vec{k_s}$ ..... wave vector of the scattered beam
A ..... beam area in scattering experiments
A_0 ..... optimal surface area of a surfactant
a_B ..... free surfactant ion activity
A_L ..... surface area of the lipid
A_w ..... fitting parameter for scission energy
A_{D_t} ..... surface area of bile salt surfactant
b ..... Kuhn length
b_l ..... scattering length
c ..... concentration
C_0 ..... spontaneous curvature
c_g ..... counterion concentration, i.e. c_g=$cmc + c_s$
c_i ..... coefficient for the Gaussian deconvolution model
C_L ..... spontaneous curvature of lipid aggregates
c_L ..... total lipid concentration, also referred to as L for simplification
c_s ..... salt concentration of the electrolyte/buffer
C_{D_t} ..... spontaneous curvature of bile salt aggregates
c_{D_t} ..... total detergent concentration, also referred to as D_t for simplification
cmc ..... critical micelle concentration
d ..... bilayer with plus water spacing
D_b ..... concentration of detergent bound to the aggregate
d_b ..... bilayer width
d_c ..... width of the hydrocarbon chain of the lipid
d_h ..... width of the headgroup of the lipid
d_L ..... 2 times width of the hydrocarbon chain of the lipid
D_t ..... total detergent concentration
D_w ..... concentration of detergent in the aqueous phase
D_w^{sat} ..... concentration of detergent at the saturation boundary line
D_w^{sol} ..... concentration of detergent at the saturation boundary line
d_{cell} ..... pathlength of the scattering cell
E ..... potential
$E^{0'}$ ..... standard electrode potential
$F(q)$ ..... formfactor
F_C ..... formfactor of chain
F_H ..... formfactor of headgroup
F_V ..... formfactor of vesicels, i.e. spherical shell

F_{chain} ..... formfactor of chain
F_{cs} ..... formfactor of the cross-sectional contribution
F_{rod} ..... formfactor of a infinitely thin rod
F_{wc} ..... formfactor of a wormlike chain
H ..... enthalphy
H_D ..... demicellisation enthalpy
$I(q)$ ..... scattered intensity
k_B ..... Boltzman constant
k_{CH} ..... Corrin-Harkins coefficient
l_p ..... persistence length
L_s ..... length of the hydrophobic tail of the surfactant
N_a ..... Avogadro Number
N_c ..... measure for smoothness
p ..... pressure
q ..... heat q per mole of injectant
q ..... scattering vector
Q_{pol} ..... polymerisation charge
Q_{redox} ..... redox charge
R_e ..... detergent to lipid concentration
R_e^{sat} ..... detergent to lipid concentration at the saturation boundary line
R_e^{sol} ..... detergent to lipid concentration at the solubilisation boundary line
$S(q)$ ..... structure factor
V_s ..... volume of the hydrophobic tail of the surfactant
W ..... concentration of water, i.e. 55.5M
x ..... doping level of the polymer film
x_b ..... molar fraction of the bile salt in the aggregate
x_w ..... molar fraction of the bile salt in the aqueous phase
Z ..... atomic number
(PNMP/A) ..... PNMP polymer matrix with Anion A in the matrix
$\boldsymbol{q}$ ..... scattering vector
BH ..... bile acids
BS ..... bile salts
CE ..... counter electrode
cryo-TEM ..... cryo-Transition electron microscopy
CV ..... cyclic voltammetry
D ..... diffusion coefficient
DLS ..... dynamic light scattering
DLVO ..... Derjaguin Landau Verwey Overbeck

EQCM ..... electrochemical quartz crystal microbalance
EYL ..... egg yolk lecithin
GC ..... glaucocholate
HPLC ..... High pressure liquid chomotography
Hz ..... Hertz
IFT ..... inverse Fourier transform
$LiClO_4$ ..... lithium perchlorate
LS ..... light scattering
LSV ..... linear sweep voltammetry
M ..... metal electrode
MCT ..... modified Caille theory
MHz ..... megahertz
min ..... minutes
ml ..... millilitre
MLV ..... multilamellar vesicle
Na PSS ..... sodium poly(styrenesulfonate)
Na pTS ..... Sodium Para-toluenesulfonic acid
NaC ..... sodium cholate
NaCDC ..... Sodium chenodeoxycholate
NaCl ..... sodium chloride
NaDC ..... Sodium deoxycholate
NADH ..... 3-α-hydroxysteroid dehydrogenase
NaDH ..... reduced nicotinamide adenine dinucleotide
NaDhC ..... Sodium dehydrocholate
NaTC ..... sodium taurocholate
NaTCDC ..... sodium taurochenodeoxycholate
NaTDC ..... sodium taurodeoxycholate
NHE ..... normal hydrogen electrode
P ..... partitioning coefficient
PNMP ..... Poly-*N*-Methylpyrrole
$PNMP^0$ ..... neutral Poly-N-Methylpyrrole
POPC 1-palmitodyl-2oleolyl-*sn*-glycero-3-phosphotidylcholine
PP ..... packing parameter
PPY ..... Pyrrole
PRISM ..... Polymer Reference Interaction Site Model)
PVC ..... poly(vinyl chloride)
QCM ..... Quartz Crystal Microbalance
QCMD ..... Quartz Crystal Microbalance with Dissipation

R ..... universal gas constant
RE ..... reference electrode
SANS ..... small angle neutron scattering
SAXS ..... small angle X-ray scattering
SCE ..... standard or saturated calomel electrode
SLS ..... static light scattering
STS ..... sodium tetradecyl sulfate
T ..... sample transmission
ULV ..... unilamellar vesicles
WE ..... working electrode

Contents

Chapter 1

Introduction

1.1 Surfactant Aggregation of Amphiphiles

The term surfactant is a contraction of ”**Sur**face **act**ive ag**ent**”. Surfactants lower the surface tension of a liquid, which allows easier spreading, and also lowers the interfacial tension between two liquids. Surfactants are organic amphiphilic molecules, meaning they contain both hydrophobic (“water-loving”) groups, their ”tails”, and hydrophilic (“water-hating”) groups, their ”heads”.

An important property of many surfactants is that they are able to self–assemble in bulk solution into many types of aggregates. This is driven by relatively weak hydrophobic and electrostatic, interactions. Most single-chained surfactants form micelles, whereas double chained surfactants form bilayers. The type of assembly is mostly governed by the geometry of the molecule and the properties of the solvent. The concentration at which surfactants begin to form micelles is known as the critical micelle concentration, *cmc*. When micelles form in aqueous solution, their tails form a core that is like an oil droplet, and their heads form an outer shell, or corona, that maintains favourable contact with water and shields the tails [1].

The driving force for the aggregation process is the tendency of the hydrophobic part to minimise contact with water. A variety of shapes and structures is observed. The simplest model to explain the structure of the aggregates is based on geometrical considerations and summarised in the packing parameter $PP = V_s/L_s A_0$ where the hydrophobic volume V_S is divided by the length L_S of the hydrophobic tail and the surface area A_0, which corresponds to the surface area per molecule at which the free energy is minimised [1]. Therefore the PP determines the preferred curvature, also called spontaneous curvature of the aggregate.

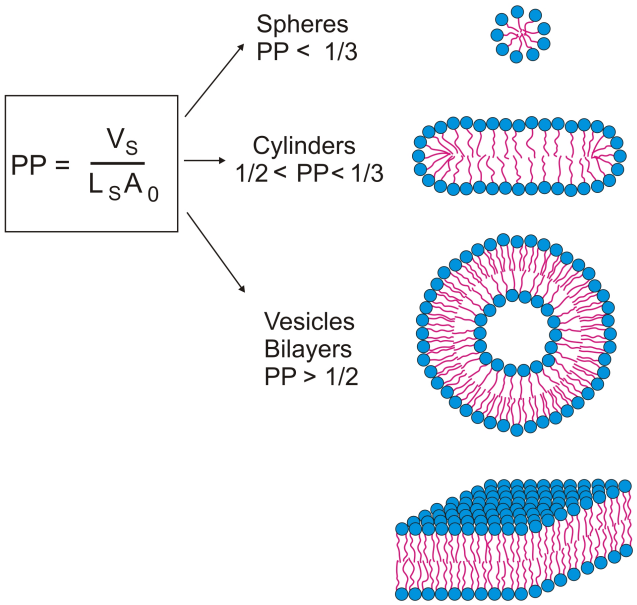

Figure 1.1: Packing properties of the lipids and the aggregate structures. When the packing parameter PP$< \frac{1}{3}$, one typically has single chained amphiphile (detergents) with a large headgroup and spherical micelles are formed. If PP is increased to 1/2<PP<1/3, cylindrical micelles are formed. Flexible bilayers, vesicles or planar bilayers are formed for PP$> \frac{1}{2}$. At a packing greater than 1 inverted structures are formed, which are not displayed here. After Israelachvili [1]

1.1.1 Packing Constraints of Aggregate Structures

The maximum extended chain length L_s in nm of a saturated hydrocarbon chain can be calculated using the results of X-ray scattering [2] with n the number of hydrocarbons in the surfactant tail.

$$L_S \approx 0.15 + 0.127n$$

The 0.15 nm in this equation comes from the van der Waals radius of the methyl group (0.21 nm) minus half the bond length of the first atom not contained in the hydrocarbon core (0.06 nm). The 0.127 nm is the carbon-carbon bond length (0.154 nm) projected onto the direction of the chain in the all-*trans* configuration. [3]. The volume in nm^3 of the hydrocarbon region can be calculated with:

$$V_S \approx 0.0274 + 0.0269n$$

The aggregation is not only governed by geometrical consideration, i.e. optimal space filling, but also the surfactant concentration, valency and concentration of the electrolyte, the pH, the temperature and of course the nature of the aggregate molecule itself, like its charge. Surfactant aggregates are influenced by many factors and show a huge variety of structures. Nevertheless, for a given composition, always the same structures are formed.
In this thesis, a mixture of two surfactants in aqueous solution is used as a biological model system, namely egg yolk lecithin mixed with a bile salt. A non-binding salt (NaCl) is added to change the ionic strength and thus the electrostatic repulsion in this system. The solutions are at almost neutral pH (pH 8.0, adjusted by TRIS buffer).

1.1.2 Spontaneous Curvature C_{S}

The formation of aggregates with different geometrical structures can also be described in terms of the spontaneous curvature or mean Gaussian curvature. Surfactants are aggregating to shapes characterised by the mean radii of the curvature of the interface. For instance flat structures as bilayer have zero curvature C_{S}= 0 and spheres with a radius r_{sphere} and a corresponding curvature $C_{\mathrm{S}} = \frac{1}{r_{sphere}}$. The mean spontaneous curvature C_{S} of a surfactant aggregate is the sum of the inverse main radii R_1 and R_2, they are characterised as the maximal and as the minimal radii and are known as the principal curvatures of the surface. The direction of the radii are related to a unit normal of the surface:

$$C_{\mathrm{S}} = \frac{1}{2}\left(\frac{1}{R_1} + \frac{1}{R_2}\right), \tag{1.1}$$

Lecithin and bile salt have different mean curvatures. Lecithin forms lamellar bilayer structures with effectively no mean curvature. Whereas bile salt aggregates are highly curved. The structure of the mixed system will be discussed in detail below [4].

1.1.3 *cmc* and Methods of *cmc*- Determination

Increasing the length of the hydrocarbon chain decreases the solubility of the molecule and increases the *cmc*. The presence of a double bond in the chain also increases the *cmc*.
Adsorbed counterions stabilise the ionic micelle. The micelle charge density defines the extent of adsorption on the ionic micelle surface. The higher the adsorption of counterions, the lower the *cmc*.
Figure 1.2 b)-d) shows the *cmc* determined by the physical change of various parameters with increasing surfactant concentration. These methods can be referred as a direct method, since no mediator molecule is used to obtain the *cmc*. Fluorescence techniques, dye titration and many others are an indirect method, where a molecule is added to the system, but this“reporter”

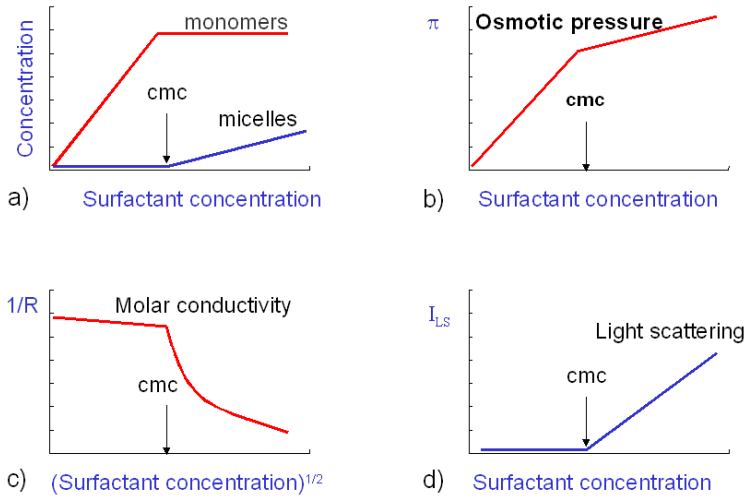

Figure 1.2: (a) Concentration of monomers and micelles against total surfactant concentration. Below the *cmc* all surfactant exist as monomers and above most as micelles. The cmc can be measured in the change (b) of the osmotic pressure, (c) of the conductivity and (d) of the intensity from a light scattering experiment as a function of the surfactant concentration.

molecule might already change the system, e.g. the nature of the charge, the shape and hydrophobicity of the micelles and thus affect its *cmc*.
Also light scattering experiments were performed in [5, 6, 7, 8, 9], but the deduced *cmc*s are generally higher than determined with other methods.
In this thesis a calorimetry technique, also a direct method, will be used to determine the *cmc* of the bile salt NaTCDC by increasing the ionic strength of the buffer, which will be discussed in chapter 6 in greater detail.

1.2 Bile salt

Bile salt is stored in the liver. Due to their amphiphilic nature, bile salts carry out two important functions. Firstly, they emulsify lipid aggregates in foodstuff into minute, microscopic droplets passing through the intestine to enable fat digestion and absorption through the intestine wall. Emulsification is not digestion in itself, but is of importance because it greatly increases the surface area of fat, making it available for digestion by lipase, which cannot access the inside of lipid droplets. And secondly, bile salts are lipid carriers and are able to solubilise many lipids by forming micelles - aggregates of lipids such as fatty acids, cholesterol and monoglycerides - that remain suspended in water. Bile salts are also critical for transport and absorption of the fat-soluble vitamins [10].

The most abundant of the bile salts in humans are cholate and deoxycholate, and they

are normally conjugated with either glycine or taurine to give glycocholate or taurocholate, respectively. Taurocholate and taurochenodeoxycholate are used in the experiments in this thesis. Large amounts of bile acids are secreted into the intestine every day, but only relatively small quantities are lost from the body. This is because approximately 95%, (20-30) g of the bile acids are absorbed back into the blood. Each bile salt molecule is reused about 20 times, often two or three times during a single digestive phase. The bile acids have a concentration of about 7-20 mM in the duodendum. The determination of the bile salt concentrations in the body, i.e. blood, is of great importance, because the disturbance of the bile acid metabolism is an important feature of many human diseases, such as liver dysfunction or gallstone formation. The measurement of bile acid concentration can be used as an indicator for a number of pathological conditions.

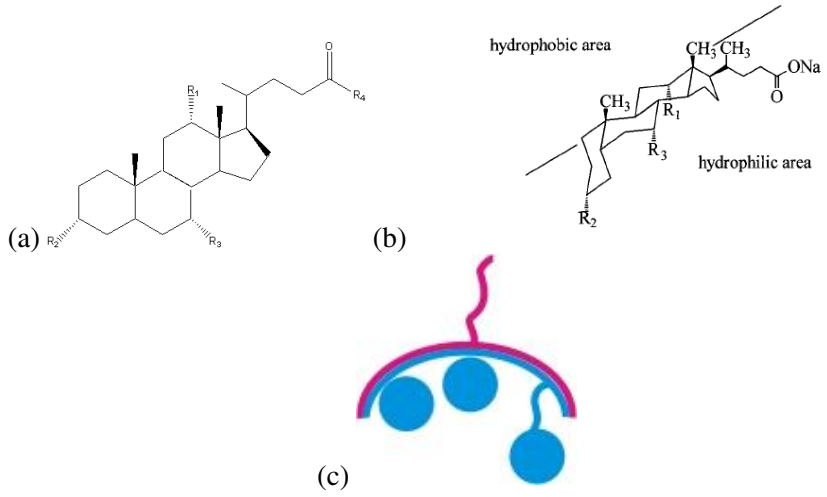

Figure 1.3: (a) The structures of bile acids with the groups R_1, R_2, R_3 and R_4 as given in table 1.1. (b) Structure of the bile salts with the hydrophobic and hydrophilic parts of the molecule. (c) Schematic representation of a bile salt with hydrophobic side (pink) and hydrophilic side (blue) of the backbone. The two OH-groups are of the dihydroxy bile salt are represented by the blue circles and the R_4 restgroup is represented by a circle connected to the hydrophilic side. This scheme will be used throughout the thesis.

The structure of bile salt does not correspond to the classical head-tail structure as other surfactants, where hydrophilic headgroup and hydrophobic tail are clearly separated. The hydrophilic and hydrophobic parts are rather on both sides of a steroid backbone with the hydrophilic part on the concave side with hydroxyl groups and the hydrophobic part at the convex side with methyl groups. The optimal headgroup area ($A_{\mathrm{D_t}}$) for bile salts tends to

BILE ACID	R1	R2	R3	R4
TC	-OH	-OH	-OH	$-NH(CH_2)_2SO_3^-$
TCDC	-H	-OH	-OH	$-NH(CH_2)_2SO_3^-$
TDC	-OH	-OH	-H	$-NH(CH_2)_2SO_3^-$
C	-OH	-OH	-OH	$-COO^-$
CDC	-H	-OH	-OH	$-COO^-$
DC	-OH	-OH	-H	$-COO^-$
DhC	=O	=O	=O	$-COO^-$

Table 1.1: The structures of bile acids taurocholate (TC), taurochenodeoxycholate (TCDC), taurodeoxycholate (TCD), cholate (C), chenodeoxycholate (CDC), deoxycholate (DC), Dehydrocholate (DhC)

be large and the measured values are ranging from 150Å to 250Å [11, 12, 5]. Because of this particular structure and also the rigidity [1] of the molecules, the aggregation properties are completely different when compared to surfactants with hydrocarbon chains. One of the consequences are the much smaller aggregation numbers in the range of 6 to 12, depending on the bile salt species [11, 13].

Bile salt ionises in water and carries a negative charge. The *cmc* also depends on the position of the OH groups and the conjugation. Since bile salt is charged the ionic strength of the solute plays an important role for the *cmc*, because of the screening of the headgroups and consequently the decrease monomer solubility leads to lower values for the *cmc* [6, 14, 15]. The effect is higher for dihydroxy than for trihydroxy bile salts [6, 7, 15]. This will be further discussed in chapter 6.

The rather small hydrophobic part of bile salts results in much higher monomeric solubility than lecithin (typical *cmc*s are a few mM [12].) Especially for bile salts with low aggregation numbers a very wide range of *cmc*s are reported, which ranges for NaTCDC from 0.47mM [16] to 3.8mM [17]. The range of NaC, the most investigated bile salt, is even wider. These properties mean that beyond the *cmc*, bile salts pack into small spherical or elliptical micelles with high spontaneous curvature. Small *et al.* suggested a two-step (also referred to as two-stage) aggregation model for bile salts, which will be discussed later.

The research on the properties of bile salt started in the mid 50ies with Ekwall et al. [18]. NaTC and NaTDC are the two bile salts, that have been most extensively studied [6, 12, 19, 20, 21]. Much less is known, for the commonly occurring bile salt TCDC, but this bile salt is investigated in chapter 6, where the *cmc* of this particular bile salt is determined. It was found that the bile salt molecule is 20Å long and 6-7Å wide with a volume of about $600Å^3$ depending on the type of bile salt molecule [22]. In table 1.2 the important parameters for TCDC and TC

[1] four rigid rings and one flexible side chain

are listed.

Parameter	NaTCDC	NaTC
molecular weight/g · mol	521.7	537.7
cmc / mM	~ 2	~ 10
solubility/ g/ml	0.1	0.1
volumes / Å^3	660 [23]	680
$A_{\mathrm{D_t}}$ / Å	200	220

Table 1.2: Important parameters of NaTCDC and NaTC.

1.2.1 Two-stage Model of Bile Salt Aggregation

Various models of bile salt aggregate structures have been discussed in the past 50 years. [6, 7, 15, 22, 19, 24, 25, 26].

Model I

According to Small [14, 24, 27], the initial stage of bile salt aggregation at low concentration involves the formation of a "globular, *primary*" micelle, in which the bile salt anions have their hydrophobic surfaces facing each other and build up the core. Their hydrophilic surfaces are in contact with water. The aggregation number is lower than 10 for "*primary*" micelle. At higher bile salt concentration, Small postulated, the "*primary*" micelles polymerise into rodlike "*secondary*" micelles via hydrogen bonding. The basis of this two-stage concept considers the molecular space filling, where a maximum of ten bile salts could be hydrophobically associated without creating a cavity in the core.

Mazer and Benedek [6, 15] performed dynamic light scattering experiment to measure the concentration-dependent hydrodynamic radius R_{hyd} of trihydroxy and dihydoxy (NaTC, NaTCDC, NaTDC) bile salts at two different ionic strength, at 0.15 M and one at 0.6 M NaCl concentration. The data was quantitatively consistent with the two-stage model by Small. At physiological salt concentration (0.15 M) the aggregation number was weakly dependent on the bile salt concentration, but at 0.6 M NaCl the micelles grew appreciably with increasing bile salt concentration for dihydroxy bile salts, but no growth for NaTC, a trihydroxy bile salt, was observed. Even at high ionic strength of about 3M [6]. A comparison between the R_{hyd} and aggregation number N, which was determined by the scattered intensity at a single scattering angle was consistent with a rodlike structure of the micelles. However, neither interactions nor polydispersity has been taken into account.

Model II

Kratohvil *et al.* [7] very critically evaluated some previous studies about bile salt aggregation and concluded: "We emphasize that studies of the aggregation patterns of bile salts in solutions of unpurified or inadequately purified samples at low concentrations are meaningless." Kratohvil and Kawamura [28] proposed another model on the basis of model I, where the aggregates form disk-like structure. The hydrophobic surfaces are oriented towards the interior of the micelle and the hydrophilic sides towards the solvent. Hydrogen bonding was excluded from the model. The orientation of the monomers are alternatively up and down. Coello *et al.* [29] supported model II with freezing point depression experiments for NaC, nevertheless revised the work published on the aggregation behaviour of bile salts in aqueous solutions in a later study [19], where they extended the freezing point depression experiments for further bile salts like NaTDC. It was noted that although model II, i.e. disklike structure with hydrophobic interaction, shows the best agreement with the experimental results in the literature (including [19]), the increase in aggregation number with increasing buffer salt concentration cannot be explained by model II entirely. Especially for dihydroxy bile salts, which show a strong salt dependence than the trihydroxy NaC.

Model III

Giglio *et al.* [30] have proposed a helical structure stabilised by polar interactions. The lateral surface of the helix is covered by nonpolar groups and the interior is filled with sodium surrounded by water molecules. The model shows similarities to inverted micelles. In this model III the hydrogen bonding is again taken into account as in model I. This model has the advantage of being compatible with progressive aggregation and high aggregation numbers.

From the ongoing discussion and research, it can easily be seen, that further studies are necessary even to understand the aggregation behaviour and structure of bile salt aggregates alone.

1.3 Lecithin

Lipids are amphiphiles with small headgroups and two hydrocarbon tails. The long tailed lipids can be very insoluble in water (monomeric solubility 10^{-10} M). Lecithin belongs to the family of phospholipids (lipids, which have one or more phosphate groups).
When lipids are dispersed into an aqueous solution, they self-assemble into aggregated structures like two-dimensional bilayers, one-dimensional tubes or networks depending on concentration, applied pressure, etc. [31]. Phospholipids are major components of biological

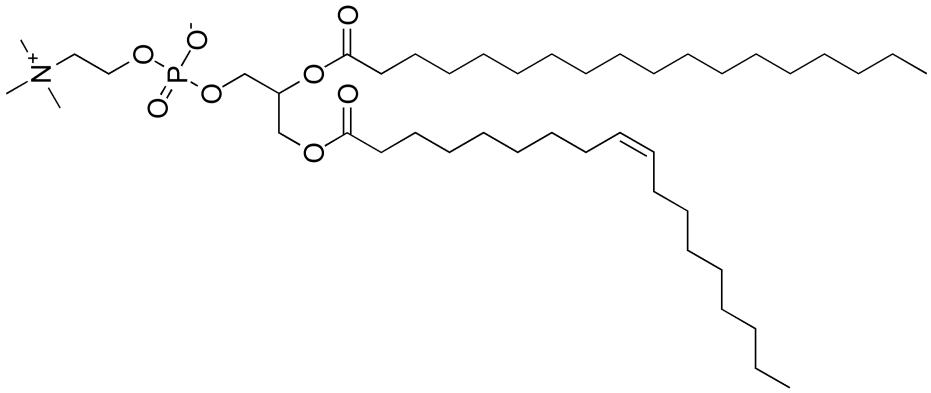

Figure 1.4: Structure of a phosphatidylcholine molecule (POPC)

membranes. In figure 1.4 the phosphatidylcholine molecule is shown.

In this thesis egg yolk lecithin (EYL)[2] will be used to investigate the bile-salt/lecithin system. The exact composition of EYL varies slightly depending on the eggs. Lecithin is zwitterionic at the pH used in our experiments, i.e. the overall charge is zero, and consequently there is no charge interactions between opposing bilayers only dipole-dipole interactions. The insolubility is due to the two long tails combined with the relatively small hydrophilic headgroup ($A_{\mathrm{D_t}} \approx$ 72Å [32]) and this also results in lecithin having a small spontaneous curvature $C_{\mathrm{S}} \approx 0$. Adding more lecithin into the solution results in the formation of flat bilayers or in closed up, shell-like bilayer structures, the vesicles. Lecithin is fully hydrated with water/buffer at about 35-45 $\%$ w/w [33] after which it separates into two phases, water and a lamellar phase. This can be seen in figure 1.5 [34].

In mixed lipid detergent systems, as EYL/octyl glucoside mixtures, a separation into two bulk phases has been observed close to the coexistence of micelles especially at low lipid concentration, i.e below 2mM [35]. The composition of the lower viscous phase is enriched in lipid and detergent, whose structure was not determined, and the upper phase is assumed to be in the lamellar phase. A similar behaviour was found in our EYL/bile salt system and will be investigated in this thesis.

Table 1.3 lists some parameters of EYL.

[2]Lecithin is now used to refer specifically to egg yolk lecithin unless otherwise specified

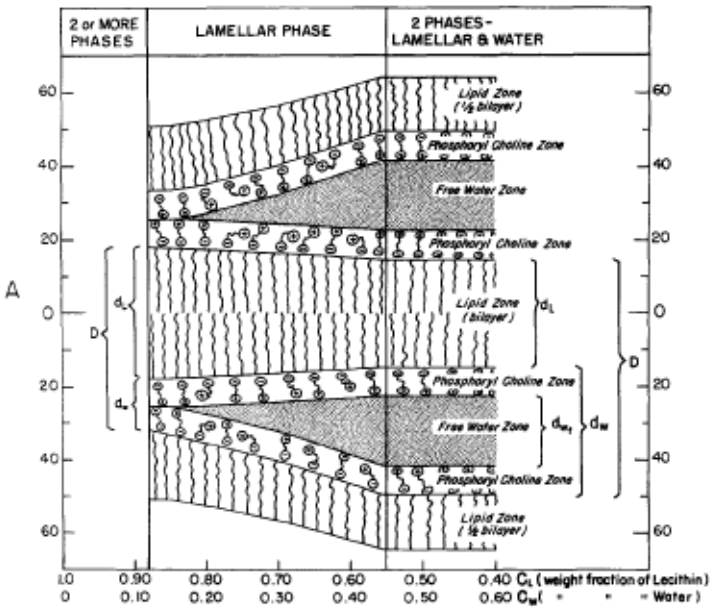

Figure 1.5: Phase equilibria and structure of dry and hydrated egg lecithin. D is the repeat distance, d_L the thickness of the lipid bilayer, d_w the thickness of the water layer including the phosphoryl choline zone and d_{w_F} the thickness of the "free water layer". The hydrocarbon parts of the lipid layers are represented as wavy lines to emphasize their partially liquidlike state. The choline groups of the phosphoryl choline zone are represented in a more or less random order within a zone 8 Å thick. For further explanation see reference [34].

1.4 Motivation

The major structural elements in biological membranes are phospholipid bilayers, into which many more molecules, as cholesterol, proteins with lipid anchors and proteins with transmembrane domains are incorporated. Phospholipid bilayers are a basic structural unit for all living cells. It has been hypothesized that the first form of life may have been a simple lipid vesicle with the ability to produce (or reproduce) more phospholipids [50]. Hence phospholipid bilayers can be used as a model to understand many features of biological membranes, e.g. the topology, shape fluctuations, phase behaviour, permeability, fission and fusion. These model membranes are studied in a broad spectrum of scientific disciplines (from [51]):

- In **mathematics**, the topology of two-dimensional surfaces in three-dimensional space governed by the bilayer elasticity
- In **biology**, model biological membranes with and without functional units, e.g. specific proteins or the cell fusion and the bilayer permeability

Parameter	EYL
molecular weight [g mol^{-1}]	770
cmc [mM]	$\sim 10^{-10}$
volume [34, 36] [Å^3]	1266
A_{D_t} [Å^2]	72

Table 1.3: Important parameters and values of EYL.

- In **pharmaceutics**, studies of drug action, medicine drug-delivery, medical diagnostics and gene therapy
- In **physics**, the aggregation behaviour (as in this study), inter- and intra-aggregate forces, soft and high-strength materials composed of phospholipids. Or one can use the well-defined physical characteristics of model lipid systems to investigate the colloid behaviour.

In this thesis the focus is set on the aggregational behaviour of bile salt/lecithin mixtures. Their properties have been studied with respect to different parameters, e.g. total concentration, lecithin-to-bile salt ratio, temperature and bile salt species [42, 43, 44, 45, 46]. However, these studies were performed under physiological conditions (neutral pH, 150mM salt) due to the biological and medical relevance. This will be explained in detail in section 1.5.

Nature produces giant unilamellar vesicles (GUVs) with diameters on the order of micrometers by a mixture of these two molecules. GUVs can be regarded as pre-forms or biological cells. But up to now, the formation of GUVs from a mixture of bile salt and lecithin in laboratory were not successful, vesicles formed were in the nanometer scale. The transitional pathways leading from micellar to vesicular aggregates and all compositional changes need to be understood to be able to mimic nature and produce GUVs, which would then serve in basic research as models for cell membranes.

With decreasing total amphiphile concentration, aqueous mixtures of lecithin and bile salt form a sequence of mixed aggregates: micelles, micelles coexisting with vesicles and then vesicles. This transition is driven by bile salt leaving the aggregate due to its high monomeric solubility [60].
In this thesis, the effect of deviations from physiological conditions was studied, namely the dependence on higher salt concentration, i.e. up to about 1M NaCl. This changes already the composition of the aggregate by an increased bile salt-to-lecithin ratio, since bile salt is charged and the repulsion within the aggregate is screened by the increased ionic strength. A detailed study of the effect of electrolyte concentration thus promises to lead to a better understanding

of the compositional and structural changes in lecithin-bile salt mixtures and its transitional pathways, which will hopefully lead to laboratory produced GUVs of this mixture.

1.5 Lecithin and Bile Salt: A Model Biological System

The concentration of phospholipids in bile is high. The main phospholipid is phosphatidylcholine. Both molecules together form a huge amount of mixed aggregates, like mixed vesicles, mixed micelles with a huge variety of structures depending also on the lipid (EYL) to detergent (bile salt, BS) ratio. [37].

First models for the structure of BS/EYL mixed aggregates were proposed in the early sixties by Small [33, 38] and Dervichian [39], where the hydrocarbon tails of the lipids are oriented towards the core of a disk, whose rim is made of bile salts. Mazer *et al.* [6, 40] expanded this disk model to the mixed-disk model, where they introduced bile salt dimers, which are hydrogen bonded in the inner part of the aggregate.

In the last two decades enormous variation from this model was found with light scattering experiments by Egelhaaf [41] and with neutron scattering experiments by Hjelm and others [42, 43, 44, 45, 46]. The aggregates are considered to be flexible rods with a radius r=27 Å [42] and a length of 50-3000 Å [43] depending on the lipid to bile salt ratio. Pedersen *et al.* [45] deduced a persistence length of 180 Å for flexible rods. Actually it was first proposed by Ulmius and Lindblom [47] and by Nichols and Ozarowski [48]. In these studies the deuterated lecithin headgroups were contrast matched and compared with the non-deuterated lecithin.

The endcaps are mainly consisting of around six bile salt molecules. The impossibility of the mixed-disk model at that time was shown by Cohen [49] with light scattering who showed that the bilayer thickness has to be about 1nm under the mixed-disk model assumptions. Lecithin stacked as bilayer are already 4 nm.

As lecithin and bile salt form mixed aggregates and have different spontaneous curvatures, changing the relative amounts of lipid and surfactant in the aggregates can be used to form aggregates of different average curvature.

The equilibrium behaviour of the lecithin-bile salt systems is well understood at physiological salt concentration, and has been studied using egg lecithin or a single lipid component as well as various different bile salts [39, 41]. The behaviour of the mixed system is complicated with a multitude of phases, and will not be discussed in more detail.

1.5.1 Vesicle-Micelle Phase Transition - A Thermodynamic Model for the Phase Behaviour

The vesicle-micelle phase transition, also known as membrane solubilisation, describes the transition of the lipid bilayers in mixed lipid/detergent systems by addition of detergent.

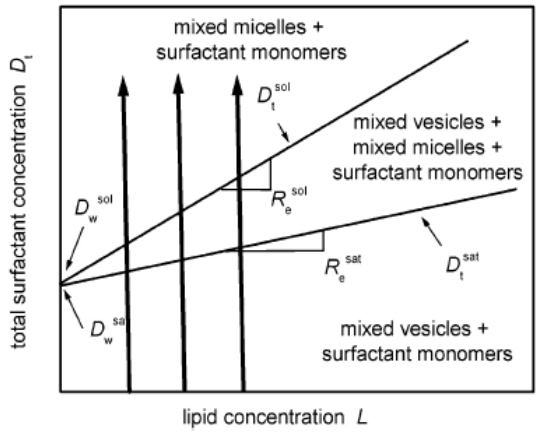

Figure 1.6: Typical phase diagram for a lipid-detergent system. It [52] shows the phase boundaries between the vesicular range to the coexistence region with mixed micelles and mixed vesicles and then to the micellar range. The slopes of the phase boundary lines represent the molar ratio of detergent to lipid at that point. D_w, the amount of detergent in the aqueous phase. In the ideal case, D_w for saturation and solubilisation should be the same and should correspond to the cmc of the system.

The vesicles incorporate the detergent molecules until they reach the critical detergent to lipid molar ratio, R_e^{Sat}, of full saturation, then vesicles transform into mixed micelles and mixed vesicles in coexistence phase. In the coexistence phase, mixed vesicles with a molar composition of R_e^{Sat} and mixed micelles with R_e^{Sol} are present [4, 53, 54, 55, 56, 57]. Above the saturation phase boundary is D_w^{Sat}, the mixed vesicles decompose to mixed micelles. Above the second critical molar ratio of detergent to lipid R_e^{Sol}, and the solubilisation phase boundary D_w^{Sol}, only mixed micelles exist. The solubilisation is finished, but by further adding of detergent the composition, the size and the form of the mixed micelle can change, for instance from a cylindrical to a spherical structure.

The vesicle-to-micelle transition is illustrated by Lichtenberg [56] in the scheme in figure 1.6. There is a straight line dependence and R_e^{Sat} and R_e^{Sol} represented the slope of the line, i.e. the phase boundaries of vesicle to coexistence and coexistence to micellar phase, respectively.

$$D_t^{sat} = R_e^{Sat} L + D_w^{Sat}, \tag{1.2}$$

and

$$D_t^{sol} = R_e^{Sol} L + D_w^{Sol}. \tag{1.3}$$

The total detergent concentration is D_t composed of D_w the detergent concentration in water and the detergent concentration in the mixed aggregate D_b, i.e. $D_t = D_b + D_w$. D_w^{Sat} and D_w^{Sol} are given by the intercepts of the two phase boundaries with the ordinate and represent the aqueous concentration of the surfactant monomer and correspond very closely to the *cmc* of the detergent [54].

The model introduced above represents an appropriate description at fairly high lipid concentration, but at very low concentration ($< 2mM$) this description cause inconsistency, since deviations from the linearity have been observed [58]. Roth *et al.* [54] have developed a model taking these deviations into account. They included the effects of finite size of a threadlike micelle on the phase behaviour of the system and, in addition the assumption, that the mixed micelles are a separate thermodynamic phase were refined by a more complex thermodynamic description. The chemical potentials of the lipid and detergent in the micellar phase differ to the chemical potential of the other phases. Based on this the phase boundaries were described by:

$$D = D_w + [\alpha R^{Sat} + (1 - \alpha)] \cdot L - \frac{A_{\mathrm{w}}}{\alpha^{0.5} L^{0.5}} \tag{1.4}$$

with α is the ratio between the concentration of the lipid in micellar form and the total lipid concentration, and A_{w} a fitting parameter taking the scission energy into account [54]. $\alpha = 1$ determines the solubilisation phase boundary with a complete transformation of mixed vesicles into mixed micelles (all lipid is in the mixed micelles):

$$D = D_w + R^{sol} \cdot L - \frac{A_{\mathrm{w}}}{L^{0.5}} \tag{1.5}$$

With the assumptions of this model the micelles need to be sufficiently long to have a nonvanishing lipid contribution in the micelle, so for $\alpha \ll 1$ equation 1.4 for the saturation line can be approached with a small α_{min} by:

$$D = D_w + R^{sat} \cdot L - \frac{A_{\mathrm{w}}}{\alpha_{min}^{0.5} L^{0.5}} \tag{1.6}$$

The equations 1.5 and 1.6 show that the deviation from linearity are contained in the third term. For high lipid concentrations this corrections can be neglected. But still the difference

between the intercepts D_w for saturation and solubilisation as experimentally observed cannot be explained. In chapter 6 this will be discussed in detail.

Partition Coefficient

In another terminology the phase state of the dilute mixture of detergent and lipid can be described in terms of the partition coefficient P, which characterised the ratio of the molar fraction of the bile salt in the aggregate x_b and in the aqueous phase x_w:

$$P = \frac{x_b}{x_w} \tag{1.7}$$

Both mole fractions can be transformed back to detergent concentrations in aqueous media D_w or aggregate bound D_b by:

$$x_b = \frac{D_b}{D_b + c_L} \qquad\qquad x_w = \frac{D_w}{D_w + W} \tag{1.8}$$

W is concentration of water, which is 55.5M and c_L the lecithin concentration.

Partition coefficients are useful, for example in estimating distribution of of the amphiphile in different phases. Hydrophobic molecules with high partition coefficients are preferentially distributed to hydrophobic compartments within lipid bilayers while hydrophilic molecules (low partition coefficients) preferentially are found in hydrophilic compartments such as shell of lipid bilayer.

Spontaneous Curvature

The micelle-to-vesicle transition is induced by dilution. This is due to the differences in the solubilities and in the average spontaneous curvature of bile salt and lecithin. Since bile salt is highly curved (C_{D_t}) and lecithin flat (C_L=0) and bile salt is more soluble than lecithin. Thus, upon dilution bile salt is leaving the aggregate and changes, i.e. decreases, the average spontaneous curvature of the mixed aggregate. A growth of the micelles is induced to avoid the energetically unfavourable endcaps [41, 43]. The difference of the free energy of the mixed aggregate can be divided into the entropy of mixing and the curvature energy.

Andelman *et al.* [4] estimated the average curvature of the mixed aggregate by weighting the occupied surface area (A_{D_t} and A_L surface area of detergent and lipid, respectively).

$$C_{\mathrm{S}} = \frac{A_{\mathrm{D_t}} n_{\mathrm{D_t}} C_{\mathrm{D_t}} + A_L n_L C_L}{A_{\mathrm{D_t}} n_{\mathrm{D_t}} + A_L n_L}. \tag{1.9}$$

1.5.2 Effect of Dilution

Most studies on lecithin-bile salt systems have been performed through a dilution series. Upon dilution micelles decrease in length, since the concentration decreases, but later a growth sets in due to a decrease of spontaneous curvature. Then the coexistence region of mixed micelles and vesicles is crossed and upon further dilution only vesicles exist. The size of the vesicles decreases with dilution, since upon dilution bile salt is leaving the aggregate and leaves aggregates with increased line tension and thus decreased closure time (See ref. [59]. The opposite direction, i.e. vesicle-to-micelle transition, was already described in the thermodynamic description.

The dilution dependent transition from micelles-to-vesicles and the described growth characteristics were measured by Arleth et al. [37] for a EYL/bile salt system and can be seen in figure 1.7. In (a) micellar growth behaviour can be obtained by fitting the appropriate model to the scattering pattern upon dilution and in (b) the typical oscillatory behaviour of vesicular structures can be observed. With increasing dilution the minima in the scattering pattern shift to higher q values, indicating smaller radii with increasing dilution.
Various scattering studies dealt with the structure determination of lecithin/bile salt system upon dilution. Generally the lecithin to bile salt molar ratio has been kept constant to 0.9 in [41, 45, 60], 0.5 in Hjelm *et al.* [44] and 1.1 in Arleth *et al.* [37] under physiological salt conditions. All these studies, despite the different molar ratios, showed the dilution dependent transition from micelles to vesicles. A schematic sequence of structures along the axis of dilution for one lecithin/bile salt molar ratio is shown in figure 1.8. The composition change of the surfactant aggregate leads to the transition from wormlike micelles to bilayer vesicles.

On the left side of the figure, i.e. the mixed micellar region (1.), there are long wormlike micelles due to the high amphiphile concentration in solution. Upon dilution they become shorter first due to the decrease of amphiphile concentration, but then the growth sets in again. Since bile salt is removed from the surfactant aggregate due to its higher solubility in contrast to the nearly insoluble lecithin, the average spontaneous curvature decreases with bile salt removal and the energetically unfavourable endcaps of the cylinder are avoided. A growth starts to avoid the "exposed" edges of the wormlike micelles. Further dilution leads to an increase in the lecithin to bile salt molar ratio in the aggregates, i.e. decrease in R_e. Especially, it was found, that the length of the micelles increase dramatically, when the cmc of the bile salt is reached and bile salt is leaving the mixed surfactant aggregate [43, 44, 46].

If was found [37] that the wormlike micelles can grow to a total length of more than several persistence lengths, where the persistence length is approximately 100 Å to 200 Å and the

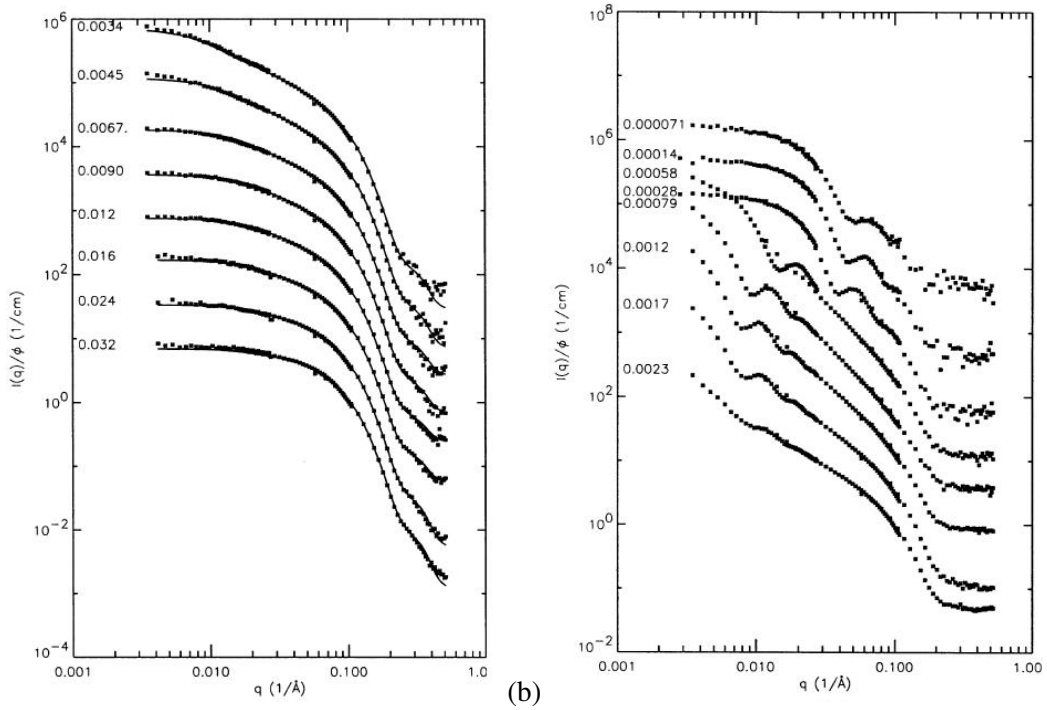

(a) (b)

Figure 1.7: SANS measurements of a dilution series with EYL and the bile salt, GCDC. (a) In the plot, each data set is multiplied by 4^n, where n runs from -3 to +4 starting from the lower-most spectrum. The sample volume fractions corresponding to the data are listed to the left of the data. The results of the simultaneous fit with the model for wormlike micelles are shown as the lines. (b) shows lower dilutions were vesicles are formed.

contour length along the cylinder can be greater than 1000 Å.

Actually, an empirical growth law describes the effect of dilution on the wormlike micelles with length L with a double power law [37]:

$$L(\Phi) = K_1\Phi^{0.5} + K_2\Phi^{-2} \tag{1.10}$$

Φ is the volume fraction of total amphiphile, K_1 and K_1 are positive constants. The first term describes the concentration induced growth and the latter the dilution dependent one.

Upon further dilution mixed micelles coexist with vesicles (region 2) as described in the thermodynamic model. At even higher dilutions, the only aggregates in solution are vesicles (region 3).

Most of the bile salts in lipid mixtures show the same behaviour, the only difference arises from their different cmcs. Trihydroxy bile salt as taurocholic sodium salt with respect to dihydroxy bile salt such as taurochenodeoxycholic sodium salt with higher cmcs shift the changes in the morphologies to lower dilutions.

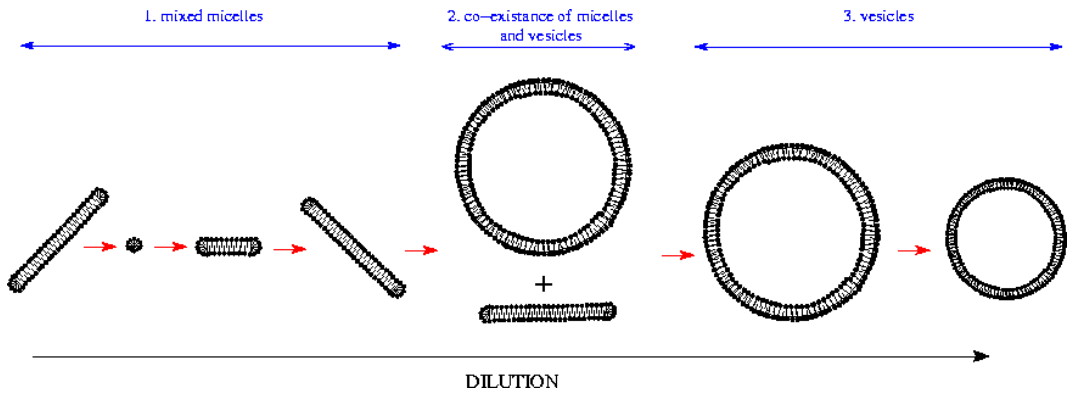

Figure 1.8: A schematic sequence of structures of the lecithin bile salt system upon increasing concentrations of water (i.e. higher dilutions). Scheme from the PhD thesis of Anniina Salonen. [61]

The concentrations at which the structural changes occur can also be affected by the solute. For instance, D_2O instead of H_2O for neutron scattering experiments, shifts the transitions to higher dilutions. The shift of the micellar phase boundary was reported to be shifted by 30% towards higher dilutions. [45].
A detailed description of the regimes is reported in Leng et al. [60] and [37, 62].

1.5.3 Effect of ionic strength

As stated above, the *cmc* of the bile salts has an effect on the onset of the micelle to vesicle transition in the phase diagram of the mixed system. The *cmc* is affected by the ionic strength of the solution. The effect of the salt concentration on the *cmc* of NaTCDC is investigated in chapter 6. The salt screens the electrostatic repulsion between the bile salt molecules, the Debye screening length increases, and thus changes the *cmc* towards lower concentrations and reduces the amount of free bile salt concentration in the solution.

The same should happen in mixed surfactant system, i.e. mixed micellar systems. Instead of lowering the *cmc*, the concentration of bile salt in solution is lowered (D_w). This is also part of the investigations performed in chapter 6 and the measured quantities for the *cmc* and D_w can be found there. Furthermore, the dilution dependent micelle-to-vesicle transition shifts with increasing ionic strength to lower dilutions, e.g. vesicular phase will be shifted to lower dilution, where the coexistence phase has been at lower ionic strength [60, 59]. The vesicle radius increases with added electrolyte. This is explained by a kinetic argument, that considers the formation of vesicles resulting from coalescence of intermediate micelles before closure becomes much faster than growth of the intermediate micelle. The growth rate increases with increasing ionic strength, but the rate of closure is not affected [59].

1.6 Thesis Layout

The outline of the thesis is as follows: The introduction gives an overview of the system used in this thesis, especially lipid, i.e. lecithin, and bile salt systems were described on their own first to then understand mixed lecithin/bile salt systems.

Chapter 2 describes the attempt to control the bile salt concentration using electrochemical methods. Since the background to this chapter and the experimental method used there are different to the rest of the thesis, this chapter has its own introduction with respect to electropolymerisation. Various electropolymerised films were characterised in terms of their bile salt exchanging properties upon redox cycling. Since removal of bile salt drives the micelle-to-vesicle transition of the EYL/bile salt system, the free bile salt content in solution (concentrations below the *cmc*) was aimed to be controlled. The dihydroxy bile salt NaTDC was investigated with respect to its redox activity in poly-n-methylpyrrole films. Poly-n-methylpyrrole showed excellent anion exchanging properties to monovalent anions with a molar weight of about 120g/mole. But unfortunately bile salts could not be exchanged with the polymer film and the focus was turned to the direct observation of the bile salt/EYL system.

Chapter 3 gives a description of the experimental techniques used along with a motivation why these techniques are applicable for investigating our system. The main experimental method used in this study is scattering to investigate the shape and size of the surfactant aggregates, but also isothermal titration calorimetry is used to determine the phase boundaries where the structural transitions occur.

In chapter 4 all materials, i.e. chemicals and solvents used for the sample preparation for the scattering and calorimetry experiments are listed. And in the next brief chapter 5, the first visual observations after sample preparation of our mixed NaTCDC/EYL and NaTC/EYL samples at higher ionic strength are shown. Both systems have a visible separation of“viscous” precipitate in the “non-viscous” phase.

In this study especially the influence of the higher ionic strength and the nature of the“two-phase” region was investigated: First in chapter 6 using the isothermal titration calorimetry technique, where the *cmc* of NaTCDC is determined with increasing ionic strength. Also the heat release and heat adsorption during the solubilisation process, i. e. the vesicle-to-micelle transition, of the EYL/NaTCDC system were observed and the phase boundaries between the micellar phase, coexistence phase of mixed micelles with mixed vesicles and the vesicular phase were determined. Further thermodynamic properties are extracted from the data, such as the amount of counterion binding and the partitioning coefficient.

Three different scattering techniques were used in chapter 7 and in chapter 8. In chapter 7 mostly the separated "non-viscous" phase was investigated by SANS and LS. In the next chapter 8, the "viscous" phase was studied with X-ray scattering.

In chapter 9 the results of the last three experimental chapters are compared. The last chapter summarises all the results and gives an outlook, in which direction the research of this system could evolve.

Chapter 2

Towards the Control of Bile Salt Concentration Using Electrochemical Methods

2.1 Aim

The aim of this work was to make a system to electrochemically control the bile salt concentration below the *cmc* in aqueous solution to enable control (and potentially monitor) of the surfactant aggregation to form vesicles. To achieve this, an electrochemically formed conducting polymer film has been investigated with respect to its ion exchange properties, especially to its bile salt anion permeability. Such a film would be used for the controlled ejection of bile salt anions into a solution of EYL to probe the kinetics of the surfactant aggregation of the chosen bile salt/EYL model system. Particularly this would enable the study of the way changes in local bile salt concentration effect vesicle formation, since bile salt concentration is the controlling parameter in the pathways to vesicle formation.

For this purpose, the polymer film should display high selectivity with respect to our chosen bile salt without allowing any other species in the solution to enter the polymer film. This is generally achieved with selective binding of the bile salt to favourable sites in the polymer film. This chapter therefore details studies of film permselectivity and sensitivity to bile salt anions.

2.2 Electrochemical Studies of Surfactants

There are many techniques to study micelles and micellar aggregation. Techniques such as light and neutron scattering are used for studying micellar systems, as they provide information on the structure and size of these systems, as they primarily give information about aggregates.

With surface tension measurements cmc of the surfactant can be determined.

Methods such as osmotic pressure or the conductance measurements gives again further information about the contribution of surfactant monomer in solution with and without micelles as stated in the introduction. Ion selective electrodes would provide a direct way of measuring the surfactant monomer concentration alone, during the formation of the surfactant aggregates in their natural environment. One would obtain data how surfactant monomer concentrations in equilibrium with the aggregate vary in different phases and also about the way surfactant monomer concentrations vary within mixed surfactant aggregate formation of various surfactants in different phases. Methods to obtain this kind of data have not been available up to now. This is a severe limitation as surfactant-selective electrodes give a response that is directly proportional to the surfactant monomer concentration.

The surfactant specific electrodes should be designed in a way to be highly specific to the surfactant of choice in the presence of other ions. Previously this has involved trying to design specific molecular recognition. There has been some initial studies in this area.

Surfactant-specific electrodes for measurements of the kinetic transition behaviour from micelles to vesicles in the lecithin-bile salt systems has not been exploited, yet. But this would be an optimal method to understand the phase transition from a micellar system to vesicles.

Evans *et al.* [63] used a Surfactant Ion Electrode to characterise the dimerisation constant and the aggregation behaviour of surfactants such as sodium dodecyl sulfate (SDS), decyltrimethylammonium bromide (DTAB), tetradecylammonium bromide (TTAB). The electrodes contained a liquid membrane ion exchanger, which permitted a direct determination of the surfactant monomer concentration. The measured voltage, E is.

$$E = E_0 + \frac{RT}{F} \ln a_B \tag{2.1}$$

In the following the term voltage and potential will be used interchangeably for *E*, since the potential difference is measured to a potential zero. E_0 is constant and obtained through calibration, and a_B the free surfactant ion *B* activity. The surfactant electrodes had three main parts, firstly the inner filling, which consisted of the sodium salt or bromide salt of surfactant anion or cation as appropriate. Secondly, a liquid membrane, the crucial sensing part of the electrode, which itself can be subdivided into mechanical support (a porous membrane) and an organic solution of a salt formed from the surfactant anions or cation and an ion exchanger cation or anion, respectively. For anionic surfactant, the ion exchanger was tributylhexadecylammonium [$Bu_3(C_{16}H_{33})N^+$]. And third part is the test solution. The selectivity of the electrode is based on the surfactant solubilities, therefore surfactants with similar chain length could not be discriminated. But the authors claim, that there was no significant response to simple anions such as chloride. The detection limits and the long term stability of the electrodes was never investigated nor stated.

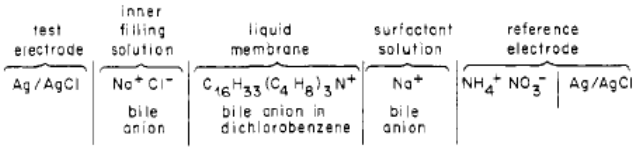

Figure 2.1: The surfactant electrode cell including the liquid membrane [64]

In a later study [64] micellar solutions of bile salts were investigated. A scheme for the surfactant electrode is shown in figure 2.1. The voltage E response of the bile salts, sodium taurodeoxycholate and sodium taurocholate in the presence of sodium chloride, and of egg yolk lecithin were investigated. Each showed nearly ideal Nernstian 2.1 response until the *cmc* was reached. The electrodes responded to the unaggregated bile salt but not to bile salt aggregates, i.e. only to changes in concentrations below the *cmc*. No measurements were made on the response time of the electrode.

These potentiometric ion sensors show promise in selective bile salt ion detection. However, in order to electrochemically change local bile salt concentration to study and monitor the kinetics of micelle to vesicle transition, an electrode is needed, which is able to inject into the solution and not only respond to the species.

Gharibi *et al.*[65, 66] studied the micellisation of sodium tetradecyl sulfate (STS) in the presence of poly(vinyl chloride) (PVC) membrane with a suitable plasticiser, containing an active ionic species (ionophore) of opposite charge to the surfactant. The ionophore was ”conditioned” with the surfactant to make the complex and the electrode could then be used to investigate the surfactant. But the complex did not have long term stability and was solubilised by the investigated solution.

Therefore Bloor *et al.* [67] used the same surfactant-specific electrode but with the membrane altered to covalently bond the ionic species to the PVC, which resulted in a membrane with an immobile complex and longer-term stability. This electrode can measure surfactant concentration of about 0.001 mM to 50 mM. But actually for the lower concentration the reading was never stable. However, Bloor *et al.* [67] measured the lamellar and micellar phase of hexadecyltrimethylammonium/hexadecanol upon dilution. But all the measurements were close to the lower limit of the recommended concentration range for the electrode.

In ion selective electrodes the cavities should be designed in a way that they are of same size of the target species and offer chemical binding sites that are specifically binding to the relevant species. This task seems to be relatively easy, but this is generally very difficult to achieve, since most of the ”ion selective electrodes” exhibit a lack of selectivity.

This ”type of problem can be described as challenging or highly impossible, depending on whether you are an optimist or pessimist.” [68].

Albery *et al.* [68] also worked an alternative strategy for surfactant selective electrodes, which are selective to a surfactant, where enzymes are used with molecular recognition. To develop such an electrode using synthetic chemistry with the specific ability to recognise a target ion with complicated shapes, they refer as an evolutionary step in chemistry.

To avoid this Albery *et al.* [68] worked on amperometric enzyme sensors. These use enzyme molecular recognition to measure the concentration of the solute. Particularly, they used the cofactor NADH enzyme electrodes [1], where NADH is oxidised on an electrode made of a conducting organic salt. The organic salt is NMP^{+}-$TCNQ^{-}$, i.e. a *N*-methylphenazinium tetracyanoquinodimethanide, which is then coupled to a reaction with the enzyme, which is selective for a certain substrate. For bile acids [69] the enzyme 3-α-hydroxysteroid dehydrogenase was used. The enzyme catalysed reaction follows the scheme below with the amount of reaction being determined by the reactants generated in the oxidation of NADH at the electrode:

$$BH_2 + NAD^{+} \longrightarrow B + NADH + H^{+}$$

$$NADH \longrightarrow NAD^{+} + H^{+} + e^{-}$$

BH_2 stands here for the reduced form of bile acids found in solution. Four bile acids were studied as TC, TCDC, CDC, and DC.

Albery *et al.* [68] studied the equilibrium between free monomers of bile acid and the bile acid present in the aggregates. This discrimination of the two types was possible by introducing a dialysis membrane, through which only the monomer diffuses and which is though to exclude the aggregates without perturbing the equilibrium. Then the free monomer was measured by the above enzyme electrode.

Although this enzyme electrode has the ability to measure specifically monomer concentration with a detection limit of about 1 μM, the long transport times (of the order of 5 min) of the substrate through the membrane would be undesirable for measurements of the changes in bile salt concentration as a result of bile salt/EYL aggregation, which has kinetics in the ps to ms range [69].

Recently, Shiigi *et al.* [70, 71] used polypyrrole to detect the bile acids, cholate, chenodeoxycholate, deoxycholate, taurocholate and dehydrocholate. They claim by potentiodynamically overoxidising a polypyrrole film doped with bile acid, a shape-complementary cavity of the dopant is created, which leads to selecitve recognition of the bile acid investigated. Due to

[1] commercially available surfactant-specific ion electrodes with Orion ion-selective electrode body [68]2-00-00

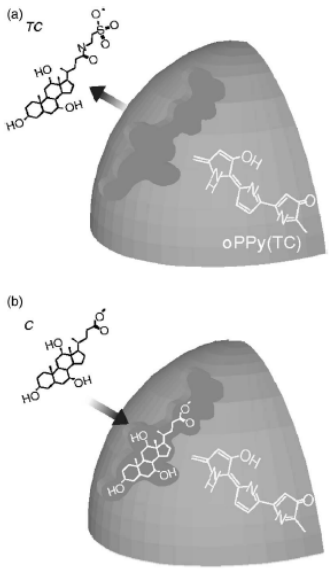

Figure 2.2: A model of selective cavity: (a) extraction of taurocholate, TC, from PPY film (dedoping), (b) and recognition of bile acids, cholate. From Shiigi et al. [70]

their so-called ”selective cavity”, they claim to be able to sense trace concentrations of 25 nM. But the experimental data of the cyclic voltamograms show hardly any conductivity or charge produced and therefore little ingress/egress of bile salt ions, which would be undesirable for the control of the bile salt concentration in our aggregation experiments. Especially they never tested the response of the film towards cation, although it is well known in literature [72, 73, 74], that polypyrrole tends to exchange cations by deprotonation as it will be explained later.

Up to now, there is no method that can monitor fast enough the bile salt aggregation in mixed surfactant aggregates. In this thesis the aim is not only monitoring, but also controlling the free monomer concentration in aqueous solution with a high selectivity. A prospective bile salt selective system could be achieved by producing a conducting polymer film, which has pores for specific binding of bile salt and allows continuous ingress and egress of the bile salt anion on oxidation and reduction, respectively.

Therefore, bile-salt electrochemical studies on these systems could offer a method to investigate the phase behaviour and the kinetics of aggregation.

2.3 Conducting Polymer Films

Daily life cannot be imagined without synthetic or polymeric materials. Polymers are compounds consisting of small structural units (monomers) connected by covalent bonds

to form macromolecules with high molecular weights. The monomers can be atoms or molecules themselves and the assembly results in linear chains or various other branched or interconnected structures. Polymers generally have a high stability and properties can be tuned to give hardness or elasticity [75]. In general they are non-conducting and are used as insulators, but one can obtain conducting properties by adding conducting material, e.g. graphite, ironoxide, copper or aluminum particles into the polymer matrix. These polymers are named extrinsic conducting polymers. With the creation of polyacetylene and the doping with AsF_5, iodine and bromine Shirakawa, MacDiarmid and Heeger [76] realised a new class of materials, the intrinsic, electrically conducting polymer film, which combines the mechanical properties of synthetic materials with the conductivity of metals [77]. Their electrical conductivity can be adjusted by several orders of magnitude by doping from insulators through semiconductors to metals. Research in conducting polymers over the past three decades has proceeded to rechargeable batteries, organic light-emitting diodes, sensors for gases, pH or organic materials. Many polymers have been studied intensively in the last decades, but in this thesis the concentration lies on polypyrrole, PPY, and *N*-substituted Poly-*N*-Methylpyrrole, PNMP. In figure 2.3 the structure of polyacetylene and polypyrrole can be seen.

2.3.1 Conduction Mechanism

Delocalised band model

From the general reference [78].
Instead of having discrete energies, as in the case of free atoms, the available energy states of the atoms form bands by successive addition or overlap of *n* atoms. This results in a formation of a band of n molecular orbital of finite width and finite number of separate orbital of discrete energy. In metals the bands overlap to form a continuous band. Whether the energy levels are occupied and whether specific bands are empty, partially filled or completely filled, classifies materials as insulators or semiconductors. Crucial to the conduction process is whether or not there are electrons in the conduction band. In insulators the electrons in the valence band, VB, are separated by a large gap from the conduction band, CB; in conductors like metals, the valence band overlaps the conduction band; and in semiconductors there is a small enough gap

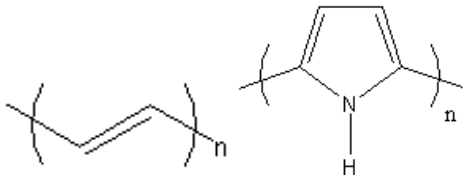

Figure 2.3: The stucture of a polyacetylene and a polypyrrole unit.

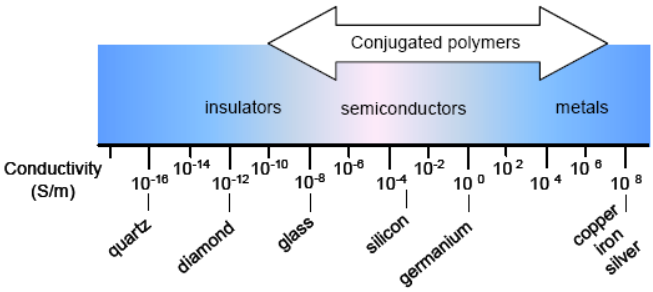

Figure 2.4: The conductivity of conjugated polymers. Taken from reference [77]

between the valence and conduction bands that thermal or other excitations can bridge the gap. With such a small gap, the presence of a small percentage of a doping material can increase conductivity dramatically. The size of this band gap defines the amount of energy required to promote the electron in the CB. Materials with a band gap of 1.5 eV are considered to be insulators. Most conducting polymers are in the semiconducting range, but can be increased to the metallic range upon doping. See 2.4.

The semiconducting properties of CPs arise from the polymers having a delocalised electron system along the polymer backbone. The (bonding) orbital forms a delocalised valence band and the (antibonding) orbital forms a delocalised conduction band.

To increase the number of charge carriers and enhance the semiconductivity is done by doping, which causes a change in the electronic population in the band. Dopants can be either electron-donating or electron-withdrawing species. If electron withdrawing dopants are used electrons are withdrawn from the filled band by forming a narrow band that accepts electrons from the valence band, leaving behind positive 'holes', which are also mobile and the substance becomes a p-type semiconductor. Alternatively, if the dopant carries access electrons, then a narrow band is formed just below the vacant conduction band of the semiconductor and can supply electrons to the conduction band, giving rise to n-type semiconductor.

In the delocalised band model for conducting polymers, the charge carriers are radical cations (polarons [2]).

Redox Chemical Model

In another model it is assumed that the conductivity is due to the charge hopping between oxidised and reduced states. The model is based on polypyrrole or polyaniline. These consist of extended $z\,\pi$ -electron systems from which electrons can be withdrawn or into which additional electrons can be injected. The unpaired electrons of the produced radical cations or anions are delocalised over several monomer units of the polymer chain and form polarons, that interact

[2] A polaron is formed, if a charge within the polymer matrix polarises by its electric field the local nuclear geometry around it, causing new electronic states in the gap.

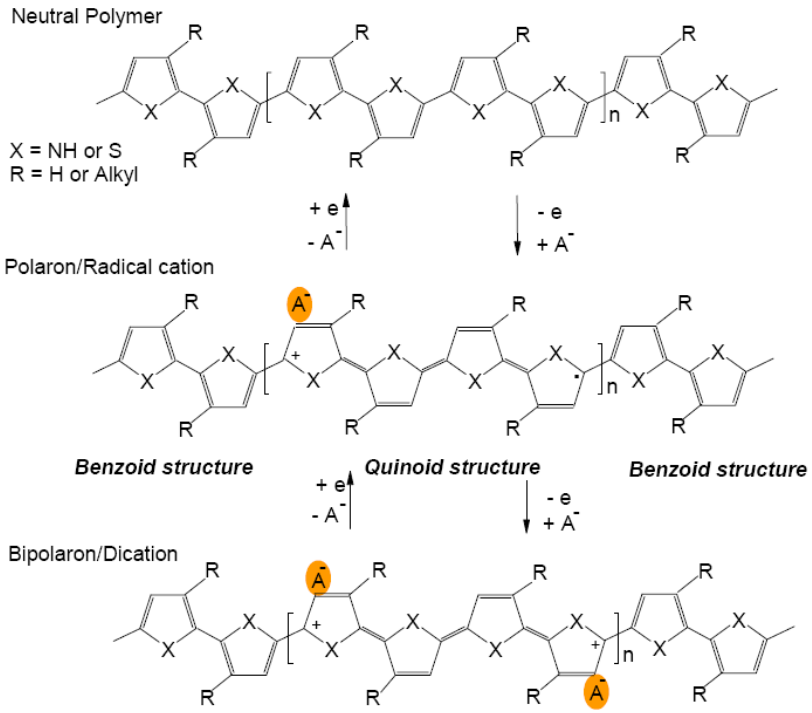

Figure 2.5: Redox scheme of conducting polymers.

with one other. See figure 2.5 and below.

2.3.2 Electrochemical Polymerisation

Electrooxidation of a conducting polymer takes place from a solution of the monomer in a suitable solvent, where the oxidation of the monomer is within the solvent limit, in background electrolyte. Since pyrrole has a relatively low oxidation potential, the electropolymerisation can be carried out in aqueous electrolytes. The loss of one electron from the monomer unit upon electrooxidation gives a radical cation that reacts with other monomers present in the solution to form oligomeric products and finally polymer 2.2. The overall concentration of the radical cation $[R^{\bullet+}]$ at the electrode is high as the electron transfer reaction is much faster than the diffusion of fresh monomer from the bulk. As a result, the monomeric molecules near the electrode find themselves in the oxidised state, where they can undergo dimerisation. These cationic species polymerise through a linkage predominately at the α position, where they have greater electron density. The cations, R, link between themselves to form carbon-carbon bonds by losing two protons. See figure 2.6. Further linkage via the same sequence of oxidation, coupling, deprotonation 2.2 leads to a chain of monomer units linked via their α-positions. This sequence can be seen below:

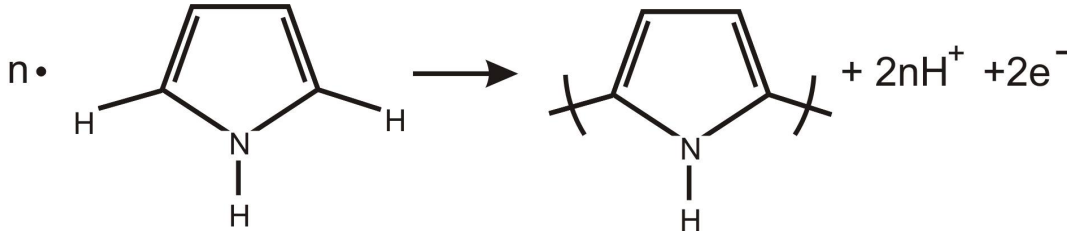

Figure 2.6: Mechanism of formation of Polypyrrole, where the ring on the left hand side stands for R and on the right hand side R_n stands for polymerised form.

$$R^{\bullet+} + R^{\bullet+} \longrightarrow R_2 + 2H^+ \xrightarrow{e^-} R_2^{\bullet+} + R^{\bullet+} \longrightarrow R_3 + 2H^+ \xrightarrow{e^-} \ldots \longrightarrow R_n + 2H^+ \quad (2.2)$$

With electropolymerisation the neutral non-conducting polypyrrole is not obtained, but the oxidised (doped) form. Actually, the final polymer chain, which is counter balanced by an anion, carries a charge every 3 to 4 pyrrole units, which can be seen in figure 2.7, where the brackets illustrate an oxidisable unit. The fully doped film consists therefore of about n monomers for every 2/n anions. The number of electrons removed in polymerisation per monomer is generally around 2.3, where the 2 electrons serve in the film formation 2.6 and the excess charge is consumed by the polymer oxidation. This number corresponds well to the number of anions found in the polymer. In first investigation of pyrrole by Kanazawa and Diaz *et al.* [79, 80], they carried out the electrochemical oxidation of pyrrole in aqueous H_2SO_4 on a platinum electrode. The product is a conducting polymer known as Pyrrole Black. Kanazawa *et al.* [79] synthesised films of polypyrrole, PPY, with a conductivity of 100Scm^{-1} which exhibited excellent air stability. The polypyrrole film formation is according to mechanism 2.2. This mechanism was confirmed by theoretical studies by Waltman and Bargon [81] and is the accepted polymerisation mechanism proposed for polypyrrole.

Of crucial importance for the successful use of conducting polymer films for the selective incorporation and expulsion of bile salt is the precise understanding and control over which ionic species are mobile in the conducting polymer film. During oxidation and reduction of PPY, electroneutrality is preserved by the movement of charge carriers: `(i)` on oxidation of the polymer by insertion of the anions or expulsion of the cations, `(ii)` on reduction of the polymer by insertion of the cations and expulsion of the anions or by a combination of `(i)` and `(ii)` [82].

In acidic solution the insertion and expulsion of the dopant is observed, in contrast to basic solution where the anion is replaced by hydroxy ions [83]. The stability of polypyrrole in aqueous solution is pH dependent, because polypyrrole can undergo (de)protonation processes. The polymer chain undergoes a deprotonation in basic solutions which results in

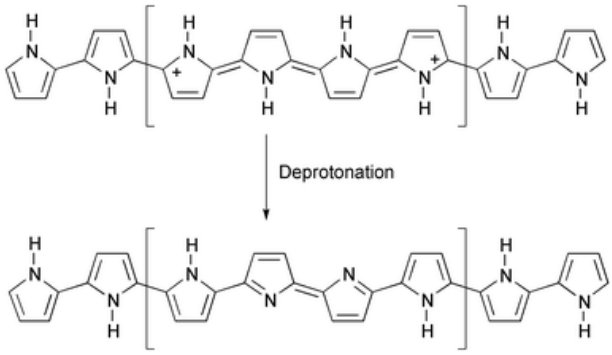

Figure 2.7: Deprotonation process.

the modification in the electronic structure and a decrease in conductivity and protonation in acid solutions [72, 73, 74]. See fig. 2.7.
The understanding of ionic ingression and egression into and out of polypyrrole films is very complicated and affected by size and valency of the dopant, the electrolyte solvent, pH of the solution or pH change near the electrode upon oxidation and reduction, (de)protonation and also hydrophobic sidegroups of the dopant, which might be shielded due to an orientation of the polymer chain parallel to the electrode surface to shield these hydrophobic groups in aqueous solutions. [84]
All these processes will affect the bile salt ingression/egression process. By using *N*substituted pyrroles, the deprotonation should play no role anymore [74]. In this chapter the ionic exchange process of poly-n-methylpyrrole (PNMP) doped with bile salt anions will be investigated [85].

PNMP

Among the derivatives of pyrrole, PNMP has attracted a great deal of attention and is widely studied. The biggest difference between the parent and its derivative are the methyl groups of PNMP at the nitrogen site: this introduces steric hindrance, which disrupts the chain planarity of pyrrole [86]. This results in a lower conductivity of PNMP, which is three orders of magnitude less than of pyrrole [86, 87]. This result was further confirmed by monitoring the conductivity of poly(3,4-dimethoxyl *N*-methylpyrrole, which was found to be also three orders of magnitude lower than that of poly(3,4-dimethoxypyrrole). The higher redox potential of PNMP, which increases from 0.7V vs. the saturated calomel electrode (SCE) for pyrrole to 0.8V vs. SCE for PNMP, might be due to steric effects caused by the methyl group at the nitrogen atom site [88] and in other studies [89].

Despite the lower conductivity, PNMP, is certainly a promising material for modified electrodes. The apparent colour change upon redox reactions from a brown at the reduced to a yellow at the oxidised end, may be used as material for electrochromic display [90]. Another

argument for PNMP could be that the ion channel size is enlarged by the introduction of methyl group on the nitrogen atom, so that relatively large anions can penetrate in the doped PNMP polymer film more freely than with pyrrole. The exchange behaviour of PNMP doped film will be investigated in section 2.5

Methodology

2.3.3 Electrochemistry

General reference: [91]
In electrochemical reactions a redox-active species is oxidised or reduced, i.e. a redox electron transfer process occurs on a chemically inert, but a conducting material, i.e. the electrode. For example, the electrochemical equilibrium of a metal electrode M, that exchanges its metal ions M^{Z+} with the solution, is obtained, when the electrochemical potential μ^* of the species in two phases is the same.
The electrochemical potential is defined as

$$\begin{aligned} \mu^*(M) &= \mu + zF\phi \\ &= \mu^0 + RT\ln a + zF\phi \end{aligned} \tag{2.3}$$

where *F* is the Faraday constant, *R* the universal gas constant, ϕ the electrical potential, z the number of exchanged electrons, μ^0 the standard chemical potential and *a* the activity. In case of a metal electrode the deposition and stripping of the metal in equilibrium is given by:

$$M^{Z+} + ze^- \leftrightarrows M \tag{2.3}$$

Depending on the conditions, positive or negative charges are collected at an interface and a potential difference can be observed. A metal electrode charges already by dipping into the solution, without an outer electric field. This effect results in a electrolyte double layer. The Galvani potential $\Delta\phi^0$ between the metal ions can be obtained from the equilibrium condition.

$$\Delta\phi^0 = \Delta\phi^{0'} + \frac{RT}{zF}\ln a_{M^{Z+}} \tag{2.4}$$

with $\phi^{0'}$ being the standard Galvani potential and it corresponds to the potential difference of the electrode and the solution with activity $a_{M^{Z+}} = 1$. The potential refers to the potential in solution (ϕ_s) and cannot be observed in measurements. For the equilibrium potential ϕ^0 of a metal ion electrode with a reference point of $\Delta\phi \equiv 0$ is:

$$E^0 = E^{0'} + \frac{RT}{zF} \ln a_{M^{z+}} \tag{2.5}$$

The activity of the metal electrode is equal to one and therefore does not appear in equation 2.5, which is known as the Nernst equation and $E^{0'}$ as the standard electrode potential. For the determination of this potential a second electrode, i.e. a reference electrode is needed. Measurements of potential difference, E, is made between two electrodes and the observed voltage is:

$$E^0 = \phi^0_W + \phi^0_{Ref} \tag{2.6}$$

$$= E^{0'} + \frac{RT}{zF} \ln a_{M^{z+}} \tag{2.7}$$

The equilibrium potential E^0 of the electrode results from the standard electrode potential $E^{0'}$. This is also known as the Nernst equation. For reducible and oxidisable, i.e redoxactive, species eq. 2.7 can be rewritten as:

$$E^0 = \phi^0_W + \phi^0_{Ref} \tag{2.8}$$

$$= E^{0'} + \frac{RT}{zF} \ln \frac{a_{ox}}{a_{red}}$$

where the index *ox* and *red* represents oxidation and reduction, respectively. The determination of equilibrium potential is possible for a defined reference point. A typical reference electrode is the normal hydrogen electrode, NHE, which is defined to be the origin of the electrochemical potential chart. The combination of a measuring electrode and reference electrode makes up an electrochemical cell. Oxidation occurs at the anode and the reduction at the cathode. If the electrochemical reaction occurs spontaneously without an applied current, this is called Galvani element in contrast to the ”forced” electrolysis reaction. The amount of the chemical change produced is according to Faraday proportional to the quantity of electricity passed,

$$m = \frac{QM}{zF} = \frac{ItM}{zF} \tag{2.8}$$

where M is the relative ionic mass, F the Faraday constant, z the charge on the ion, I the current and t time of the current flow. The current related to the chemical change is called Faraday current. The equilibrium of a electrochemical cell with current flow is a perturbed equilibrium with a non ohmic electrode resistance. When current flows, the electrode potentials are shifted

towards the direction of the current to new values. This deviation of E from the equilibrium value is called overpotential ν.

$$\nu = E - E^0 \tag{2.9}$$

In the case of electrolysis this overpotential occurs at both electrodes. The reason for the overpotential is the significant activation energy for the electron transfers at the electrodes. To determine the electrode potential with current flow, a three electrode system is used, comprising a working electrode, WE, where the reaction of interest occurs, a reference electrode, RE, which provides a reference potential against the driving force of reaction and a counter electrode, CE, which completes the circuit, allowing the passage of current for the WE reaction. The current in this set up, therefore, flows between the WE and CE and the potential of the WE is controlled relative to the RE, which is often placed close to the WE to minimise iR_s drop. Additionally, a background electrolyte reduces the electrolyte resistance, R_s, and therefore further minimises iR_s drop. The voltages in the system, can be described as

$$E_{appl} = (E_W - E_s) + iR_s + (E_s - E_{Ref}) \tag{2.10}$$

where E_{appl} is the voltage applied between the electrodes, $(E_{We} - E_s)$ the potential drop between WE and solution, i.e.the driving force for electrochemical reaction and $E_s - E_{Ref}$ the potential drop at the RE E_{Ref} solution interface. The last term is constant and dependent on the chemical composition of the reference electrode.
Adding background electrolyte ensures that *R* is small, hence the iR_s term is negligible, and $E_s - E_{Ref}$ is fixed, so the reaction driving force at the working electrode $E_{We} - E_s$ is solely dependent on the applied voltage E:

$$E_{appl} = (E_{We} - E_s) + constant \tag{2.11}$$

For low electrolyte concentrations or resistive solvents the iR_s term is no longer be negligible. Different potential pertubations such as a constant potential (potentiostatic method) or linear potential sweep voltammetry (potentiodynamic method) with different sweep rates can be performed. The resulting current will be recorded as function of time (current-time transient) or as a function of voltage (current-potential plots). The resulting currents represents the electrode reaction, which are governed by the rates of *i)* mass transport processes, e.g. of the material from the bulk solution to the electrode surface, *ii)* electron transfer at the electrode surface and *iii)* chemical reaction following the electron transfer, such as protonation or dimerisation at the

electrode surface.

2.3.4 Linear Sweep and Cyclic Voltammetry

Voltammetry provides valuable information about the rate and mechanism mechanism in electrochemical reactions direction by measuring the electrode current, the experimental observable, as a function of the applied voltage.
In **l**inear **s**weep **v**oltammetry, the working electrode potential is varied linearly with time, i.e. the applied signal is a voltage ramp, at a sweep rate $\nu[mVs^{-1}]$ in a stagnant solution. The current response is generally recorded as a function of the potential and produces for the oxidation a linear sweep voltamogramm, LSV. As the LSV begins at $E < E^{0'}$ (see 2.8 (b)), there is no current flow. As the voltage is increased to the reduction values, a current flow commences and eventually reaches a peak current (i_{pa}), which is characteristic of electrode reactions which have rapid electron transfer kinetics. If the electrochemical reduction reaction of the species in solution is fast a chemical equilibrium is established at the electrode surface at concentrations given by the Nernst equation. As the voltage is further swept all reactant close to the electrode is converted, i.e. reduced. The peak occurs, when the diffusion layer at the electrode has grown sufficiently high and the current drops. The applied potential E_{appl} varies as:

$$E_{appl} = E_1 + \nu_s t \tag{2.12}$$

Generally the sweep rate ν is in the range of 2 mVs^{-1} to 100 Vs^{-1}.
The curve in 2.8 (b) is for one sweep rate, but if the sweep rate is increase, each curve has still the same form, but current increases with increasing scan rate. Obviously the linear sweep voltamogram will take longer to record as the scan rate is decreased. Accordingly the size of the diffusion layer above the electrode surface will grow much further from the electrode in comparison to a faster scan. Thus, the flux to the electrode surface is smaller at slow scan rates than it is at faster rates. The current is proportional to the flux towards the electrode. A final point to note from the figure is the position of the current maximum, it is clear that the peak occurs at the same voltage and this is a characteristic of electrode reactions which have rapid electron transfer kinetics. These rapid processes are often referred to as reversible electron transfer reactions
If the sweep is repeated and the changes in the voltagramm on each cycle are monitored, the technique is called **C**yclic **V**oltammetry, CV. (Figure 2.8 (d)) The sweep in the forward direction produces obviously the same response as the linear sweep. When the scan is reversed, then basically the backward reaction is occurring (for a reversible reaction), and the backward reaction can be explained in the same manner as for LSV with i_{pa} the anodic peak current with

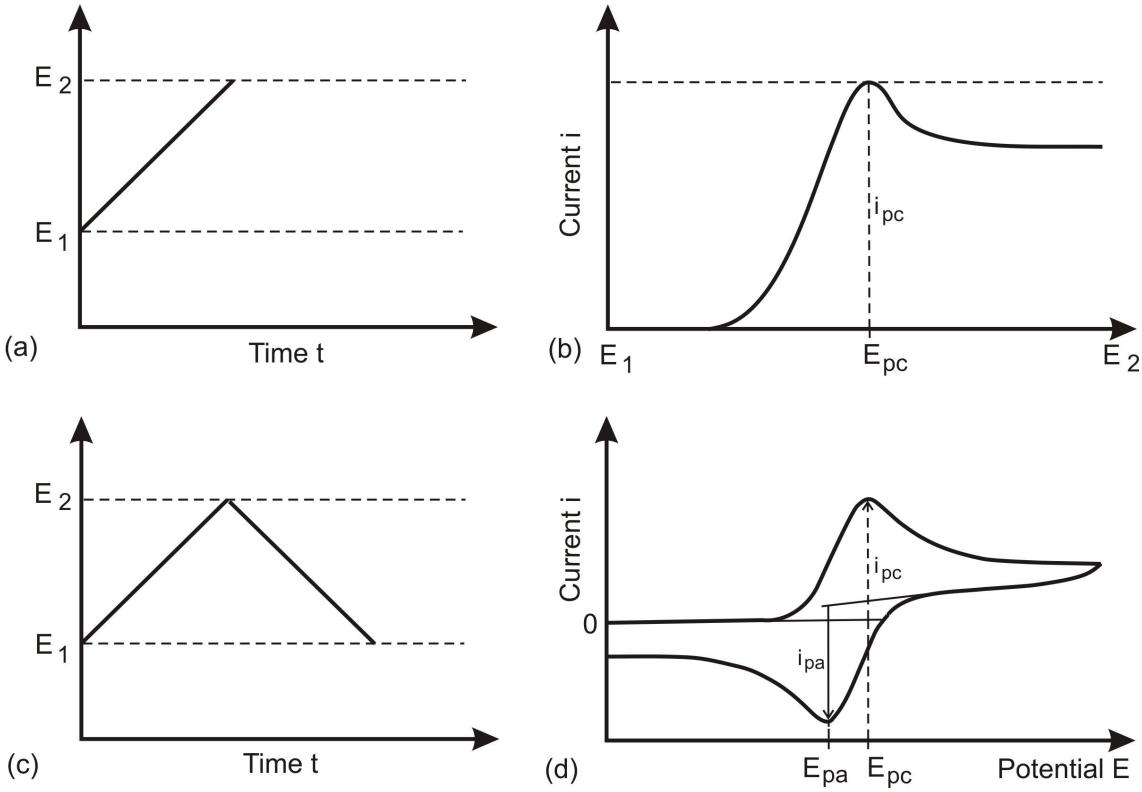

Figure 2.8: (a) The potential sweep (b) and the corresponding current response for an electron transfer oxidation reaction in a Linear Sweep experiment. (c), (d) correspondingly for a Cyclic Voltammetry experiment.

the corresponding potential E_{pa}.

A CV is very often used to characterise conducting polymer film, because the reversibility of the electron transfer process in oxidation and reduction can be monitored in form of a current-potential diagram, which shows the influence of chemical reaction on the observed voltammetric behaviour.

2.3.5 Electrochemical Quartz Crystal Microbalance

When monitoring the electrodeposition and doping/dedoping of a conducting polymer film with voltammetry, the electrochemical quartz microbalance (EQCM) can be used additionally. The linear relationship between the accumulated mass on the electrode and the change in frequency of the quartz oscillator allows the study of electrochemical processes coupled with mass changes due to ingress/egress of ions and solvent into/out of the polymer film with the simultaneous measurement of the polymer oxidation state observed by current, potential or charge.

The physical basis of EQCM measurements is the inverse piezoelectric effect, in which an

application of an electric field across the piezoelectric material induces a deformation of the material. By applying the resonant frequency, which is geometry and material dependent, the piezoelectric material will be induced to oscillate, and a standing acoustic shear wave is created within the crystal. For use in the determination of mass changes in thin films, quartz is by far the most commonly used piezoelectric material.

The material can be in various resonant modes. By cutting the crystal, modes can be suppressed. The AT cut is the most commonly used for EQCM measurements. The fundamental frequency of AT cut crystal is reciprocally related to the thickness of the crystal. The mass sensitivity increases as the square of the fundamental frequency of the crystal and linearly with the harmonic number for a crystal with a given fundamental frequency.

$$\Delta f = -\frac{f_0^2 \Delta m}{N\rho} = -\frac{f_0^2 \Delta m}{n(\rho\mu)^{1/2}} \tag{2.13}$$

Where Δf is the frequency change induced by the gain or the loss of mass, f_0 is the resonant frequency of the crystal before the addition/loss of mass, Δm is the mass per unit area in, N is a frequency constant of the quartz used (containing the material properties of the shear modulus), the harmonic number n, the density ρ and the shear modulus μ of quartz. Eq. 2.13 is often written as

$$\Delta f = -C_f \Delta m \tag{2.14}$$

in which C_f is a combined constant which contains all above material properties. This equation was named after Sauerbrey [92], who did a pioneering work on EQCM.

For very small masses increases the above equation performs well, i.e. Sauerbrey‘s assumption holds that the additional mass on the crystal has the same acousto-elasto properties. This holds for small mass loadings, where the change in resonant frequency is less than 2%. But for thicker film, where the deposited mass can be sheared as well, the above equation becomes inaccurate. Lu and Lewis [93] analyzed a loaded crystal, where the properties of the deposit become important, described by treatment of the difference of the acoustic impedance of the quartz substrate and the acoustic impedance of the material. This new description is often referred as Z-match (impedance-match) with $Z = (\rho\mu)^{1/2} = \rho\nu$ with ν the speed of sound in the material. The use of this treatment requires the knowledge of the shear modulus μ_f and the density ρ_f of the deposited material, which is in general unknown, especially for electrochemically generated films.

$$tan\left(\frac{\pi f_c}{f_0}\right) = -\frac{\rho_f \nu_f}{\rho_q \nu_q} tan\left(\frac{\pi f_c}{f_f}\right) \tag{2.15}$$

In this equation f_c is the resonant frequency of the quartz crystal plus the deposited film, f_0 is the resonant frequency of the QCM without film and $f_f \nu/2$ is a quantity referred to as the resonant frequency that the free standing deposited film would have.

The experiments in this report will be performed within the thin film limit. But for organic polymer films the possibility of viscous loss within the deposited film is significant especially under conditions of solvent swelling, where in the solution shear wave damping is occurring. Kanazawa et al. [94] described the general case for such films, but unfortunately there are several unknown quantities in his master equation (see [94]) like viscosity, density, velocity of the acoustic wave in the deposit, shear modulus of the deposited film and the resonant frequency of the free standing deposited film.

There is also the possibility to measure with a QCMD, which is a Quartz Crystal Microbalance with Dissipation monitoring. They are especially designed to characterise thin films such as polymer films on surface in a liquids. If the film consists of a high amount of water or solvent, then the rigid film regime and consequently Sauberbrey equation does not hold and the dissipation of the crystal is measured by response of the freely oscillating crystal that has been vibrated at its resonance frequency. In QCMD also the viscoelastic properties can be extracted. However, a QCMD, was not available for the experiments performed in this chapter.

2.4 Experimental

2.4.1 Chemicals

All chemicals were obtained from Fisher Scientific, unless otherwise stated. Pyrrole(Fisher Scientific, analytical grade), *N*-Methylpyrrole (Aldrich) was distilled prior to use and stored in a refrigerator.

2.4.2 Commercial Chemicals

All salts such as NaCl, KCl, LiCl, CsCl, Na pTS (sodium para-toluene sulfonic acid, analytical grade), TEACl (tetraethylammonium chloride, purum), were used as received. Lithium perchlorate (Aldrich, 99.99%) was dried in an oven for 2 days at 80° before use. NaTDC (Sodium taurodeoxycholate hydrate, purum 98%) was used as received. The residues (2%) in NaTDC is mainly due to cholate and taurcholate residues.

2.4.3 Solvents

All water was doubly deionised from a Millipore-Q water system (resistance $18M\Omega$ /cm). Acetonitrile, MeCN (for rinsing Fisher Scientific, HPLC grade and for the background electrolyte J. T. Baker, Ultra Low Water grade), ethanol (Aldrich, analytical grade), DMSO (Aldrich) were all used as received.

2.4.4 Apparatus

The Autolab potentiostat PGSTAT30 combined with the General Purpose Electrochemical System software (GPES) from Autolab, providing a fully computer controlled electrochemical measurement system, was used to carry out the electrochemical experiments [95].

The EQCM measurement were performed with the Research Quartz Crystal Microbalance by Maxtek and connected to the Autolab GPES system. The Maxtek system also is fully computer controlled and is connected to the current and voltage outputs of the potentiostat [96].

2.4.5 The Electrodes

A standard three-electrode system was used with a SCE reference electrode and a 2 cm^2 Pt gauze counter electrode, which was cleaned with acetone or sulphuric acid, subsequently rinsed with dionised water and flamed with a bunsen burner before use.

For non-aqueous work, a Ag/Ag^+ (0.437V w.r.t. SCE) reference electrode was used (Russel Electronics). For aqueous work a saturated calomel electrode (SCE) was used.

For the EQCM measurements at room temperature AT cut 5 MHZ crystals (Maxtek) were used as a working electrode. The electrode material is gold on a crystal and has a overall diameter of 1 inch, i.e. an area of 5.07 cm^2, which is clamped via an O-ring. The area of the gold alone is 1.37cm^2. The frequency constant for an AT cut crystal is 166.8 Hz cm. This corresponds to a crystal thickness of about 333 μm and a sensitivity factor of about 0.056 Hz cm^2 ng^{-1} at 20 $^\circ$C.

(PNMP/TDC) films were grown at between 0 to 0.8 V in a solution of 0.1 M PNMP and 0.05 M NaTDC. The film thickness was estimated by assuming that 240mC cm^{-2} corresponds approximately to 1 μm with consideration of the reported value [97, 98]. Unless stated otherwise, cyclic data are those of the second cycle of two consecutive cycles after being held a positive potential was plotted.

2.4.6 Electrochemical Synthesis

Conducting PNMP was obtained by of electrochemical deposition by cyclic voltammetry from aqueous, degassed solution, where argon was bubbled into the electrolyte solution prior to the experiment: 0.1M N-methylpyrrole with 0.1 M of the appropriate salt yielded a PNMP film doped with the counteranion of the respective salt. In a typical experiment, an electrolysis charge of 160 mC was used, producing a conducting polymer film of about 920nm. The film thickness was estimated by assuming that 240mC cm^{-2} corresponds to approximately 1 μm [98, 97].

In this thesis, the mass of the polymer film will be calculated from the value of the mass change, obtained by the frequency data in the electrochemical preparation of the film. Unless stated otherwise, cyclic data are those of the second cycle of two consecutive cycles after being held at a negative or positive potential below the potential limit.

All experiments were performed at T=25°.

2.4.7 Electrochemical Studies

After deposition, the films were carefully rinsed with distilled water and characterised in a monomer free 0.1 M aqueous solutions of NaCl, KCl, LiCl, TEA^+Cl^- as appropriate. With simultaneous cyclic voltammetry and EQCM measurements the obtained films were characterised in these background electrolytes. The potential was swept between a lower and an upper limit at a potential sweep rate, ν. Usually the potential was cycled from -800 mV to 200 mV or to 600 mV at 50 mV/s. Also repeated potential step experiments were performed between the oxidised and reduced forms of the polymer film.

2.5 Results and Discussion

The combination of the voltammetry and the QCM data from the EQCM, i.e. mass, charge and potential can be used to determine the permselectivity of the polymer film. As described in section 2.3.2, it has been shown that PNMP can be used as a modified electrode to investigate the mass transport mechanism of several ions in/egressing in/out of the conducting polymer film.
The work presented here is mainly concerned with the exchange behaviour of electrodeposited PNMP films on a gold electrode surface in the presence of TDC^- anions, either initially doped in the film during polymerisation or subsequently doped into a film made with a smaller, non-surfactant anion by redox cycling. Efforts have been directed to the elucidation of the charge transport mechanism to understand the bile salt anion exchange in these films. Charge

transport in a film consists of electron transport and of ion transport, because ion transport in most conducting polymer films is much slower than electron transport, it governs the redox properties of polymer films.

There are three possibilities for the mode of ion transport.

1. Anion exchange
   The film is permselective to anion. Upon oxidation the polymer film has a positive backbone. Therefore oxidation results in anion ingress and reduction in anion as well as solvent egress. The ingress/egress is accompanied with a mass increase at the positive potential limit.

2. Cation exchange
   The film is permselective to cations. Upon oxidation the polymer film has a positive backbone, whose charge is counterbalanced by immobile anions in the film already. Reduction (to give a neutral polymer backbone) with anions still in the polymer film results in an ingress of cations. Mass increase occurs therefore upon reduction by insertion of cations.

3. The film is neither permselective to cations nor to anions. Therefore both simultaneously ingress/egress in the polymer film.

Moreover, when the mass change is less than the ion-specific transport, the small mass change has been explained by counterion transport or counter directional solvent transport or even with neutral salt transport. The solvation itself depends on the nature of the ion inserting the film and also the lyophilicity or lyophobicity of the polymer film.
The purpose of the following studies was to obtain information about the ion exchange behaviour for the controlled injection of bile salt anions into the solution for further studies of lecithin-bile salt aggregation.

2.5.1 (PNMP/Cl)

It has been previously shown for PNMP the dominant ionic species depends on the choice of the dopant anion and the solvent and electrolyte system [72]. Anion transport is dominant in film doped with a small sized anion such as (PPY/Cl) films [99] and (PPY/Cl) films [100].
PNMP polymerised with Cl counterions (PNMP/Cl) was investigated in different electrolytes by cyclic voltammetry. This was also performed the calibrate the electrochemical studies of various PNMP polymer films in comparison with the already published data about similar polymer film.

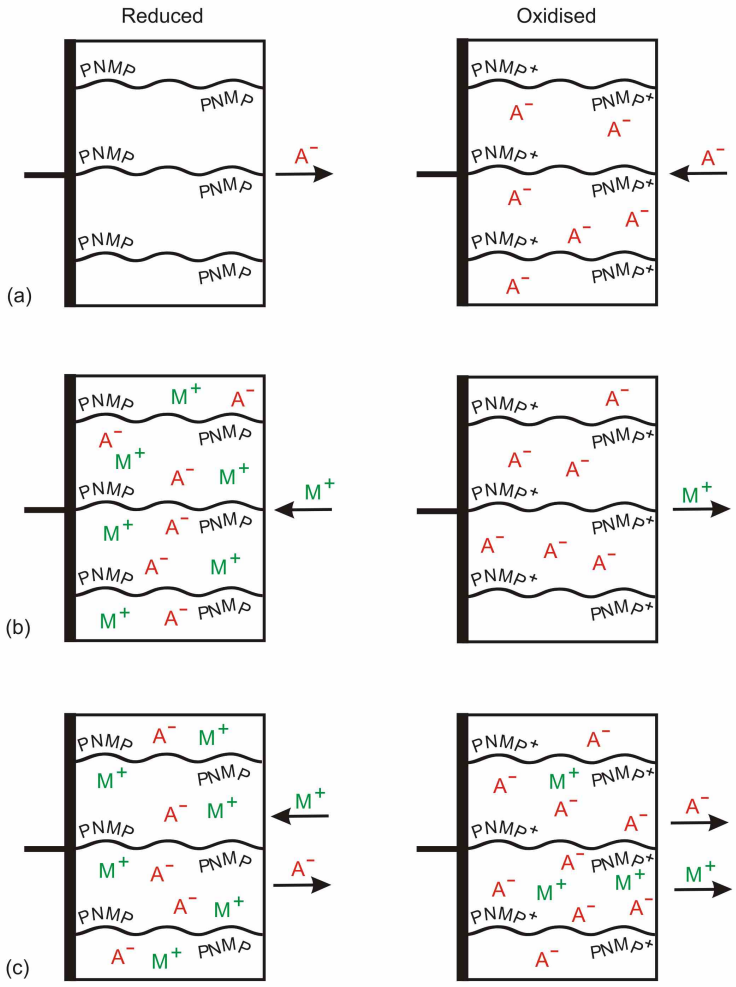

Figure 2.9: (a) Schematic diagram of the anion (b) cation and (c) simultaneous anion and Cation exchange behaviour:

The voltamogramms tell us about the electron transfer processes of the polymer film, whereas the EQCM tells us about the ion transfer processes. Both CV and the EQCM experiment are monitored at the same time to extract the ion exchange behaviour of the film.

In figure 2.10(a) the typical mass and current data for potentiodynamical film formation of (PNMP/Cl) are shown. In the first cycle, starting from the negative potential to the positive limit (shown as zero mass change Δm), the oxidation of the monomer can be observed between 0.7 V and 0.8 V. This is accompanied with an increase in mass on the electrode due to polymerisation and film growth. The increase in mass ends on the return sweep at about 0.65V. The polymer film grows in the subsequent cycles as shown by the continued mass increase.

Also redox reaction with an incorporation of electrolyte ions (between 0 V to 0.6 V) (seen by an increase in mass in this region during polymerisation) and expulsion between 0.55 V to 0 V

(mass decrease) of the electrolyte anion can be observed. The grown film has a broad oxidation peak and a sharper reduction peak. The total frequency change of the film is of around 2760 Hz, which corresponds to a mass of 48.75 ug/cm^2.

Figure (2.10 b) shows an extract of three individual CVs (starting from the 3rd cycle) of the polymerisation of (PNMP/Cl). Especially looking more closely at the mass increases and decrease in the area of redox cycling, one can already associate qualitatively the doping and dedoping from the bulk solution with Cl anions following the redox scheme, which corresponds to the scheme from figure 2.9(a).

$$PNMP^0 \quad \underset{\leftarrow -Cl^-,+e}{\overset{+Cl^-,-e\rightarrow}{}} \quad PNMP^+(Cl^-) \tag{2.16}$$

The grown film was afterwards cycled in a solution of 0.1 M NaCl (figure 2.11). The film should display in this electrolyte simple Cl exchange, since it is a small and mobile anion, which is unlikely to be entrapped [101]. This (PNMP/Cl) film can be used as a "calibration" for the combined electrochemistry and EQCM measurements to follow. Also the reliability of the analysis procedure can be verified.

Fig. 2.11 (a) shows a CV. Each cycling of the potential is accompanied with a reversible mass change. The mass increases as the oxidation current increases. This confirms that selectively anions go in and out during redox cycling.

The plots of the mass change (Δm) vs. the charge (Δ Q) during the redox reaction of the (PNMP/Cl) film in a solution of 0.1 M NaCl are shown in figure (2.11 b). As it is linear, i.e. the redox charge is proportional to the anion mass change. From the slope of mass vs. charge plots, the apparent molar weight of the charge compensating species can be deduced. By using the Faraday$'$s law 2.8, the slope simply gives the molar mass of the ion exchanged per electron:

$$M = zFA\frac{\Delta m}{\Delta Q} \tag{2.17}$$

with M as the molar mass, z as the electric charge of the charge compensating species, F the Faradays constant, A as electrode area and Δm the change in mass and ΔQ the change in charge, respectively. The Δ m vs. Δ Q plots are linear, i.e. the redox charge is proportional to the anion (chloride) exchange in (PNMP/Cl) films and shows hardly any hysteresis behaviour (discussed later) as can be seen in fig. 2.11 b). The number of water molecules k_{H_2O} transported with chloride ion can be expressed as,

$$M = M_{Ion} + k_{H_2O}M_{H_2O} \tag{2.18}$$

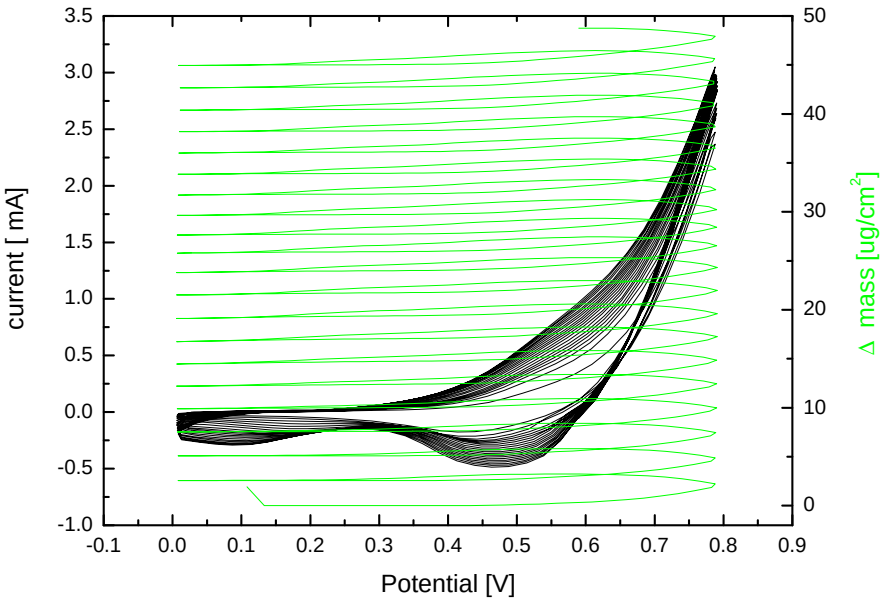

(a)

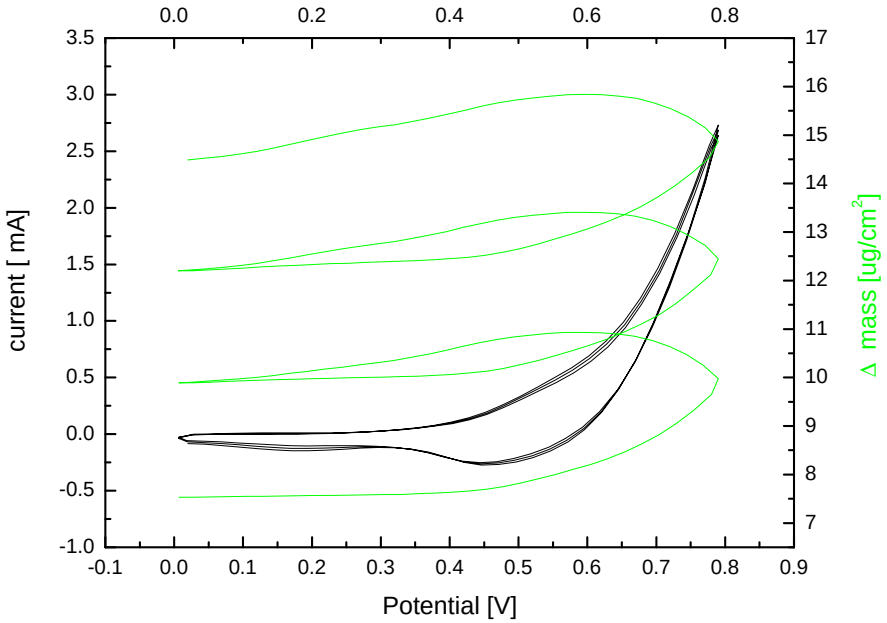

(b)

Figure 2.10: (a) Polymerisation of 0.1 M PNMP in 0.1 M NaCl. Potential swept between 0 mV and 800 mV with a sweep rate of 50 mV/s. Mass change Δm starts at 0μg/cm^2. (b) Three individual cycles during polymerisation, 3rd to 6th cycle.

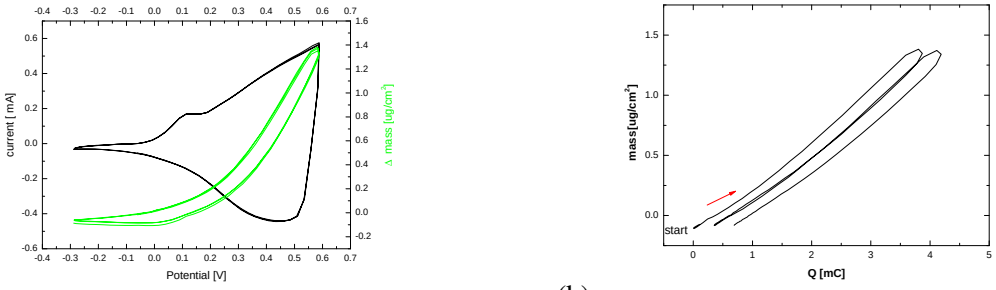

(a) (b)

Figure 2.11: (a) Current and mass responses of a (PNMP/Cl) film on a gold electrode to cyclic potential sweeping in 0.1 M NaCl solution with a sweep rate of about 5mV/s. (b) Mass change Δm vs. charge plot under the same experimental conditions as in (a)

where M is the observed ionic molar mass, M_{Ion} the unsolvated molar mass of the ion and M_{H_2O} the molar mass of the water molecule. [102, 103]. This relationship can be used to determine the number of water molecules which accompany ion ingress, as the total mass increase can be attributed to the mass increase due to both anion and solvent.

The molar mass of chloride is 35.45 g/mol, the obtained average value obtained in five consecutive cycles is 58 $\pm$ 2 g/mol, which corresponds to one chloride ion coordinated with 1.25 water molecules.

Although a lot of work has been done in transport mechanism in polymer films, there are only a few studies referring to the number of accompanying water molecules per ion and ingressing and egressing a polymer film. Xie et al. [74] investigated the pH dependence of PPY and PNMP conducting polymer films and showed in their electrochemical studies, that water-free chlorine ions are inserted into a polypyrrole film, but that the cations are solvated during the ingression into the polymer matrix. Kwak et al. [104], [105] investigated the mass transport with electrochemical and electrogravimetric impedance techniques in PNMP and PPY films doped with chlorine and copper phthalocyaninetetrasulfonate, where in the latter cation transport prevails. They deduced the number of accompanying water molecules per ion in different electrolytes. Although the polymer films had comparable thickness to the polymer film characterised in the study of Xie et al., the number of accompanying water per anion was larger In (PNMP/Cl) films tested in 0.1M $MgCl_2$, 1.3 water molecules were found to ingress/egress into the coat with Cl^-, which agrees well with our result.

In subsequent CVs with simultaneous mass acquirement, the total mass change (Δ M) and charge change (Δ Q) during the scan decreases gradually, but the ratio of M to Q is constant. This shows that the ion transport behavior and k_{H_2O} are uniform independent of the number of redox cycles and the redox cycling capacity.

As known for PPY films doped with Cl, PNMP films doped with Cl exhibit the simplest

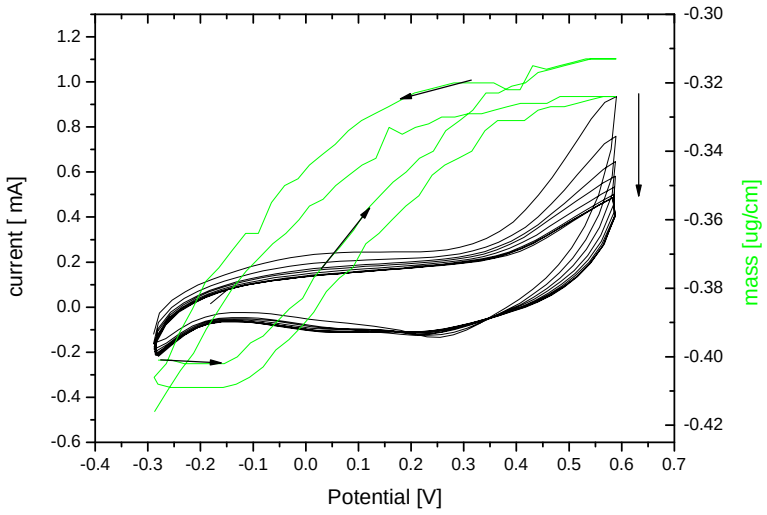

Figure 2.12: CV and mass measurement of a (PNMP/Cl) film with 0.1M NaTCD with a sweep rate of 50mV/s. The film is afterwards detached from the working electrode.

possible ion exchange behaviour: a film formed with chloride dopant with the ingress and egress of anions upon redox reaction. Obviously this polymer film can therefore be used for further investigation and will be used as a reference for all other PNMP modified electrodes.

An exchange with heavier anions such as the bile salt anion, TDC^- in (PNMP/Cl) films was not observed. This can be seen in figure 2.12. The film exchanges hardly any mass, the measured mass change per cycle is 0.08 μg/cm^2 and with a total mass of 35.45 μg/cm^2, this corresponds to a 0.23% of the total polymerised mass of the film. With each cycle the film becomes less and less electroactive and it visibly detaches from the surface of the working electrode.

The PNMP was also polymerised in the presence of different supporting electrolytes as in 0.1M $LiClO_4$ making a (PNMP/ClO_4) film or 0.1M Na pTS forming a (PNMP/p TS) film. This tested the concept of changing the dopant to achieve a different ion selectivity.

2.5.2 (PNMP/ClO_4)

PNMP was polymerised in the presence of $LiClO_4$ as before with NaCl, see figure 2.13. A (PNMP/ClO_4) film containing perchlorate anions was obtained in form of a thin film covering the gold crystal of the electrode. With perchlorate a heavier dopant anion is used. The redox peak position (both positive) and the increase of mass associated with this redox peaks, shows clearly anion doping of the polymer film as before for (PNMP/Cl). Again by looking closely at the mass change connected with the redox cycling, the following the redox scheme can be

	MW[g/mol]		mean MW [g/mol]	k_{H_2O}
	Cation	Anion	Oxidation	
NaCl	22.99	35.45	80.7 ± 0.4	2.1
$LiClO_4$	6.94	99.45	137.5 ± 0.9	2.1

Table 2.1: The molar weight of the electrolyte ions for the (PNMP/ClO_4) film.

inferred:

$$PNMP^0 \quad \underset{\leftarrow -ClO_4^-,+e}{\overset{+ClO_4^-,-e\rightarrow}{\rightleftharpoons}} \quad PNMP^+(ClO_4^-) \tag{2.19}$$

If one calculates the polymerisation charge from the linearly increasing current observed between 0.6V to 0.8V, i.e. Q_{pol}, with the redox charge at the reduction peak, which is assigned to perchlorate anion redox reaction between -0.05V to 0.45V Q_{redox}. Then one can calculate the doping level x, which is defined as:

$$x = \left(\frac{1}{2}\left(\frac{Q_{pol}}{Q_{redox}} - 1\right)\right)^{-1} \tag{2.20}$$

With polymerisation charge of 108mC and a redox charge of 12.5mC, a doping level *x* of 0.26 is obtained. This means that for every 3.8 PNMP rings, one will find a redox charge, and assuming complete permselectivity for the perchlorate anion, i.e. one associated perchlorate anion preserves electroneutrality. Calculating the mass by just including the mass of the pyrrole rings and the mass of one perchlorate anion, times the amount of moles produced by the polymerisation charge, one obtains 53 μg (the area of the electrode is 1.37cm^2) and therefore the polymer film mass density is 38.7μg/cm^2, which is lower, but in still very good agreement with the measured mass by the EQCM of 48.58 μg/cm^2. The discrepancy between these values can be easily understood in terms of water molecules entrapped in the film or neutral salt transport during the polymerisation, which are not represented in the charge. The use of Sauberbrey equation holds and the polymerisation efficiency can be seen to be near 100%.

This doping level is similar to the ones reported in literature, *x* was found to be 0.3 for chloride ions. Again the modified electrode with the polymer film was afterwards cycled in different background electrolytes at various sweep rates, starting with a solution of 0.1 M $LiClO_4$ (figure 2.11). The film displays simple ClO_4 exchange. Figure 2.13(c) shows, how closely the mass follows the current. The analysis performed to calculate the molar mass of the perchlorate anion and for all other anions is as in section 2.5.1.

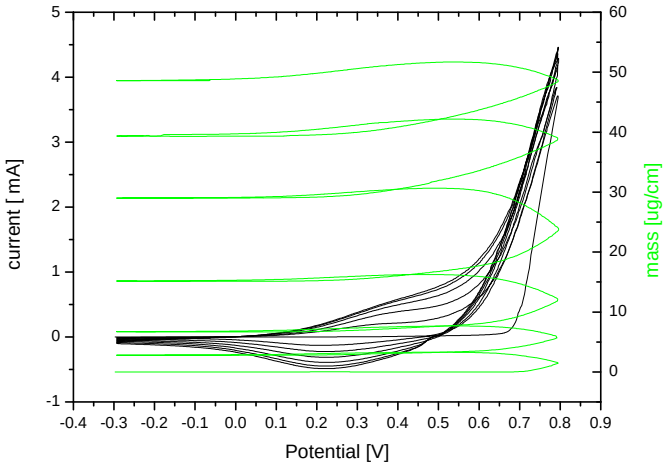

(a)

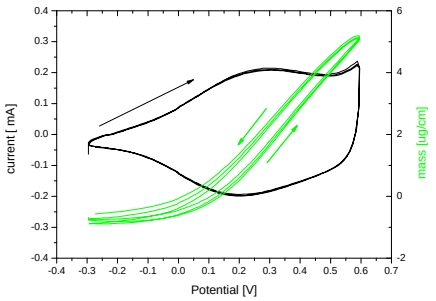

(b)

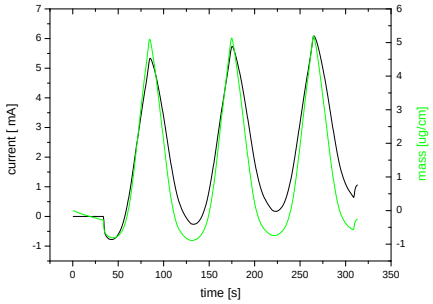

(c)

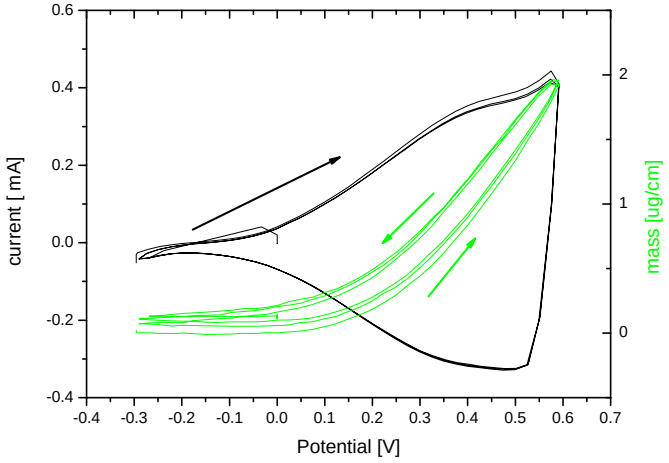

(d)

Figure 2.13: (a) Polymerisation of 0.1 M PNMP in 0.1 M $LiClO_4$. Swept between -0.3 mV to 0.8 mV with a sweep rate of 50 mV/s. Mass change starts at 0 μg/cm^2. (b) Three consecutive CVs from the same polymer film afterwards cycled in a 0.1M solution of $LiClO_4$. The peak position in both pictures do not change. individual cycles during polymerisation, 3rd to 6th cycle. (c) Shows how the mass follows the current in the experiment. (d The same polymer film was cycled in a 0.1 M solution of NaCl with 50 mV/s.)

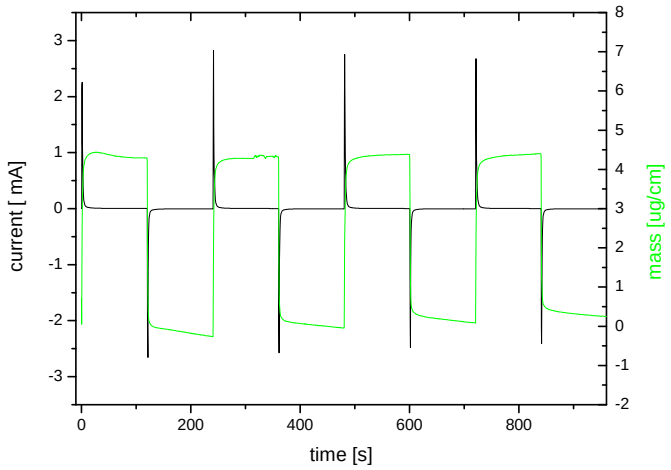

Figure 2.14: Chronoamperometric curve of the (PNMP/ClO_4) polymer film in a 0.1M solution of $LiClO_4$ between the negative and positive limit at -0.2V and 0.5V, respectively.

The obtained average values in three consecutive cycles are shown in table 2.1, which corresponds to one chloride ion and one perchlorate in ion each coordinated with 2.1 water molecules in (PNMP/ClO_4) film .

Also potential step experiments were performed between the two potential 0.5V and -0.2V. As it can be seen, the film simply displays anion permeability. See figure 2.14. Upon oxidation anion ingress into the film and upon reduction egress can be seen, respectively. In producing a (PNMP/ClO_4) polymer film, one finds a film with very similar properties to (PNMP/Cl) in terms of its doping level, its degree of solvation and its ability to dope both ClO_4 and Cl. This suggests a similar coat structure.

Cycling a bile salt anion in and out of the polymer film destroyed the film within the first cycles as it was observed for (PNMP/Cl), before. In the first run the film is electroactive, but hardly exchanges any mass and then detaches from the electrode surface. The concept of increasing the ion molar mass, did therefore not lead to an increased permeability of bile salt anions.

2.5.3 (PNMP/pTS)

A film of 0.1M PNMP in the presence of 0.1M sodium paratoluene sulfonic acid (NapTS) was formed for the first time. The polymerisation looks very similar to the prior formed films in the presence of chloride and perchlorate with mass increase coupled with anion ingress into the film. The exchange studies again in 0.1M NaCl, 0.1M $LiClO_4$ and 0.1M Na pTS also showed anionic permeability as already observed in sections 2.5.1 and 2.5.2. The following table summarise the calculated molar mass of the anion, which is ingressing during oxidation.

	MW[g/mol]		mean MW [g/mol]
	Cation	Anion	Oxidation
NaCl	22.99	35.45	49.3 ± 0.2
$LiClO_4$	6.94	99.45	144 ± 0.9
NapTS	22.99	155.2	134 ± 0.7

Table 2.2: The molar weight of the electrolyte ions ingressing into the (PNMP/p TS) film upon oxidation the film.

From the results, it can be seen, that for chloride and perchlorate the fitted molar weight are higher than the molar weight of the naked anion, which can be again explained in terms of associated water molecules, 0.8 water molecules for chloride and 2.5 for perchlorate, but the fitted molar weight of the (PNMP/pTS) afterwards cycled in a solution of 0.1M Na pTS shows clearly ion ingress upon oxidation, but the fitted molar weight is smaller then the molar weight of the naked anion.

Exchange of bile salt anions could not be observed as before. The next step is to form a film directly in the presence of bile salt anions.

2.5.4 (PNMP/TDC)

A novel PNMP film was grown in an aqueous solution in the presence of a bile salt anion TDC^- for the first time with unusual properties.

The film was grown grown as before, i.e. potentiodynamically with 50 mV/s in a 0.1 M *N*-methylpyrrole solution with 0.1 M NaTDC in the potential range from -0.3 V to 0.8 V containing no other electrolytes. This results in the formation of a (PNMP/TDC) film with 34.5 $\mu g/cm^2$ mass which corresponds to a frequency change of around 1900 Hz. The film formation can be seen in figure 2.15 a.

The aim was the "direct" film formation with already incorporated TDC^- anion, which obviously would then be expected to have the right cavity size for TDC^- anions and therefore a kind of molecular imprint. Figure (2.15) (a) shows the film formation of (PNMP/TDC). Figure 2.15 b) shows an extraction of the 3rd to 6th cycle as it was previously shown for the (PNMP/Cl) film. Both plots look qualitatively very similar and again one can deduce anion doping.

In the first cycle, the oxidation of the PNMP monomer can be seen as before for (PNMP/Cl) films. In the second cycling, there is a oxidation peak at 0.3V, which increase on further cycling. and two reduction peaks at 0.38V and at -0.04V. Looking at a single CV during film formation, the peaks near 0.3V and -0.04V could be associated with a reversible anion doping and dedoping, respectively. The reduction peak at 0.38V could be associated with countercation insertion, as sodium or could be due to impurities. Another possible explanation

for the second reduction peak would be an incomplete film formation of the PNMP polymer film. This peaks starts to appear after a few cycles, when 20% of the polymer is deposited onto the electrode. Especially due to incomplete polymerisation PNMP dimers, trimers, oligomers might attach at the polymer film to give rise to this second reduction peak.
This is consistent with the assumption that the dopant anions get entrapped in the inner layer of the polymer matrix and only those anions at the outer layer can be exchanged with the electrolyte, then the entrapped charges with in the polymer matrix would make it difficult to attach to the polymer film as in the proposed polymerisation scheme 2.2 due to the steric hindrance from the bile salt anions. Another indication for this assumption is that this reduction reaction is not coupled to a mass change.
To characterise this second, irreversible reduction peak the polymer film was cycled in a solution of 0.05M NaTDC with 5mV/s between -0.3 V and 0.45 V. See figure 2.16. The redox peak positions match well with the reversible redox peaks during film formation. The assumption of the entrapped anions introduced above will be used and expanded in the following.
If one calculates polymerisation charge between 0.65V to 0.8V c_{pol} with the redox charge at the reduction peak, which is assigned to NaTDC redox reaction between -0.3V to 0.2V c_{redox}. Then one can calculate the doping level x (eq. 2.20) as in section 2.5.2
With polymerisation charge of about 61.28mC and a redox charge of 1.74mC, a doping level of one TDC^- for every 17.1 rings is obtained. This means that for every 17.1 PNMP rings, one will find a redox charge and assuming complete permselectivity for bile salt anion, one associated bile salt anion to preserve electroneutrality. Calculating the mass by just including the mass of 17.1 pyrrole rings and the mass of one bile salt anion, times the amount of moles produced by the polymerisation charge, one obtains 34.0 μg, which is lower, but in still very good agreement with the measured mass by the EQCM. (34.5 $\mu g/cm^2$) and with the area of the electrode of about 1.37cm^2, the calculation gives us 24.8$\mu g/cm^2$. The discrepancy between the values can be easily understood in terms of water molecules present in the polymerisation, which are not represented in the charge and/or a slightly lower polymerisation efficiency then 100%. The use of Sauberbrey equation holds.

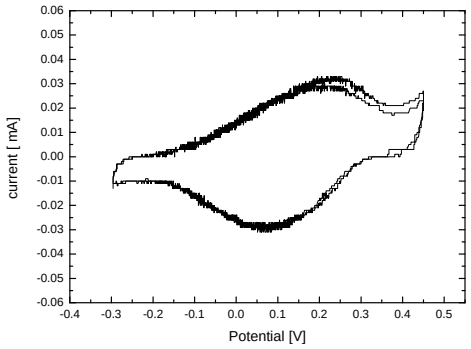

Figure 2.16: The same polymer film was afterwards cycled in a 0.05 M solution of NaTDC with 5 mV/s.

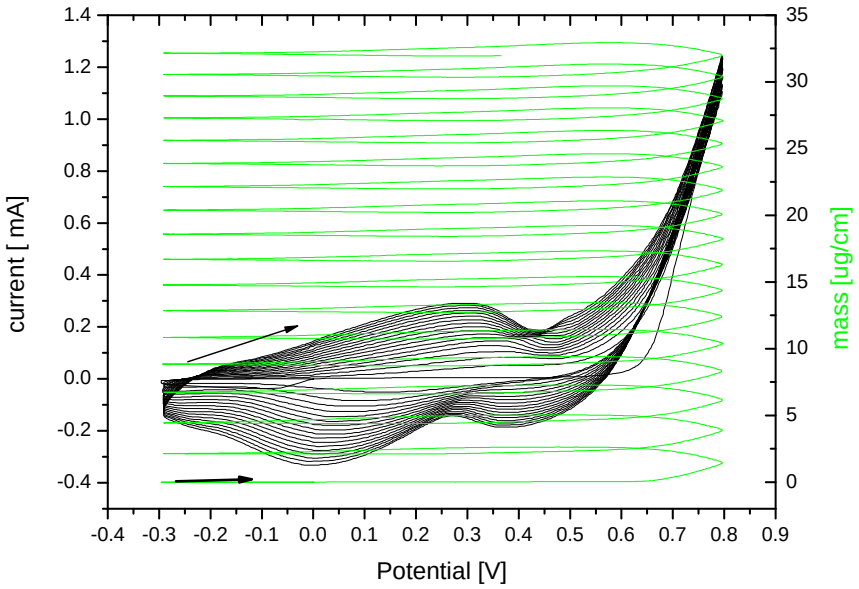

(a)

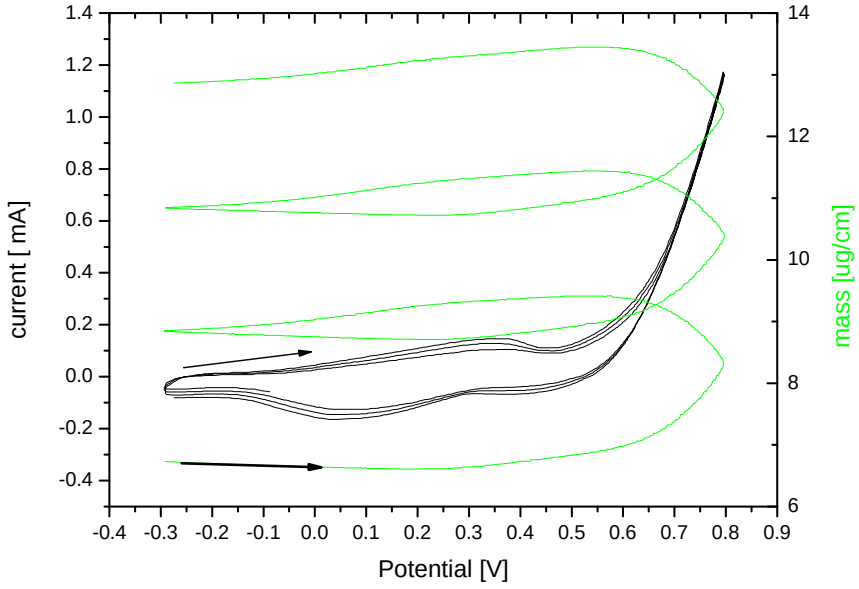

(b)

Figure 2.15: (a) Polymerisation of 0.1 M PNMP in 0.1 M NaTDC. Swept between -300 mV to 800 mV with a sweep rate of 50 mV/s. (b) Extract from the polymerisation from the 3rd to the 6th cycle.

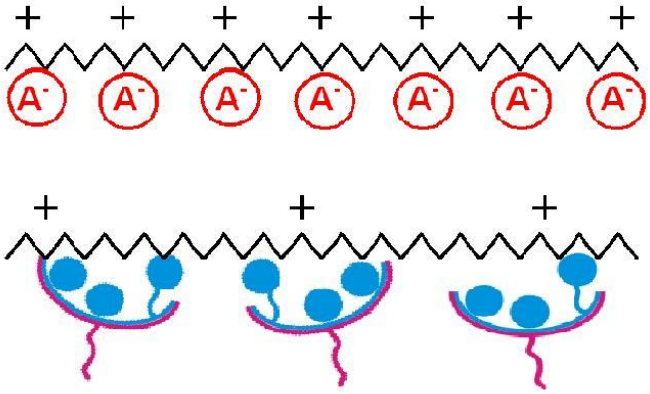

Figure 2.17: Scheme about the difference in the doping level x (Top) for a simple anion doping A^- after polymerisation and (Bottom) doping with a surfactant bile salt NaTDC.

This is a very low doping level, much lower then anything reported in the literature. However the doping level for PNMP films can be found for smaller ions as chloride, but was never reported for entrapped bile salt anion or surfactant. 3.8 rings were needed for perchlorate anions, roughly one fourth in comparison to the incorporated bile salt anion. The size of an bile salt anion is bigger than a chloride and also this should give a higher doping level.

The direct film formation of a PNMP doped with TDC^- anions was successful. The next step is the expulsion of these dopants from the polymer film. Although the doping level is about 6%, the release of the TDC^- anions with their high molecular weight of 502.23 g/mol, should be still visible in a mass decrease of the polymer film on reduction. A release of the dopant anions in 0.05M NaTDC electrolyte could not be observed. Hence, the mass did not drop accordingly, since hardly any mass change was observable. And one can conclude that the anions are trapped in the polymer film or cannot be exchanged by cycling in a NaTDC electrolyte. Generally, the polymer film gets desolved by the surfactant within the first three cycles, which is already visible on the electrode surface, where the polymer film detaches from the gold surface. This is one of the major problems by incorporation of the detergent bile salt.

A (PNMP/TDC) film was then cycled in an electrolyte with small, mobile anion, i.e. Cl, to test, if the bulky TDC^- anions might be replaced by the mobile chloride anions. The oxidation and reduction of LiCl, KCl and CsCl electrolyte (all 0.1 M, sweep rate 5 mV/s) occurs over a wide potential range, i.e. between -0.3 V to 0.6 V, where oxidation and reduction peaks arising from the redox activity of the polymer layer is visible. The salts in the electrolyte were chosen in a way that the bare cation size is increasing from Li^+, K^+ to Cs^+ and the anion is the same for all to investigate the influence of the cation size in the exchange behaviour. But it must be remembered that the solvation shell is increasing from Cs^+ to K^+ to Li^+.

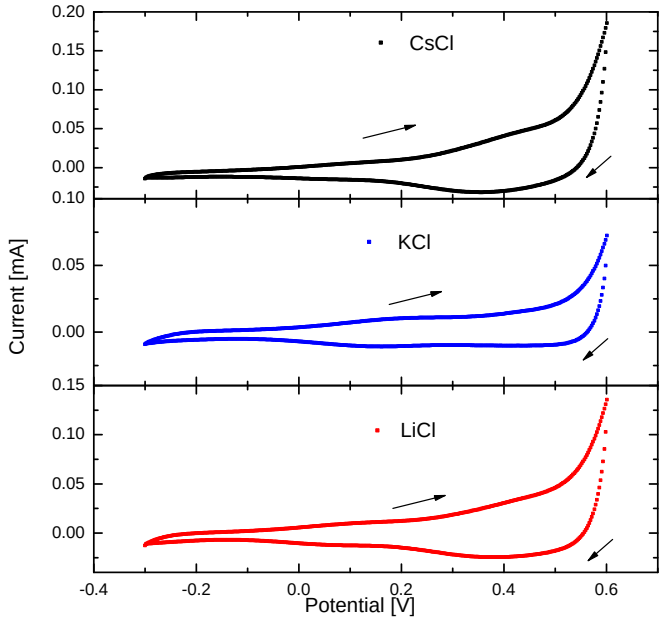

(a)

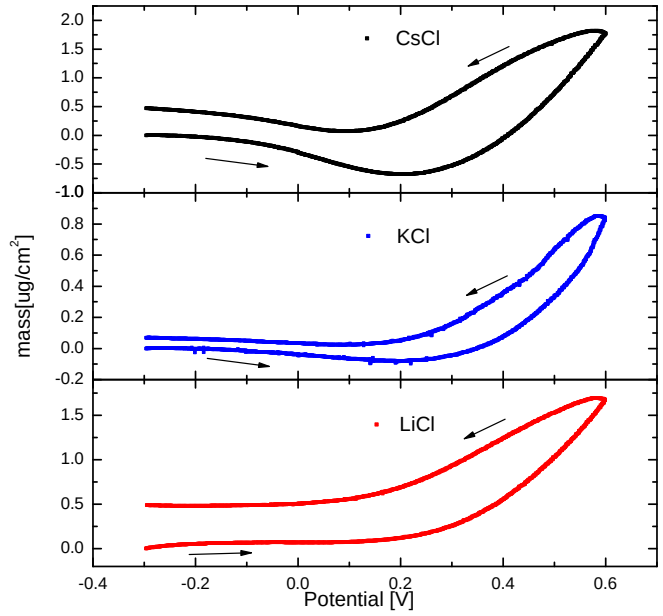

(b)

Figure 2.18: Data from CV experiment employing a (PNMP/TDC) film on Au. Second Cycle. (a) current vs. potential curve. (b) Mass change per unit area vs. potential curve. The solution contained 0.1 M LiCl (red), KCl (blue) and CsCl (black) in water. The scan rate was 5 mV/s. The mass change is referred to the initial value at -0.3 V and the arrows indicate the scan direction.

The film was first held for an equilibrium time of 10 s at more negative potential. In the first sweep, it was first oxidised then reduced. This electrolyte show two sets of oxidation and reduction peaks near 0V and near 0.3V in all the CVs (figure 2.18(a)), where the redox charge below is smaller. The peaks are broad, making it difficult to accurately determine the peak positions. But below 0.2V the current response is different for the different cations. But the comparison of all CV shows that the peaks are very similar for chloride at the positive potential limit.

From the mass data (figure 2.18(b)), first one finds a decrease in mass with increasing potential from the negative limit until 0.2 V and then an increase in mass up to the positive limit with increasing potential. Upon reduction the same can be seen vice versa. This can be especially seen for the electrolyte with the heaviest cation, i.e. Cs^+. K^+ is smaller and therefore the mass drop/increase is less pronounced and is even hardly visible for Li^+ due to the low molecular weight of the Li^+ cation. The quantitative analysis of the ions exchanged will be shown below.

A general model can now be inferred from the experimental results based on the PNMP film polymerised with a simple anion such as chloride and then with bile salt anion, i.e. a surfactant anion (taurodeoxycholate). Where the first polymerised film seemed to respond to anions only, the second seems to respond to both anion and cation.

A (PNMP/Cl) film shows anion response behaviour, in contrast topolymer films formed in the presence of large anions as polystyrenesulfonate. The dopant anions are trapped within the film as known for ”bulky” anions films as sodium poly(styrenesulfonate), NaPSS, (PPY/PSS) [103]. Those films show pure cationic exchange behaviour upon redox cycling. Here both properties, i.e. an anion and cation exchange is observable.

Since the film polymerises in the presence of bile salt anions and forms a polymer film with entrapped anions, this layer or region is able to exchange cations with the solution upon redox cycling. Since the doping level of bile salt is relatively small with respect to forming films with simple anions as reported in literature (see introduction) and observed in this thesis, the same amount of cations are needed to balance the charge. The polymer layer at the outer side is able to release its bile salt anions and the layer becomes able to exchange cations.

If the TDC^- anions are trapped deep inside the polymer backbone, it is difficult for them to get involved in the redox reaction with the coat. But besides the ”trapped TDC^-”, there are also ”mobile TDC^-”, which have escaped the film and can be exchanged by other anions. Upon redox cycling therefore both species, i.e. electrolyte cations M^+ and anions A^-, can be exchanged according to the scheme given in fig. 2.19

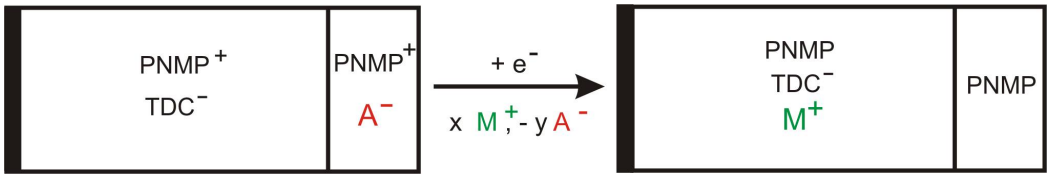

Figure 2.19: Scheme of the model for the (PNMP/TDC) film with an inner part with entrapped TDC anions and an outer part without. In the oxidised form (left hand side) the polymer film exchanges anions with outer layer of the polymer film and in the reduced form (right hand side) the inner layer exchanges cations. The thick black line symbolises the electrode. y stand for the amount of ions exchanged.

$$PNMP^0(TDC^-M^+) \quad \underset{\leftarrow +xM^+,-(1-y)\ A^-,+e}{\overset{-yM^+,+(1-y)A^-,-e\rightarrow}{}} \quad PNMP^+(y\,TDC^-(1-y)\ A^-) \tag{2.20}$$

The compact (PNMP/TDC) film is put in a solution with mobile negative and positive ions after formation. The TDC^- anions are trapped, except those at the outer layer of the polymer matrix. As already assumed in the model for the polymerisation process, an inner and an outer layer of the polymer matrix can be discriminated. The polymer film is again held for an equilibration time of 10 s at the negative potential limit, where cations counterbalance the charge of the entrapped anions. Upon oxidation cations are first expelled to leave free spaces, leading to a mass loss, but during further charging of the polymer backbone the free spaces left behind from the cations in the inner layer will be gradually filled with solvated anions, here chloride.

Now, there will be a more quantitative analysis of the molar weight of the exchanged ions see figure 2.18. In figure 2.20 the Δ Q vs. Δ m plots of these electrolytes are displayed. When the mass is plotted as a function of the charge during redox cycling, then the sign of the slope before and after 0.2 V changes as for the mass vs. potential plots. The boundary between anion exchange to cationic exchange as said earlier is around 0.15V. For the linear fits the vicinity around the inflexion point was not considered.

The linear fits between -0.3 V to 0.15 V reflect the apparent molar mass of the in/egressing cations and between 0.2 V to 0.6 V of the anions, respectively. In table 2.3 the fitted molar weights in the above intervals are listed, which include additionally solvent transport or neutral salt (diffusive flux, where anions and cations are moving together) discussed earlier. The minus sign describes the direction of the overall ion plus solvent transport with ingress + into the polymer and egress - out of the polymer matrix. The given values are averaged over 3 to 4 successive values, ignoring the increase in mass at the reduced end has occurred as well. In table 2.4 the number of surrounding water molecules is listed without taking solvent or neutral

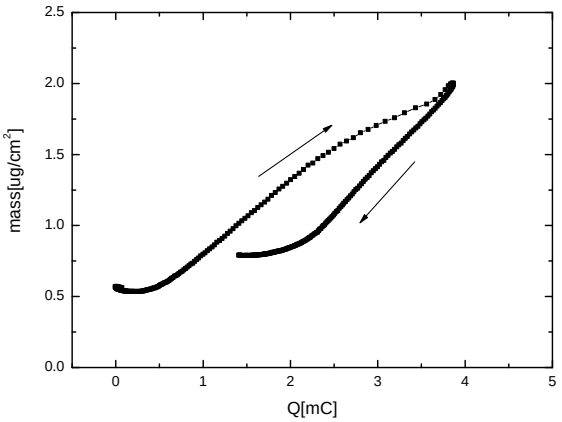

(a)

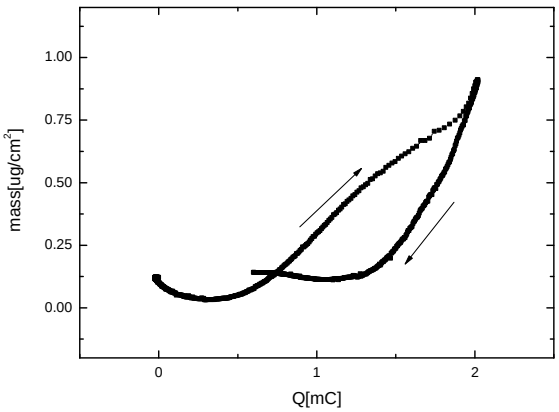

(b)

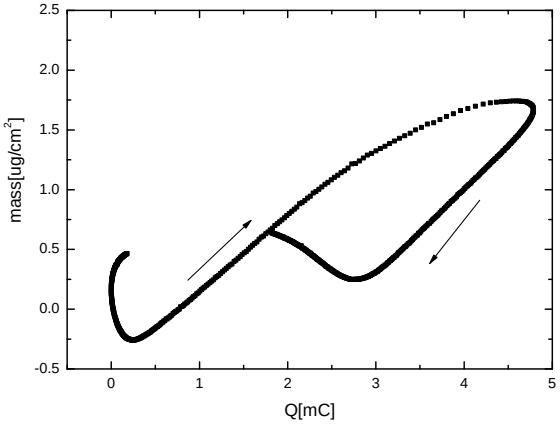

(c)

Figure 2.20: The corresponding 0.1M of (a) LiCl (b) KCl (c) CsCl solution, swept with 5mV/s. The shape of the plots shoes mass ingress at both potential limits.

	MW[g/mol]		fitted MW [g/mol]			
	Cation	Anion	Oxidation 1 cation out [-0.3; 0.3]V	Reduction 1 cation in [0.2;-0.3]V	Oxidation 2 anion in [0.3 ;0.6]V	Reduction 2 anion out [0.6; 0.2]V
LiCl	6.94	35.45	-11.38 ± 1.09	-15.56 ± 0.60	61.69 ± 0.51	-84.81 ± 0.32
KCl	39.10	35.45	-34.50 ± 0.97	+9.39 ± 0.20	71.37 ± 0.58	-146.72 ± 2.16
CsCl	132.91	35.45	-245.46 ± 2.66	+51.16 ± 0.55	72.42 ± 0.79	-98.01 ± 0.38

Table 2.3: Molar weight, with oxidation 1 and reduction 1 at the rather negative side of the potential window and oxidation2 and reduction 2 at the rather positive side of the potential window. The - sign indicates the expulsion of the ion from the film and + sign the ingression, respectively. For the polymer cycled with an potential step of 5 mV/s.

	MW[g/mol]		k			
	Cation	Anion	Oxidation 1 [-0.3; 0.3]	Reduction 1 [0.2; -0.3]	Oxidation 2 [0.3 ;0.6]	Reduction 2 [0.6; 0.2]
LiCl	6.94	35.45	-0.24 ± 0.06	-0.48 ± 0.03	1.46 ± 0.03	-2.74 ± 0.02
KCl	39.10	35.45	-	-	2.00 ± 0.03	-6.18 ± 0.12
CsCl	132.91	35.45	-6.25 ± 0.14	-	2.07 ± 0.04	-3.47 ± 0.02

Table 2.4: The appropriate number k of surrounding water molecules assuming all mass increase is due to ion mass and the surrounding solvent.

salt transport into account.

In the oxidation step 1 (see table 2.3) the increase in the experimentally determined molar weight of the expelled ion corresponds well with the increase in the electrolyte ion mass from Li^+, K^+ to Cs^+. Although in K^+ the determined value is lower, which can be attributed to some sort of counterdirectional transport. In the oxidation step 2 the ingress of Cl^- anion can be seen. The number of surrounding water molecules is nearly uniform for the different electrolytes, but this is not true for the exclusion of those anions (reduction step 2). At reduction step 1 even an ingress (should be egress for solely cation expulsion at this range for the lightest cation Li^+) is visible. But with increasing molar weight of the electrolyte cation the determined molar weight for reduction step 1 increases, too, but stays still below the molar weight of the cations. An explanation is again counterdirectional solvent or neutral salt transport. In figure this behaviour was already seen in the mass increase at the reduced end.

The next tested electrolyte was 0.1 M TEACl, where the size of the cation is again bigger, see table (2.5). The fit of the molar mass of the ion per electron, shows clearly, that anion exchange becomes here favourable compared to cation insertion. The same is true for the surfactant CTAB, where the size of the cation is bigger than TEA^+, but also the anion size of Br^- is bigger. But a clear pure anionic exchange can be seen, although the fitted molar weights of the anion is smaller than the real value, which as explained above might be again due to counterdirectional neutral salt and solvent transport.

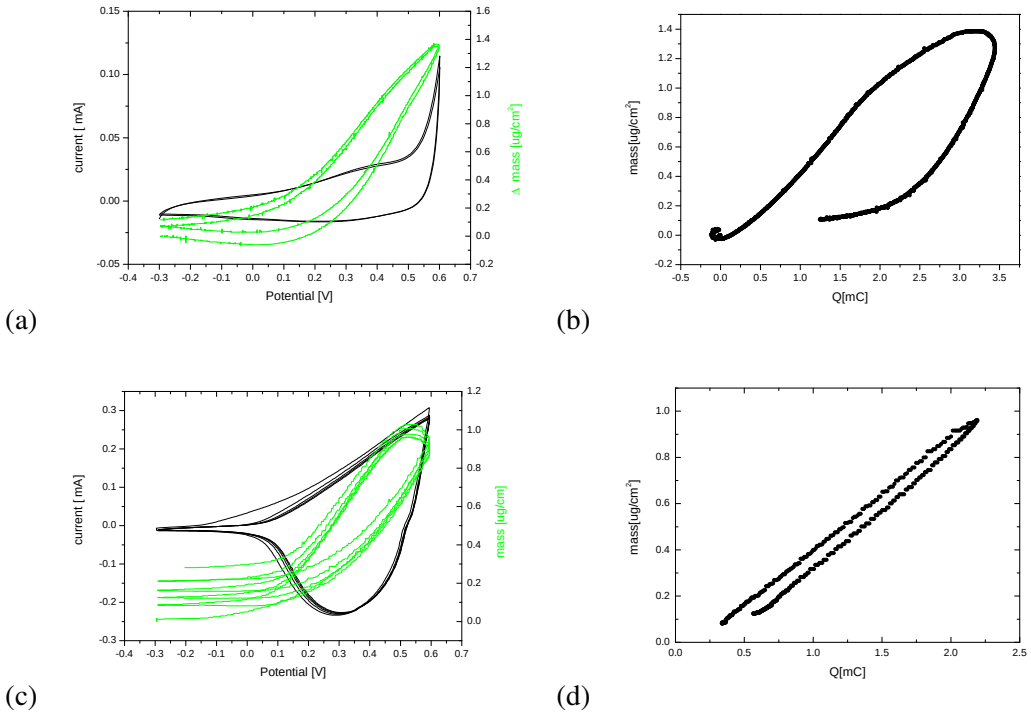

Figure 2.21: (a) Cyclic voltamogramm and (b) mass change in a 0.1M TEACl solution, scan rate = 5mV/s. (c) Cyclic voltamogramm and (c) mass change in a 0.1M CTAB solution, scan rate = 50mV/s.

	MW[g/mol]		**fitted MW [g/mol]**	
	Cation	Anion	Oxidation	Reduction
TEACl	130.25	35.45	70.2 ± 0.8	103.5 ±1.1
CTAB	280.1	79.9	63.8 ± 0.7	64.0 ±0.8

Table 2.5: The molar weight of the electrolyte ions ingressing into the polymer film upon oxidation and egressing upon reduction.

The spatial distribution of TDC^- and A^- will be tested with a potential step experiment. Here the experiment performed in 0.1M CsCl is picked out, since the qualitative differences to LiCl and KCl are negligible. In potential step experiment the voltage is stepped from the reduced end to the oxidised end and back for 240s. The reduced end corresponds to -0.3V and the oxidised end to 0.6V.

An unusual mass behaviour can also be seen in potential step experiments, where the potential is stepped from the negative potential limit at -0.3 V to the positive potential limit at 0.6 V and held for 240 s. Unusual because a simple anion exchanging polymer film would display an immediate mass increase accompanied by current flow and afterwards slight swelling of the film with hardly any current flow, the reversible reaction would occur for stepping to the negative potential limit.

Figure 2.22(a) presents the chronoamperometric curves. In the first oxidation step shows an initial loss in mass (solvated cations), which immediately is compensated by a mass increase due to the anions insertion. The timescale of the initial cation exclusion is faster (less than 0.5s) than the initial anion insertion (a timescale of seconds) until hardly current is passed and the polymer gains mass due to solvation. Upon reduction, both concurring processes lead to an increase of the polymer matrix. Figure 2.22(b) and (b) shows an expansion of (a) redox peaks. The integration of the peak current shows matches very well. The reduction peak current (b) is about 1.8 mC and the corresponding oxidation peak is about 1.77 mC although there is difference in reduction and oxidation kinetics.

This mass behaviour during potential step fits in the proposed two layer model. In the figure 2.23(b) the experimental results are explained with the model at hand. Upon reduction of the film, in the beginning cations are excluded from the inner part of the film, then the film gets further reduced up to the outer layer and the anions are able to ingress into the polymer film. Upon oxidation figure 2.23(a) the outer parts are first able to eject the anions back into the solution and at a later time, the film gets more oxidised until the inner layer and the cation ingress into the film.

Also the swelling behaviour of the (PNMP/TDC) polymer film supports and can be explained by the two layer model.

Figure 2.24 shows for four successive CVs with simultaneous mass measurement for 0.1 M CsCl with a sweep rate of 50 mV/s after being held at the negative potential (-0.3 V) for 10 s. This cannot be explained just with kinetic arguments, where processes in the polymer film upon reduction and oxidation are slower than the scan rate and lead to hysteresis, which disappears at slow scan rates. Such hysteresis effect did not seem to appear at least until a scan rate of about 2mV/s. It seem that upon oxidation less solvent is excluded from the film than can enter upon reduction, which leads to an continuous swelling at the negative potential limit. How can this be understood?

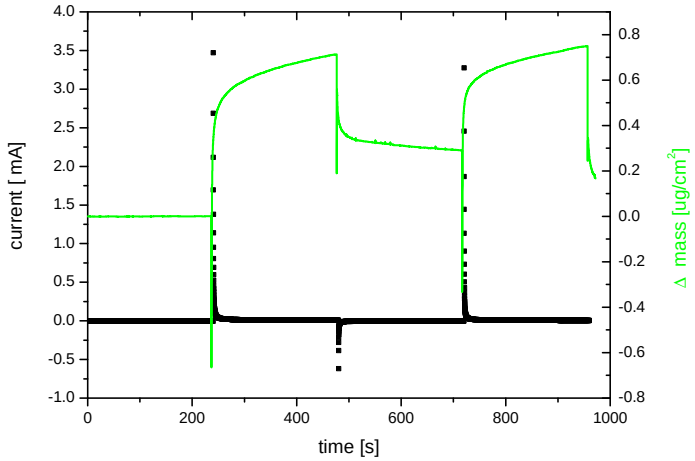

(a)

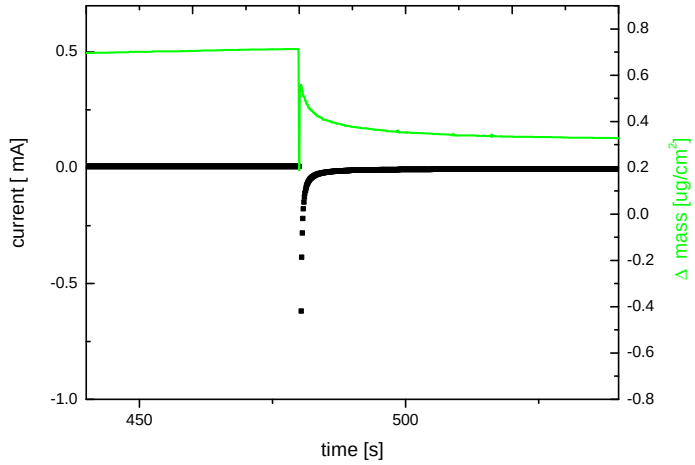

(b)

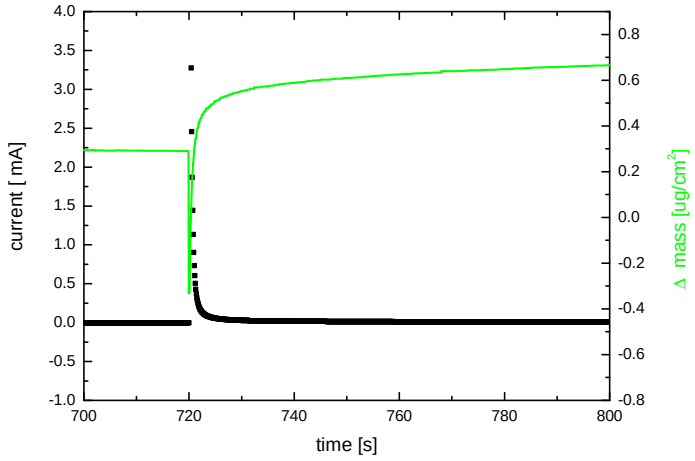

(c)

Figure 2.22: (a) Potential step experiment in a 0.1 M CsCl solution for 240s, where the voltage was stepped from the reduced end at -0.3 V to the oxidised end at 0.6 V (b) extraction of the reduction process (c) extraction of the oxidation process.

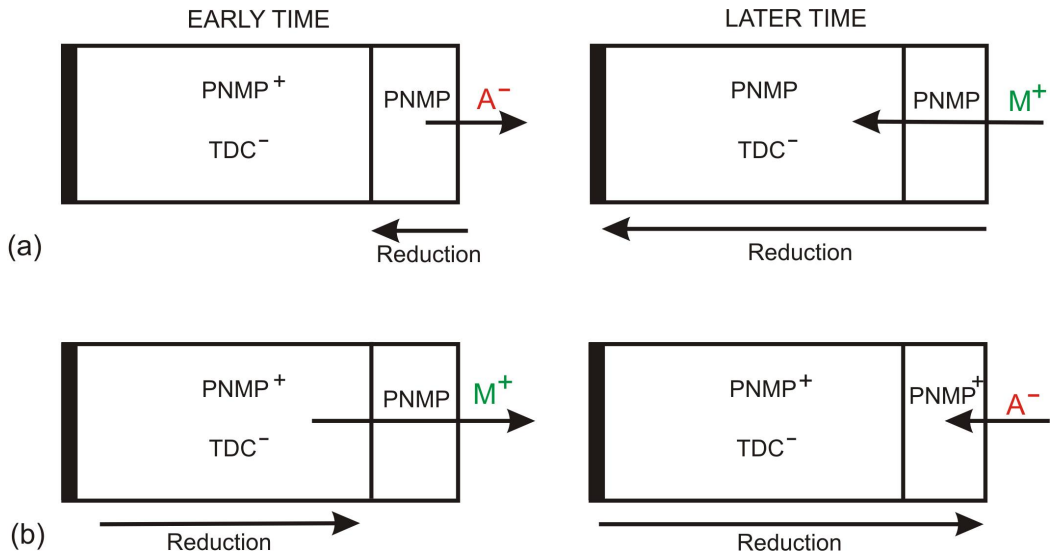

Figure 2.23: (a) shows the initial reduction of the oxidised polymer film with two layers, an inner layer with entrapped bile salt anions and an thin outer layer, which was able to eject the bile salt anions. The outer layer starts to inhibit anions and upon further reduction all polymer backbone is neutral and cations ingress to counterbalance the charge of the bile salt anions in the inner layer. Whereas in (b) the neutral backbone of the inner layer gets first oxidised and an expulsion of cations occur and at a later the time, the film is fully oxidised and the outer layer is permeable for anions again.

The film after its deposition is quite compact. When cation insert into the compact film during the first cathodic scan, they will change the polymer film structure. But, when an anion excludes from the film the film does not need to rearrange.

To interpret this hysteresis or swelling of the polymer film, one can follow the opposite argument to (PNMP/Cl) polymer films, where swelling of the polymer matrix occurs during accommodation of the dopant anions with the solute and where the matrix dilates to leave free spaces. But on the positive potential limit, the polymer film shrinks to fill the voids or channels left behind from the ejected dopants with adjacent polymer chains. Since the film is hold at the neutral end, where the film is compact, swelling occurs at the oxidised end. This shrinking and swelling reaction is a slow process, therefore with fast sweep rates there will be visible hysteresis effect in each individual redox cycle, but decreases for slow sweep rates, i.e. 5 mV/s. This was observed for (PNMP/Cl) films with Cl^- exchange [104].

However, in (PNMP/TDC) continuous swelling of the polymer occurs at the negative potential limit.

During the redox cycling a structural rearrangement due to orientation and reorientation of the adjacent polymer chains with solvent and ion ingress/egress will occur as well. Since TDC^- is an amphiphile, where the whole cholesterol skeleton is hydrophobic and the polar

groups are hydrophilic, the interaction of this anion with the PNMP polymer will affect the hydrophobicity of hydrophilicity of the polymer film. But on the other hand the bile salt anion also interacts with the countercation. These two effects could be the major contributions in the structural rearrangements in the polymer matrix. In the oxidised state, TDC^- will have interactions with the polymer, whereas upon reduction of the polymer backbone hydrophobic interactions between TDC^- and polymer will be expected to dominate along with electrostatic interactions with the cations. Due to the electrostatic force the ionic interactions between the polar groups of the entrapped bile salt anions and the charge of the ingressed cation will gain importance. If the TDC^- and the countercation ion pair, this would lead to a hydrophobic film, i.e. solvent exclusion at the reduced end. This cannot be observed in the CV experiments. Instead a swelling of the polymer matrix can be seen. If the structural rearrangement is a slow process compared to the scan rate of the CV experiment, then there will be solvent ingress to solvate the charges of the ions. Therefore upon reduction, the polymer film first egresses the ingressed electrolyte anions of the outer layer of the polymer film and then the solvated cations will ingress into the film.

But all these structural rearrangement processes due to the interactions have different time scales as the insertion of the cations at the reduced end, the insertion of the anions at the oxidised end, the (re)orientation of the polymer chains and they are difficult to differentiate. This leads in CV experiments to a swelling at the negative potential end. This timescale can also be seen in the potential step experiments, cation expulsion is a fast process compared to the swelling of the polymer film. See in figures 2.22.

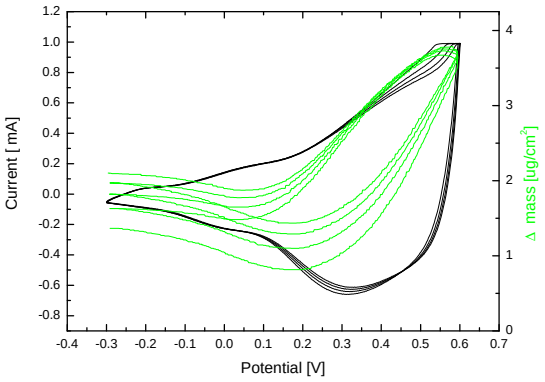

Figure 2.24: Cyclic voltamogram and mass change in a 0.1 M CsCl solution, scan rate = 50 mV/s.

The developed two-layer model explains the polymerisation of PNMP with bile salt anions with mass increase coupled with anion expulsion and also explains the results of the exchange studies with different electrolytes with differently sized anions and cations. The model was also tested with potential step experiments. Nevertheless a permeability of bile salt anions could not be found, which was the aim for further experiments for the bile salt/EYL aggregation, but the outer layer seems to be able to release bile salt anions, which would mean, that in following

studies a (PNMP/bile salt anion) with a high surface structure could be used to release bile salt from the outer layer into the solution.

2.6 Conclusions

Several novel polymer films were formed in order to test the bile salt exchange behaviour of PNMP film. PNMP was polymerised in the presence of chloride, mainly to test the reliability of data presented. The film showed excellent anion exchange behaviour for small anions, but there was no response for TDC^- anions. TDC^- anions are rather big to go into a compact film. PNMP was also polymerised in the presence of perchlorate anions, which showed no difference to a film with chloride ion. The doping level with the anion (three to four PNMP rings per inhibited anion) was found in as claimed in literature for PPY and PNMP films. Also the polymerisation of paratoluene sulfonic acid in the film showed anion exchanging behaviour. All formed films as (PNMP/Cl), (PNMP/ClO_4) and (PNMP/pTS) were detached from the electrode surface, when bile salt anions were forced into the film.

It is also shown in this chapter, that it is possible to electrochemically form polymer films in the presence of bile salt anions such as TDC^-. This is a novel polymer film, which displayed good redox activity. This film was also cycled in NaTDC solution, but the bile salt anions solubilised the film after cycling.

(PNMP/TDC) film was further characterised and cycled in various electrolyte solutions. A model was developed, which is consistent with our data, in which our polymer film is made up of two layers, an inner and an outer layer. The inner layer consists of entrapped bile salt anions from the process of electropolymerisation. In the outer layer, bile salt anions were able to leave the polymer film after electropolymerisation and leave layers of the film, which is now able to allow anion ingress/egress.

The results of the combined electrochemical and quartz crystal microbalance measurements confirm that both cations as well as anions take part in the ion exchange process during redox cycling in (PNMP/TDC) films. The inner layer of the polymer film with entrapped bile salt anions exchanges cations, whereas the outer layer is able to exchange anions. The film showed simultaneous exchange of anion and cation, like M^+Cl^-, where M^+ was small enough as for Li^+, Cs^+, K^+.

Pure anionic exchange was observed for a bulky cation in the electrolyte as for TEA^+Cl^- and the ingress/egress of the cation was completely stopped. Even if entangled bile salt anions of the inner layer would be forced to leave the polymer film, this still shows clearly that it is

kinetically unfavourable for the (PNMP/TDC) film to allow the ingress of a bulky cations.

The main problem in the experiments presented in this chapter was the ability of the bile salt anion, TDC^-, to solubilise the polymer film. This did not happen during polymerisation, but during the attempt to force these anions into the film, it generally detached and further studies were not possible.

This is obviously not desirable, since the research was heading towards the control of bile salt concentration using electrochemical methods for further investigations on the aggregation behaviour on bile salt/EYL systems. Since this cannot be achieved within the timescale of this thesis, the focus will turn back to the bile salt/EYL aggregation.
But nevertheless, bile salt anions were able to be released from an outer layer of the (PNMP/TDC) film. If an electrode would be designed with a higher surface area, as on a microarray, this might lead to sufficient exchange of bile salt anions.

Chapter 3

Experimental Method and some Background

3.1 Isothermal Titration Microcalorimetry

3.1.1 Why use ITC?

Isothermanl Titration Microcalorimetry (ITC) is an experimental method that allows to measure the heat Q associated with the change of composition ξ [106, 107, 108, 109, 110]. Since the temperature and pressure are kept constant within the experiment, one can directly relate Q to the enthalpy change ΔH (first law of thermodynamics) and give a complete thermodynamic description of the system under study by calculating the change in free energy ΔG_d and the change in entropy ΔS_d, where the subscript d stands for the demicellisation process. This method is therefore extremely useful to determine equilibrium phase transitions in solutions and has already been widely used for surfactant solutions. For example, one can typically deduce the critical micellisation concentration or solubilisation of vesicles and bilayers. This method has already been applied to bile salt systems such as NaC and NaDC [106, 111], where the cmc has been deduced from ITC measurements. The main advantage of this method is the simultaneous determination of thermodynamic quantities such as the enthalpy change ΔH_d of the micellisation or demicellisation, i.e. the cmc within a single experiment. This is indeed of prime importance when dealing with biological samples where the raw material is often only available in small quantities and involves tedious preparation steps.

3.1.2 Basic Principles of Calorimetry

The key condition for isothermal titration microcalorimetry is the thermodynamic equilibrium. By injecting a chemical substance from the syringe into the sample cell, the reaction partner, a chemical or physical reactions occurs and the intramolecular and intermolecular interactions

of molecules in an aqueous media can be measured. The calorimeter then measures the heat Q associated with the change of composition ξ due to this reaction. From the first law of thermodynamics for a closed system, the change in enthalpy ΔH (with $H = H(p, T, \xi)$) corresponds directly to the heat Q at fixed pressure [112].
Actually, the direct determination of the change in enthalpy of a system on going from one defined state to another is not possible with any other method. In other methods ΔH can be derived indirectly using the temperature dependence of K, the equilibrium constant, with the vant Hoff relation.

$$\left(\frac{\partial \ln K}{\partial T}\right)_p = \frac{\Delta H_{vH}}{RT^2} \tag{3.1}$$

with R the universal gas constant.
If the temperature dependence of the enthalpy is measured, the change of heat capacity ΔC_p at constant pressure can be determined from calorimetry measurements (DSC-differential scanning calorimetry) as well with:

$$\Delta C_p = \left(\frac{\Delta H}{\partial T}\right)_p \tag{3.2}$$

In surfactant systems, ΔC_p gives information about the exposure of the solvent to the hydrophobic surface of the molecule or aggregate investigated, since the solvent behaves differently in bulk and on a surface. The heat capacity is different (actually lower) for an aqueous solution with than without surfactant aggregates. If water is released from the surface, the heat capacity will be negative and is also proportional to the amount of surface involved. So ΔC_p contains information about the binding and incorporation reaction. [1]
At chemical equilibrium the Gibbs free energy G is at a minimum for a closed system at fixed temperature and pressure. Therefore by injecting titrant into the the system, this moves the equilibrium state into a new equilibrium state with different composition. Since $G = H - TS$, the thermodynamic variables enthalpy and entropy determine the minimum Gibbs free energy, which means that also information about the compensation of entropy and enthalpy is gained from microcalorimetry measurements.

The Chemical Equilibrium

The equilibrium constant K can be determined in an ITC experiment and is directly related to the Gibbs free energy G. If a small amount of substance i, i.e. dn_i moles, is added to the system whilst keeping pressure and temperature constant, the free energy increases, which is

then defined via the chemical potential μ as:

$$\mu_i = \left.\frac{\partial G}{\partial n_i}\right|_{p,T} \tag{3.3}$$

The free energy ΔG of a mixture composed of a certain number of moles of each constituent, tcan be written as:

$$\Delta G = \sum_i n_i \mu_i \tag{3.4}$$

For an ideal mixture of different components of a gas or solution as in our case (at constant pressure and temperature), one obtains for the chemical potential in mole fractions x_i of the substance i:

$$\mu_i = \mu_i^0 + RT \ln x_i \tag{3.5}$$

with *R* the universal gas constant. If we now look at the free energy of mixing, then one obtains from equation 3.4 and 3.5:

$$\Delta G = -RT \sum_i n_i \ln x_i \tag{3.6}$$

In equilibrium the chemical potentials of two phases are equal ($\mu_i = \mu_j$) and one obtains the dependence of the free energy ΔG on the equilibrium constant:

$$\Delta G = -RT \ln x_i \tag{3.7}$$

This will be discussed in greater detail in chapter 6 in the context of the pseudo phase-separation model.

3.1.3 Instrumental Setup

The ITC experiments were performed using a MicroCal OMEGA titration calorimeter [113, 114]. Figure 3.1 shows a schematic diagram of the instrumental setup. The core of the device is composed of two identical cells located inside the calorimeter. One cell contains the sample under study, the sample cell, and the other one is used as a reference cell and contains the same solvent. Both cells are completely filled through a very long and tight capillary. The cells are

surrounded by an adiabatic coat made of aluminum that prevents the exchange of heat with the environment.

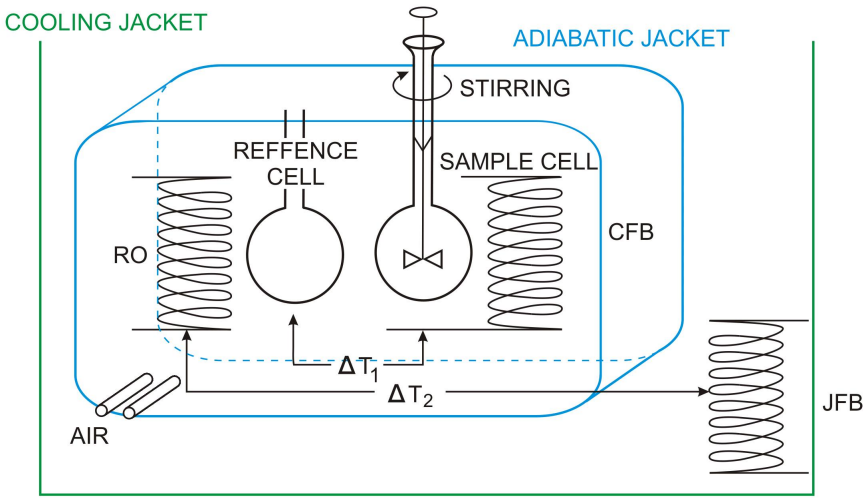

Figure 3.1: Schematic diagram of the Microcal ITC setup.

The cell capacity is 1.4129 ml and the reaction partner is injected with a Hamilton syringe. The syringe volume is of 250 μl and the needle has a flattened tip which is used to stir the sample immediately after injection of an aliquot into the sample cell. The stirring speed can be adjusted, and for all experiments a constant rotation speed of $\sim$310 rpm is used.

The calorimeter works isobar and isotherm", although the temperature in the cell rises during a measurement by 2-40 mKh^{-1}, because the reference cell is heated with a low power of a few μW. This heating system is called "reference offset" (RO). With a second heating system, the "cell feedback" (CFB), the temperature difference ΔT_1 between the sample and reference cell is measured and a third, the "jacket feedback" (JFB), measures the temperature difference between the reference cell and the coat. The temperature of the sample cell and the coat is both adjusted with respect to the reference cell. The comparison of the temperatures is performed 30 times per second.

If there is heat produced or absorbed by a reaction in the sample cell, a signal proportional to the occurred temperature difference in the CFB is recorded. In the case of an exothermic reaction, the temperature will be reduced, and for an endothermic reaction the temperature will be regulated back to zero. This signal, i.e. the heat flow to keep the temperature constant, is recorded as a function of time and can be seen in figure 6.1. The calorimeter allows measurements from 5°C up to 85°C and measures temperature difference in the μK regime. The heat produced per time interval is recorded as μJs^{-1}.

A thermoelectric device measures the temperature difference between the two cells and a

second device measures the temperature difference between the cells and the jacket. As chemical reactions occur in the sample cell, heat is generated or absorbed. The temperature difference between the sample and reference cells (T1) is kept at a constant value (i.e. baseline) by the addition or removal of heat to the sample cell, as appropriate, using the CFB system. The integral of the power required to maintain T1 = constant over time is a measure of total heat resulting from the process being studied. Figure 2 is a schematic drawing of the ITC cells and syringe.

3.1.4 Experimental Procedure

In all experiments the reference cell is filled up with water. The sample cell and the injection syringe were filled with the reaction partners. The concentrations of both reaction partners were chosen such that the desired reaction occurred during the experiment. The time interval between two injections depends on the size of the heat signal. The time interval was chosen to be 180 to 240 s. The experiments were mainly performed at room temperature T = 25°C, but also at T = 5°C, T = 10°C, T = 40°C and T = 55°C.
Prior to the experiment both reaction partners were degassed under stirring for 7-10 min to prevent air bubbles (ThermoVac, MicroCal Inc., Northhampton, USA).

Demicellisation Experiments

In demicellisation experiments the sample cell is filled with a buffer solution with salt concentration c_s. The injection syringe contains a highly concentrated bile salt solution at a concentration above the *cmc*, either 25 mM or 50 mM bile salt. The bile salt, NaTCDC, was injected into the sample cell in 100 steps of 1 μl every 180 s. All demicellisation experiments were performed at constant temperature for 25°C, 40°C and 55°C.

Solubilisation Experiments

In solubilisation experiments the sample cell is filled with a lipid/bile salt mixture with a salt concentration c_s and the injection syringe contains a highly concentrated bile salt solution with a concentration of 25 mM, i.e. well above the *cmc*. The measurements were performed with lipid/detergent mixtures with concentrations between 0.5 and 4 mM, where the salt concentration c_s is kept constant. To test the effect of the ionic strength, the experiments have been performed with different salt (NaCl) concentrations c_s. The bile salt, NaTCDC, was injected into the sample cell in 50 steps of 1 μl every 180 s to 240 s. All solubilisation experiments were performed at constant temperature, T=25°C.
The heat produced by dilution is measured by an analogous experiment performed by titration of buffer into the aggregate and then subtracted from the heat determined in the above

experiment.

3.1.5 Data Treatment

The experimental results were evaluated using the MicroCal Origin Software, Version 6.0. Since in solubilisation experiments the mixed aggregates consist of EYL/NaTCDC and the titrant is NaTCDC, the concentrations of each species were calculated to achieve a phase diagram of NaTCDC concentration c_{D_t} against EYL concentration c_L.

3.2 Scattering Technique

3.2.1 Why use Scattering?

The direct observation of particles with an optical microscope is limited by the spectrum of visible light, which ranges from violet-blue, i.e. 380 nm, to red, i.e. 760 nm. To obtain information on particles and their structures and length scales outside this range, scattering techniques can be used, together with imaging techniques suitable for the lengthscale of interest. The information content of scattering data is very different from directly observed, real space images, since scattering does not provide direct images, but the experimental results need to be modelled.

Scattering methods are also a powerful technique to investigate particles or aggregates in solutions or suspensions. They offer the possibility to investigate the particles without disturbing their natural environment. In dilute systems, the shape and structure of individual particles can be studied, whereas in concentrated systems the spatial arrangement of the particles can be investigated. The apparent molar weight of the particles can be extracted from the measured absolute scattered intensity.

Various scattering techniques are used in this thesis. Dynamic light scattering can probe the overall size of the aggregates on the nanometer level, but does not provide information about the structure. Small angle X-ray scattering resolves structures on this length scale, but the energy used in SAXS experiments (keV) is a few orders of magnitude higher then the energies used in neutron scattering experiments (meV), which provide information on similar lengthscale. Especially with biological samples, this carries the risk to damage the sample.

3.2.2 Basic Principles of Scattering- Static Light Scattering, Small-Angle X-ray and Neutron Scattering

An experiment is performed by exposing the sample to a beam of light, X-rays of neutrons, and measuring the intensity scattered by the sample at an angle θ [115, 116]. The important physical parameter is the scattering vector $\vec{\mathbf{q}}$, which is the difference between the wavevectors of the incident ($\vec{\mathbf{k_i}}$) and scattered ($\vec{\mathbf{k_s}}$) beams.

$$\vec{\mathbf{q}} = \vec{\mathbf{k_s}} - \vec{\mathbf{k_i}}, \tag{3.8}$$

where λ is the wavelength of the radiation in the sample. In case of elastic scattering, no change of energy occurs between the incident and scattered beam, and thus the magnitudes of the wavevectors before and after the scattering event are equal:

$$\left|\vec{\mathbf{k_i}}\right| = \left|\vec{\mathbf{k_s}}\right| = \frac{2\pi}{\lambda} \tag{3.9}$$

$$|\vec{\mathbf{q}}| = \mathbf{q} = \frac{4\pi}{\lambda}\sin(\theta/2) \tag{3.10}$$

Substituting equation 3.10 into Braggs Law $\lambda = 2d\sin(\theta/2)$ yields the often used expression.

$$d = \frac{2\pi}{q} \tag{3.11}$$

where d is the characteristic length scale investigated at the particular scattering vector $\vec{q}$. The length scale of the systems in this thesis range from 2 nm to 200 nm. The corresponding q-values range from 0.3 to 0.003Å^{-1} and the scattering angles lie between 7° to 0.14° and thus at *small* angles. One of the reasons to use small angle neutron scattering for this work is that only a few techniques give information about the detailed structure on the nanometer level. Light scattering only gives the overall size of our molecules. SAXS, on the other hand, resolves structures at the same lengthscales, but the scattering contrast for neutrons is much higher. This is because the scattering cross-section for x-rays increases linearly with the number of electrons or the atomic number Z, whereas for neutrons it varies irregularly with Z. Even isotopes of the same element have different neutron cross-sections. The most significant variation of isotopes occurs for hydrogen. The advantage of SAXS measurements is its easier availability, since no large facilities are needed as for SANS measurements.

Contributions and Description of the Scattering Curve

The scattered intensity as a function of a scattering vector q can be described by:

$$I(q) = I_0 \Omega_0 \epsilon A \, d_{cell} \, T \frac{\partial \sigma}{\partial \Omega} \tag{3.12}$$

The equation can be divided in two parts, one instrument specific contribution and a sample dependent part. The instrument specific contribution contains the incident neutron flux I_0, the beam area A, the solid angle element Ω_0 and the detector efficiency ϵ. They can be determined independently using a reference sample. The sample dependent ones are the sample thickness d_{cell}, the sample transmission T and the differential cross-section per unit volume $\frac{\partial \sigma}{\partial \Omega}$.
The differential cross-section $\frac{\partial \sigma}{\partial \Omega}$ contains all the information about size, structure and arrangement of the scattering particles. It can be represented as

$$\frac{\partial \sigma}{\partial \Omega} = \frac{c \Delta \rho_m^2}{N_A} F(q) S(q) \tag{3.13}$$

where c is the particle concentration, N_A Avogadro s number, $\Delta \rho_m$ the excess scattering length density, $F(q)$ the formfactor of the particles (which depends on intraparticle interference effect and thus on the shape and structure of the particles) and $S(q)$ the structure factor (which depends on interparticle interference effectrd and thus on the particle arrangement).

Scattering length density and contrast

The cross section σ of the particle describes its ability to scatter the incoming beam. σ is related to the scattering length b, which characterises the *scattering ability* of a nucleus to scatter radiation. The X-ray radiation interacts with the electron density of the atoms, σ increases proportional to Z, the atomic number giving also the number of electrons. Organic materials consists mainly of light atoms, such as hydrogen (1e-), carbon (6e-), nitrogen (7e-) and oxygen (8e-) similar to the solvent. On the contrary neutrons interact with the nucleus. Therefore, even the isotopes of the same element have different neutron cross-sections, such as hydrogen ^{1}H and deuterium ^{2}D (table 3.1) and thus H_2O and D_2O.

In light scattering experiments the *scattering ability* is proportional to the refractive index of the material.

If molecules or particles are used instead of atoms, it is convenient to use an average scattering length density ρ rather than the scattering length b. The scattering length density ρ is calculated by:

Nucleus	b $[10^{-15}m]$	σ_{coh} $[10^{-28}m^2]$	σ_{inc} $[10^{-28}m^2]$
H	-3.742	1.76	79.9
D	6.674	5.59	2.04
C	6.648	5.55	0.001
O	5.805	4.23	0.000
N	9.362	11.02	0.501

Table 3.1: Neutron scattering length b and coherent and incoherent cross section σ. From [117].

$$\rho = \frac{\varrho N_A}{M} \sum_i b_i \tag{3.14}$$

where *M* is the molar mass, b_i represents the coherent scattering length of nuclei i and ϱ is the mass density.

Solvent or Sample	b $[10^{-15}m]$	ρ $[10^{-6}\mathring{A}^{-2}]$
D_2O	1.915	6.38
EYL tail	3.350	2.65
EYL headgroup	1.651	0.56
TCDC	5.880	0.89

Table 3.2: Scattering length densities for the solvents and amphiphiles used in this thesis.

For a meaningful scattering experiment, a contrast between the particles and the solvent is needed. The *contrast* $\Delta\ \rho$ is given by the difference between the scattering length densities of the sample (s) and solvent (sol):

$$\Delta\rho = \rho_s - \rho_{sol} \tag{3.15}$$

The contrast in SAXS measurements is given by the difference in electron density of the particles and the solvent and for light scattering the difference in refractive index determines the contrast.

Instrumental Resolution

For example, the wavelength distribution, the finite beam divergence after the neutron collimation and the size of the beam and sample aperture and the detector pixel leads to finite instrumental resolution. A mechanical velocity selector defines the range of neutron wavelengths (typically 10%) that are transmitted to the instrument, this spread in wavelength results in a distribution of scattering vectors. This smearing due to the instrumental resolution has to be considered when comparing experimental results with models.
The smearing has an almost Gaussian shape and all effects influencing the smearing can be summarised in a distribution of q around a mean value $\langle q \rangle$ by:

$$I(q)\Big|_{\text{data}} = \int R(\langle q \rangle, q) I(q)\Big|_{\text{model}} dq \tag{3.16}$$

with $R(\langle q \rangle, q)$, the distribution of scattering vectors q around $\langle q \rangle$. For further details, see chapter 6 in refs. [116] and [118].

3.2.3 Dynamic Light Scattering (DLS) or Quasi-elastic Light Scattering

A detailed description of dynamic light scattering experiments is given by various textbooks [119, 120]. When the scattering wave vector $\vec{\mathbf{q}}$ changes its direction, but (almost) not its magnitude, it is named quasi-elastic. For aggregates in a solution, the fluctuations of the scattered intensity at a given angle are due to the Brownian motion of the particles, (i.e. concentration fluctuations), which leads to a randomly changing phase relation between light scattered by different particles. The intensity fluctuations are measured and the size of the particles determined through an analysis of the intensity fluctuations. Dynamic light scattering (DLS) or quasi-elastic light scattering is one of the most important methods to study the dynamics of soft matter in particular colloids and surfactants, in solution.

Information can be extracted from the intensity fluctuations by using the time correlation function. From the normalised time correlation function $g^{(1)}(\tau)$ of the scattered electric field information about the dynamics of the system can be obtained.

$$g^{(1)}(\vec{\mathbf{q}}, \tau) = \frac{< E_s^*(\vec{\mathbf{q}}, 0) E_s(\vec{\mathbf{q}}, \tau) >}{< I(\vec{\mathbf{q}}) >} \tag{3.17}$$

$g^{(1)}(\tau)$ is also referred to as the "intermediate scattering function". The normalised time correlation function $g^{(2)}$ is given in terms of the scattered intensity and is the observable of

the experiment. It is related to the autocorrelation function $g^{(1)}$ through the "Siegert relation":

$$g^{(2)}(\mathbf{q},\tau) = \frac{< I(\vec{\mathbf{q}},0)I(\vec{q},\tau) >}{< I(\vec{\mathbf{q}}) >^2} \tag{3.18}$$

$$= 1 + [g^{(1)}(\mathbf{q},\tau)]^2. \tag{3.19}$$

If the particles investigated are monodisperse and very dilute, i.e. we are in the non-interacting limit, $g^{(1)}(\tau)$ is a simple exponential function.

$$g^{(1)}(\tau) = e^{-\Gamma\tau} \tag{3.20}$$

where $D = \Gamma/q^2$ is the"free-particle" diffusion coefficient. If Γ is plotted as a function of $\mathbf{q}^2$, the slope of this line is D. From D the hydrodynamic radius R_h can be determined by the Stokes-Einstein equation

$$R_h = \frac{k_B T}{6\pi\eta D}, \tag{3.21}$$

where k_B is Boltzmanns constant, T the temperature and η the viscosity of the liquid. In the general case, the particles are not monodisperse, but have a distribution of sizes (polydispersity). This leads to a deviation from the exponential function (eq. 3.20) and is described by the distribution of relaxation frequencies $G(\Gamma)$. The autocorrelation function can then be rewritten as the integral

$$g^{(1)}(\tau) = \int_0^\infty G(\Gamma) e^{-\Gamma\tau} d\Gamma. \tag{3.22}$$

For reasonably small polydispersity, $g^{(1)}(\tau)$ can be approximated by the cumulant expansion [121].

$$g^{(1)}(t) = A\, e^{(-\Gamma_1 t - \frac{\Gamma_2}{2}t^2 + \frac{\Gamma_3 t^3}{3!} - \cdots)} \tag{3.23}$$

Consequently $g^{(2)}(t)$ is

$$g^{(2)}(t) = B + A\, e^{(-2\Gamma_1 t - \Gamma_2 t^2 + \frac{2\Gamma_3 t^3}{3!} - \cdots)} \tag{3.24}$$

with Γ_i the i-th cumulant. Γ_1 describes the average relaxation rate $\langle\Gamma\rangle$, Γ_2 the width of the distribution, i.e. the deviation of the correlation function from the simple exponential, and Γ_3 is a parameter which describes the symmetry of the distribution. In equation 3.24, A is the

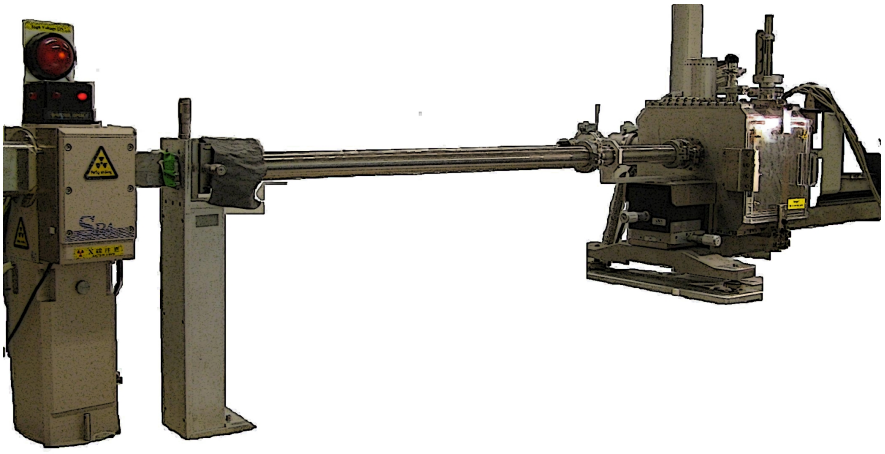

Figure 3.2: The SAXS instrument at the University of Åarhus. The X-ray source is shown on the left, with the attenuator to the right. The collimation is performed with three pin holes in the long tube ending at the sample chamber (right). Behind the sample chamber is the two-dimensional beryllium gas detector.

amplitude and B the baseline, that needs to be added to arrive at the general case of 1 for the intensity time correlation function.

3.2.4 Scattering Instruments

Light Scattering (LS)

A LS Instruments 3D light scattering device was used. The light source is a 25 mW He/Ne laser operating at λ_0 =632.8 nm and the scattered light is detected by fibre optics with avalanche diodes.

To avoid dust, the buffer was first filtered multiple times through a membrane with 250 μm pore size before diluting the stock solution with buffer. Afterwards the sample was filled into the sample cell for, i.e. in simple glass cuvettes with a rounded bottom and an inner diameter of about 8 mm and a wall thickness of about 0.5 mm, the cell was centrifuged at 5000 g for 30 min to remove dust particles to the bottom of the cell. The temperature of the sample was adjusted to 25°. The particle size distribution was calculated using the Contin analysis program [122, 123]. Contin is one of the most frequently used and is based on a constrained Laplace transform to find a smooth non-negative relaxation frequency distribution $G(\Gamma)$ consistent with the measured data.

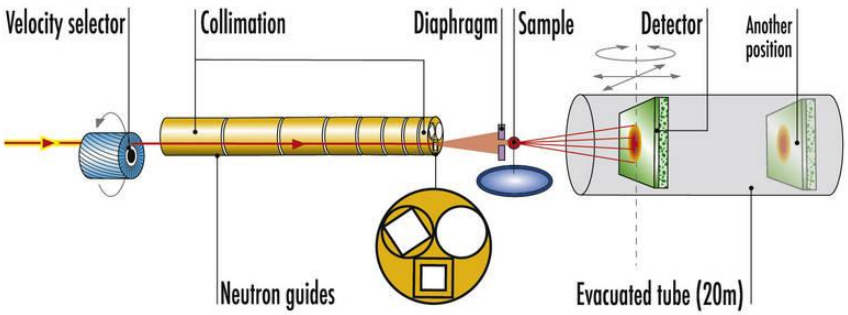

Figure 3.3: A schematic picture of a neutron scattering setup of D22 at ILL. Scheme taken from the ILL website.

Small-angle X-ray Scattering (SAXS)

The measurements were performed on the SAXS instrument at the University of Åarhus, group of Prof. J. S. Pedersen. The instrument is a modified version of the commercially available NanoSTAR SAXS instrument, produced by Anton Paar (Graz) and distributed by Bruker AXS. The X-ray source is a rotating copper anode with a 0.3 x 0.3 mm^2 source point. The Cu K_α radiation is monochromatised and parallelised by two Göbel mirrors. The beam is then collimated by three pin holes. The instrument is optimized for solution scattering in terms of flux and background and is therefore ideally suited for our experiments. It was configured to have a range of scattering vectors between 0.01 $Å^{-1}$ and 0.9 $Å^{-1}$ and has a flux of about 1.7 $\times$ 10^7 photons s^{-1} in the standard configuration. The data was recorded using a two-dimensional position-sensitive beryllium gas detector by HiSTAR. For further information see [124].

The sample cell is held in a home-built quartz capillary holder (sealed with caps and o-rings) and located in a thermostated sample block for good thermal contact. The capillary and the thermostated block are placed inside the integrated vacuum chamber of the instrument. All SAXS experiments were performed with mark-tubes (Hilgenberg) made of quartz glass with a length of 80 mm and a wall thickness of 0.01 mm. The capillaries were sealed by flaming one of the ends with a bunsen burner to avoid leakage in the vacuum sample chamber.

Small-angle Neutron Scattering (SANS)

The SANS experiments were performed at the beamline D22 of the **Institute Laue-Langevin** (**ILL** in Grenoble, France). The schematic setup is shown in the figure 3.3. The neutrons are produced in a nuclear reactor. The neutron beam is made to pass through a rotating velocity selector, where the neutrons are monochromatised although with a wavelength spread of about 10%. Afterwards the neutrons pass through a collimation with eight guide tube sections of

λ [Å]	Collimation $[m]$	Detector $[m]$	q-range $[Å^{-1}]$
8	8	2	$[0.02; 0.2]$
8	14.4	14.4	$[2 \times 10^{-3}; 0.05]$
18	17.6	17.5	$[1 \times 10^{-3}; 0.02]$

Table 3.3: Configuration of the SANS experiment.

55 mm x 40 mm resulting in nine different possible source-to-sample distances from 1.4 m to 17.6 m. A diaphragm, i.e. an aperture, controls the maximum sample area irradiated to avoid extra scattering from the cuvette or sample holder. The neutrons scattered by the sample are recorded by a 2-dimensional ^{3}He detector with 128 x 128 pixels each of 0.75 cm x 0.75 cm. The sample-to-detector distance can be varied between 1.4 m and 20 m as well as the detector offset between 0 and 0.5 m. The measurements were performed to provide a q-range from 0.003 to 0.32 Å^{-1} by using three different settings (table 3.3).
The samples were kept in round quartz cuvettes (Hellma, Germany). The neutron spectra of water was measured in a cell with 1 mm pathlength, whereas the samples were in cells with 2 mm pathlength. The measured raw data was corrected for the solvent, the sample cell and the external background. Further details will be given in section 3.2.6.

3.2.5 Sample Preparation

The samples were prepared as explained in chapter 4. In the SAXS measurement, all samples are in aqueous solution, whereas in the SANS and the LS measurements deuterium oxide was used.

3.2.6 Data Treatment

Small-angle Neutron Scattering (SANS)

The measured scattering intensity I_S contains the scattering by the sample (incl. solvent) only, while I_{SB} is the measured scattering intensity of the sample including cell and background and I_{Cd} by the measureds intensity of the background. (See chapter 2 of [116] and [125]). The background can be separated into an internal and an external background. The internal background originates from the sample itself, for instance scattering from a sample containing hydrogen will contain incoherent scattering without a q-dependence. In contrast, the external background stems from natural (cosmic) radiation or from the "noise" of other instruments. By placing Cadmium sample or a Bor containing plastics, which are highly absorbent, at the sample position, the external background can be determined. This measured intensity corresponds to the general external background I_{Cd} and can be directly subtracted from all

measured intensities. Another correction, especially for solution scattering, concerns the cell and solvent, I_{EC}.

H_2O is predominantly an incoherent scatterer and thus its scattering intensity is independent of q, and is used to determine the detector efficiency ε . A determination of the transmission $T_{\mathrm{H_2O}}$ and intensity $I_{\mathrm{H_2O}}$ of the water sample and the container only, $T_{EC_{\mathrm{H_2O}}}$, $I_{EC_{\mathrm{H_2O}}}$ is required. A water sample in a quartz cell with 1mm path length is used.

In order to subtract the background contributions from the sample, we calculate:

$$I_S = \frac{\frac{I_{SB}-I_{Cd}}{T_S} - \frac{I_{EC}-I_{Cd}}{T_{EC}}}{\frac{I_{H_2O}-I_{Cd}}{T_{H_2O}} - \frac{I_{EC_{H_20}}-I_{Cd}}{T_{EC_{H_20}}}} \tag{3.25}$$

After this correction, azimuthal averaging is performed to reduce the 2-dimensional intensities $I(\bar{q})$ into an intensity as a function of the magnitude of the scattering vector $\vec{q}$. This is possible, since our aggregates should be randomly oriented in solution.

Small-angle X-ray Scattering (SAXS)

The measured data has been azimuthally averaged by the data acquisition programme to obtain intensity in arbitrary units as a function of q. For intensity normalisation, the photon counts received at the detector must be properly measured. A wedge-shaped slit, which is placed in front of the detector to cover and protect portions of the detector surface creates a shadow (a blackened area in the detecting volume and consequently on the measurement). This shadow is measured in a separate experiment with a glassy carbon sample and is afterwards normalised with water as a primary standard. Further details can be found in [124]. The normalisation and data treatment is performed with a Fortran77 based home-built program produced by Prof. Jan Skov Pedersen and his group.
The measured intensity was corrected with the "noise" or background scattering from wiggler and slit sources. For this purpose the direct beam is blocked by a piece of lead. The scattering from the buffer was subtracted. All data are routinely converted to absolute scale using the scattering from water as a standard using the following expression:

$$I(q) = \left[\left(\frac{I_S(q)}{\Phi_S T_S t_S} - \frac{I_{BG}(q)}{\Phi_{BG} T_{BG} t_{BG}} - \frac{I_{\mathrm{noise}}(q)}{t_{\mathrm{noise}}(\Phi_S T_S - \Phi_{BG} T_{BG})}\right)\frac{1}{I_{\mathrm{shadow}}}\right]\frac{d\Sigma/d\Omega_{H_2O}}{I_{H_2O}} \tag{3.26}$$

where I is the resultant scattering intensity after corrections, I the scattering intensity, Φ the

intensity of the incident beam with the subscripts 'S', 'BG', 'noise', 'H_2O' and 'shadow' referring to the sample, the solvent, the background, the noise, the H_2O and the beam stopper shadow, respectively, t is the measurement time and T the sample transmission. $d\Sigma/d\Omega_{H_2O}$=0.01632 cm^{-1} is the theoretical scattering cross section for water at 20° C

Chapter 4

Sample Preparation

4.1 Chemicals

All salts such as NaCl (Fisher), TRIS-HCl ($NH_2C(CH_2\ OH)_3 \cdot HCl$), and TRIS-base $NH_2C(CH_2\ OH)_3$ (both Sigma-Aldrich) and the bile salts used in these experiments: taurochenodeoxycholate acid sodium salt (NaTCDC) and taurocholic acid sodium salt (NaTC) purchased by Calbiochem were used as received. NaTCDC and NaTC is dissolved in water, methanol or ethanol. The molecular weight of NaTCDC is 521.7g mol^{-1} and of NaTC 537.7g mol^{-1}. Egg yolk lecithin (Lipid Products, South Nutfield, Surrey, UK (grade I)) a natural lecithin with an average of 17.5 carbons, arrives in 500mg ampoules dissolved in a mixture of chloroform and methanol. EYL has an average molar weight of 770g mol^{-1}.

4.1.1 Stock Solution

All water was doubly dionised in a Millipore water system (resistance $18M\Omega$ /cm). Ethanol (Fisher Scientific, analytical grade) was used for rinsing and sample preparation. Deuterium oxide, D_2O, grade 99.92%, was purchased from Eurisotop. All solvents were used as received. A TRIS base/HCl buffer in either D_2O for neutron scattering experiments or in H_2O for SAXS measurements are used. For LS either D_2O or H_2O was used as specified in each paragraph. TRIS-HCl and TRIS-base is used to buffer the solution at pH 8.0. The solution is mixed with the appropriate concentrations of acid and base and adjusted with a pH-meter. The total concentration of the buffer at pH 8.0 is 21.8 mM for the TRIS-Base and 28.2 mM for the TRIS-HCl and gives a total TRIS concentration of 50 mM. The contribution of the TRIS buffer towards the ionic strength of the buffer is 28.2 mM and investigations at higher electrolyte concentration are done by adding NaCl to the desired total electrolyre concentration c_s. The electrolyte concentrations used in this thesis varied from 100 mM to 2000 mM.

A stock solution containing 20mg/ml of the bile salt is prepared for the mixture with the lipid.

The lipid is added into ethanol obtaining a lecithin content of 20mg/ml. Appropriate amounts of both stock solutions in ethanol are mixed to result in a molar ratio of bile salt to lecithin of 0.9. This mixture is then dried using a rotavaporator and reduced pressure of 50 mbar until the ethanol is evaporated and a dried film of EYL with NaTCDC or NaTC is obtained. The film was dried at least for 8 hours in the rotavaporator until cracks of the thin film were visible. If necessary the film was further dried in a vacuum oven for another 12-24 hours. The film is flushed with an inert gas like argon or nitrogen, then removed from the rotavaporator or from the vacuum oven. Buffer is added to make a concentrated stock solution with 50mg/ml total amphiphiles, also referred as dilution 1 (d=1), the contribution of the lecithin is 37.1 mM and of the NaTCDC bile salt 41.1 mM with bile salt to lecithin ratio of 0.9. After equilibration of about 24-48h the stock solution is diluted with the buffer to the new total aggregate concentration c_t, but at constant total electrolyte concentration c_s. For dilutions higher than 100, first a dilution step to d=10 was performed, and then another form d=10 to the appropriate dilutions. For all scattering experiments, the samples were prepared several days before use, flushed with an inert gas, sealed tightly and kept at constant temperature (at 25C).
As noted above the total salt concentration c_s originates from the buffer, with an effective concentration of 28.2 mM, and added NaCl. The counterions of the dissociation of bile salt are not included in the concentration c_s, since the typical dilution $d > 10$, the bile salt concentration was typically below 4.1mM.

Chapter 5

First Observations

Samples at various dilutions d and electrolyte concentrations c_s were prepared in H_2O and D_2O solutions with buffer added as explained in chapter 4.

At increased NaCl concentrations c_s the samples are macroscopically heterogenous with a more *viscous* phase sedimenting in aqueous (H_2O) solutions and floating on top in D_2O solutions. In the case of D_2O, the heterogeneous samples were observed at lower salt concentrations c_s. Both "bulk phases" are clear. The non-viscous phase becomes slightly turbid at higher dilutions d. Figure 5.1 shows a picture taken from a phase separated sample in D_2O solution with $d = 80$ and $c_s = 1000$mM. When shaken carefully the viscous phase is floating in the solvent as it can be seen in figure 5.1 in a red circle. When shaken vigorously, the sample becomes homogeneous and overall turbid, but will generally phase separate after a few hours to days. Samples at physiological concentration are well studied [41, 60]. Samples in the vesicular range, i.e. at high dilutions, became slightly turbid. Ollivon *et al.* [35] found macroscopic phase separation on EYL/octyl glycoside mixtures for low EYL concentrations, $c_L < 2$mM. For EYL/bile salt the bulk phase separation also occurs at this low lipid concentration. Another macroscopic phase separation was found for mixtures of cholesterol in bile salt/lipid systems [40], where the relative amount of cholesterol in the mixture of the bile salt/lipid system exceeds the limit of the solubilisation of the micelles and a state of supersaturation exists according to Mazer et al. [40] the insoluble phases containing the excess cholesterol shall precipitate.

Figure 5.1: Phase separated sample in D_2O with dilution d = 80 and c_s = 1000mM. Red circle shows aggregates of the viscous phase floating in the sample after shaking.

To be able to distinguish between the two bulk phases, will be referred to as ”viscous” and ”non-viscous”.

For mixtures of NaTC/EYL prepared under the same condition as NaTCDC/EYL, the two-phase region was found at higher salt concentration, i.e. at 1200 mM$\leq c_s \leq$1900] mM. NaTC is a trihydroxy bile salt and is therefore far more soluble compared to dihydroxy bile salt NaTCDC. Therefor the more soluble NaTC bile salt will be found in aggregates at higher concentrations (increase of cmc), so in terms of dilution, the phase boundaries from micellar to micelle vesicle coexistence or coexistence to vesicular phase will be shifted to lower dilutions or to higher salt concentrations.

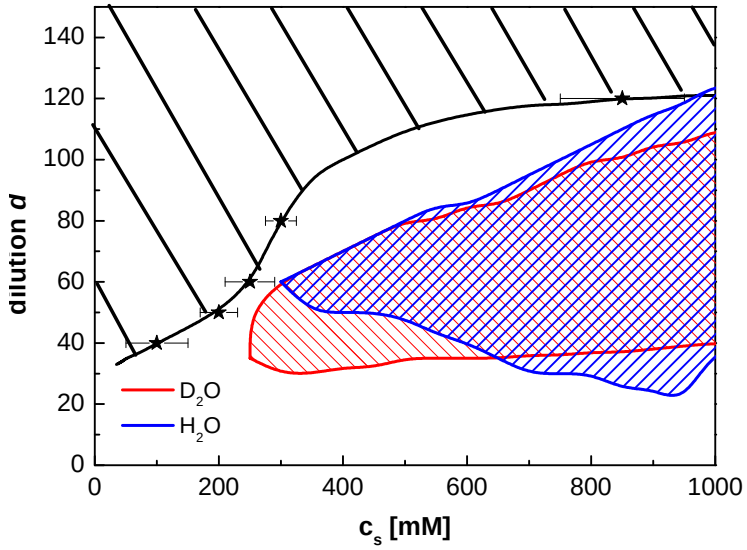

Figure 5.2: The phase diagram of the NaTCDC/EYL system. The blue and red hatched areas corresponds to the region, where two phases are observed in H_2O (blue) and D_2O (red), respectively. The data points refer to changes in the light scattering behavior while the back line is a guide to the eye. The data points and black line show the boundary between vesicular and vesicle micelle coexistence range measured and is from reference [60].

In figure 5.2 the hatched areas display the concentrations, where two phases were observed. The blue area corresponds to H_2O as a solvent and the red to D_2O. The difference between the two is a slight shift with salt and amphiphile concentration, i.e. the dilution. The black solid line and the black hatched area indicate the area where vesicles were observed using light scattering experiments [60].

In the X-ray scattering experiments in chapter 8, the structural properties of the viscous phase in H_2O will be investigated and the mainly non-viscous phase with neutron scattering experiment

in chapter 7.

In the microcalorimetry experiments (in chapter 6), the *whole* sample is mixed and used to find the phase boundaries between micellar, coexistence and vesicular phases in the bile salt concentration against the lecithin concentration plane at various buffer salt concentrations c_s. Based on the obtained phase diagram the diagram in the dilution d against salt concentration c_s plane is calculated, which is the phase diagram usually used for scattering experiments.

Chapter 6

cmc of Bile Salts and Bile Salt-Lecithin Phase Diagram: Microcalorimetry

The influence of the increasing salt concentration on both the *cmc* of the bile salt, NaTCDC, and on the phase behaviour of mixtures of bile salt and egg yolk lecithin (EYL) will be investigated by isothermal calorimetry (ITC). A phase diagram in the EYL concentration-bile salt concentration plane will be obtained and compared with results from literature. This phase diagram, will be translated into the total aggregate concentration salt concentration c_s plane, which will be used in the following chapters.

6.1 Demicellisation Experiments

As already explained in section 1.1.3 there are many experimental methods to deduce the *cmc* of surfactants. In the following the *cmc* of NaTCDC at the temperatures T=25° C and T=40° C will be determined for several salt concentrations, c_s, and the temperature range from 5° C to 60° C for one salt concentration c_s=200 mM. The determination of *cmc* values by microcalorimetry experiments is well established [126]. In one single experiment the *cmc* and the enthalpy change of the micellisation can be inferred. For bile salts generally low aggregation numbers have been found, which has been attributed to their structure [52, 127].

Figure 6.1 shows the result of a demicellisation experiment with NaTCDC micelles at high salt concentration (c_s=1 M) at T=25° C and T=40° C. As described in chapter 3.1.3, a bile salt solution with a concentration above the cmc (here: 20mM) is injected into the sample cell, which contains only buffer at the same salt concentration. Each injection of the titrant, i.e. the bile salt solution, produces a heat flow. The following injection is performed, when the signal has reached its baseline, i.e. no more heat is produced by the reaction. This takes 3 to 4 minutes in the present experiments. The height of the endothermic peak decreases with

increasing number of injections, i.e. by increasing the bile salt concentration in the sample cell and thus decreasing the difference in bile salt concentration; upon each injection the bile salt micelles will disintegrate until the concentration of the surfactant reaches the cmc and the heat flow decreases to almost zero towards the end of the experiment.

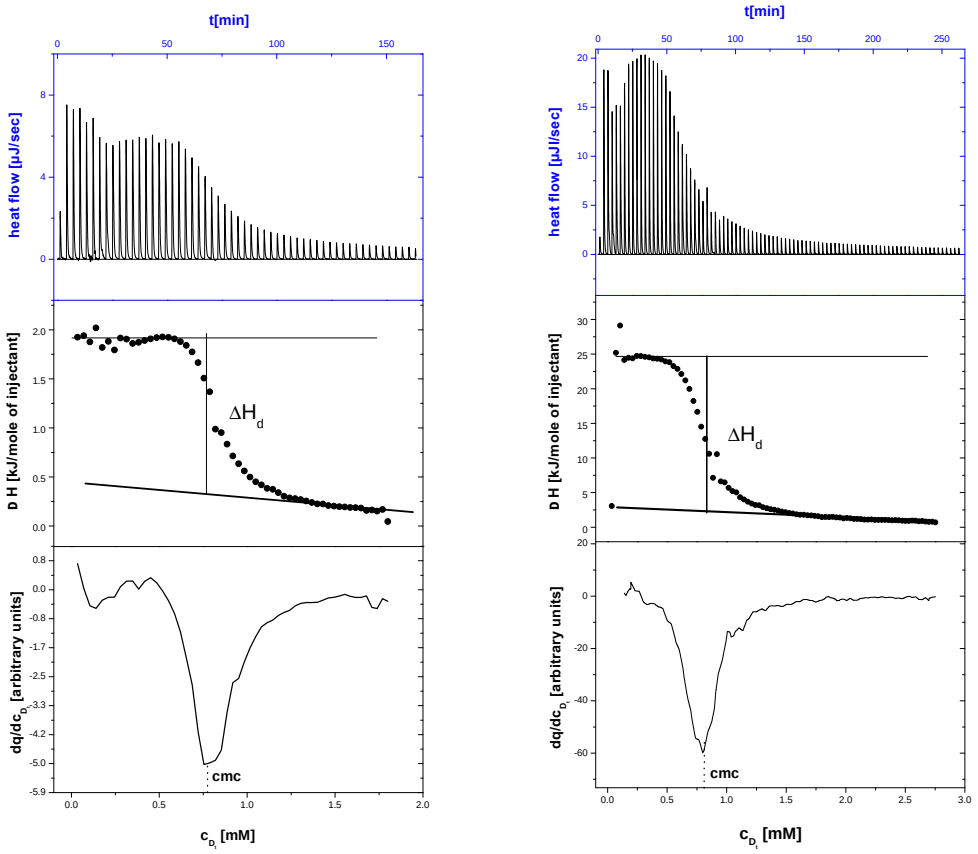

(a) (b)

Figure 6.1: Isothermal calorimetry (ITC) experiment to deduce the cmc and enthalpy parameter: Titration of 50 $\times$ 1μl of a 20 mM NaTCDC into a 1 M NaCl solution (pH=8.0). The (top) plot shows the heat produced per injection of bile salt solution into the sample cell plotted versus time t (top axis) indicated by the blue box, the integrated heat (middle) and derivative of the integrated heat (bottom) are plotted against the detergent concentration c_{D_t} (bottom axis). The temperature was (a) at T=25° C and (b) T=40° C

When the bile salt concentration in the sample cell is below the *cmc*, the determined enthalpy ΔH contains the contributions from demicellisation into monomers ΔH_d, the release of bound counterions $\Delta H_{d_{release}}$ and the effect of micelles $\Delta H_{d_{mic}}$ and monomers $\Delta H_{d_{mon}}$. At concentrations above the *cmc*, only the contribution from dilution of micelles $\Delta H_{d_{mic}}$ is determined, since a micellar solution is titrated into a micellar solution. In contrast, $\Delta H_{d_{mon}}$

is obtained by titrating highly diluted detergent solution into buffer. By subtracting these contributions the demicellisation enthalpy ΔH_d is obtained.

$$\Delta H_d = \Delta H - \Delta H_{d_{mic}} - \Delta H_{d_{mon}} - \Delta H_{d_{release}} \tag{6.1}$$

The integrated heat as function of bile salt concentration c_{D_t}, i.e. the determined enthalpy ΔH (fig. 6.1 (middle)) shows the ΔH above and below the *cmc*. In the two limits at low and high c_{D_t}, where the reaction enthalpies are almost constant and correspond to $\Delta H_{d_{mon}}$ and $\Delta H_{d_{mic}}$, respectively. The point of inflection indicates the *cmc*, which is more accurately determined by the first derivative of the enthalpogramm (fig. 6.1 bottom).

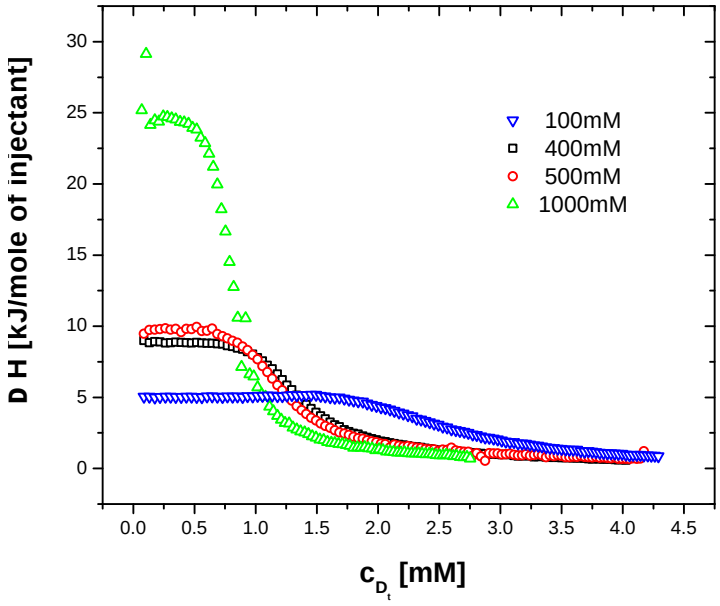

Figure 6.2: Enthalpogramm, i.e. reaction heat transfer against the total detergent (NaTCDC) concentration at T=40° C by increasing the salt concentration c_s with NaCl of the buffer.

For a surfactant, demicellisation (above room temperature) is usually an endothermic process while micellisation is an exothermic process, which is due to the hydrophobic effect, i.e. the clustering of the hydrophobic, apolar parts in aqueous solution [128]. The number of water molecules in the solvation shell around the hydrophobic part is reduced by micellisation. This results in an entropy increase, i.e. a positive entropy change, during micellisation and a negative entropy change during demicellisation. By increasing the temperature the contribution due to entropy decreases and thus the contribution of the enthalpy *H* in micellisation gains importance. This phenomenon is known as: entropy-enthalpy compensation [26, 128, 108, 129, 130]. The

entropy-enthalpy compensation is due to the hydrophobic effect, which originates in the large energy required to form a cavity in the water for the hydrocarbon solute. This is driven by the loss of hydrogen bonding and the entropic cost of forming this cavity around the non-polar molecules. These losses can be minimised by the association of non-polar molecules [128]. In [131], it is said: "The temperature dependence of the entropy/enthalpy of transfer is entirely determined by the water structuring since the contribution arising from the cavity formation is assumed to be temperature independent. It is the balance between these two contributions that causes the minimum in the cmc, the maximum in adsorption with respect to temperature for ionic surfactant systems and minimum in solubility for non-polar molecules in water".

6.1.1 Demicellisation Enthalpy and *cmc*: Dependence on Salt concentration and Temperature

The entropy change ΔS_d (table 6.1) is always negative, but its magnitude increases with decreasing temperature and increasing salt concentration. This is also reflected in the integrated reaction heat per mole of injected bile salt on the bile salt concentration c_{D_t} at $T = 40°$ (fig. 6.2). The demicellisation heat ΔH_d increases with increasing c_s. Furthermore, the point of inflexion and thus the *cmc*, is shifted towards lower concentrations with increasing c_s. (Figure 6.2 and table 6.1).

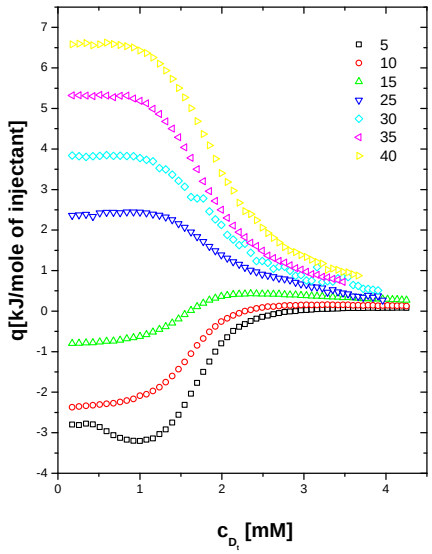

Figure 6.3: Enthalpogramm, i.e. reaction heat transfer, as a function of the total NaTCDC c_{D_t} concentration at various temperatures and salt concentration c_s = 200 mM.

Although the tendency of the entropy-enthalpy compensation has been investigated for all different salt concentrations c_s at the two temperatures T = 25° C and T = 40° C, a wider temperature range has been studied for c_s=200 mM only (figure 6.3). The point of inflexion, the *cmc*, does not change significantly (figure 6.3 and table 6.1). The demicellisation below room temperature is an exothermic reaction and becomes endothermic above room temperature. This agrees well with literature [128]. The entropy-enthalpy compensation is illustrated in figure 6.4 for c_s=200 mM. At room temperature the demicellisation enthalpy ΔH_d is low and at T=20° the heat could not be measured. This is well known in the literature, where enthalpy should approach zero at room temperature and increase with increasing the temperature [26, 29].

Having determined the *cmc* and the demicellisation enthalpy ΔH_d, many thermodynamic quantities can be deduced, particularly interesting are the Gibbs energy of demicellisation ΔG_d and the entropy of demicellisation ΔS_d [129]. The value of the parameters are calculated using the pseudo phase-separation model, which will briefly be introduced in the following [1, 26, 129, 128, 130]: In equilibrium, the chemical potential μ of molecules in different phases must be equal. For a demicellisation or micellisation process, this implies that μ of the monomers in bulk and in micelles are equal in equilibrium.

$$\mu = \mu_{n_{\text{agg}}} = \mu^0_{n_{\text{agg}}} - \frac{RT}{n_{\text{agg}}} \ln \frac{c_{n_{\text{agg}}}}{n_{\text{agg}}} \tag{6.2}$$

where n_{agg} is the aggregation number, *R* the universal gas constant and $c_{n_{\text{agg}}}$ the concentration of molecules in an aggregate with aggregation number n_{agg}.
In the pseudo phase-separation model, micelles and monomers are considered as separate phases. The change in free enthalpy (Gibbs energy) during the transfer of a surfactant molecule from a micelle into the solution can therefore be expressed as the difference in chemical potential of a monomer in water μ_{w} and in an aggregate $\mu_{n_{\text{agg}}}$. This can be rewritten in terms of the cmc given in mole fractions units [1] and the activity coefficient of the monomers in water a_{w}.

$$\begin{aligned} \Delta G_d &= -\mu_W + \mu_{n_{\text{agg}}} \\ &= -RT \ln cmc' + RT \ln a_w - \frac{RT}{n_{\text{agg}}} ln \frac{cmc'}{n_{\text{agg}}} \end{aligned} \tag{6.3}$$

The phase-separation model assumes a large n_{agg} and an ideal behaviour of the monomers in the solvent ($a_w = 1$), so that the last two terms in equation 6.3 are negligible, and $\Delta G_d \approx -RT \ln cmc'$ (Fig. 6.4, Tab. 6.1). With ΔG_d the change in entropy ΔS_d can be obtained using the Gibbs-Helmholtz equation:

$$T\Delta S_d = \Delta H_d - \Delta G_d \tag{6.4}$$

The values are summarised in fig. 6.4 and tab. 6.1. In the case of bile salt the assumption $n_{\text{agg}} \gg 1$ seems not justified, because the aggregation number is much lower than for most other surfactants [19, 13, 132, 14]. The aggregation number of trihydroxy bile salt micelles at physiological conditions is between 15 to 20 monomers [6, 21]. There is no other study on the aggregation number of NaTCDC micelles with increasing ionic strength. However, this model was used to calculate sodium cholate (NaC) and sodium deoxycholate (NaDC)

[1] Mole fractions are calculated with respect to water, i.e. $cmc' = cmc/[c_{water}]$.

micellisation enthalpies from the *cmc* by comparing and validating the results with surfactants with much higher aggregation numbers as in Paula *et al.* [129] and facilitated with results from the literature. Garidel *et al.* [106] again measured the *cmc* of NaC and NaDC at various temperatures using ITC to improve the thermodynamical description by using the mass action model instead of the phase-separation model and obtained quite similar results with both descriptions.

Upon increasing the salt concentration c_s, the *cmc* in general decreases, which implies micelle

c_s [mM]	T [°C]	*cmc* [mM]	ΔH_d [kJ· mol^{-1}]	ΔG_d [kJ·mol^{-1}]	T ΔS_d [kJ·mol^{-1}]
100	25	2.49	1.27	24.82	-23.55
	40	2.22	3.86	26.37	-22.51
200	5	1.66	-3.32	24.09	-27.41
	10	1.64	-2.44	24.56	-26.99
	15	1.55	-0.97	25.13	-26.10
	25	1.75	2.02	25.70	-22.36
	30	1.79	3.33	26.06	-22.74
	35	1.73	4.71	26.58	-21.87
	40	1.90	5.84	26.78	-20.94
300	25	1.71	2.36	25.76	-23.39
400	25	1.71	2.32	25.76	-23.43
	40	1.23	7.27	27.91	-20.63
500	25	1.12	3.07	26.79	-19.52
	40	1.19	7.28	27.99	-24.92
750	25	1.04	3.24	26.80	-23.56
	40	1.07	7.98	28.26	-20.27
1000	25	0.78	1.61	27.63	-26.02
	40	0.85	22.45	29.18	-6.71

Table 6.1: Thermodynamic parameters of the demicellisation of NaTCDC in aqueous solution at different salt concentration c_s and temperatures T. The *cmc* and demicellisation enthalpy ΔH_d were measured in an ITC demicellisation experiment and the Gibbs free energy ΔG_d and the entropy T ΔS_d calculated using the pseudo phase-separation model.

formation at lower total bile salt concentration for higher c_s. This is due to electrostatic interactions with electrostatic screening increased at higher ionic strength. This is more important for charged bile salt molecule in the micelles than the well-separated monomers in solution. This favours micelle formation [129, 106, 133]. Furthermore, with increasing salt concentration the aggregation number n_{agg} has been reported to increase.

NaTCDC has not been extensively studied compared to NaC, a trihydroxy, and NaTDC, a dihydroxy bile salt, although NaTCDC is one of the most abundant of bile salts [111]. One of the main reasons might be its lower solubility, and therefore lower *cmc*, which makes it experimentally more difficult to determine. Table 6.2 shows some literature values of the *cmc* of NaTCDC. Most of the studies evaluated the *cmc* at physiological condition, i.e. neutral pH

and c_s=150 mM. With dye titration and surface tension experiments a value of around 1.5 mM was found [27], while a two times higher value was determined with light scattering in the same study [27].

In microcalorimetry studies [106, 111] they argued, this might be due to the fact, that in light scattering experiments hydrodynamic interactions with surfactant concentration could influence the results. This was not taken into account in the studies [6, 5].

The salt dependence on NaTDC has been investigated in [6] with respect to the aggregation number for *primary* and *secondary* aggregates and in [21] with respect to the *cmc*, the counterion binding and micellar aggregation number. Also the other bile salts have not been investigated much with respect to the changes in the *cmc* or aggregation number with varying the ionic strength of the micellar solution. This will be further discussed in the next section. Kawamura *et al.* [28] investigated with spin-label studies the micellar interior and found an indication of the two-stage model for dihydroxy bile salts (actually NaTCDC was measured), that exhibited two different kind of micelles coexisting for 100mM dihydroxy bile salt solutions. The spin-label studies displayed differences in the internal structure of the micelle, where taurine conjugated dihydroxy bile salts immobilised the spin probes in the micelle compared to trihydroxy bile salt.

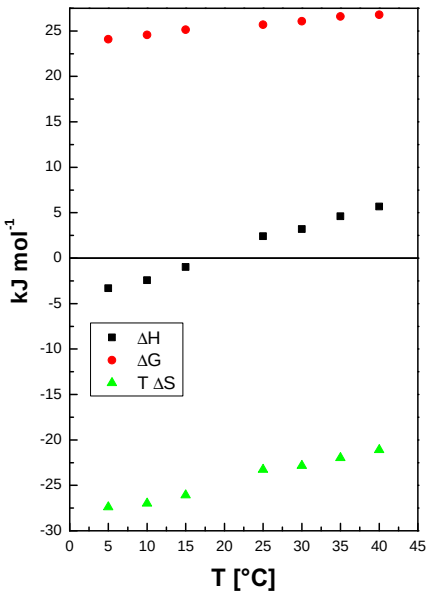

Figure 6.4: Thermodynamic parameters demicellisation enthalpy ΔH_d, Gibbs free energy ΔG_d and entropy ΔS_d of the demicellisation of NaTCDC micelles in an aqueous solution with pH=8.0 and NaCl concentration c_s=200mM.

We only observed one *cmc*. If one assumes a two stage model for NaTCDC, then either this cannot be measured by ITC, because the *cmc* values are too close to each other or the measurements are not sensitive enough for a continuous deaggregation process, where little heat is produced. Nevertheless, in [21] two *cmc* for various bile salts could be identified, which has not been observed before. The direction of the experiment, however, is different in their fluorescence and our microcalorimetry experiment. They are forming micelles, whereas we study deaggregation, by injecting NaTCDC solution with concentration above the *cmc*. The deaggregation is found to occur in one step and if there are two steps, the heat produced in each step of deaggregation cannot be separated and the determined cmc thus corresponds to the *primary cmc*.

In the concentration range of the second *cmc* of [21] no heat was produced during our demicellisation experiments.

Hildebrand *et al.* [111] have investigated bile salt demicellisation in a microcalorimetry experiment and also found one *cmc*, but by studying sodium oleate micelles two *cmc*s were deduced. (Also for sodium oleate a two stage model for aggregation is proposed.) They do not discuss, why two *cmc* can be seen for sodium oleate but not for bile salts.

They mention that although the heats overlap and the enthalpy of the two stages of demicellisation cannot be separated, the thermodynamic nature of the two stages might be different. The cmc of bile salt and the first *cmc* of sodium oleate show a temperature dependence of the *cmc* with a minimum at room temperature, while the second *cmc* of sodium oleate increases with increasing temperature, which might be the reason that two *cmc* can be seen by measuring various temperatures.
An isothermal microcalorimetry study on the dihydroxy bile salt NaC and NaDC has been performed [106]. The only difference between the two bile salt is the position of one of the hydroxy groups, which influences the *cmc*. This can be seen at the concentration range of the *cmc* for trihydroxy, which is higher and ranges between 10mM to 20mM. [136, 137, 106]. The dihydroxy bile salts have *cmc* values below 10mM, depending on the position of the dihydroxy groups even far below 10mM as for NaTCDC examined here. Also the aggregation number is affected by the ionic strength and are higher for dihydroxy than for trihydroxy bile salts. In the following NaTCDC will be compared with another bile salt, where the position of one of the hydroxy groups is changed: NaTDC (in figure 1.3, table 1.1). NaDC was measured with ITC with c_s=100 mM and 100mM (NaCl). The cmc value is lower at higher c_s. Their thermodynamic parameters are in good agreement with most previous studies (see table 1.1) and also with our study. The cmc value of NaTCDC is as expected lower [106].

The values obtained for the *cmc* by our ITC experiments agree not only well with microcalorimetry studies (of other dihydroxy bile salts), although those were measured at low salt regime, but also to most values for the *cmc* of NaTCDC itself inferred with various methods (table 6.2).

6.1.2 Degree of Counterion Binding to Micelles: Corrin-Harkins Relation

The ionic strength also affects the counterion binding to the micelles. The *cmc* values of ionic surfactants obey the Corrin-Harkins relation [138, 139, 140, 141, 142, 143, 144], which relates the *cmc* of the ionic surfactant to the total counterion concentration c_g. The counterions originate from bile salt dissociation and added salt of concentration c_s; $c_g = c_s + cmc$. The relation is:

Method	**Added Salt**	$T[^{\circ}C]$	**pH**	***cmc*[mM]**	n_{agg}
[6]					
Quasieleastic LS	0.15 M NaCl	20-60	$\approx$ 7.5	-	$\approx$ 20
	0.6M	20			$\approx$ 95
[17]					
dye titration	0.15 M NaCl	25	7.0	1.6	-
surface tension	0.15 M NaCl	25	7.0	1.3	-
light scattering	0.15 M NaCl	25	7.0	3.8	15-16
[134]					
surface tension	H_2O	25	8	7	-
	0.15 M NaCl	25	8	1.8	-
dye titration(orange)	0.15 M NaCl	25	8	2.2	-
dye titration(azulene)	0.15 M NaCl	25	8	3.0	-
[135]					
UV-VIS	0.4 M imidazole	26	7.80 $\pm$ 0.02	2.5 - 3.0	
[28]					
electron spin resonance					
(spin label 5-NS)	0.06 M	37	7.8	2.0	
(spin label 16-NS)	0.06 M	37	7.8	3.0	
[132]					
Chomotography	0.154 M NaCl		-	1.7	-
[21]					
Flouresence	0.015 M NaCl	25	7.5	$4.4^{(a)}$,$7.6^{(b)}$	-
spectroscopy	0.075 M NaCl	25	7.5	$2.7^{(a)}$, $5.6^{(b)}$	-
	0.15 M NaCl	25	7.5	$1.3^{(a)}$, $3.4^{(b)}$	-
	0.30 M NaCl	25	7.5	$0.5^{(a)}$, $2.0^{(b)}$	-
Static Light Scattering	0.15M NaCl	25	7.5		11.9

Table 6.2: Experimental results for the *cmc* of NaTCDC in the literature taken from the stated references. In ref. [21] two *cmc* values are found in the fluorescence experiments; superscript (a) gives the *cmc* of smaller aggregates and superscript (b) of bigger, stable aggregates.

$$\log cmc \quad = \quad -k_{\mathrm{CH}} \log c_g - b_{\mathrm{CH}} \tag{6.5}$$

where k_{CH} is the Corrin-Harkins coefficient and b_{CH} a constant. The counterion species must be the same for both the surfactant and the added salt. Here, it is sodium. At low concentrations the coefficient k_{CH} has been known to be experimentally equivalent to the degree of counterion binding β [143]. The theoretical basis for this equivalence has been given by Hall [145, 146] and Evans *et al.* [144] and was further developed by Maeda [141] for micellar solutions with added salt under the assumption that the micelles are always in equilibrium with the monomer surfactant ions and counterions. This equality was later confirmed over a wide range of micellar compositions and salt concentrations [139].

$$k_{\mathrm{CH}} = \beta = \frac{n_g^{\mathrm{bound}}}{n_{\mathrm{agg}}} \tag{6.6}$$

where n_g^{bound} is the number of bound counterion and n_{agg} is the aggregation number.

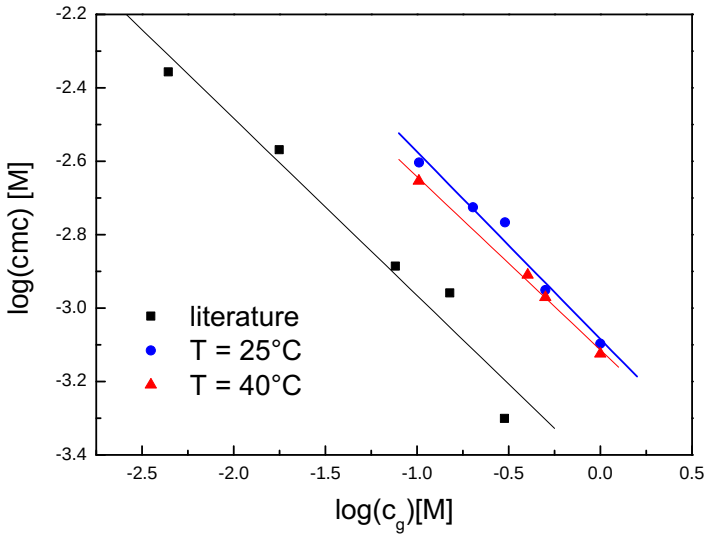

Figure 6.5: Dependence of the cmc on counterion concentration c_g (Corrin-Harkins plot) for temperatures T = 25° C (circles) and T = 40° C (triangles). For comparison results for NaTCDC are shown[21].

In figure 6.9 the relationship between the *cmc* and the counterion concentration c_g for the ITC measurements at T=25° C and T=40° C can be seen and β is given in table 6.3. The experimental results for the *cmc* of *primary* micelles [21], is plotted for comparison in fig.

6.9. Matsuoka *et al.* [21, 147] determined by pyrene fluorescence probe experiments the *cmc* of various bile salt by changing the ionic strength of the buffer. From the changes of the fluorescence intensity as a function of the bile salt concentration, they inferred 3 regimes. A first one with a monomeric solution, then after the primary *cmc*, *primary* micelles, and then above the second *cmc*, the *secondary* micelles (chapter 1 in section 1.2.1). Based on the Corrin-Harkins relation, they evaluated counterion binding $\beta = 0.37$ for the second *cmc* for NaTCDC, which corresponds well to most of the studies performed for bile salts. Generally trihydroxy bile salts such as NaC have a lower counterion binding; the values range from $\beta = 0.08$ and n_{agg} of 5.5 ($c_s = 100$ mM, T=10°) [106] to $\beta < 0.3$ for $c_s < 0.2\ M$ [148, 149]. Mostly the counterion binding of the trihydroxy bile salts have been determined to be $\beta = 0.3$. For the dihydroxy bile salts such as NaDC the counterion binding in titration calorimetry investigation with further analysis using the mass action model was inferred as $\beta = 0.3$ with n_{agg}=12.3 or for another dihydroxy bile salt, NaTDC, $\beta = 0.32$ and n_{agg}=15.9 were deduced at T=36° C with a Corrin-Harkins analysis of the *cmc* and static light scattering experiment [21]. There seems to be a consensus in literature, although only a few values of the fraction of bound counterions has been published yet, that the counterion binding of trihydroxy $\beta \leq 0.3$. Usually the values for dihydroxy are higher.

We determined a counterion binding β higher than most literature values. It roughly corresponds to 1 sodium per two TCDC monomers in the aggregate (table 6.3). It corresponds well with the first *cmc* determined in [21]. It has not been analysed in the paper, but the experimental values are listed and are used here for comparison with our ITC results here. Instead, the second *cmc* was evaluated in the article and corresponds well with other literature values. They argue that the second *cmc* corresponds to the aggregation of the more stable *secondary* micelles. However, here a demicellisation experiment is performed, and thus rather the first *cmc* determined in [21] should be compared to our results.

6.1.3 Conclusion

ITC was used to determine the *cmc* and the demicellisation energy ΔH_d of the dihydroxy bile salt NaTCDC as a function of salt concentration and temperature. The values determined for

	$k_{CH} = \beta$
Literature [21] @ T = 36° C	0.48 ± 0.05
T = 25° C	0.51 ± 0.05
T = 40° C	0.47 ± 0.02

Table 6.3: Results obtained from the fit of the Corrin-Harkins relation as can be seen in figure 6.9 for degree of counterion binding. All for the bile salt NaTCDC with increasing c_s.

the *cmc* at low salt concentration, where literature values exist, correspond well with values obtained previously with various other methods. The *cmc* tends to decrease with increasing c_s. A thermodynamic characterisation of micelle formation or demicellisation was performed using the pseudo phase-separation model to obtain the Gibbs energy ΔG_d and subsequently the entropy change ΔS_d. The temperature dependent measurements at c_s=200 mM were evaluated in detail and correspond well with literature with respect to the enthalpy-entropy compensation of bile salt aggregates at room temperatures. A more detailed temperature dependence could be measured in future experiments, but the work focused mainly on the influence of increasing ionic strength. By using of the Corrin-Harkins relation, the counterion binding was determined. The faction of bound counterions seems higher than in most other studies, with one counterion bound to two NaTCDC molecules in the micelles (instead of three NaTCDC in previous studies). We attribute this to the fact that we examined demicellisation, i.e. the primary cmc, while other studies investigate micellisation and focused on the second cmc.

6.2 Solubilisation Experiments

Microcalorimetry was also used to characterise the vesicle-to micelle transition in NaTCDC/EYL mixtures. Experiments using ITC on lipid or mixed lipid-detergent systems has already been established [54, 58, 107, 110, 150, 151], experiments studying the solubilisation of bile salts, such as NaTCDC, into lipid vesicles, e.g. formed by phosphatidylcholine or soy bean lecithin, have been performed earlier [108, 109, 152, 153, 154]. Here the solubilisation of the bile salt NaTCDC into mixed aggregates of NaTCDC and EYL is investigated. Especially the effect of ionic strength. The results of the solubilisation experiments will also be converted to a “dilution representation”. Based on these experiments the phase diagram in the bile salt-lecithin concentration plane will be established in dependence of the salt concentration. The phase diagram at the physiological salt concentration (150mM) is well established (figure 6.6) [41, 42, 59]. At low bile salt concentration vesicles form and at high bile salt concentration micelles, while at interim concentrations a coexistence is observed. In dilution experiments, which are performed in the following chapters, vesicles are formed in the high dilution regime, where the bile salt, which is better soluble than the lecithin, leaves the aggregates and thus the lecithin-to-bile salt ratio in the aggregates increases. In order to observe a complete solubilisation of this system from vesicles to micelles, highly diluted NaTCDC/EYL solutions are used to which then bile salt is added.

The solubilisation experiment was performed for NaTCDC/EYL mixtures with a molar lecithin-to-bile salt ratio of 0.9 by injecting more of the detergent NaTCDC, which is already incorporated in the aggregate. The experiment follows the purple solubilisation line in fig. 6.6. It is performed by titrating the detergent into the sample cell which has a fixed volume

and contains a NaTCDC/EYL mixture (with low lecithin concentration $c_L \leq 1$ and $c_{\mathrm{D_t}} \neq 0$). Therefore the EYL concentration decreases and the NaTCDC concentration increases in the course of the experiment. The solubilisation process can be observed through all three areas of the phase diagram for highly diluted aggregates. This is ensured by titrating with a detergent solution with a concentration sufficiently high, i.e. far above the cmc. For all experiments a detergent concentration of 25 mM of NaTCDC was used. For more concentrated aggregates, the purple solubilisation line starts in the vicinity of the saturation phase boundary. Upon increasing the detergent concentration, a critical concentration D^{sat} is reached at which vesicles are saturated with detergent. Beyond this concentration, coexistence of mixed vesicles and mixed micelles is observed. The solubilisation concentration D^{sol}, the maximum detergent content in the sample at which vesicles still exist, is reached, and the transformation of vesicles into micelles is completed. This can be also seen in the scheme (figure 6.6), where in range 1, vesicles can be seen. In range 2, first the saturation boundary can be seen, where the vesicles have a high bile salt concentration, than. the coexistence of micelles and vesicles and on the right hand side of range 2 the solubilisation boundary line. The structures are in equilibrium with one another indicated by the double-headed arrow. In range 3 everything is dissolved into mixed micelles.

Figure 6.7 shows the raw data, which were obtained as described in section 3.1.4. In solubilisation experiments the sample cell is filled with lipid/detergent aggregates in buffer and added salt (NaCl), into which detergent solution with a concentration above the *cmc*, i.e. 25 mM, is injected. The measurements were performed with lipid-detergent aggregates of concentrations between 0.5 and 4 mM in constant salt concentrations, which ranged from c_s=100mM up to c_s=1000mM.
The titration heat flow as a function of time for dilution $d = 120$ (chapter 4) for different salt concentration c_s was measured at 25°C. For heat flow in time, three regimes with endothermic, exothermic and finally endothermic reactions can be discriminated. As in the previous section, the heat peaks in time are integrated to obtain the enthalpogramm with heat q per mole of injectant, which is plotted vs the total detergent concentration after each injection.
In the range $c_{D_t} < D^{sat}$ the peaks in the heat flow (figure 6.7 (a) (TOP) in range 1) are caused by the transfer of bile salt molecules from pure micelles into the mixed vesicles, i.e. by demicellisation of the pure bile salt micelles and solubilisation into the vesicles. Accordingly, the endothermic heat flow reflects the demicellisation enthalpy plus the partitioning enthalpy of NaTCDC monomers into the vesicle bilayer. Upon further injection of NaTCDC micelles, the heat flow changes to an exothermic peak (range 2, $D^{sat} < c_{D_t} < D^{sol}$). In this range the vesicles are saturated by detergent and vesicles are successively transformed into micelles [60, 41, 155]. The heat flow reflects the energy, which is required to transform the mixed vesicles into mixed micelles initiated by the change in aggregate composition, i.e. lecithin and

detergent content. As it can be seen in figure 6.7 (bottom) the exothermic heat peaks are almost constant in this range [156]. For $c_{D_t} > D_{sol}$ (range 3) solubilisation of detergent in mixed micelles leads to endothermic peaks, similar to range 1.
The heat flow in range 2 has a reaction heat of $q \sim$ -3.4kJmol^{-1} at d=120 and $c_s = 100$ mM and shows no significant dependence on c_s (figure 6.7 (a)-(c)). At 1000 mM (figure 6.7(d)) the experiment starts already within region 2 and therefore the produced heat q$\sim -0.5kJmol^{-1}$ corresponds to a partial transformation only and our observations of no significant change in reaction heat q is in agreement with predictions [156].

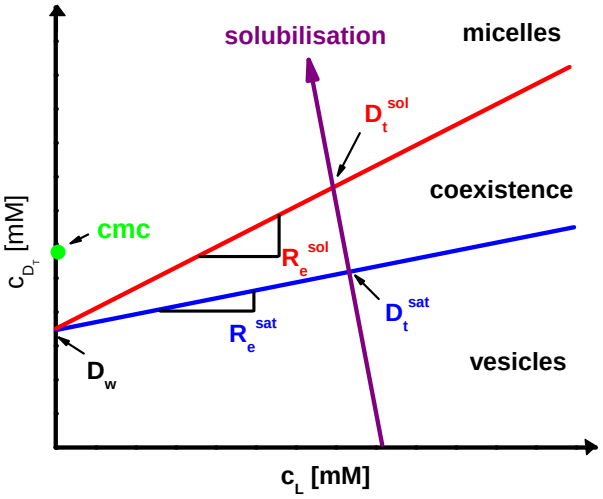

Figure 6.6: Schematic phase diagram of lipid/detergent mixtures of the total detergent concentration c_{D_t} and the lipid concentration c_L. The phase boundaries are represented by the blue and red line. The concentration of detergent during saturation and solubilisation is given by D^{sat} and D^{sol}, respectively. The purple solubilisation line indicates, that by increasing the detergent concentration into a sample cell with fixed volume, L is decreasing with each injection.

The boundaries between the regimes, i.e. D^{sat} and D^{sol} are obtained from the derivative of the heat q with respect to total concentration of the bile salt c_{D_t}. Figure 6.8 shows an example of the derivative for the sample with dilution $d = 120$ and $c_s = 100$ mM. The minima and the maxima in this figure correspond to the D^{sat} and D^{sol}. This is evaluated for all enthalpogramms. Both values D^{sat} and D^{sol} decrease with increasing c_s (tab. 6.4). Above 600 mM and for low dilutions experiments start within the coexistence (range 2). Therefore a value for D^{sat} cannot be obtained with satisfactory sccuracy at higher salt concentrations. At this high ionic strength the total detergent concentration at the start of the experiments is $c_{D_t} \approx D^{sat}$. This is the reason for the high values for the error of the fitted results. See table 6.4. In other studies no

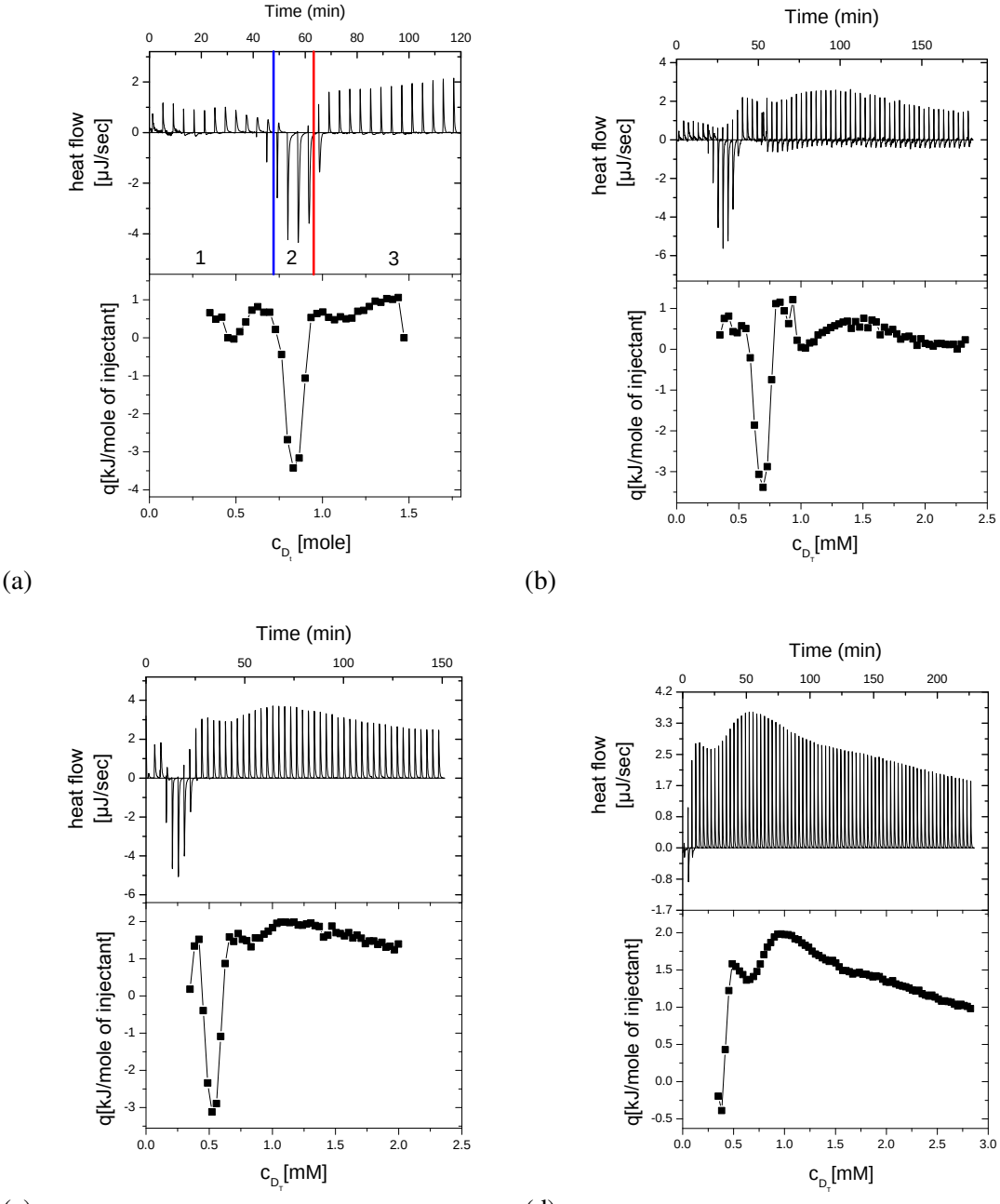

Figure 6.7: Isothermal calorimetry (ITC) solubilisation experiments of mixed NaTCDC/EYL aggregates at dilution d=120, pH 8.0 and T=25° for various salt concentration; (a)100 mM (b) 200 mM (c) 500 mM and (d) 1000 mM. (top) Raw data of a solubilisation experiment with heat flow as a function of time. (bottom): Integration of the heat flow gives the heat q pro mole as a function of the titrated NaTCDC concentration c_{D_t}. The three regimes with endothermic (1), exothermic (2) and finally endothermic (3) reactions are indicated in part (a).

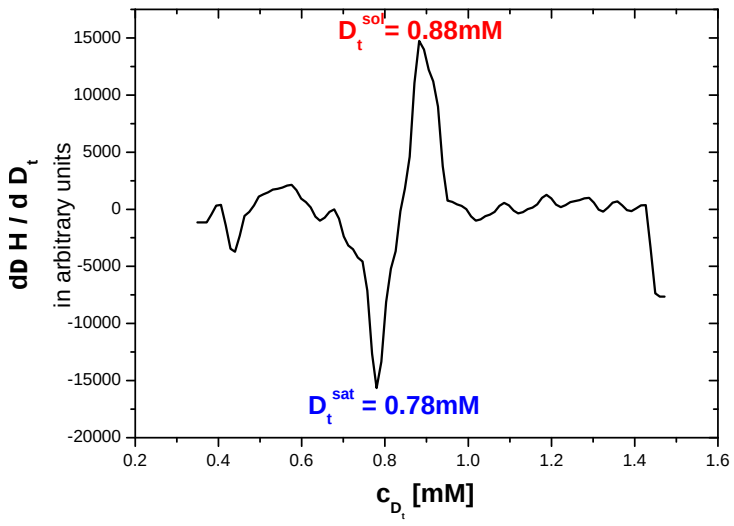

Figure 6.8: Derivative of the enthalpogramm for the sample with c_s=100 mM and d=120.

error bars for the fitted values are given, but should be similarly high as in this study.

The samples with $c_s \geq 800$ mM, d=120 are turbid (chapter 5). The turbidity does however not affect the ITC experiments. As said above the sample is already in or in the vicinity of the coexistence region which is usually indicated by turbidity [53]. The turbidity and the separation of the samples into a more viscous phase and a less viscous phase, indicates that these samples might be located in the previously mentioned coexistence region. The experiments in this region are performed with the whole sample, i.e. both phases; the sample is mixed due to the stirring during degassing prior to the experiment and also after transferring the sample into the sample cell of the ITC.
D^{sat} and D^{sol} depend on the total lipid concentration. However the effective detergent to lipid ratio at saturation and solubilisation, R_e^{sat} and R_e^{sol}, respectively and thus the compositions of the aggregates at the phase boundaries is constant and given by the slopes of the phase boundaries. The phase boundaries are modeled by [54, 56]:

$$D^{sat} = R_e^{Sat} \cdot L + D_w^{Sat}, \tag{6.7}$$

$$D^{sol} = R_e^{Sol} \cdot L + D_w^{Sol}. \tag{6.8}$$

From the table 6.4 it is clear that $D_w^{Sat} \neq D_w^{Sol}$ as expected from equation 6.8. (Deviations from linearity are especially observed for lipid concentration below 2 mM as discussed in the introduction, section 1.5.1.

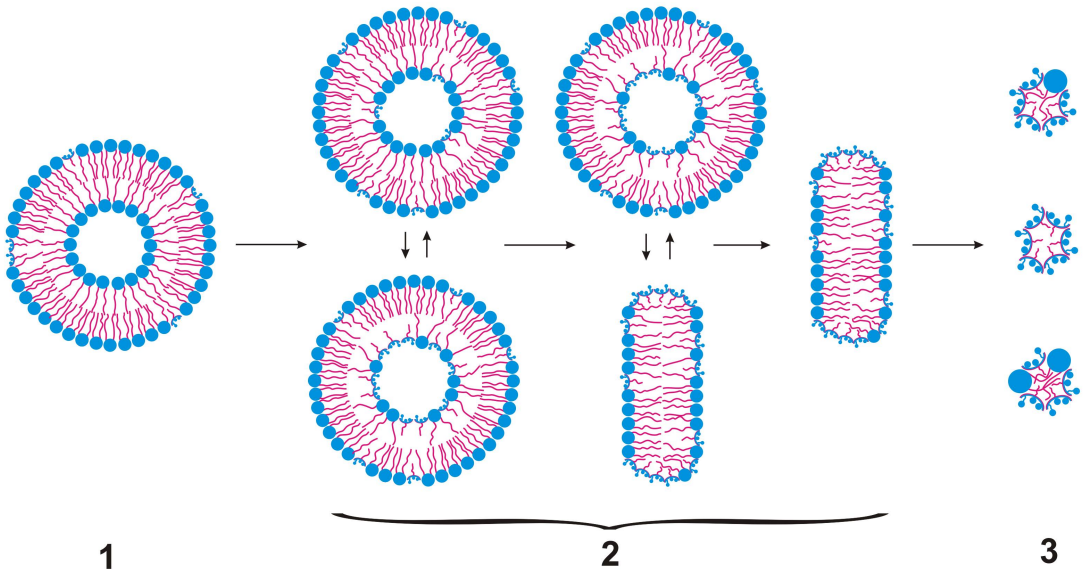

Figure 6.9: Schematic transition process in a dilution experiment. In range 1, vesicular structures can be seen that get dissolved by the bile salt in range 2, i.e in the coexistence region. The structures are in equilibrium with one another indicated by the doublearrow. In range 3 everything is dissolved.

The linear model is used, since the experiments are performed in one of the concentration limits which display linearity [54]. This linearity implies that each "subsystem" (region), i.e. the vesicle, coexistence and the micellar region, are real thermodynamic phases. Some datapoints at high lecithin concentration deviate from this linearity, but this is due to the measurement: at high aggregate concentration, i.e. high lipid-bile salt ratio in the aggregates, one starts in the two phase region and the deduced extrema have large uncertainties and are quite often underestimated. Some of those datapoints were not taken into account for the fit.

6.2.1 Dependence On Salt Concentration c_s

Upon increasing the salt concentration (c_s), R_e^{sat} and R_e^{sol} increase. This indicates that the capacity of the aggregates to incorporate detergent increases. Simultaneously for increasing the detergent concentration in the aqueous phase is decreasing, reflected in decreasing D_w^{sat} and D_w^{sol} values . This is the analogous result as already observed for the *cmc* of NaTCDC with increasing salt concentration. This is consistent with the fact that the electrostatic interactions are more pronounced in the aggregates due to smaller separation of the charged bile salt molecules compared to monomers in bulk. Increased screening thus mainly decreases the electrostatic interactions in aggregates. The D_w^{sat} value is around zero at $c_s \geq 800$ mM, which implies that even at very low lipid concentration all detergent is bound to the lipid and the coexistence region starts in the origin of the bile salt to lecithin phase diagram.

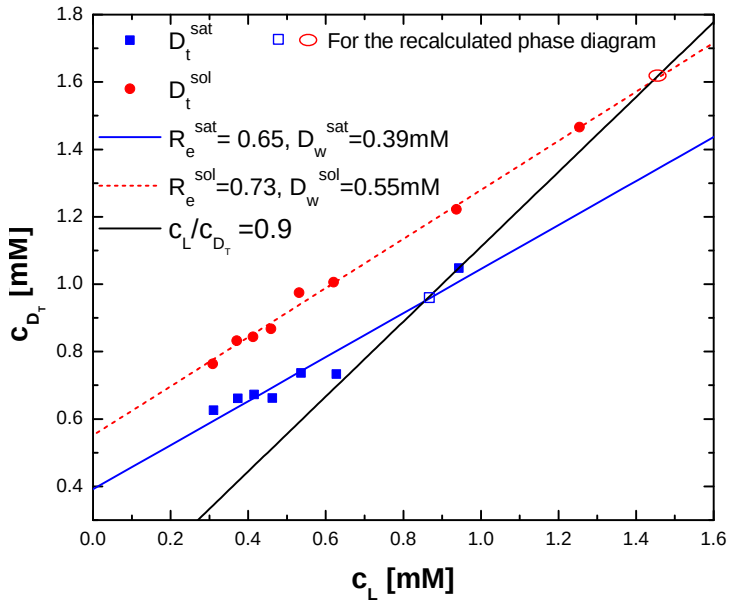

Figure 6.10: Measured phase diagram for NaTCDC/EYL mixtures solubilised by NaTCDC at T=25°C and pH 8.0 and $c_s = 200$ mM. The straight lines are linear fits to the saturation (blue) and solubilisation (red) boundaries. The black line corresponds to a aggregate composition of lecithin-to-bile salt of 0.9 used for preparation.

In figure 6.11 the results from measurements at eight different initial concentrations, all with c_s =200 mM are shown. From each experiment two datapoints are obtained, D^{sat} and D^{sol}. If $c_{D_t} > D^{sat}$, as for the initial concentration D^{sat} can not be determined.The values for the lipid and detergent concentration at the saturation line are slightly underestimated, since many of the datapoints were the first datapoints measured and seem to be located at about the start of the coexistence as already said above. These datapoints are used for the fit of the saturation (blue line) and solubilisation line (red line). The slopes of the two phase boundaries, i.e. the bile salt-to-lipid ratios R_e^{sat} and R_e^{sol} increase with increasing salt concentration c_s increases (figures 6.11). For c_s=200 mM the vesicles can accommodate a maximum of 0.58 NaTCDC molecules per lecithin molecule R_e^{sat}=0.58 and are completely solubilised for 0.63 NaTCDC molecules per lecithin molecules in the aggregates R_e^{sol}=0.63. The average bile salt-to-lecithin ratio is thus only slightly increasing from the saturation to the solubilisation phase boundary and the slopes are thus almost identical, The results for different c_s are summarised in table 6.4.

The obtained results are in agreement with results from similar systems (table 6.5) [108, 109, 110, 150]; an increased salt concentration results in an increase of detergent bound to the

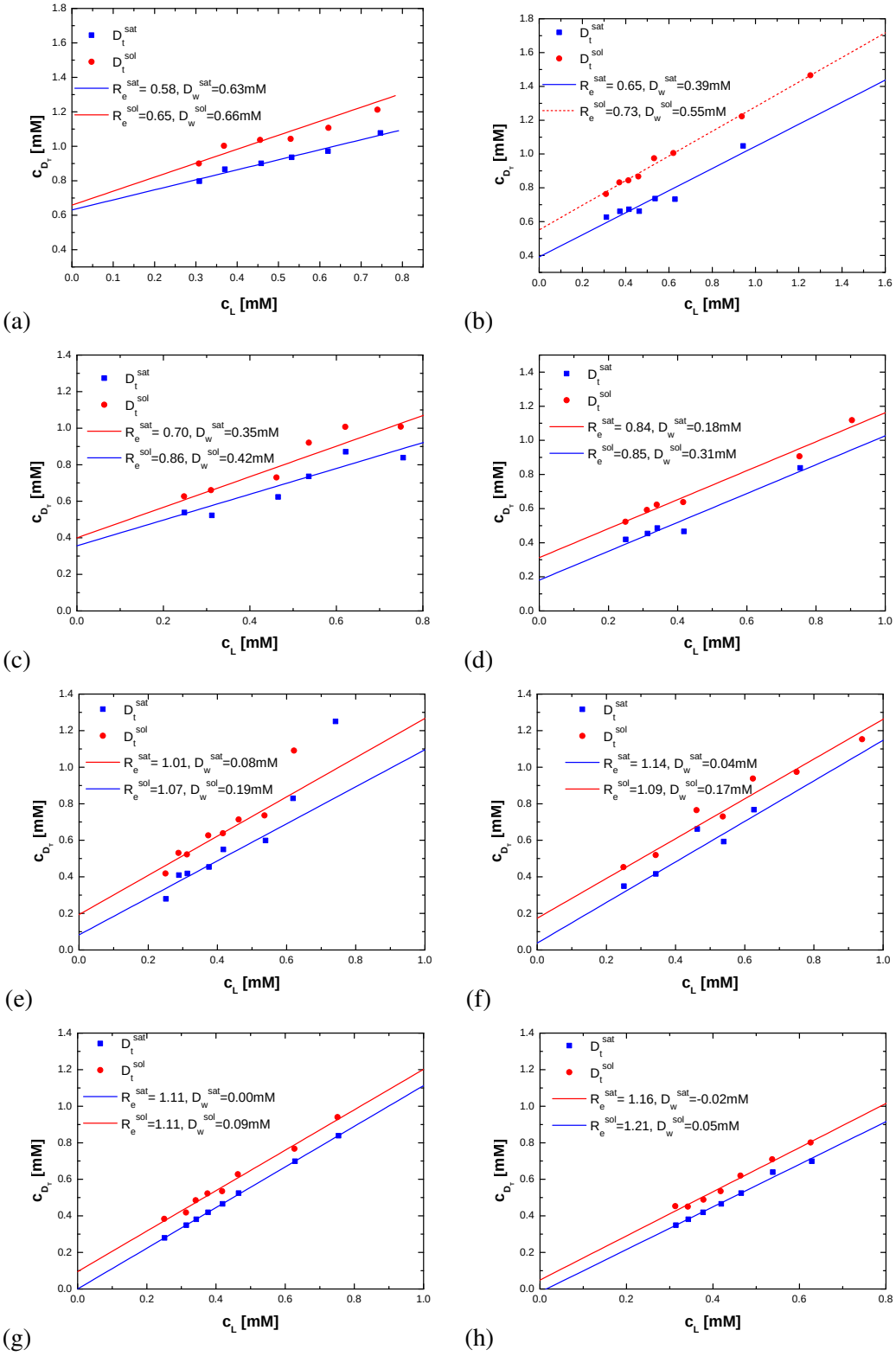

Figure 6.11: Measured phase diagram for NaTCDC/EYL mixtures solubilised by NaTCDC at 25° and pH 8.0. The straight lines are linear fits. (a) 100 mM, (b) 200 mM (c) 300 mM, (d) 500 mM, (e) 600 mM, (f) 700 mM, (g) 800 mM and (h) 1000 mM.

c_s [mM]	R_e^{sat}	R_e^{sol}	D_w^{sat} [mM]	D_w^{sol} [mM]
100	0.58 ± 0.05	0.63 ± 0.08	0.63 ± 0.02	0.66 ± 0.04
200	0.65 ± 0.08	0.72 ± 0.02	0.39 ± 0.05	0.55 ± 0.02
300	0.70 ± 0.14	0.86 ± 0.12	0.35 ± 0.07	0.42 ± 0.07
500	0.84 ± 0.11	0.85 ± 0.06	0.18 ± 0.05	0.31 ± 0.03
600	1.01 ± 0.19	1.07 ± 0.12	0.08 ± 0.07	0.19 ± 0.05
700	$>1.14 \pm 0.17$	1.09 ± 0.09	0.04 ± 0.07	0.17 ± 0.05
800	$>1.11 \pm 0.05$	1.11 ± 0.04	0.00 ± 0.03	0.09 ± 0.02
1000	$>1.16 \pm 0.05$	$>1.21 \pm 0.07$	-0.02 ± 0.02	0.05 ± 0.03

Table 6.4: Compositions of a mixed aggregate of NaTCDC/EYL at saturation (R_e^{sat}) and solubilisation boundary (R_e^{sol}) at T=25° and pH 8.0. The bile salt concentration extrapolated to zero lecithin concentration, the detergent concentration in bulk D_w^{sat} and D_w^{sol} are also given.

aggregate. Bile salt systems have been investigated in [108, 109] with the overall detergent to lipid ratio in these aggregates found to be lower. In their study lipid aggregates alone and not a mixture of bile salt and lipid were solubilised by the detergent. Also in their case D_w does not correspond to the cmc of the detergent without the lipid, but is lower than the cmc.

Partition coefficient

So far the composition of the aggregates, i.e. the bile salt-to-lecithin ratio R_e^{-1} in the mixed vesicles and micelles, was considered. Now, the partitioning of the amphiphiles between the aggregates and bulk is addressed. While the solubility of the lipid in bulk is very low, it is interesting to investigate the distribution of bile salt between bulk and aggregates. This can be quantified by the partition coefficient P the mole-ratio of bound and free detergent (as defined in equation 1.7 in section 1.5.1). At the phase boundaries, P can be written as:

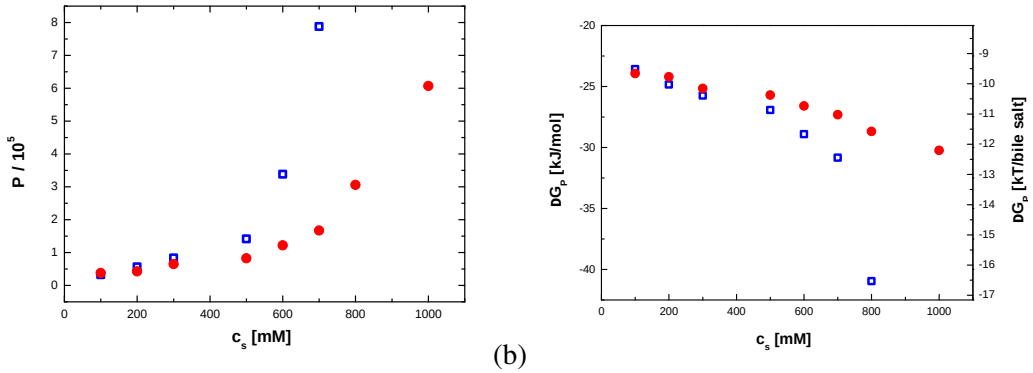

(a) (b)

Figure 6.12: Dependence on salt concentration c_s of the (a) partition coefficients P^{sat} (square) and P^{sol} (circle) and (b) the free energy G. At T=25°C.

Detergent	System	T[°C]	Buffer	R_e^{sat}	R_e^{sol}	D_w^{Sat} [mM]	D_w^{Sol} [mM]	cmc [mM]
[150]								
SDS	DMPC	30	H_2O	0.57	0.57	4.4	5.0	
SDS	DMPC	60	H_2O	0.59	0.63	7.4	8.3	
DTAB	DMPC	30	H_2O	0.29	0.36			
DTAB	DMPC	60	H_2O	0.4	0.64			
[108]								
NaC	DPPC	60	H_2O	0.11	0.15	16.5	17.8	
NaC	DPPC	60	0.1M NaCl	0.19	0.29	5.6	6.6	14.3
NaDC	DPPC	60	H_2O	0.21	0.23	6.4	7.5	
NaDC	DPPC	60	0.1M NaCl	0.20	0.39	1.4	1.7	4.1
[109]								
NaC	DPPC	60	0.1M NaCl	0.21	0.32	5.52	6.51	14.3
NaDC	DPPC	60	0.1M NaCl	0.19	0.38	1.39	1.75	4.1
[110]								
SDS	POPC	65	0.1M NaCl	1.5	2.7	0.9	1.4	

Table 6.5: Compositions of a mixed aggregate of NaTCDC/EYL at saturation (R_e^{sat}) and solubilisation boundary (R_e^{sol}) at various temperatures and experimental conditions as referred. The detergent concentration extrapolated to zero lecithin concentration, the detergent concentration in bulk D_w^{sat} and D_w^{sol} are also given. Values taken from literature as referred.

$$P^{sat,sol} = \frac{x_b^{sat,sol} \cdot W}{D_w^{sat,sol}} \tag{6.9}$$

with $x_b = \frac{D_b}{D_b + c_L}$ the molar ratio of the bound detergent concentration $D_b = c_{D_t} - D_w$ and the total amphiphile concentration and W the mole fraction of water (figure 6.12 (a)). The partition coefficient is sharply increases with increasing salt concentration c_s as all bile salt is in the aggregate. The free energy $\Delta G_P^{sat,sol} = -RT\ln(P^{sat,sol})$ can be calculated (figure 6.12 (b)) based on the P^{sat} and P^{sat}.

The fraction of bile salt in aqueous solution and bile salt bound to bile salt-lecithin aggregates have been determined by dialysis [16, 157]. These are the only experiments, where the cmcs of the bile salts NaC, NaTCDC in the presence of mixed aggregates consisting of bile salt and lecithin (at pH = 7.2, c_s=10 0mM) were evaluated by extrapolation from the bile salt monomer concentration in bulk as a function of the of bile salt-to-lecithin ratio in mixed aggregates. The cmc was extrapolated to be 0.47 mM. Although it is called "cmc", this extrapolation is rather comparable to the D_w value obtained by solubilisation experiments (see also discussion

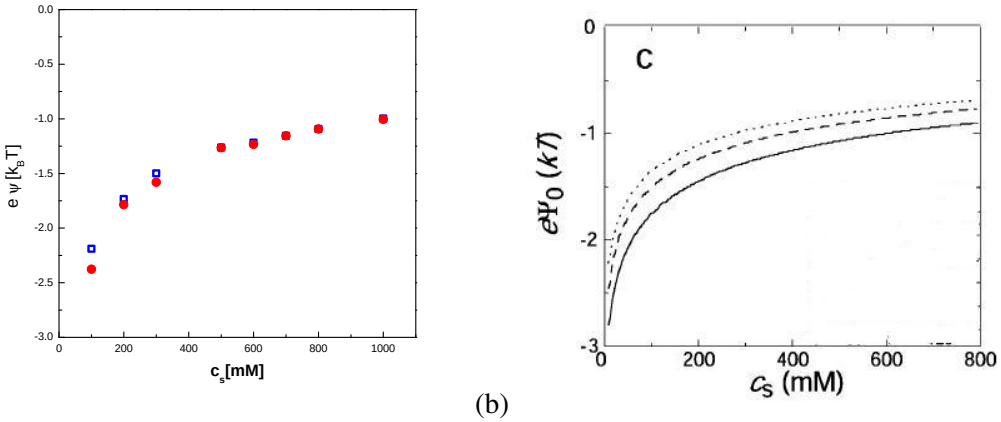

(a) (b)

Figure 6.13: (a) Electrostatic energy $e\Psi_0$ at saturation and solubilisation for increasing salt concentration c_s. (b) Electrostatic energy calculated by composition model of bile salt and lecithin in disclike micelles by Leng et al. [59] for dilution d=40 (solid line), d=80 (dashed line) and d=120 (dotted line).

below). The "cmc" of bile salt in the presence of mixed micelles is therefore also lower aso the cmc without mixed aggregates (as in this study). This can also be seen in the microcalorimetry results mentioned above [108, 109, 150] but preformed with different systems (table 6.5).

Surface Potential

With the obtained bile salt-to-lipid ratio R_e the surface charge density σ can be evaluated [158, 159] by geometrical considerations:

$$\sigma = \frac{ze_0}{A_{D_t} + A_L/R_e} \tag{6.10}$$

with z=1 the valency of the bile salt (at the present pH (8.0), EYL is zwitterionic and thus overall neutral), e_0 the elementary electron charge, A_L the surface area of a lipid and A_{D_t} the surface area of a bile salt molecules. The values taken are $A_L = 72$ Å^2 [32, 33] and A_{D_t}=200 Å^2 as an average value, since a range of values 150 Å^2 $< A_{D_t} <$ 250 Å^2 can be found in literature [5, 11, 12].

The surface charge density creates a surface potential Ψ_0 at the interface according to the Grahame equation [1]:

$$\Psi_0 = -\frac{k_B\,T}{e_0}\text{acosh}\left(\frac{(\sigma)^2}{4\varepsilon_0\varepsilon_r N_A k_B T c_s} + 1\right) \tag{6.10}$$

with k_B the Boltzman constant, ε_0 the permittance of vacuum, ε_r the dielectric constant of water and N_A Avogadros number. The surface potential Ψ_0 for both saturation and solubilisation increases for increasing salt concentration c_s (fig 6.13(a)). In Leng et al. [59], the surface potential was calculated from the composition, i.e. the volume fraction of lecithin and bile salt in aggregate in different disc-like structures, which are proposed to exist in the kinetic model of the micelle-to-vesicle transition. They found a nearly dilution independent, but strongly c_s-dependent surface potential, which agrees with the results obtained here. The model proposed in ref. [59] is thus supported by this study. Also the micellisation energy in ref. [59] was accounted as $10k_BT$, which is in accordance to the free energy ΔG of the NaTCDC molecule bound to the aggregate and in aqueous solution (fig. 6.13(b)).

Relation between D_w and the *cmc*

The main argument for the salt dependence of D_w and the *cmc* of NaTCDC was that the electrostatic interactions are more pronounced in aggregates due to the smaller separation of the charged bile salt molecules in aggregates as compared to in bulk. Increased screening thus mainly decreases the electrostatic interactions in aggregates. This argument can be further developed with respect to pure and mixed aggregates and leads to lower D_w and *cmc* values. The solubility of EYL is various magnitudes lower than that of bile salt and lecithin in bulk is neglected. Tanford [26] proposed that bile salt is treated as the solute of lecithin. If in addition one assumes ideal mixing within the mixed micelle, then Raoults law can be used to estimate the detergent concentration in bulk

$$D_w^{sol,calc} = x_b^{sol} cmc \tag{6.11}$$

where D_w^{sol} is the detergent concentration in bulk, cmc is the bile salt cmc in the absence of lecithin and x_b is the mole fraction of bile salt in the mixed micelles. A comparison is given in the table 6.6. The lowering of aqueous detergent concentration due to presence of an solute

c_s	D_w^{calc} [mM]	$D_w^{meas} = cmc$ [mM]
100	1.47	2.47
200	1.31	1.75
300	0.91	1.71
500	0.68	1.12

Table 6.6: Comparison between calculated and measured monomer concentration in bulk D_w.

can be seen in the table 6.6.

Phase boundaries on Dilution d Salt Concentration c_s Plane

The microcalorimetry phase diagrams in the lecithin-bile salt concentration plane (figure 6.10, table 6.7) can be converted to phase diagrams showing the dilution d versus the salt concentration c_s (figure 6.14), which is often used in experiments, where the dilution dependent micelle-to-vesicle transition is observed. This is done by calculating the crossing points of the saturation and solubilisation lines with the $R_e = 1/0.9$ line (black line, open square and open circle in figure 6.11) in the bile salt/lecithin phase diagram for different salt concentrations c_s.

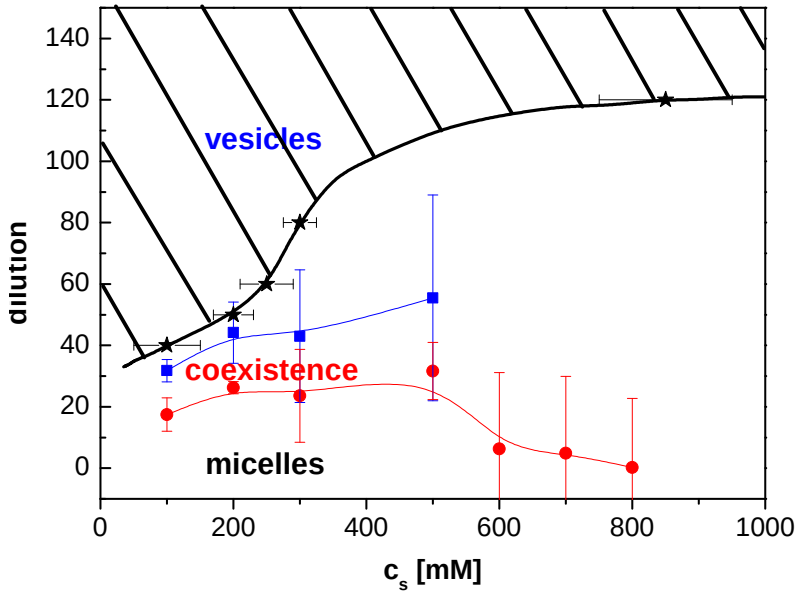

Figure 6.14: Phase diagram for aqueous mixtures of bile salt and lecithin with a molar lecithin-to-bile salt ratio of 0.9. The saturation and solubilisation line are shown as red and the blue lines, respectively. The hatched area indicates the previously determined compositions resulting in vesicles [60].

This phase diagram can be compared to our direct observations (chapter 5) and results from scattering experiments (chapters 7 and 8) as well as a previously published phase diagram [60]. Several light scattering experiments at physiological salt concentration (150 mM) [41, 60], determined the transition from micellar to vesicular structures as well as the coexistence region. In figure 6.14 some datapoints obtained by light scattering studies [60] for the boundary between micelle and vesicle coexistence and vesicles is shown; the black line is a guide for the eye. The results agree within the error with our phase diagram based on ITC, where at low salt concentration the error bars are not high. Although three regimes can be identified in the phase diagram established by ITC, the coexistence region at this physiological salt concentration is limited to dilutions between 20 and 35. Since coexistence means that structurally both micelles

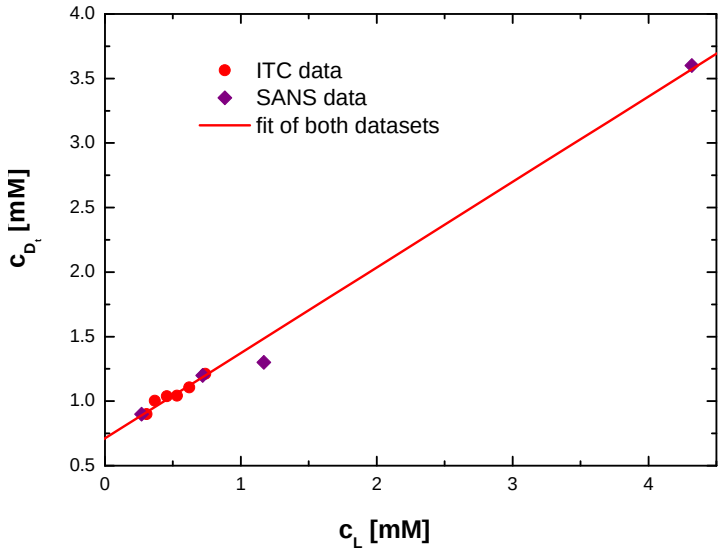

Figure 6.15: Solubilisation boundaries as determined by ITC (red dots) and SANS (purple squares) from [61]. Both data sets are fitted together (line).

Method	$\mathbf{R}_e^{sol}$	$\mathbf{D}_w^{Sol}$ **[mM]**
ITC	0.63 ± 0.08	0.73 ± 0.04
SANS	0.68 ± 0.02	0.66 ± 0.02
both	0.66 ± 0.02	0.69 ± 0.02

Table 6.7: Composition at solubilisation of mixed NaTCDC/EYL aggregates at pH 8.0 and at T= 25°.

and vesicles exist, one can presume that at low salt concentration detergent rich micelles coexist with a few vesicles, which would make both measurements completely identical in their results. This allows the assignment of the ranges discussed in solubilisation experiments with the aggregate structures.

Above c_s=600 mM the saturation line does not cross the black line, i.e. for all dilutions investigated all detergent is bound to the mixed EYL/bile salt aggregates. This is due to sample preparation, since the total lecithin-to-bile salt has a molar ration is 0.9, which correspond to $R_e = \frac{1}{0.9} = 1.11$. The value of R_e at high salt concentration is about or higher than this value. The phase boundary can thus not be determined by our preparation. Furthermore, the error of the values is very high because it, which accumulates from one calculation to the next. Although the R_e values (table 6.4) have a large error bar, the tendency is clearly an increase of bound detergents with increasing salt concentration c_s.

In SANS experiments by S. U. Egelhaaf at the ILL, four different R_e^{-1} ratios (at dilution d= 1 were examined, namely 0.3, 0.6, 0.9 and 1.2 all at various dilutions, and at c_s=100 mM. [61] The samples were prepared in the same way as in the microcalorimetry experiments in this thesis. The boundary between the coexistence region and the vesicular region was determined based on the SANS experiment and compared to the ITC results obtained here (figure 6.15, table 6.7). They agree although they are based on two completely different experimental techniques.
Especially the use of the equations 6.8 seems reasonable, since in the ITC experiments only low lipid concentrations were investigated. Especially at low lipid concentration deviations from the linearity in the phase boundaries were observed, but together with the experimental results from SANS from [61], a wide lipid concentration up to 4 mM can be observed.

6.2.2 Conclusion

The solubilisation studies were performed to investigate the phase boundaries during a vesicle-to-micelle transition of the NaTCDC/EYL mixed system of, especially with respect to the influence of increasing the salt concentration c_s.

At 100 mM salt concentration the microcalorimetry result in very good agreement with previous studies. In Pedersen *et al.* [45] the phase boundaries correspond well to the boundaries obtained here. With increasing salt concentration the aggregates are becoming detergent richer in the micellar as well as the vesicular region. Due to the different curvature bile salt and lecithin, this should have an effect on the shape of the aggregates. Since bile salt is charged, the surface charge density is increasing, too.

The *cmc* of the mixed aggregate, which corresponds to D_w is decreasing with increasing salt concentration and is even close to zero at high c_s=800 mM. This implies that all bile salt monomers are bound, either in mixed aggregates or they could be in pure bile salt micelles.

At higher salt concentrations the error bars are quite large, since the experiments already start close to the saturation line or in the coexistence region. This makes it difficult to unambiguously define the phase boundaries at higher salt concentrations. But in subsequent microcalorimetry studies by preparing various molar ratios of EYL/NaTCDC (higher than the 0.9 used here) the phase boundary between mixed micelles and coexisting to mixed micelle and vesicles and especially between vesicles and and coexistence mixed micelles and vesicles and vesicles could be determined more precisely.

Chapter 7

Structure Determination using Small-Angle Neutron and Light Scattering

A systematic small-angle neutron scattering (SANS) study was performed on the NaTCDC/EYL system with respect to changes in the structure with changing surfactant concentration at two different ionic strengths, c_s = 300mM and c_s = 1000 mM. Furthermore the effect of the increase of salt concentration c_s on a more concentrated (d=20) and dilute samples (d=120) was measured. In figure 7.1 the studied samples (black dots) are indicated.

The phase diagram was already introduced in chapter 5. There is a two-phase area with a "viscous" and a "non-viscous" phase. Additionally, there is also the coexistence region, where mixed micelles coexist with mixed vesicles. Many studies have been performed to understand the structures that form in aqueous solutions of EYL and various bile salts in various molar ratios, but mainly under physiological conditions, i.e. neutral pH and 150 mM electrolyte concentration [41, 43, 46, 155, 62]. Hjelm *et al.* [42, 43, 44], and later also Long *et al.* [46, 160] and Arleth *et al* [161, 37] studied with SANS to study the structures upon dilution. A model was introduced, where concentrated solutions of lecithin/bile salt form cylindrical micelles with a radius of about 27$\mathring{A}$, (section 1.5). Upon dilution the structure changes to vesicles. Since the samples are sufficiently dilute, generally interparticle interactions can be neglected and a spherical core-shell model is used. Long *et al.* [46, 160] used the random phase model, RPA [162], to describe the stiff cylindrical micelles, which interact. The composition of core and shell was also treated independently. Pedersen *et al.* [45] studied also the EYL/NaTCDC system with the same lecithin-to-bile salt molar ratio of 0.9 at c_s=150 mM. They interpreted mixed micelles as flexible cylindrical structure, where the longitudinal and transversal structural contribution can be decoupled, i.e. infinitely thin wormlike chains with

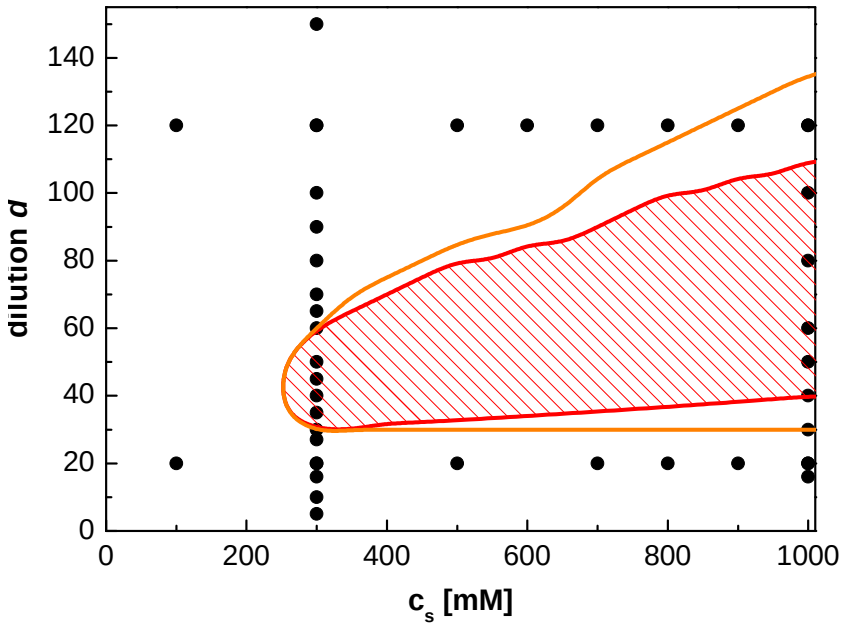

Figure 7.1: Schematic phase diagram in the dilution d vs. salt concentration c_s plane. The red area represents conditions, where visible phase separation occurs. Just around this region the samples are turbid, indicated by the orange line. A two phase separation can occur here as well.

a seperate cross-section contribution. Interactions were not included, but were considered in Arleth *et al* [161, 37]. Again the compositions of the core and shell were individually considered as in Long *et al.* [46, 160]. The formed vesicles were modeled by a spherical core-shell model.

7.1 Some background to the Structure Determination

The data were fitted using a model of polydisperse bilayer vesicles and a wormlike chain model with a cross-sectional contribution for the micelles. The coexistence region in the phase diagram between the micellar and vesicular regions was successfully modeled using a mixture of both. The onset of the typical oscillatory behavior of bilayer vesicles can already be seen at dilution d=40 and gets more pronounced at higher dilutions until the vesicular phase is reached. The scattering pattern will be fitted with a model like in Pedersen *et al.* [45]. In detail the scattering pattern of the data for all dilutions and ionic strength is fitted using one expression for the scattering cross-section $d\sigma(q)/d\Omega$. This quantity has units of cm^{-1}.

$$\frac{d\sigma(q)}{d\Omega} = \frac{c_{\mathrm{t}}}{d}\Delta\rho_s^2\{f_{\mathrm{v}}F_{\mathrm{v}}(q) < M_{\mathrm{v}} > + (1-f_{\mathrm{v}}) < M_{\mathrm{m}} > \left[f_{\mathrm{s}}F_{\mathrm{wc}}(q)F_{\mathrm{cs}}(q) + (1-f_{\mathrm{s}})\frac{F_{\mathrm{rod}}(q)}{1+\nu(X)F_{\mathrm{rod}}(q)F_{\mathrm{wc}}(q)}F_{\mathrm{cs}}(q)\right]\} \tag{7.1}$$

with c_{t} the total amphiphile concentration of the stock solution, d the dilution factor and $\Delta\rho_{\mathrm{s}}$ is the average excess scattering length density per unit mass. The dependence on other parameters than q for the individual formfactors is omitted.

The first row of equation describes the scattering of polydisperse bilayer vesicles, where f_{v} is the mass fraction of vesicles, $F_{\mathrm{v}}(q)$ the form factor for a vesicular structure, i.e. of a spherical shell with radius R, and the weight averaged molar mass $\langle M_{\mathrm{v}}\rangle$ of the vesicles.

The second row describes the contribution of the wormlike micelles. Two different models were used for the fits. The first term describes the formfactor of an infinitely thin wormlike chain F_{wc}(q) which and is combined with a cross-sectional contribution $F_{\mathrm{cs}}(q)$. Interactions are not taken into account, since this model was used for higher dilutions, where the interactions of the surfactant aggregates are negligible. At lower dilutions, the interactions were included in the model. In this case the scattering is described by the second term, where the formfactor of a infinitely thin wormlike chain $F_{\mathrm{wc}}(q)$ and the formfactor for an infinitely thin rod $F_{\mathrm{rod}}(q)$ were used. Each term is switched on or off in the fit with f_{s}=0 or 1. Each contribution is now discussed in detail.

7.1.1 Wormlike micelles

Scattering curves provide information on structural parameters on different length scales depending on the scattering vector q (Fig. 7.2). At small q, the Guinnier regime, the overall size of the surfactant aggregate (the radius of gyration R_g) and its apparent molar mass M are probed. At intermediate q the self-avoiding random walk dominates with a power law behaviour of $q^{-\frac{5}{3}}$ (in the case of an ideal Gaussian chain, the dependence is q^{-2}. By further increasing q, the stiffness or flexibility of the chain can be seen. A q^{-1} behaviour is typical for stiff rodlike structures. The flexibility is given by the location of the crossover and quantified by the persistence length l_p. The Kuhn length b is used as a fit parameter ($b = 2\ l_p$) together with the contour length L. High q values represent the length scale of the local structure, characterised by the cross-sectional radius R_{cs}, which goes alongside with a strong decrease in intensity.

The wormlike structure of the mixed system of bile salt and lecithin can be seen at low dilutions until the transition towards vesicle structure upon bile salt removal starts.

Therefore in order to fit the SANS data of the NaTCDC/EYL surfactant aggregate system in this regime, f_v=0 was used. At high concentrations interactions between the surfactant

aggregates were included, i.e. f_s=0. This corresponds to the samples with dilution 5 and 10 at c_s=300 mM. Here the micelles can be regarded as short, since $L < 10R_{cs}$. In this regime, it is also possible to fit a model of short thick rods to the data, giving similar results.

For micelles with a length $L > 10R$, it is not necessary to include interactions, since they only occur at higher dilutions, due to the strong dilution dependent growth instead of a concentration dependent growth in this regime. A decoupling approximation for the scattering of the wormlike micelle into a local cross-sectional contribution, F_{cs} and a longitudinal contribution, F_{wc}, i.e. a formfactor of a wormlike chain, can be used. Pedersen et al. [45, 163] investigated with extensive Monte-Carlo simulations on semi-flexible chains with and without excluded volume effects a suitable model for F_{wc} to be able to use it with the least-square analysis. Based on a numerical procedure of Yoshizaki and Yamakawa [164], the following expression for the analysis of SANS data for semi-flexible polymers or wormlike micelles was obtained:

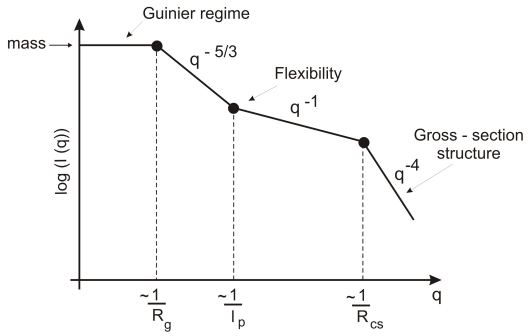

Figure 7.2: Schematic representation of scattering data for a wormlike chain. The scattering shows the characteristic $q^{-\frac{5}{3}}$ or q^{-2} dependence for self avoiding or Gaussian chains, respectively, q^{-1} for rodlike structures and q^{-4} at sharp interfaces.

$$F_{\mathrm{wc}}(q,L,b) = \{[1-\chi(q,L,b)]F_{\mathrm{chain}}(q,L,b) + \chi(q,L,b)F_{\mathrm{rod}}(q,L)\}\Gamma(q,L,b) \qquad (7.2)$$

F_{chain} is the scattering function of a flexible chain with excluded volume effects and F_{rod} is the scattering of a infinitely thin rod, which is given in [165] and references therein.

$$\begin{aligned} F_{\mathrm{chain}}(q,L,b) =& w(qR_g)F_{\mathrm{Debye}}(q,L,b) \\ &+[1-w(qR_g)][C_1(qR_g)^{-1/\nu}+C_2(qR_g)^{-2/\nu}+C_3(qR_g)^{-3/\nu}] \\ F_{rod}(q,L) =& 2\cdot \mathrm{Si}(qL)/(qL) - 4\sin^2(qL/2)/(q^2L^2) \end{aligned} \qquad (7.3)$$

where $F_{\mathrm{Debye}}(q,L,b)$ is the Debye function with $F_{\mathrm{Debye}}(q,L,b) = 2[\exp(-u)+u-1]/u^2]$ (u is the ensemble averaged square of the radius of gyration $u = \langle R_g^2\rangle q^2$) and C_1, C_2 and C_3 are constants and $\nu = (1+\epsilon)/2 = (1+0.176)/2 = 0.588$ describes chains with excluded volume effects. Besides $\mathrm{Si}(x) = \int_0^x t^{-1}\sin t\ dt$. Depending on q, F_{chain} (low q) or F_{rod} (high q) is

dominating and in the crossover region both are contributing combined by a crossover function $\chi(q, L, b)$ and a correction function $\Gamma(q, L, b)$. [165, 164]
As said above, interactions were taken into account for short micelles. Therefore f_s was set to 0 in equation 7.1 and a structure factor was included. This part of the equation comes from the Polymer Reference Interaction Site Model (PRISM) [166, 167], where $\nu(X)$ is related to the reduced concentration X.

$$\nu(X) = \frac{1}{8}\left(9X - 2 + \frac{2\ln(1+X)}{X}\right)\exp\frac{1}{4}\left[\frac{1}{X}(1 - \frac{1}{X^2}\ln(1+X)\right] \tag{7.4}$$

The reduced concentration X is related to the real concentration c, through the second virial coefficient A_2 and the molar mass M. For monodisperse polymers, it was found that $X = 16/9A_2cM$ [168].

The micelles are expected to be polydisperse in length. We thus consider a size distribution and calculate the weight-averaged formfactor of the micelles.

$$\langle F_{\text{wc}}(q, L, b)\rangle = \frac{\int N(L)F_{\text{wc}}(q, L, b)L^2dL}{\int N(L)L^2dL} \tag{7.5}$$

with $N(L)$ the number distribution of wormlike chains given by the Schultz-Zimm distribution.

$$N(L) = \frac{L^z}{z!}(\frac{z+1}{< L >})^{z+1}\exp(\frac{-L(z+1)}{< L >}) \tag{7.6}$$

where $\langle L\rangle$ is the average length of the micelles, and z is related to the relative standard deviation $\sigma = \sqrt{1/(z+1)}$.
At high q, information about the cross-section of the micelles can be extracted via the cross-sectional formfactor F_{cs}. The cross-sectional formfactor of a homogeneous cylinder:

$$F_{\text{cs}}(q, R_{\text{cs}}) = \left[\frac{2J_1(qR_{\text{cs}})}{qR_{\text{cs}}}\right] \tag{7.7}$$

where J_1 is the first order Bessel function and R_{cs} the cross-sectional radius. But when the scattering from heads and tails can be distinguished, a core shell model is more appropriate:

$$F_{\text{cs}}(q, R_{\text{cs}}, R_{\text{h}}) = 2\frac{\frac{\rho_h}{\rho_c}\pi R_h^2\frac{J_1(qR_h)}{qR_h} - (\frac{\rho_h}{\rho_c} - 1)\pi R_c^2\frac{J_1(qR_c)}{qR_c}}{\frac{\rho_h}{\rho_c}\pi R_h^2 - (\frac{\rho_h}{\rho_c} - 1)\pi R_c^2} \tag{7.8}$$

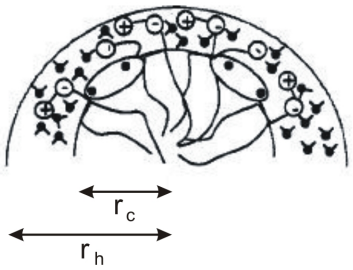

Figure 7.3: Core-shell model of a cylindrical micelle. The core is made up mostly of lecithin tails and the shell consists of lecithin headgroups and bile salt and solvent molecules. The composition of the core and shell was treated independently. Figure from reference [160].

R_c and R_h are the core and the head (or shell) radii, respectively and ρ_h and ρ_c are the core and head scattering length densities, respectively, as illustrated in figure 7.3.

7.1.2 Vesicles

The details of the used model for the scattering of vesicles was previously published in the study of Pedersen et al. [45]. A core-shell model for the scattering of layered spherical shells with different scattering length densities of the heads and tails of the surfactant molecule is used. The scattering of homogeneous spheres is given by:

$$F_{\mathrm{s}}(q,R) = \frac{3[\sin(qR) - qR\cos(qR)]}{(qR)^3} \tag{7.9}$$

For the layered spherical shell this leads to the equation for the normalised form factor $F_v(q)$:

$$\begin{aligned} F_{\mathrm{v}}(q) =& \{ \int N_v(R_v)[\frac{\rho_h}{\rho_c} V(R_v{+}R_h)F_s(q,R_v{+}R_h) \\ &- \left(\frac{\rho_h}{\rho_c} - 1\right) V(R_v{+}R_c)F_s(q,R_v{+}R_c) \\ &- \left(1 - \frac{\rho_h}{\rho_c}\right) V(R_v - R_c)F_s(q,R_v - R_c) \\ &- \frac{\rho_h}{\rho_c} V(R_v - R_h)F_s(q,R_v - R_h)]^2 dR_v \} / \int N_v(R_v)M_{sm}^2(R_v)dR_v \end{aligned} \tag{7.10}$$

$N_v(R_v)$ is the size distribution, for which a Schultz-Zimm distribution is used analoguous to the wormlike micelles in equation 7.6. $V(R)$ is the volume of a sphere with the radius R and as before all scattering functions are normalised and mean values are given as for the radius of the vesicle R_v. $2{\cdot}R_c$ is the width of core and $2{\cdot}R_h$ is the width of the total bilayer. As for the micelles ρ_h and ρ_c are the scattering length densities of the head and the core.

	volume [Å]	$\rho[10^{10}\text{cm}^{-2}]$
EYL tail	970	0.176
EYL headgroup	296 [1]	0.558
TCDC	660 [2]	1.153
D_2O	30.2	6.382
D_2O in c_s=300mM	30.2	6.413
D_2O in c_s=1000mM	30.2	6.488

Table 7.1: Volume and Scattering length density of the molecules present in our sample.

$M_{\text{sm}}(R_{\text{v}})$ is the mass of the scattering volume and is given by:

$$\begin{aligned} M_{\text{sm}}(R_v) =& \frac{\rho_h}{\rho_c} V(R_v{+}R_h) - \left(\frac{\rho_h}{\rho_c}{-}1\right) V(R_v{+}R_c) \\ &- \left(1{-}\frac{\rho_h}{\rho_c}\right) V(R_v{-}R_c) - \frac{\rho_h}{\rho_c} V(R_v{-}R_h) \end{aligned} \tag{7.11}$$

Equations 7.10 and 7.11 are used for the fitting routine of the vesicles.

7.1.3 Absolute Scattering Intensity

The excess scattering length density of the surfactant aggregate is the difference between the average scattering length densities of the surfactant aggregate and the D_2O at different salt concentrations c_s. This value was fixed appropriately for the different salt concentration regimes as it can be seen in the table 7.1 for pure D_2O and D_2O with c_s=300 mM or c_s=1000 mM. The scattering length density of TRIS-buffer was not included. Furthermore, the composition of the surfactant aggregate was taken into account using the results of the microcalorimetry experiments, i.e. the ratio of bile salt to EYL as represented in R_e.
The micelle and vesicle composition is the sum of the shell and core volume fractions. We assume, that the core consists of EYL tails only and since EYL is hardly soluble, the assumption is done, that all lecithin is in the aggregates. The volume fractions of the core $\phi_{\text{c}} = n_{\text{L}} V_{\text{tail}}$, where n_L is the number of lipids per unit volume V_{tail}. The shell on the other hand therefore consists of the bile salts, the EYL headgroup and solvent, thus the head volume fraction $\phi_{\text{h}} = n_{\text{D}} V_{\text{D}} + n_{\text{L}} V_{\text{head}} + n_{\text{D}_2\text{O}} V_{\text{D}_2\text{O}}$. For the shell scattering length density one obtains:

$$\rho_h = \frac{n_{\text{D}} b_{\text{D}} + n_{\text{L}} b_{\text{head}} + n_{\text{D}_2\text{O}} b_{\text{D}_2\text{O}}}{V_{\text{D}} + V_{\text{head}} + V_{\text{D}_2\text{O}}} \tag{7.12}$$

In table 7.1 the values used in calculating the core and shell composition and scattering length are given. Based on these equations and values, the scattering length densities were

calculated. The amount of solvent molecules, deuterium oxide in the shell, is not included in the calculation, i.e. n_{D_2O}=0, but in the fits of our model to the data a lower scattering density of shell was assumed, then the one calculated from the values. The difference between the fits and the calculated values allows us to an estimate the number of associated solvent molecules n_{D_2O} in the shell.

7.1.4 The Fitting Routine

After background reduction and corrections of the background from sample cell and solvent as described in chapter 3, the intensity as a function of q can be seen in figures 7.4-7.11. Two to three different settings (for details see section 3.2.4) were used to cover the desired q-range. The number of setting is listed for all measurements in the results tables 7.2 - 7.7.
The least square method was used, where the deviation is measured between the experimental data and the model. Further details on modeling and least-square fitting of small-angle scattering can be found in [169, 116]. The program used here was developed by Jan Skov Pedersen with modifications for the fitting procedure to our specific scattering data.
The intensity across the whole q range is fitted simultaneously for the two to three settings with different wavelength and sample-to-detector distances. The resolution of the various settings is included in the fitting procedure by measuring the direct, but attenuated beam on the detector. For details see section 3.2.2 and references therein. Especially between the low-q range and the intermediate-q range, the effect of the resolution for the different settings is visible (figure 7.7, the vesicles).

7.2 Effect of dilution at constant salt concentration c_s=300 mM

The dilution dependent micellar growth and the transition from micelles to vesicles in the EYL/bile salt system is well established at physiological condition, i.e. neutral pH and 150 mM salt concentration [41, 43, 46, 155, 62]. It is well established that at high bile salt content spherical or small cylindrical mixed micelles form. Upon dilution the soluble bile salt leaves the aggregate as explained earlier and the micelles grow, until eventually quite monodisperse, bilayer vesicles form. The size of the vesicles decreases with further dilution. On the other hand, if the ionic strength of the solvent is increased, the bile salt content in the aggregate increases, since bile salt is charged and the added electrolyte is screening that. This corresponds to a decrease of the cmc.

In this study as in the microcalorimetry study before, the attention was turned to the effect, that occurs at high ionic strength. First, the concentration was increased to 300 mM, i.e. higher than physiological concentration, and just at the concentration, where the two-phase region

sets in. The amount of "viscous" phase formed at 300 mM is low compared to higher ionic strengths.

On top of the micelle to vesicle transition, the two-phase region is crossed upon dilution. As it was already described in chapter 5, a macroscopic phase separation occurs. Figure 7.1 shows the datapoints, where this two-phase region is crossed, i.e. between dilution d=30 and d=60. This phase boundary is not well defined. In the microcalorimetry experiments the overall sample was measured, where the "viscous" and "non-viscous" phase was mixed. In the SANS experiments the samples were used with mostly the "non-viscous" phase. The sample was then centrifuged to have the "majority" of bigger aggregates out of the neutron beam. However the "viscous" phase cannot be completely avoided, since they drift in the sample as it can be seen in picture 5.1.

In the figures 7.4, 7.6 and 7.7 the scattering spectra from measurements on the dilution series of the NaTCDC/EYL at $c_s = 300$ mM are shown. As before for physiological condition [43, 46, 41, 155, 62], a dilution induced transition from wormlike micelles to bilayer vesicles can be seen. This transition can be easily recognised in the SANS pattern of the dilution series, since at high surfactant concentrations, i.e. low dilutions, the scattering curves monotonically decrease with increasing q. The scattering curve changes from figure 7.4 to 7.7. Here the typical oscillatory behaviour of vesicular structures can be seen. In figure 7.6 the start of the formation of the vesicles can be observed in the presence of the wormlike micelles, in the coexistence region.

In the following the analysis of the three regimes, i.e. micelles, coexistence and vesicles will be discussed in independent sections.

7.2.1 Micelles

Figure 7.4 shows the q-dependence of the measured neutron scattering intensity $d\sigma(q)/d\Omega$ and the fit results. The data is fitted using the introduced model with $f_v = 0$ in equation 7.1.
At the lower dilutions (d=5 and d=10), i.e. higher concentration, the scattered intensity at low-q is quite flat. The q dependence of the intensity in this region could arise from rigid rod structures or could also be modeled as thin rods with interactions, that flatten the low-q part.
At dilutions higher than d=16 the low-q regime reflects the self-avoiding random walk feature with $I(q) \propto q^{-5/3}$ dependence and at intermediate q ranges the scattered intensity displays the characteristic $1/q$ dependence of locally cylindrical micelles. Due to the relatively low concentration of the micelles, the interaction effects can be neglected and therefore f_s=1. (Equation 7.1).

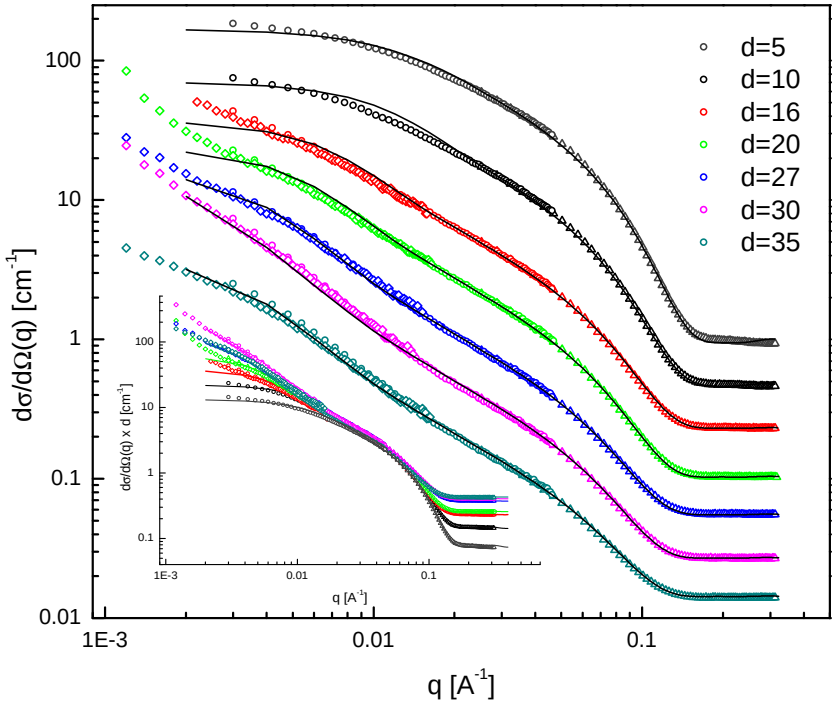

Figure 7.4: Absolute scattering intensity as a function of scattering vector q for samples with dilutions 5 to 35 at c_s=300 mM. Each data set for one dilution (which consist of 2 or 3 different instrumental settings), and its fit (solid line) is multiplied by 2^n, n=1 starting by most diluted with d=35 until n=7 with d=5. The inset shows the same data plotted multiplied by dilution d.

The model fits the data very well, especially for dilutions above d=16. For $d \geq 16$ and $q \to 0$ the intensity starts to grow, indicating the presence of large structures in the sample. We attribute this to the approach to and the crossing of the two-phase region. This can be compared with figure 7.1. (Although the value of the very first datapoints could also be affected by the subtraction of the empty cell.)

The fitted parameters for the micelles are given in table 7.2. The Kuhn length was fixed to b = 400 Å, although values in the range from b = 350$\mathring{A}$ to b = 500$\mathring{A}$ gave also sensible, similar results for the other fit parameters. In the literature similar Kuhn lengths, i.e. persistence length l_p from 155Å have been reported [37]. At dilutions d=5 and 10 the length of the micelles is smaller then the Kuhn length $L < b$, i.e. they are actually stiff rods.

If we look closer at the characteristic crossover region, i.e. between $q^{-5/3}$ and q^{-1} at higher dilutions, i.e. we see the appearance of the point of inflexion for $d \geq 10$. At higher dilutions,

the crossover is quite pronounced and can be fitted with $b = 400$ Å. No crossover is observed for dilutions d=5 and d=10.

The polydispersity of the micelles was fixed to 0.15, except for the lowest dilution. This did not vary for different dilutions. The polydispersity could have been fixed to a higher value, too, which would have slightly decreased the mean value of the contour length.

All data from d=16 onwards were fitted by cylindrical micelles without interactions. With decreasing concentration, i.e. increasing dilution, the wormlike micelles grow. At dilutions d=30 and d=35 it is difficult to fit the contour length of the micelles, because the micelles become too large for the q-range investigated . Therefore, after finding a minimal least square fitting for all other fit parameters, the minimum of L was found. This is the value given in the table 7.2.

Although the fit was not too sensitive to the contour length L of the micelles at higher dilutions, as said above, the dilution induced growth is clearly observable in the fitted parameter L. This is also shown using the empirical growth law (equation 1.10) from [37] in figure 7.5, which empirically describes dilution dependent and concentration dependent growth. Here the term of dilution dependent growth is used to describe the describe the growth of the worm-like micelle due to a change in their composition. It can be used to predict the length L of a micelle for our dilutions (from Arleth et al. [37]). The fit results are:

$$\begin{aligned} L(\phi) =& K_2\phi^{-2} + const \\ =& [(5.13 \pm 0.04) \cdot 10^{-3}\phi^{-2} + (159.14 \pm 11.52)]\text{Å} \end{aligned} \tag{7.13}$$

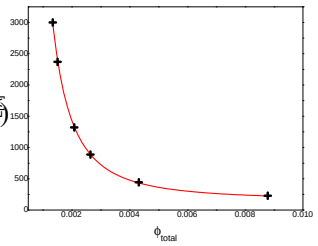

Figure 7.5: Length of the worm-like micelle as a function of the total volume fraction Φ_{total} of bile salt/EYL micelles. The line is an empirical fit to the data.

where ϕ is the total volume fraction of the TCDC and EYL in the sample ($\phi = c\,V\,N_A$, where dilution 1 refers to a concentration of 50 mg/ml of EYL and TCDC with a molar ratio of 0.9). In Arleth *et al.* [37] a comparable fitted value of $K_2 = (7.14 \pm 0.68) \cdot 10^{-3}$ for a very similar system of EYL lecithin and the dihydroxy bile salt glycochenodeoxycholate, GCDC, was found.

The radius of the core R_c varies between 8.72Å$\leq R_c \leq$ 10.11Å and the total radius 25.77Å$\leq R_h \leq$ 27.63Å. The value reported for the overall radius R_h is similar to those reported in the studies lecithin/TDC system: $(R_h = 26.7 \pm 0.4)$ Å [160]. R_c is smaller than the value found in [45], i.e. 14.9±0.06 Å, where a similar fitting routine was used and the samples were prepared as for these experiments. The only difference is the increased salt concentration, which leads to an increase of bile salt in the micelle. This would then be responsible for a smaller core radius

d	no of sets	L [Å]	σ_{mic}	R_h [Å]	R_c [Å]	ρ_h/ρ_c	$\langle M_m \rangle$ [10^3 g mol^{-1}]	cal $\langle M_m \rangle$ [10^3 g mol^{-1}]
5	2	227.80	0.58	25.77	8.72	0.35	268	286± 43
10	2	443.41	0.15	27.25	8.88	0.31	377	623 ± 93
16	2	886.90	0.15	26.27	10.05	0.45	1080	1162 ± 174
20	3	1321.6	0.15	26.74	10.00	0.45	1600	1793 ± 268
27	3	2371	0.15	27.15	10.06	0.45	2950	3314 ± 496
30	3	>3000	0.15	27.63	10.11	0.45	3730	4331 ± 650
35	3	>3000	0.15	27.34	9.47	0.45	3705	4244 ± 636

Table 7.2: Results from the nonlinear least square fits for dilutions 5 to 35 at c_s=300 mM. Wormlike micelles are fitted. Given is the number of instrumental settings as well as the fit parameters: contour length L, polydispersity σ_{mic}, the total radius R_h, the radius of the core R_c, the weight averaged molar mass $\langle M_m \rangle$ from fit and from the composition dependent calculation. $\Delta\rho$ = 5.718 cm^2 is fixed for the electrolyte with c_s=300 mM and also the Kuhn length is kept fixed at b=400 Å.

as the hydrocarbon chains of the lecithin would fill the "lack" of volume in the core arising from the unusual hydrophobic steroid backbone of the bile salt molecule, instead of a classical head-tail structure. Necessarily there is also less lecithin, which itself leads to a smaller total tail volume V_{tail} and thus to a smaller R_c.

Since the radii remain nearly constant throughout the micellar region, this implies the composition of the micelles, i.e. the bile salt-to-lecithin ratio in the aggregates, does not change significantly during growth. This is consistent with a previous finding [41, 42] that the number density of lecithin and bile salt throughout the cylinder is constant. The number of lecithin molecules per length of the cylindrical part was determined to be 0.99 Å^{-1} for a bile salt-to-lecithin with a molar ratio of 0.22 [42] and 0.7 Å^{-1} for a molar ratio of 0.9 as used in this study [41]. However, these studies were performed under physiological conditions.

In the model the weight averaged molar mass of micelles $< M >_{\mathrm{m}}$ was used as a fitparameter. Its values were compared with the molar mass calculated based on the other fitted and fixed parameters. The molar mass of a cylindrical micelle can be calculated from the volume of the micelle V_{m} and its bulk density $\rho_{b_{\mathrm{m}}}$ by:

$$\begin{aligned} < M >_{\mathrm{m}} &= V_{\mathrm{m}} \cdot \rho_{b_{\mathrm{m}}} \cdot N_A \\ &= \pi R_h^2 L \cdot \rho_{b_{\mathrm{m}}} \cdot N_A \end{aligned} \tag{7.14}$$

The error of the weight averaged molar mass of micelles $< M >_{\mathrm{m}}$ arises from the error for $\rho_{b_{\mathrm{m}}}$ obtained by the composition of

The values agree very well (table 7.2). This is another indication that the used model is consistent.

In the thermodynamic description of the vesicle-to-micelle transition the molar ratio is assumed to change at the boundaries of saturation and solubilisation (section 1.5.1). In our fit this is reflected in the value of ρ_h/ρ_c, which has been been found to be 0.45 in the micellar region, with the exception of d=5 and d=10. This could be due to the change of the model, since interactions were only included for these two dilutions. The amount of D_2O lowers this value as it can be seen from eq. 7.12. Within the micellar region the number of water molecules should be similarly high, the difference between is actually 19.5 water molecules for $\rho_h/\rho_c = 0.35$ and 16.5 for $\rho_h/\rho_c = 0.45$.

7.2.2 The coexistence region

There is a dilution range, where wormlike micelles and vesicles coexist. This range is modeled with a mixture of the structures found for lower and higher dilutions. The assumption is made that the measured scattered intensity is the sum of wormlike micelles and vesicles. That means f_v will not be fixed anymore, but will be fitted using the fitparameters obtained at the boundary between the wormlike micelles and coexistence and between coexistence and vesicles, respectively.

In d=40 and d=45 a growing oscillatory peak can be observed (Fig. 7.6 a)). This peak gets more and more pronounced. And the fraction of vesicles will increase with decreasing concentration . On top of this, the two-phase region is crossed, which again leads to an increased scattering intensity in the low-q limit. Although the best fit for d=60 is obtained for a coexistence region of micelles and vesicles, d=60 also could be modeled using vesicles only (Fig. 7.6(b)). The other fit parameters are nearly not influenced by modeling the data with coexisting vesicles and wormlike micelles or vesicles only. If the fit parameters of the coexistence region (Tab. 7.3) are compared to results of the micellar phase (Tab. 7.2) or the vesicular phase (Tab. 7.4), one can see that values fitted for the coexistence region is in accordance both contributions.
In the thermodynamic description of the vesicle-to-micelle transition the molar ratio is assumed to change at the boundaries of saturation and solubilisation. ρ_h/ρ_c in the micellar region is 0.45 (with the exception of d=5 and d=10), while it is about 0.35 in the vesicle region. In the coexistence region about these values were also observed.

7.2.3 Vesicles

For higher dilutions, beyond the coexistence region, the scattering pattern can be successfully fitted by a model of polydisperse vesicles, i.e the mass fraction is f_v=1 in equation 7.1.
Although for d=65 and d=70 only two instrumental settings were measured and the information in the low-q range is missing to definitely decide, whether the coexistence region is already crossed or if this should be modeled with a mass fraction of micelles and vesicles, they were

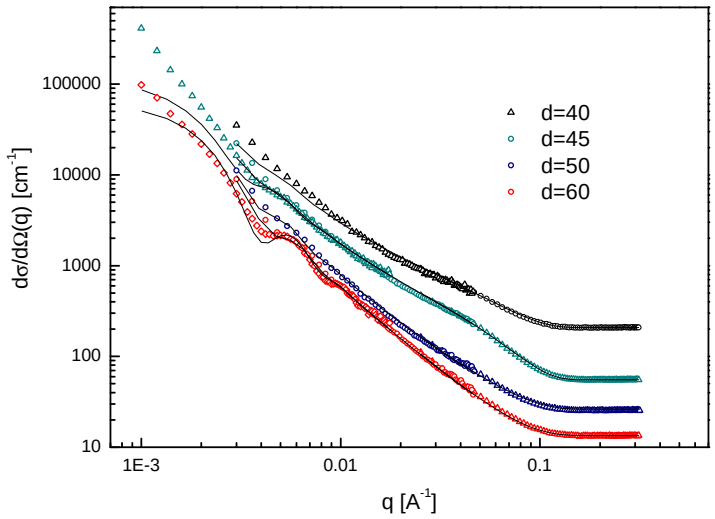

(a)

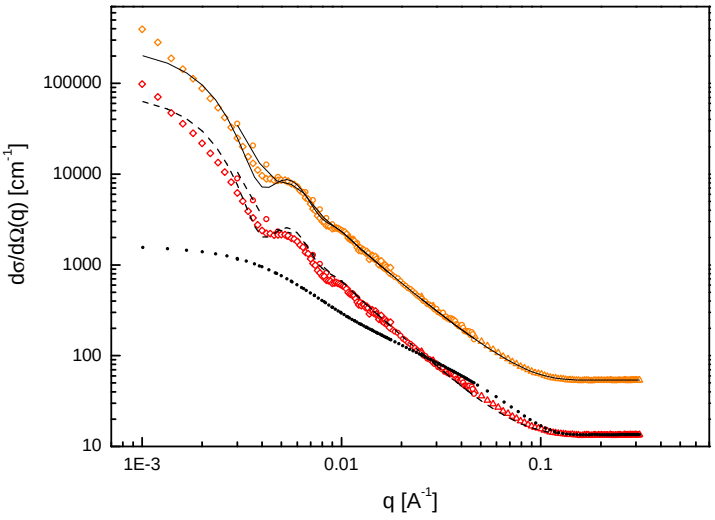

(b)

Figure 7.6: Absolute scattered intensity as function of scattering vector q (a) for samples with dilutions d=45 to d=60 at c_s=300 mM. Two or three different overlapping datasets constitute the full curve. Each data set for one dilution, i.e. surfactant concentration, and its according fit is multiplied by 2^n, n=1 starting by most diluted with d=60 until n=2 with d=40, d=45 was multiplied for a better visualisation with n=4, instead of n=3. The results of the data fitted with the model of the wormlike micelles plus vesicles are shown as the straight lines. In (b) d=60 is shown (orange), shifted with n=1. The solid line through the orange data points represent the fit of the coexisting micelles and vesicles. The individual contribution of the vesicles (dashed line) and of the micelles (dotted line) through the data points, i.e. the mass fraction is set to f_v=1 and f_v=0. The same parameters are used for the calculation of the wormlike micelles (dotted line) and vesicles (solid line) only.

			Micelles					Vesicles				
d	no sets	f_v	L [Å]	σ	R_H [Å]	R_C [Å]	$\frac{\rho_H}{\rho_C}$	R_v [Å]	σ	R_H [Å]	R_C [Å]	$\frac{\rho_H}{\rho_C}$
40	2	0.06	5000	0.15	27.64	9.96	0.44	879.91	0.15	25.05	12.81	0.30
45	3	0.09	7500	0.15	27.64	9.66	0.46	890.45	0.17	25.05	12.80	0.30
50	2	0.39	7500	0.15	26.00	9.50	0.44	870.00	0.15	24.44	13.41	0.41
60	3	0.67	2000	0.15	27.74	9.40	0.47	758.00	0.17	24.50	12.8	0.33

Table 7.3: Results from the nonlinear least square fits for dilutions 40 to 60 at c_s=300 mM. Polydisperse wormlike chain micelles with cross-section are fitted simultaneously with polydisperse vesicles. Given is the number of instrumental settings as well as the fit parameters: contour length L, polydispersity σ_{mic}, the total radius R_h, the radius of the core R_c.. $\Delta\rho$ = 5.718 cm^2 is fixed for the electrolyte with c_s=300 mM and also the Kuhn length is kept fixed at b=400 Å.

fitted as vesicles only, since this gave the slightly better result. But also $f_v \geq 0.9$ gives reasonable but similar results to f_v =1.

The structural parameters of the vesicles are given in table 7.4. It can be seen from the fitted values that with increasing dilution the vesicles are getting smaller. This is already obvious in the data, (figure 7.7), where upon dilution the oscillatory pattern shifts towards higher-q values.

d	no of sets	R_{ves} [Å]	σ_{ves}	R_H [Å]	R_C [Å]	ρ_H/ρ_C	$\langle M_m \rangle$ [10^6 g mol^{-1}]	cal M_m [10^6 g mol^{-1}]
65	2	735.00	0.15	21.95	12.60	0.22	223.44	195.6 ± 63.0
70	2	724.00	0.15	23.65	12.67	0.23	230.48	204.5 ± 65.9
80	3	706.79	0.15	24.85	12.10	0.26	213.20	194.6 ± 62.7
100	2	250.82	0.15	25.11	12.87	0.25	27.08	26.1 ± 8.4
120	2	188.52	0.15	25.00	13.84	0.25	18.21	14.7 ± 4.7
150	2	124.00	0.19	24.79	12.97	0.30	7.65	8.4 ± 2.0

Table 7.4: Results from the nonlinear least square fits for dilutions 65 to 150 at c_s=300mM. Vesicles are fitted. Given is the number of instrumental settings as well as the fit parameters: radius of the vesicle R_{ves}, the polydispersity of the vesicles σ_{ves}, the total radius R_h, the radius of the core R_c, the weight averaged molar mass $\langle M_m \rangle$ from fit and from the composition dependent calculation. $\Delta\rho$ = 5.718 cm^2 is fixed solvent with c_s=300mM.

The polydispersity is fixed to σ_{ves}/R_{ves}=0.15, except for d=150. The measurement falls a little bit out of the scheme, since the oscillatory pattern is not as pronounced as expected. But especially at high dilution, which corresponds to a concentration of about 0.52 mM, a little pipetting error, would result in a slightly different values for the fit in the vesicular regime.

R_c the radius of the core ranges 12.60Å $\leq$ R_c $\leq$ 13.84Å and R_h, the half width of the bilayer of the vesicle, i.e. the radius of the head ranges 21.95Å $\leq$ R_h $\leq$ 25.11Å. The core

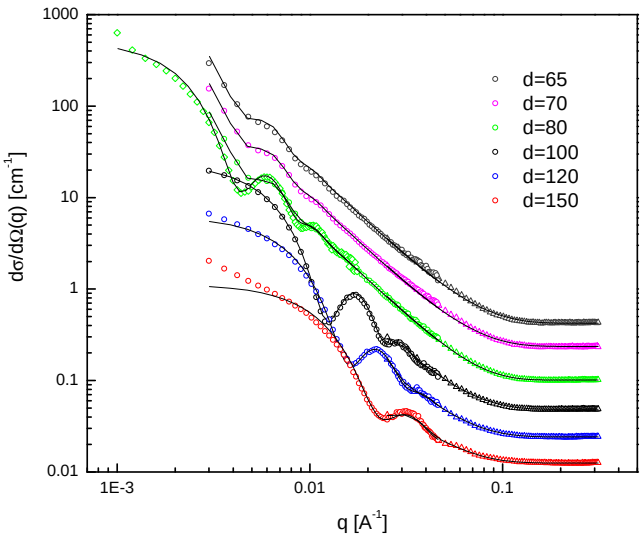

Figure 7.7: Absolute scattering intensity as function of the scattering vector$q$ for samples with dilutions 65 to 150 at c_s=300mM. The two or three different datasets can be seen in the figure. Each data set for one dilution, i.e. surfactant concentration, and its according fit is multiplied by 2^n, n=1 starting by most diluted with d=150 until n=7 with d=65. The results of the fits for the vesicles are shown as the straight lines.

radius R_{c} remain nearly constant throughout the phase, suggesting that the composition of vesicles does not change significantly upon dilution of the micelles. The half width of the core layer is bigger than for the micelles, which is consistent with bile salt leaving the aggregates upon dilution and a decreasing the curvature. At physiological concentrations, it was found, that the value of bilayer width is higher than the external radius of the cylinder, suggesting more EYL in the structure. The radius of the head The total half width of the bilayer of the vesicle R_{h} corresponds very well with values reported in the literature as R_{h}=24.7Å in a EYL/TCDC system at c_s=150 mM [41], whereas $R_{\mathrm{c}} = 14.9$Å is bigger. The comparison between physiological conditions and higher salt concentrations suggest again, that the bilayer width is mainly changed in the core due to the lack of volume from the decreased amount of EYL hydrophobic tail.

The weight averaged molar mass of the vesicles $\langle M \rangle_{\mathrm{v}}$ can be analogously defined to $< M >_{\mathrm{m}}$ by calculating the volume of the vesicle V_v and the bulk density $\rho_{b_{\mathrm{v}}}$.

$$
\begin{aligned}
< M >_{\mathrm{v}} &= V_{\mathrm{v}} \cdot \rho_{b_{\mathrm{v}}} \cdot N_A \\
&= \frac{4}{3}\pi[(R_{\mathrm{ves}} + R_h)^3 - (R_{\mathrm{ves}} - R_h)^3] \cdot \rho_{b_{\mathrm{v}}} \cdot N_A
\end{aligned}
$$

The bulk density was calculated according to the results from the microcalorimetry chapter, i.e. saturation line for vesicle solubilisation and the bile salt to lipid ratio R_e^{sat}. Again the calculated and fitted values agree very well.

7.2.4 Dynamic Light Scattering

With DLS, the hydrodynamic radius R_{hyd} at c_s=300 mM and other salt concentrations was measured as a function of dilution. The results can be seen in figures 7.8. In the analysis of the DLS data, the second order cumulant fit was taken for the hydrodynamic radius and the polydispersity. It has to be noted that in the LS as in SANS experiments, we attempted to examine the "non-viscous" phase. R_{hyd} shows the expected increase with size upon dilution,

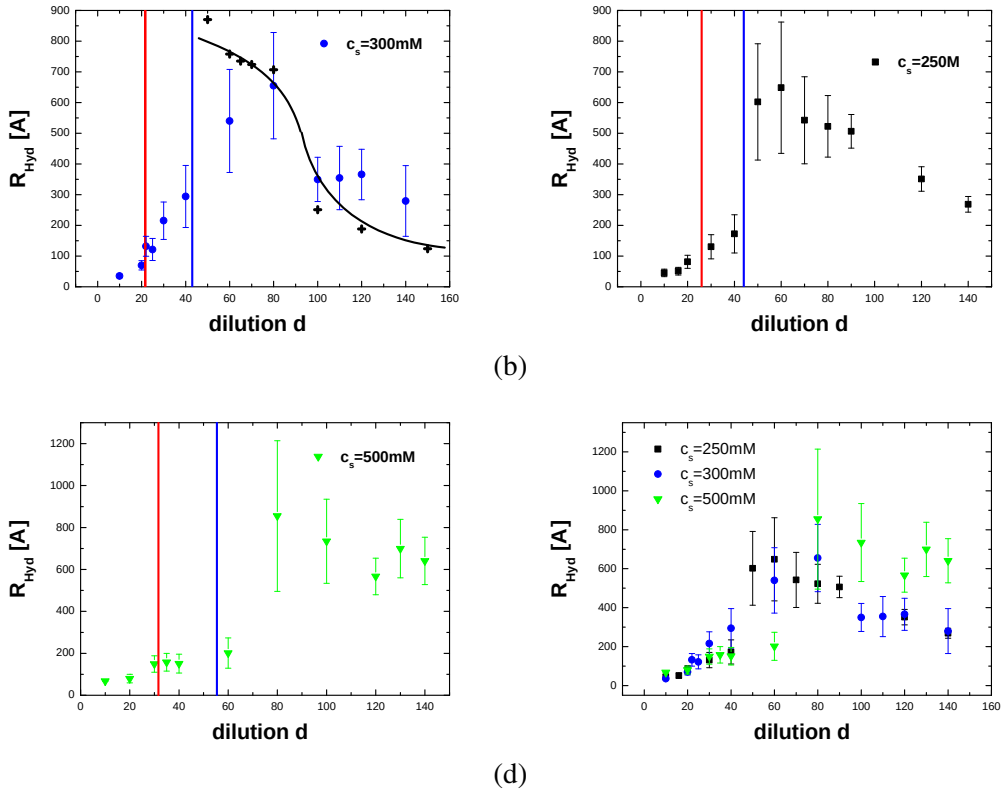

Figure 7.8: Average hydrodynamic radius R_{hyd} as determined by dynamic light scattering as a function of dilution d for different salt concentrations: (a) c_s=300 mM with R_v from SANS fit shown as black crosses (the solid line is a guide for the eye) (b) c_s=250 mM (c) c_s=500 mM and (d) all salt concentrations for comparison. Same stock solution were used, as for the SANS measurements.

i.e. the micellar growth until d=40. Simultaneously, the micelles become more polydisperse upon dilution. From d=40, R_{hyd} grows further. The corresponding neutron scattering data in this regime were fitted using f_v as a fitparameter. The coexistence of micelles and vesicles

is in good agreement with the high polydispersity measured by DLS. Then R_{hyd} decreases with further dilution after reaching its maximum of approximately 650 Å at d=80. Also the polydispersity decreases.

At salt concentration c_s=250 mM no "two-phase" region is observed. The size and polydispersity increase in the micellar region upon dilution and then, the vesicular size and polydispersity decrease again. The difference between the results at c_s=250 mM and c_s=300 mM are minor and are compared in figure 7.8 (d). Also at c_s=500 mM similar trends are observed (figure 7.8(c)). Actually until dilution d=20, the growth is very similar for all salt concentrations. Just upon further increase, the size does not grow as strongly until d=60 as for lower salt concentrations, and in the regime of the vesicles, the sizes are larger as compared to lower c_s.

7.3 Effect of dilution at constant salt concentration c_s=1000mM

At high ionic strength c_s=1000 mM the typical micelle-to-vesicle transition as observed at physiological concentration [60, 59] and also at c_s=300 mM in this study, changes qualitatively . For d $\leq$ 50 the scattering curves can be modeled by the wormlike micelle model. The typical oscillatory behaviour starting at the coexistence region of micelles and vesicles cannot be found here. Instead, for dilutions d$\geq$50 the scattering curve continues to increase in the low-q region, while it still shows the features of wormlike-micelles, that was modelled for lower dilution, at high q (figure 7.9). The transition is thus completely different at high ionic strength and there seems to be another type of "coexistence", i.e. other structures coexisting with the wormlike structures whose length scale is outside the investigated q-regime. This could be connected to the "viscous" phase. Figure 7.9 (b) shows, how the point of inflexion, which depends on $1/l_p$ (figure 7.2) moves towards higher q . This is reflected in the fitted value for the Kuhn length, which decreases with increasing dilution.
The micellar structure is pronounced at dilutions d=16 and d=20, i.e. the samples below the boundary of the "two-phase" region. At c_s=1000 mM the "two-phase" region is located between dilution d=30 and dilutions d=120, as indicated by our observation (fig. 7.1) and reflected by the fact that at low-q large structures of the "viscous" phase start to grow. Upon dilution the upturn shifts towards higher-q. Nevertheless until d=100 the wormlike micelle scattering pattern displaying the stiff rodlike and cross-sectional structures is still visible at the high-q end. Only at dilution d=120 the onset of the large structure is observed over the entire length scale measured here.
The high-q part of the data was fitted by the micelles model (table 7.5). Upon dilution the contour length L_{mic} of the cylindrical micelles first starts to grow, as observed before at c_s=300 mM. But when samples of the "two-phase" region are measured, although the sample

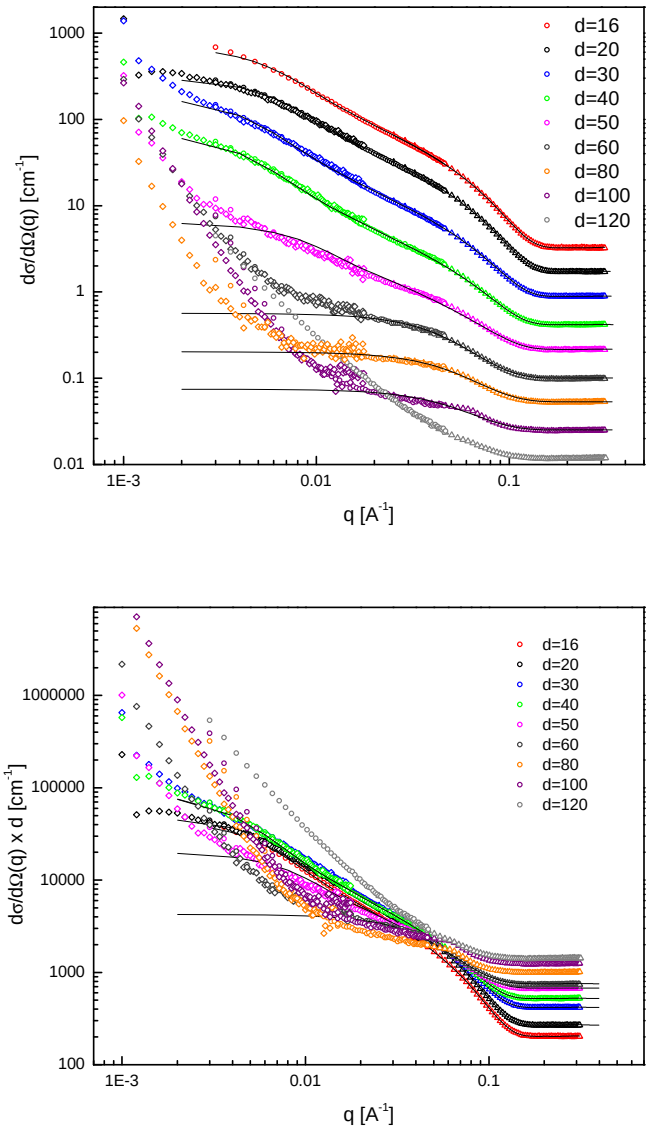

Figure 7.9: Absolute scattering intensity as a function of the scattering vector q for samples with dilutions 16 to 120 at c_s=1000mM (which consist of 2 or 3 different instrumental settings)(a) Each data set for one dilution, i.e. surfactant concentration, and its according fit is multiplied by 2^n, n=1 starting by most diluted with d=120 until n=9 with d=16. (b) Multiplied by the dilution factor.

d	no of sets	L_{mic} [Å]	σ_{mic}	R_h [Å]	R_c [Å]	ρ_h/ρ_c	b [Å]
16	2	1289.38	0.15	26.00	9.50	0.44	400.0
20	3	1128.45	0.15	25.88	9.58	0.44	400.0
30	3	1966.00	0.15	26.09	9.16	0.44	400.0
40	3	2086.00	0.15	26.50	9.36	0.44	300.0
50	3	620.0	0.15	26.35	10.39	0.43	50.0
60	3	147.81	0.15	26.00	9.50	0.44	50.0
80	3	105.66	0.15	25.02	10.10	0.47	47.5
100	3	122.16	0.15	25.74	10.43	0.44	47.5

Table 7.5: Results from the nonlinear least square fits for dilutions 20 to 120 at c_s=1000 mM. Wormlike micelles are fitted. Given is the number of instrumental settings as well as the fit parameters:: contour length L, polydispersity σ_{mic}, the total radius R_h, the radius of the core R_c, the weight averaged molar mass $\langle M_m \rangle$ from fit and from the composition dependent calculation and additionally Kuhn length b. $\Delta\rho$ = 5.793 cm^2 is fixed for the electrolyte with c_s=1000 mM.

was centrifuged prior to the measurement, a complete separation is not really possible. The large structures start exactly where the two bulk phase appears. Simultaneously to the upturn of the scattering curve, the size of the micelles decrease. This can be due to the fact that most of the material seem to have self-aggregated in the large structures or that the q-range affected by the large structures extends to larger q-values upon dilution.

The radius of the core R_c fluctuates between 9.50 Å$\leq$ R_c $\leq$ 10.43 Å and the radius of the head 25.02Å $\leq$ R_h $\leq$ 26.50Å. The value for R_c at this higher ionic strength is the same as for c_s=300 mM within the error. R_h is slightly smaller for higher ionic strength, but still the ionic strength does not affect the cross-sectional radius R_h strongly.

7.4 Effect of salt concentration c_s

7.4.1 Micellar samples (d=20)

Figure 7.10 shows the scattering curves obtained at d=20 and different salt concentration c_s. The dilution d=20 has been already presented at physiological (c_s=150 mM) and c_s=300 mM in the micellar regime. This does not change by increasing c_s further. At small dilution the scattering curves show hardly any changes with increasing c_s. If the data would not be multiplied with a constant value of 2^n, the measured curves would nearly lie on top of one another (inset of fig. 7.10). For c_s=300 mM three sets were measured and in the low-q region a growing intensity from the two-phase region can be seen. At c_s=1000 mM the two-phase region starts at higher dilutions, therefore no excess scattering at low-q is observed.

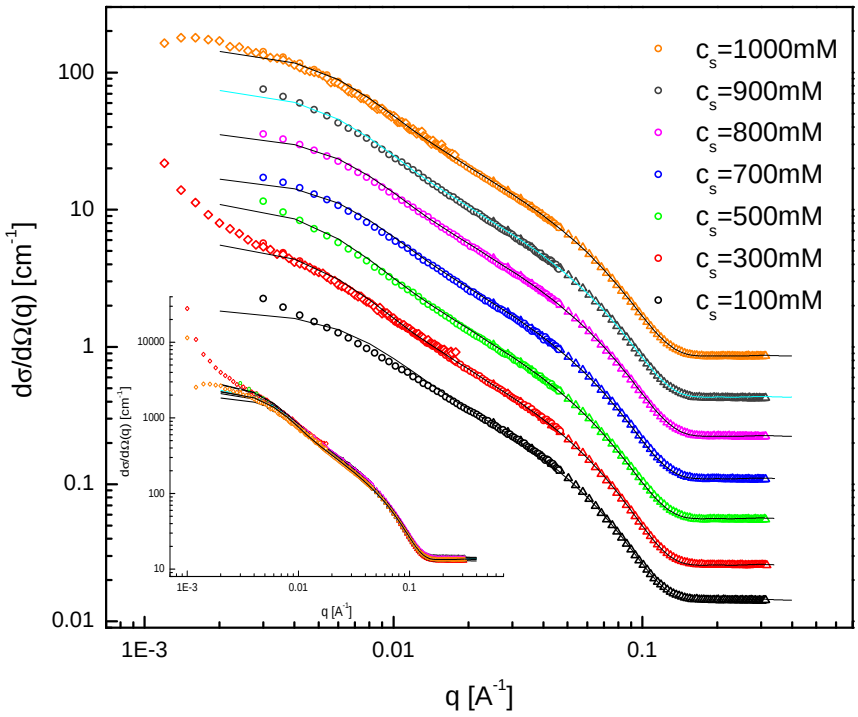

Figure 7.10: Absolute scattering intensity as a function of the scattering vector q for samples with dilution d=20 at various salt concentrations c_s. Each data set for one c_s (which consist of 2 or 3 different instrumental settings) and its according fit (solid line) is multiplied by 2^n, n=1 starting with the lowest salt concentration c_s. The inset shows the unshifted data.

Although the scattering curves are nearly identical (inset of 7.10), the values for R_h, R_c and ρ_h/ρ_c determined with increasing c_s differ slightly, which gives an idea about the possible standard deviation of each single parameter. The scattering length density between the shell ρ_h and the core ρ_c is nearly constant, R_c varies and has a mean value of (10.05 $\pm$ 0.23) Å and R_h of (26.46 $\pm$ 0.32) Å. The radii thus deviate only between 1 to 2 %. In contrast, the variation of the contour length L_{mic} is larger, about 15% There seems to be a trend to slightly larger L_{mic} with increasing c_s and, in addition, particularly large micelles present at c_s=300 mM and 500 mM, which might be related to the proximity of the "two-phase" region. This results from the interplay of two effects.

The Kuhn length is fixed at 400 Å. As argued before, with higher c_s the charges in the aggregate are better screened and thus a higher flexibility is expected. At the same time, with increasing ionic strength there is also more bile salt in the aggregates, and thus more charge, which makes the aggregates less flexible. Both effects seem to balance. At the c_s=1000 mM the screening

c_s	no of sets	L [Å]	σ_{mic}	R_h [Å]	R_c [Å]	ρ_h/ρ_c	$\Delta\rho$ cm^{-2}
100	2	814.98	0.15	26.88	9.71	0.44	5.697
300	3	1321.6	0.15	26.74	10.00	0.45	5.718
500	2	1334.0	0.15	26.88	10.01	0.44	5.740
700	2	994.84	0.15	26.69	10.35	0.44	5.761
800	2	1003.49	0.15	25.82	10.12	0.44	5.772
900	2	1143.21	0.15	26.33	10.61	0.44	5.782
1000	3	1128.45	0.15	25.88	9.58	0.44	5.793

Table 7.6: Results from the nonlinear least square fits for dilution 20 at various salt concentrations c_s. Given is the number of datasets. $\Delta\rho$ is fixed for each salt concentration according to the table.

is constant, but bile salt is removed upon dilution from the aggregates, shifting the balance to higher flexibility as observed before.

7.4.2 Vesicular samples, d=120

c_s	no of sets	R_{ves} [Å]	σ_{ves}	R_h [Å]	R_c [Å]	ρ_h/ρ_c
100	2	149.25	0.15	25.13	14.40	0.33
300	2	188.52	0.15	25.00	13.84	0.25
500	2	262.32	0.14	25.59	11.47	0.26
600	3	426.33	0.17	26.67	12.70	0.23
700	3	527.27	0.17	27.69	11.89	0.21

Table 7.7: Results from the nonlinear least square fits for dilution 120 at various salt concentrations c_s.iven is the number of instrumental settings as well as the fit parameters: radius of the vesicle R_{ves}, the polydispersity of the vesicles σ_{ves}, the total radius R_h, the radius of the core R_c $\Delta\rho$ is fixed as given in table 7.6.

The effect of increasing the salt concentration c_s was also tested on samples with a dilution of d= 120 (figure 7.11). It is known, that for $c_s = 150$ mM and dilution $d = 120$ vesicles are formed. Also for $c_s = 300$ mM, it could be seen in this study that this micelle-to-vesicle transition is not lost and vesicles form. With further increase of salt concentration c_s still the scattering pattern for vesicles is visible and the vesicle size increases with c_s (table 7.7). At c_s =700 mM it seems, that the effects of the two-phase region commence again and with an increase in scattering intensity at low-q. The oscillatory pattern at the high-q part smoothes out and the fit is not optimal with vesicle structures only. At $c_s \geq$800 mM no structural information can be gained and no fitting has been attempted. The inset in figure 7.11 shows the

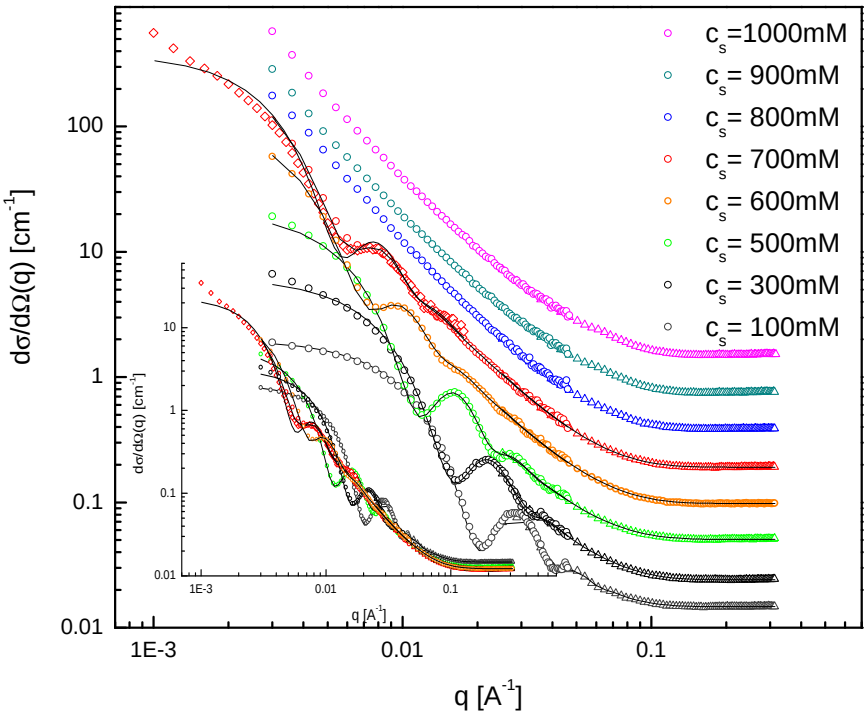

Figure 7.11: Absolute scattering intensity as a function of the scattering vector q for samples with dilution 120 at various salt concentrations c_s. Each data set for one c_s (which consist of 2 or 3 different instrumental settings) and its according fit is multiplied by 2^n, n=1 starting with the lowest salt concentration c_s. c_s=800-1000 mM is not fitted, since only an increase in intensity towards low-q is visible. The inset shows the not multiplied data for c_s=100-700 mM.

non multiplied data, and clearly exhibits the shift of the minima towards lower q-values with increasing c_s.

In Leng et al. [60] three different dilutions d=40, 80 and 120 were investigated by measuring the hydrodynamic radius R_{hyd} with increasing c_s using dynamic light scattering (fig. 7.12 a)). R_{hyd} increases moderately until c_s=700 mM, after which a pronounced growth is observed. At lower dilutions d=80 the growth starts earlier, at $c_s \simeq 250$ mM. The open symbols in 7.12(a) represent samples in the "two-phase" region. The samples in this study were in aqueous solution. The samples examined with SANS (in D_2O), were afterwards also measured with DLS (fig. 7.12(b)). Also in this measurement a steep increase in R_{hyd} after c_s=700 mM can be observed and corresponds well with the scattering pattern observed with SANS (figure 7.11). In both analysis of the DLS data, the second order cumulant fit was taken.

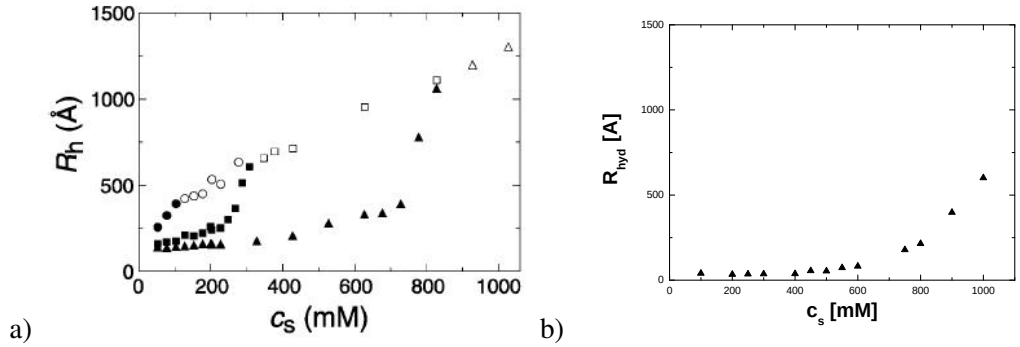

Figure 7.12: (a) Hydrodynamic radius R_{hyd} measured in the end state as a function of c_s for different dilutions d (●: 40, ■: 80, ▲: 120) in H_2O. Solid symbols correspond to vesicular samples and open symbols to samples beyond the vesicular region. From Leng et al. [60]. (b) Hydrodynamic radius R_{hyd} measured as a function of c_s for d=120 in D_2O measured here.

7.5 Conclusion

The model used for the micelle-to-vesicle transition with wormlike micelles in the lower dilution regime and vesicles at higher dilutions fitted the data presented very well. In addition to the structures present at physiological conditions we observed the upturn in the scattered intensity at low-q due to large aggregates. These growing aggregates are bigger than the length scales measured in the experiments, therefore no model for large aggregates was considered in the fits.

In figure 7.13 the different areas of the phase diagram are shown. The pure vesicles (dark blue) are outside the "two-phase" region. For low salt concentration, i.e. c_s =300 mM, they start at d=45 within the region of the two bulk phases and coexist with micelles until d=60. The vesicles have the biggest radius R_v for low dilutions and large c_s (figure 7.13). The largest vesicle radii found are just above the micelle-vesicle coexistence region. At lower, fixed salt concentration vesicles decrease in size upon dilution. At fixed dilution, the vesicle increase in size with increasing ionic strength. These highest sizes were of about R_v=700 $\mathring{A}$., The vesicles are indicated by the blue arrows in the figure 7.13.

Micelles can be found at low dilutions as known for physiological conditions and also at larger c_s as found here. At low c_s the typical dilution dependent micelle-to-vesicle transition can be observed as for c_s =300 mM. R_{c} remains roughly constant and R_{h} and ρ_h/ρ_c decreases in direction of increasing R_v, i. e decreasing d and increasing c_s.

The contour length L and the persistence length l_p of the micelles is roughly constant upon increasing the ionic strength while the micelles hardly grow increasing c_s, they grow with

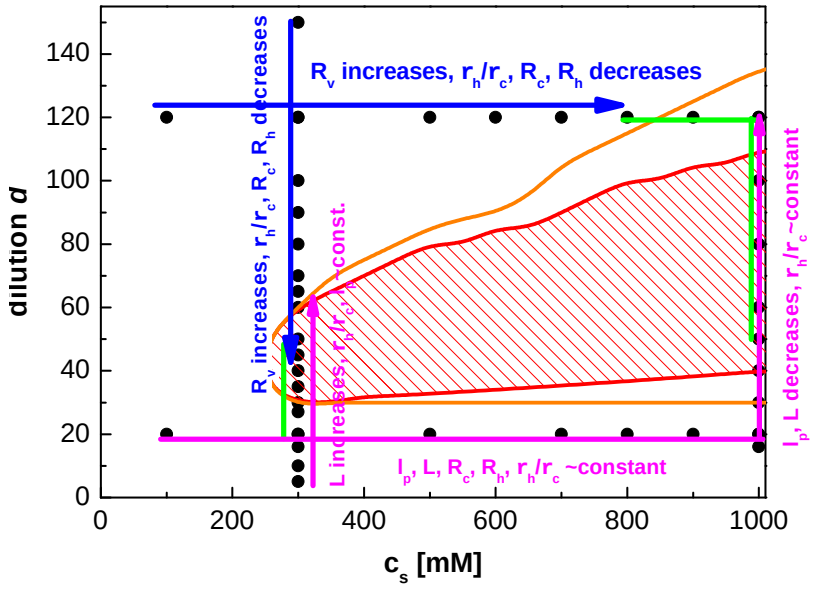

Figure 7.13: Schematic phase diagram in the dilution d vs. the salt concentration c_s plane. The red area represents the area, where visible phase separation occurs. Just around this boundary the samples are turbid, represented by the orange line.

dilution. As explained earlier the persistence length stays about constant due to two balancing effects: the flexibility is expected to increase due to the increased screening and decrease due to the increased amount of bile salt, i.e. charge in the aggregate. Also at large c_s upon dilution, bile salt is removed from the aggregate and might be responsible for the higher flexibility. All the other fit parameter R_c, R_h and ρ_h/ρ_c remain about constant in the micellar range, which suggests that the composition of the micelles and the amount of water molecules associated in the shell of the micelles, does not change with dilution or salt concentration.

ρ_h/ρ_c tends to be lower in the vesicular ($\rho_h/\rho_c \approx 0.25$) than micellar ($\rho_h/\rho_c \approx 0.45$) region. This means, the value is lowered by the higher number of heavy water molecules in the shell of the vesicles. Based on the ρ_h/ρ_c values, we can calculate the number of water molecules in the shell;(equation 7.12) as 16.5 water molecules for micelles and 22.7 water molecules for vesicles.

It is known that the shell of pure EYL bilayers swell in the presence of water [33]. Especially with more detergent in the aggregates, the swelling could be more pronounced. Supersaturated structures were observed for mixtures of cholesterol in bile salt/lipid systems [40], which macroscopically separated in a insoluble phase and can be found in the human enterohepatic system. At c_s =300 mM and dilutions between d=30 and d=60, the "two-phase" region is crossed, where micelles not only coexist with vesicles, but also with some aggregates larger

then the length scale observed. At c_s=1000 mM the two-phase region is located between d=30 and d=120 . It also shows a coexistence of micelles with large structures, i.e. the the presence of micelles can be identified for most of the dilutions except d=120. The SANS data, where the onset of the large structures can be observed, is indicated by the green lines in figure 7.13 and they lie in the region of the macroscopic phase separation. It can be presumed that this is the case for all samples in the separation into two bulk phases is observed.

The large objects coexist with micellar aggregates, whereas vesicles (with a radius observable in this length scale window) do not seem to form. In Leng et al. [60] the micelle-to-vesicle transition is described by a kinetic model. After a rapid formation of disklike intermediate micelles from wormlike micelles, a growth of these metastable micelles is proposed, before they close to form vesicles. The model also predicts, that under certain conditions a lamellar stacking becomes more likely than the closure to vesicles. This could explain the phase separation observed here and in [35]. However, a lamellar signature is not present in the scattering pattern.

In the next chapter a closer look at the ”viscous” phase of the phase separated samples will be taken using x-ray scattering and trying to explain the nature of the large objects observed here, where a discussion including these results will be presented.

Chapter 8

Structure Determination using X-ray Scattering in the "two-phase" Region

In chapter 7 the morphological changes with respect to salt concentration and dilution was investigated. At c_s=300 mM electrolyte concentration, the "classical" micelle-to-vesicle transition as observed at physiological conditions (c_s =300 mM), was found. This was at the boundary to the two-phase region. But when samples in the two-phase region (fig. 5.2) were examined, large objects were visible. At higher salt concentration the scattering of large structures was more pronounced. In SANS we focused on the "non-viscous" phase. With small angle x-ray scattering experiments (SAXS) the attention was turned towards the "viscous" phase of the two-phase region. The measurements were performed in H_2O, which shifts the two-phase region slightly (5.2). The two-phase region in H_2O is represented in figure 8.1, where the dark blue hatched area represents he "two-phase" region as determined by macroscopic observation. Just around this boundary the samples are turbid or sometimes have macroscopic precipitates, too, (this is surrounded by the light blue line). Structural length scales similar to the SANS measurement in chapter 7 were resolved, with a q-range 0.0036 $\text{Å}^{-1} \leq q \leq$0.6 Å^{-1}.

The viscous phases of two different bile salts mixed with lecithin were investigated here. NaTCDC/EYL as before in the SANS experiments and furthermore NaTC/EYL. The first system was already discussed in chapter 5, but the NaTC/EYL displayed a "two-phase" area, too. The samples were prepared as in the case of NaTCDC/EYL with the same EYL-to-bile salt molar ratio 0.9. The "two-phase" area (as well as the micelle-to-vesicle transition) appeared at lower dilution due to the higher cmc of NaTC compared to NaTCDC and furthermore at higher salt concentration, e.g. between $c_s = 1200$ mM and $c_s = 1600$ mM at dilution d=20.

A systematic SAXS study was performed to investigate the effect of the salt concentration

in the two phase region. Figure 8.1 shows the compositions studied with stars and crosses. Additionally temperature scans were performed by varying the temperature from 25° to 40° C in steps of about one degree Celsius. In this case the composition are indicated with a star. Also two samples of the NaTC/EYL system were studied. Again after background subtraction and corrections of the background from sample cell and solvent (chapter 3), the intensity as a function of q has been determined (figures 8.5-8.10). The experimental results are evaluated using a new approach which is based on the modeling of the electron density profile by a gaussian deconvolution method, which was developed by Prof. J. S. Pedersen and Dr. C. Olivera from the University of Århus, Denmark.

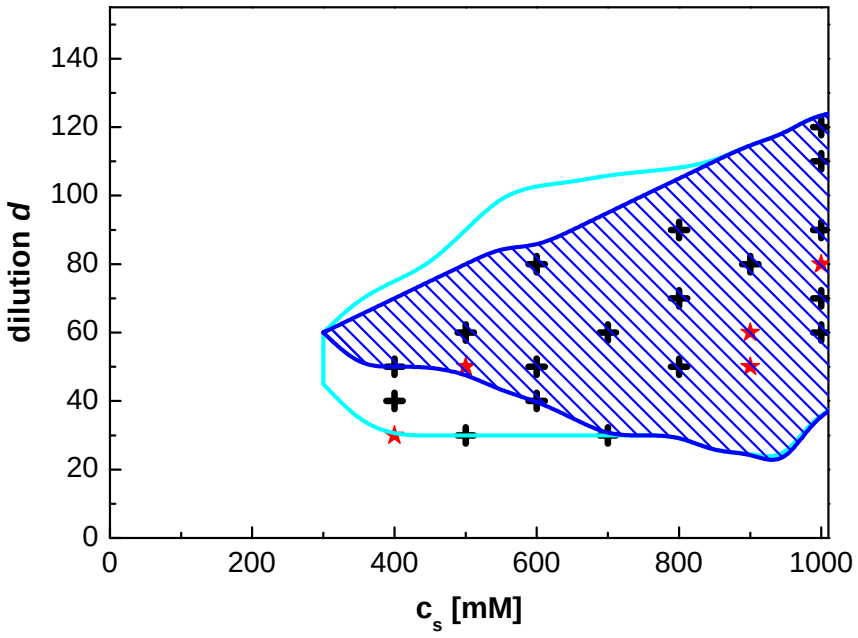

Figure 8.1: The blue area represents compositions, where the visible phase separation occurs. Just around this boundary the samples are turbid or have precipitates as well, these compositions are surrounded light blue line. The black crosses represent the composition, where the viscous phase was investigates by SAXS at 25°C, for the compositions indicated by the red stars, additionally the temperature was varied from 25° to 40° C.

8.1 Structural Characterisation of Lipid Aggregates

There is a considerable amount of research performed concerning the structure determination of phospholipid bilayer stacks [170, 171, 172, 173, 174, 175, 176, 177], since lipid bilayers are

components of every cell membrane and the determination of the physical properties provides a better understanding of the structure-function relationship, which is an important question in cell biology. Pure lipid bilayers are commonly used for modeling biological membranes. Luzzati et al. [170, 171] did pioneering work in the late sixties in investigating bilayer stacks with x-ray diffraction techniques with which they were able to determine the lamellar repeat distance of phospholipid bilayers: 50 to 150 Å depending on the lipid and the level of hydration. The so-called Luzzati method is a very basic approach to extract structural information on lamellar structures [170, 171] from the peaks observed in X-ray diffraction experiments. The peaks can be related to the lamellar repeat distance d_{b}, the thickness of the bilayer $d = 2d_{\mathrm{h}}$ and the thickness of the water layer d_{w} (fig. 8.2). In this approach all water is in the water layer and no swelling of the individual bilayers is included. In the following the Luzzati description will be used for the labeling of the bilayer distances (figure 8.2).The electron density profile $\rho(z)$ along the z-axis belonging to the bilayer stack is shown on the right hand side of fig. 8.2, where the x-rays scatter at the electron dense headgroup of the bilayer and scatter poorly at the hydrocarbon chains.

For lipids the headgroups are electron dense and the determination of the position of the electron density peaks along the normal of the bilayer gives a good measure for the bilayer thickness or in case of bilayer stacks of the bilayer repeat distance [176]. The widths of the electron density peaks gives a measure of the disorder caused by fluctuations in the bilayer.

8.1.1 Scattering from a multilamellar lipid bilayer and the Fourier Method

The scattering function of a stacked multilamellar lipid bilayer can be described as [177]:

$$I(q) =< |F(q)|^2 S(q) > \tag{8.1}$$

where the average is taken over all fluctuations. $F(q)$ is the form factor, given by the Fourier transform of the electron density profile $\rho(z)$ along the z-axis

$$F(q) \quad = \quad \int \rho(z) e^{-(iq_z z)} dz \tag{8.2}$$

$S(q)$ is the structure factor

$$S(q) \quad = \quad \int\int d^2r d^2r' \sum_{j=1}^{N} \sum_{k=1}^{N} e^{-iq_r(r-r_j)} e^{-iq_z(z-z_k)} dz \tag{8.3}$$

It describes the nearly crystal like nature of the layered system and is given as a correlation function of the number of bilayers in the stack with their position along the z-axis. If the

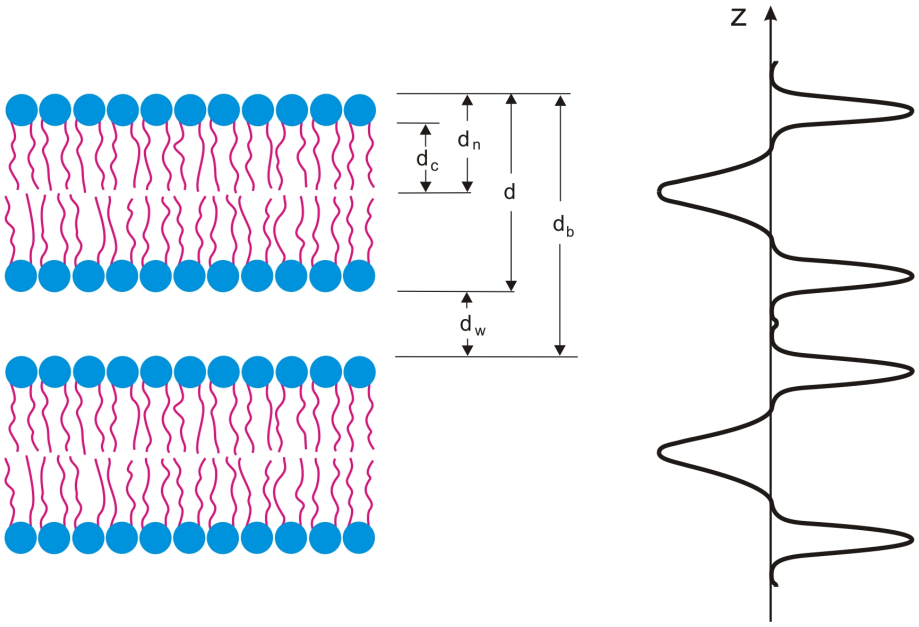

Figure 8.2: Schematic representation of a single lipid bilayer. Schematic illustration of a multilamellar array of lipid bilayers. The lamellar repeat distance is d, hydrophobic lipid bilayer is d_L and hydrophilic lipid bilayer d_h.

structure factor is disturbed by fluctuations which are caused by thermal or lattice disorder, then the structure factor is defined by paracrystalline theory. The fluctuations are assumed to be stochastic. (For a review see reference [178].) In the Caillé theory the bending of the multilamellar stacks is included to the infinite number of layers. The fluctuations are assumed to be Gaussian. The Caillé theory was modified, Modified Caillé theory (MCT), and the finite size of the lamellar stacks was taken into account [176]. By assuming a cylindrical stacking, i.e. along the z-axis, of N nearly flat bilayers of radius R in the limit of $q\ R \gg 1$, one obtains a mean displacement of the k^{th} bilayer by the amount v_k around the origin v_0 due to fluctuations by:

$$< (v_k - v_0)^2 >= \frac{d^2}{2\pi}\eta_1[\gamma + \log(\pi k)] \tag{8.4}$$

where γ is Eulers constant [1] and η_1 is the Caillé parameter. η_1 is related to the bending and compressibility of the bilayer with

$$\eta_1 = \frac{\pi}{2d^2}\frac{k_B T}{\sqrt{KB}} \tag{8.5}$$

[1] the Eulers constant is a mathematical constant is defined over the limiting difference between a harmonic series and the natural logarithm $\gamma = \lim_{n\to\infty} \sum_{k=1}^{n} \frac{1}{k} - \ln n = 0.57721566$

where K is the layer bending modulus and B the bulk modulus of compression. It is built up on the thermodynamic theory of de Gennes [179] for smectic liquid crystals which yields the free energy density g of a fluid bilayer by:

$$g = \frac{1}{2}K(\Delta_{\perp}^2 v)^2 + \frac{1}{2}B(\frac{\partial v}{\partial z})^2 \tag{8.6}$$

where v is the displacement variable.
The structure factor can now be written as:

$$S_{MCT}(q) = N\sum_{k=1}^{N-1}(N-k)cos(kqd)e^{((\frac{d^2}{2\pi})^2 q^2 \eta_1 \gamma)}(\pi k)^{((\frac{d^2}{2\pi})^2 q^2 \eta_1)} \tag{8.7}$$

The MCT theory is nowadays widely used in describing lipid lamellar stacked system. Especially many studies from Nagle and coworkers [180, 181, 182] and Nallet [183] use the MCT theory to describe their X-ray scattering data on lipid systems of Kucerka et al. [184, 182].

8.1.2 Electron density profile by a summation of three Gaussian profiles

The determination of the electron density profiles $\rho(z)$ along the normal of the bilayer, for a scattering pattern with 4 or less Bragg peaks is given by Wiener et al. [172] by a summation of three Gaussians, where each Gaussian represents two headgroup regions of the bilayer and the hydrocarbon chains. In fig. 8.2 the electron density profile is presented on the right hand side and each individual peak corresponds to one Gaussian , similarly three Gaussians represent the electron density profile in figure 8.3, where ρ_z is the electron density of the headgroup and ρ_c of the hydrocarbon chains.

$$\rho(z) = \overline{\rho_H}\left(\exp\left(-\frac{(z-z_H)^2}{2\sigma_H}\right) + \exp\left(-\frac{(z+z_H)^2}{2\sigma_H}\right)\right) + \rho_{\mathrm{CH_2}} + \overline{\rho_C}\left(-\frac{z^2}{2\sigma_C^2}\right) \tag{8.8}$$

The electron densities of the headgroup is defined relative to the bilayer methylene electron density $\rho_{\mathrm{CH_2}}$ as it can be seen in figure 8.3 with:

$$\begin{aligned}\overline{\rho_H} &= \rho_H - \rho_{\mathrm{CH_2}}\\ \overline{\rho_C} &= \rho_C - \rho_{\mathrm{CH_2}}\end{aligned}$$

and σ_H, σ_C are the FWHM of the headgroups. The obtained electron density profiles $\rho(z)$ for lipids show the electron-rich phosphate headgroups as two peaks symmetrically around the center of the bilayer, and the electron-poor methyl and methylene groups at the center of the bilayer (fig 8.3). The mixed bilayer formed by bile salt and EYL is assumed to have a similar

electron density profile as a pure of EYL bilayer.
Because of the "lattice" disorder of fluid lamellar phases, the number of peaks is limited. This also depends on the used lipid as 5 Bragg peaks were observed for dipalmitoylphosphatidl-choline (DPPC)[172] but only 4 Bragg peaks for PE [182] or due to the instrumental resolution used for the measurement. With an increased water content in the sample, i.e.between the bilayers, the lattice disorder will increase and thus generally less peaks are observed.

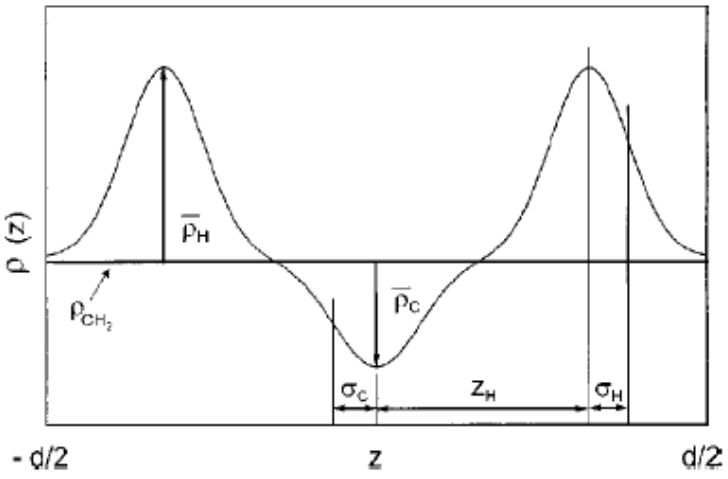

Figure 8.3: Gaussian model representation of the electron density profile. From [175].

The Fourier transform according to equation 8.2 gives the form factors of the head F_{H} and the chains F_{C}

$$\begin{aligned} F(q) &= 2F_{\mathrm{H}}(q) + F_{\mathrm{C}}(q) \\ &= 2\sqrt{2\pi}\overline{\rho_{\mathrm{H}}}e^{-\frac{\sigma_{\mathrm{H}}^2 q}{2}}\cos(qz_{\mathrm{H}}) + \sqrt{2\pi}\overline{\rho_{\mathrm{C}}}e^{-\frac{\sigma_{\mathrm{C}}^2 q}{2}} \qquad (8.6) \\ & \qquad (8.7) \end{aligned}$$

Equation 8.1 can be rewritten for stacks of N nearly flat bilayers as $I(q) = I_{1D}(q)/q^2 = \langle |F(q)|^2 S_{1D}(q)\rangle$, where $1/q^2$ is the Lorentz factor for nonoriented powder samples [176] and the subscript $1D$ stands for one-dimensional intensity or structure function along the z direction, which is normal to the bilayer plane. Using this and equation 8.7, the total scattered intensity is given by:

$$I(q) \propto \frac{1}{q^2}\left(|F(q)|^2 S_{\mathrm{MCT}}(q) + N_{\mathrm{diff}}|F(q)|^2\right) \qquad (8.8)$$

The last term in this equation is from diffuse scattering, that has been found during the data analysis and originates from strong lattice defects in the bilayers and is usually neglected, when

structural information is derived from the Bragg peaks only.

MCT requires a good set of starting values for the fitting parameters to be minimised by nonlinear least-square fitting, therefore a different approach to MCT will be used. A new approach will be introduced which is based on the MCT theory, but requires no *a priori* information of the signs and the positions of the Gaussians.

8.1.3 Electron Density Profile by the Gaussian Deconvolution Model

The model described here, has been developed by Prof. J. S. Pedersen and Dr. C. Olivera from the University of Århus, Denmark [185]. Their routines were used for the structure determination of infinite single lamellar sheets with cross-sectional profile. It is based on the MCT theory combined with a deconvolution of the pair distance distribution $\rho(r)$, which is the particle electron density from the Fourier transform of the scattered intensity [116]. For 1-dimensional lamellar symmetry, $\rho(\vec{r}) = \rho(z)$.

The electron density profile is approximated by a series of equidistant Gaussian functions centered around $+z_i$ and $-z_i$, i.e. symmetrical to the center of the bilayer. The model assumes central symmetry. The Gaussians have width $\sigma_i = \sigma$.

$$\rho(z) = \sum_{i=1}^{N} \frac{c_i}{1+\delta_i} \left[\exp\left(-\frac{(z-z_i)^2}{\sigma_i^2} \right) + \exp\left(-\frac{(z+z_i)^2}{\sigma_i^2} \right) \right] \tag{8.9}$$

The coefficient c_i describes the height of the i-th Gaussian. Furthermore, constraints are added to the coefficients c_i to obtain a stability criterion for the least square fitting procedure [186, 187]. Since measured data points always have statistical errors, stability problems arise when solving the mineralisation of the least-squares approximation of the experimental data. This can be overcome by minimising $\chi^2 + \lambda_s N_c$ instead of χ^2 [169, 186, 187, 188], where N_c is a measure of smoothness and λ_s a stabilisation parameter, which can be determined with the point of inflexion method described by Glatter [186].

The headgroup size $d_h - d_c$ can be estimated from the full width halve maximum of the Gaussian, i.e from σ.

$$z_i = (i-1)2\sigma\sqrt{2\ln 2} \qquad \sigma = \frac{z_{\max}}{2N\sqrt{2\ln 2}}$$

where $z_{\max}$ half of the total thickness of the bilayer. The scattered amplitude and intensity are

then given:

$$\begin{aligned} F(q) &= \sqrt{2\pi}\sigma \sum_{i=1}^{N} (2-\delta_{i1}) c_i \exp(-\sigma^2 q^2) cos(q z_i) \\ I(q) &= \frac{1}{q^2} |F(q)|^2 \end{aligned} \tag{8.8}$$

The structure factor is not added, since we model the cross-sectional profile of one single bilayer sheet. The program uses the intensity calculated from equation 8.8 and fits it to the experimental scattered intensity, i.e. the input parameters are the half of the total bilayer thickness $r_{\max}$ and the number of Gaussians N. No assumptions for the starting values for the coefficients c_i are required. The coefficients c_i are fitted and afterwards used to calculate the electron density profile.

8.2 Results and Discussion for Bile Salts/EYL

SAXS data were obtained for mixtures of NaTC and NaTCDC with EYL under various salt concentrations c_s and dilutions d in aqueous solution, i.e. H_2O. Only the separated "viscous" phase of the sample was used for the measurements. It is assumed, that the viscous phase consists of extended unilamellar bilayers, whose the cross-sectional profile is determined. An infinitely extended unilamellar bilayer does not require a the structure factor, therefore only the formfactor is fitted. A fit including a structure factor and form factor was tested (according to the MCT theory described in section 8.1.2), but the model did not fit the x-ray data sufficiently well and will not be presented here.Therefore the theory based on current models of lipid bilayer structures were used for the analysis with modifications described above. The background due to solvent (water) and sample cell were subtracted (chapter 3) before fitting to the measured intensity versus q with the Gaussian Deconvolution method (section 8.1.3. The number of Gaussians N in the series and the width of the bilayer $z_{\max}$ has to be chosen. The number of deconvoluted Gaussians was set to seven, but also lower values, i.e. three as in Wiener *et al.* [172, 173, 174] and in Pabst *et al* [175] were tried, but were not able to fit the experimental data sufficiently well. The fitting routine is based on a least square fitting, where the deviation between the experimental data and the model is minimised. The χ^2 error for most of the fits lies between 1 to 2, only a few have a higher least square error up to χ^2=6.

8.2.1 Results for NaTCDC/EYL

Dependence on salt concentration at d=50

The main focus has been put on the effect of increasing salt concentration c_s within the "viscous" phase. Figure 8.4 (a) shows the scattering of sample with increasing c_s with fixed

dilution d=50. In all measurements of the scattered intensity a broad peak appears in the interval 0.055 Å^{-1} $\leq q \leq$0.3 Å^{-1} followed by a small hump. It illustrates that the scattering intensity within the viscous phase seems to be independent of c_s. Furthermore the scattering pattern does not change for varying NaTCDC/EYL concentration, i.e. within the "two-phase" region.

For pure POPC samples in the L_α phase in this temperature regime, one can find a diffraction pattern of lipid lamellar stacks in this q-regime. In Pabst *et al.* [175] three Bragg peaks appear in the scattering curve (at T=2°C), where the first two peaks scatter in the same q-regime as the broad peak here and a third at the position of the small hump. By increasing the temperature to T=50°C, the third peak disappears due to the thermal fluctuation. The same scattering pattern can be seen in Kuçerka *et al.* [184] for unilamellar vesicles of DOPC.

One problem of fitting *fluid* lamellar structures is that they have only quasi-long-range order with fluctuations. And especially these fluctuation reduce the intensity of higher order Bragg peaks [176]. Since our measurements were obtained with high instrumental resolution, although performed on a laboratory instrument, it is presumed that Bragg peaks despite fluctuations observed of bilayer stacks of pure EYL sample would be resolved. So either the fluctuations are much higher than in pure EYL samples or the "lamellar" structures are quite disordered or they are individual bilayers or very small stacks.

The fitted electron density profile $\rho(z)$ does not change strongly with c_s (figure 8.4 (b)).
If it is presumed that the first peak with a distance of z_{H_1}=14.8 Å and a width of σ_{H_1}=2.3 Å corresponds to the headgroup of EYL, then the hydrocarbon chain length $d_c = z_{H1} - \sigma_{H1}/2$ can be calculated:
d_c 13.65 Å. The comparison to the literature values shows in table 8.1 show that the hydrocarbon chain size d_c is similar to the ones observed in other phosphatylcholine (PC) samples. EYL consists 70% to 80% of POPC (palmityloleylphosphatidylcholine). Also DOPC is comparable to EYL, since it is a quite similar lipid with one double bond on the *sn*-2 chain. Especially due to this double bond in the chain, significant disorder is induced compared to shorter chained lipids without the double-bond as e.g. DMPC (dimyristoylglycerolphosphocholine), where a larger d_c was found. Actually the chain is almost at its minimum length, which indicates already that it is very fluid-like.

Unfortunately the nature of the second peak is still not clear. It could be that bile salt micelles sit on the surface of the bilayer. Another idea could be that bile salt sits at certain patches of the bilayer, i.e. mostly where the coalescence of the micelles has occurred. And these patches have a wider cross-sectional profile than patches with less bile salt monomers or oligomers, since bile salt could push the headgroup of the EYL out to obtain two distinct peaks.

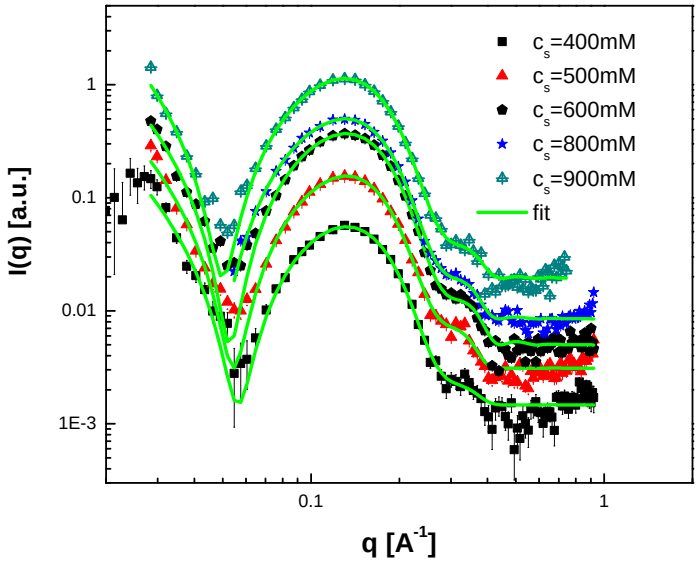

a)

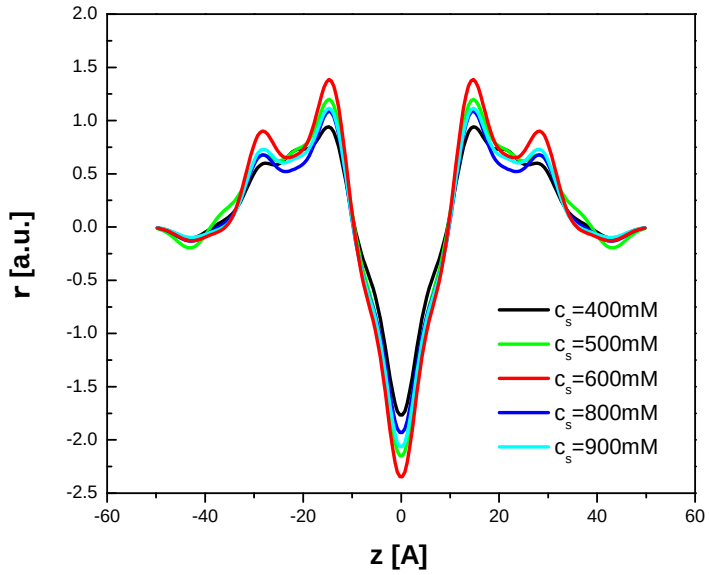

b)

Figure 8.4: (a) Scattering intensity I(q) as a function of scattering vector q as determined by SAXS for a sample with fixed dilution d=50 and different salt concentration c_s=400 mM, 500 mM, 600 mM, 800 mM and 900 mM. Each data set fit is multiplied by 2^n, with n=1 for c_s=400 mM to n=5 for c_s=900 mM. (b) Corresponding electron density $\rho(z)$

T [°]	d_c	
30°C	13.55	EYL [181]
30°C	13.55	DOPC [181]
2°C	16.0 ± 0.2	POPC [175]
50°C	12.8 ± 0.6	POPC [175]
75°C	15.4 ± 0.2	POPC [175]
30°C	13.6	POPC [182]
50°C	14.6	DPPC [180]

Table 8.1: Literature values for the hydrocarbon chain length d_c.

In McIntosh *et al.* [189] the effect of cholesterol, which is the building block of bile salt, on the structural changes on various phosphatidylcholine aggregates with different chain length, i.e. 12 of DLPC, 14 of DMPC and 16 DPPC, was investigated. They found that cholesterol increases the bilayer width due to the removal of the chain tilt in these mixed aggregates. In a further study [190] the influence of cholesterol in EYL on the bilayer separation under pressure was investigated with SAXS. These profiles although under higher pressure indicate that the incorporation of cholesterol into EYL multilayers increased the distance across the bilayer between the head-group peaks also. In both studies the electron density of the methylene chain region relative to the terminal methyl group was increased [190]. In all these studies cholesterol sits in distance of 8-18Å from the bilayer center. Although cholesterol is a hydrophobic molecule and not a detergent as bile salt, both molecules could still have a similar influence on the mixed aggregates, since bile salts could also hydrophilically associate and would then behave similarly to cholesterol. But this is one possible scenario amongst others, which cannot be proofed with the information obtained so far in this thesis.

Another scenario for the identification of the second peak could be, that bile salt dimers or oligomers sit at the surface of the membrane [191]. Since the self-aggregation of the bile salt monomers is regarded less likely then the hydrophilic or hydrophobic contact to the lipid, they are supposed to initially bind hydrophilically to the membrane surface and then hydrophobically to each another. Rodlike micelles of the bile salt cholate have been observed to grow out of PC membranes under non-equilibrium conditions by cryo-TEM studies [192].

Dependence on Temperature

A few examples for the SAXS scattering pattern will be shown for some temperatures. The temperatures were measured every degree from T=25°C to T=40°C. The scattering pattern throughout the whole "viscous" part does not change significantly with dilution and salt

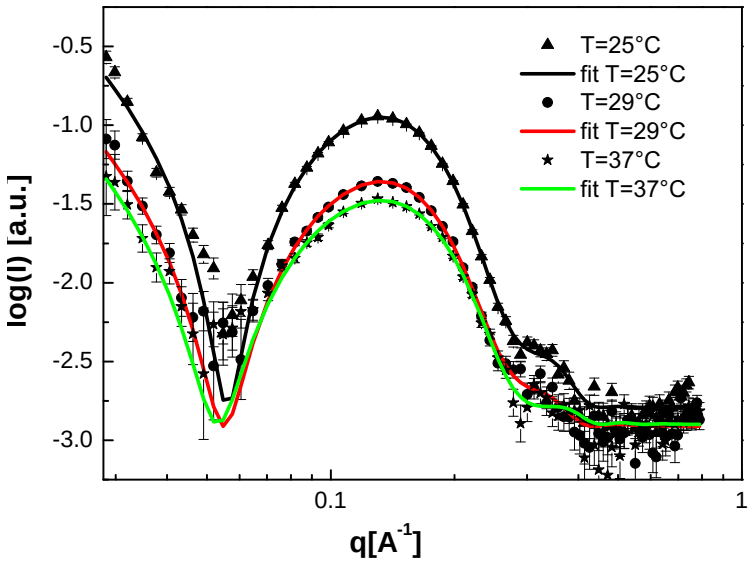

Figure 8.5: Scattering intensity I(q) as function of scattering vector q as determined by SAXS for a sample with dilution d=30 at c_s=400 mM at different temperatures T=25°C, 29°C and 37°C.

concentration and also not with temperature (fig. 8.5). The temperature scans of the samples with d=30, c_s=400 mM; d=50, c_s=500 mM; d=50, c_s=900 mM, d=60, c_s=900 mM and d=80, c_s=1000 mM have been performed. For the latter (d=80, c_s=1000 mM) the temperature was only measured up to T=32°C.

In figure 8.5 the scattering pattern of d=30, c_s=400 mM is shown for three temperatures. It can be seen that the scattering intensity decreases with increasing temperature. The solid line are the fits based on the Gaussian Deconvolution model using a series of seven Gaussians and a fixed z_{max}=50 Å. The model gives a good fit for the entire q-range.

In all measurements of the scattered intensity a broad peak appears as before in the interval 0.055 $\text{Å}^{-1} \leq q \leq 0.3\ \text{Å}^{-1}$ followed by a small hump. In Pabst *et al.* [175] three Bragg peaks appear in the scattering curve (at T=2°C), where the first two peaks scatter in the same q-regime as the broad peak here and a third at the position of the small hump. By increasing the temperature to T=50°C, the third peak disappears due to the thermal fluctuations. Also in this measurement the hump in the position of the third peaks gets smeared out (figure 8.5).

The electron density profiles of the same sample can be seen in figure 8.6 for all examined temperatures. With increasing temperature the electron density profile smoothly smears out, but the changes are small. It is strongest in the temperature range T=25°C to 32°C, and for

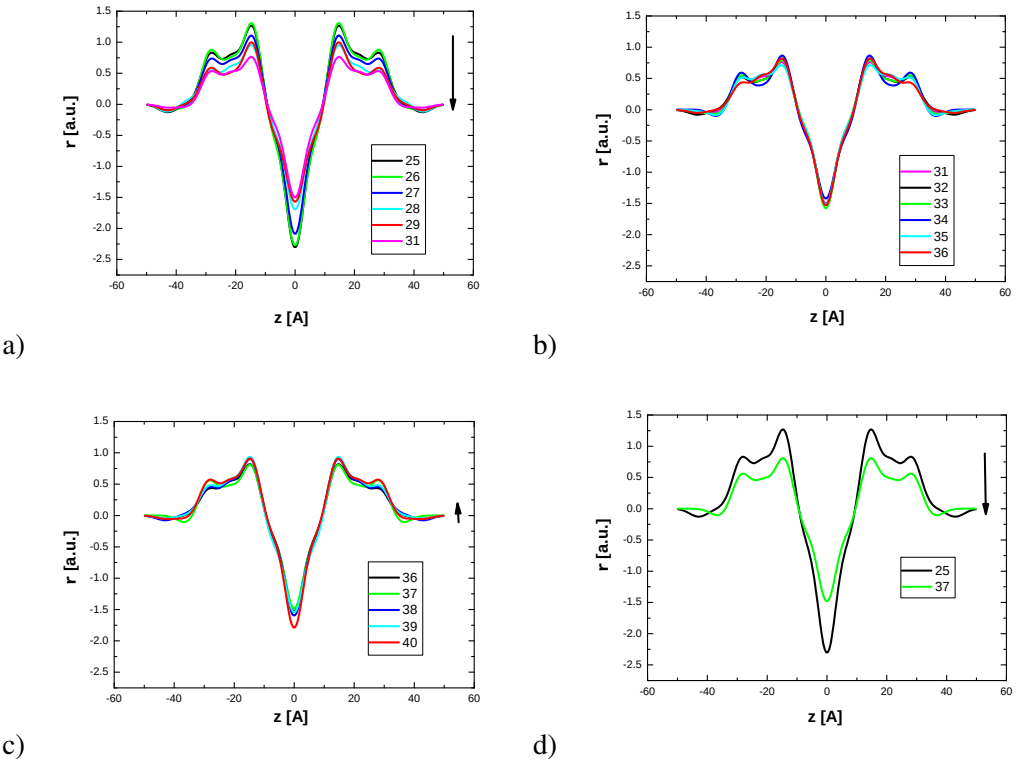

Figure 8.6: Electron density $\rho(z)$ for the sample with dilution d=30 and salt concentration c_s=400 mM for different temperature T. The arrows show the increase in T.

T=32°C the electron density profile seems to increase only slightly. The position of the first peak z_i does not change with temperature and is summarised together with the FWHM σ_i in table 8.2 for two representative temperatures.

For the samples with the next higher salt concentration (dilution d=50 at c_s=500 mM and c_s=900 mM), the temperature dependence shows a similar behaviour, where the scattered intensity first decreases ad from T=25°C to T=30°C and then increases again for T$\geq$35°C. This is particularly pronounced for d=50 at c_s=900 mM, where at T=37°C the intensity reaches again a similar level as for T=25°C (fig. 8.8 a,b). The small hump after the broad peak smoothes out with increasing temperature. Analogously the electron density profile decreases with increasing temperature and then increases again between T=34°C and 38°C and then stays constant (figures 8.7, 8.8 and 8.9).

It seems that the NaTCDC/EYL samples of the "viscous" phase undergo a temperature dependent transition above T=30°C, since the decreased scattered intensity increases again. Only four samples were measured, where the temperature was increased up to T=40°C, but all

peak distance	**NaTCDC/EYL**	
	25°C	37°C
z_{tail}	0 (fixed)	0
z_{H_1}	14.8 ± 0.0	13.9 ± 0.02
z_{H_2}	29.0 ± 0.0	29.0 ± 0.01
z_{CH_2}	42.0 ± 0.2	34.8 ± 0.3
σ_{H_1}	3.0 ± 0.0	3.1 ± 0.0
σ_{H_2}	2.5 ± 0.1	2.7 ± 0.0
σ_{CH_2}	4.7 ± 0.4	4.9 ± 0.4

Table 8.2: Peak positions z_i and the FWHM of the peak σ_i for a sample with d=30 and c_s=400 mM.

of them displays this behaviour weakly for lower salt concentration and stronger for the sample d=50, c_s=500 mM.

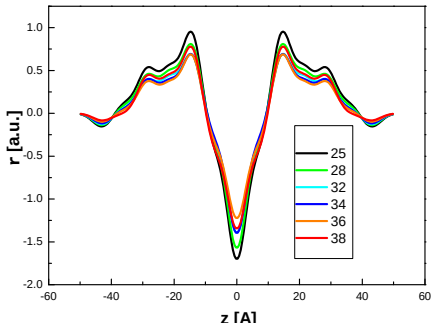

Figure 8.7: Electron density profile $\rho(z)$ as a function of position z within the bilayer for the sample with dilution d=50 and c_s=500mM from the "viscous" phase for increasing temperature.

In the case of d=60 and c_s=900 mM the increase is small and observed towards T=40°C (fig. 8.9).
But definitely further experiments are needed, where the focus of the measurement is set upon the temperature dependence, to have a more complete set with respect to ionic strength and dilution.

8.2.2 Results and Discussion for NaTC/EYL

NaTC is a trihydroxy bile salt and more soluble than the dihydroxy NaTCDC bile salt and thus has a larger *cmc*. The phase boundaries of the NaTC/EYL system shift towards lower dilutions due to the higher solubility.

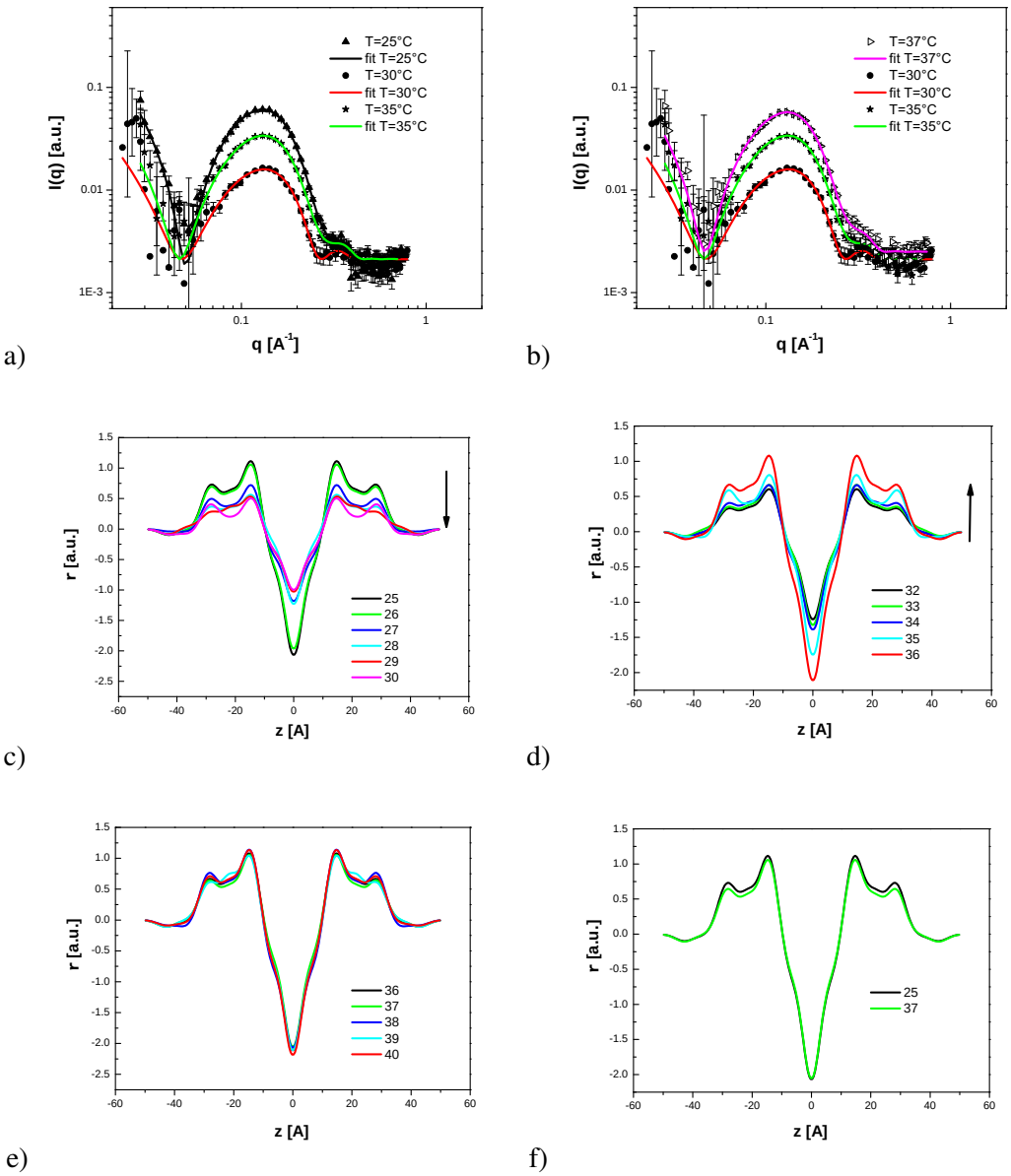

Figure 8.8: Scattering intensity I(q) as function of scattering vector q as determined by SAXS for a sample with dilution d=50 and c_s=900 mM at different temperatures T=25°C, 30°C to 35°C in a) and for the temperatures 30°C, 35°C and T=37°C in b). The results of the fits for the Gaussian deconvolution with a series of 7 Gaussians are shown as the straight lines. Parts c)-f) shows the electron density profile $\rho(z)$ for different temperatures as indicated in the legend. f) shows a direct comparison of T=25°C and T=37°C

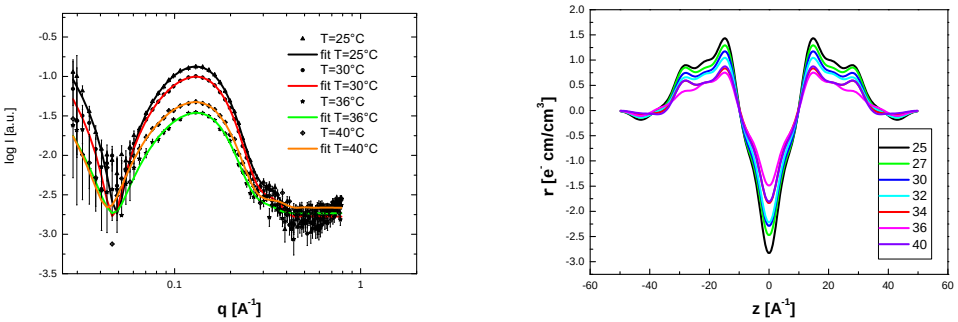

a) b)

Figure 8.9: a) Scattering intensity I(q) as function of scattering vector q as determined by SAXS for a sample with dilution d=60 at c_s=900mM at different temperature from T=25°C, 30°C, 36°C and 40°C. Part b) shows the electron density profile $\rho(z)$ for different temperatures as indicated.

Similar scattering intensities I(q) are obtained as before, the electron density profile $\rho(z)$ was fitted using a series of seven Gaussians, but the bilayer thickness could not be fixed to 50Å but needed to be increased to 60Å for a sufficiently good fit with a χ^2 between 1 and 2.

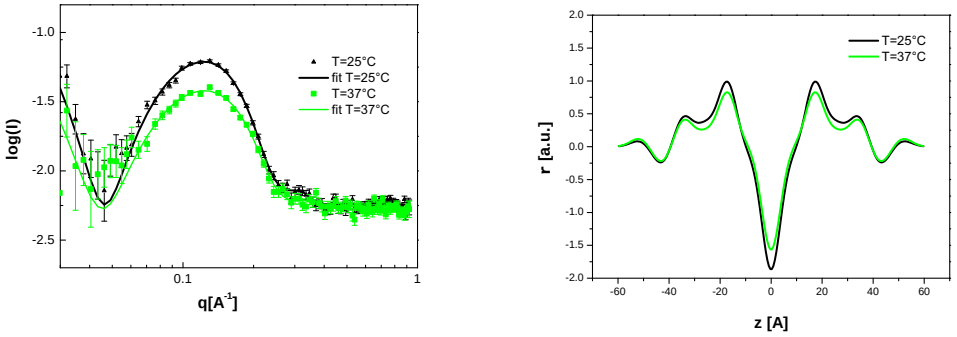

a) b)

Figure 8.10: a) Scattering intensity I(q) as function of scattering vector q as determined by SAXS for of a mixed NaTC/EYL sample with dilution d=30 at c_s=1400 mM at different temperature from T=25°C and 37°C . Part b) shows the electron density profile $\rho(z)$ for different temperatures as indicated. Sample d=30 and $c_s = 1400$mM .

The second scenario given above for the identification of the second peak, i.e. bile salt lying flat on the surface, fits well with our observations for NaTC/EYL mixtures, that bilayer width are larger for NaTC than for NaTCDC. Since it is known, that dihydroxy bile salt has a higher binding strength to EYL membranes than the more hydrophilic dihydroxy bile salts [193].

peak distances	NaC/EYL 25°C	37°C
z_{H_1}	17.10 ± 0.00	17.70 ± 0.02
z_{H_2}	33.30 ± 0.00	33.90 ± 0.01
z_{CH_2}	43.49 ± 0.15	42.92 ± 0.33
σ_{H_1}	3.3 ± 0.1	3.4 ± 0.0
σ_{H_2}	2.7 ± 0.1	2.9 ± 0.0
σ_{CH_2}	4.8 ± 0.3	5.1 ± 0.4

Table 8.3: Peak positions z_i and the FWHM of the peak σ_i for a sample with d=20 and c_s=1800 mM.

8.3 Discussion

The Gaussian deconvolution programme was used for the analysis. Fits to the SAXS data agree very well with our underlying assumption, that we have infinitely extended bilayer structures. Prior to this fit various other possible models also programmed by Jan Skov Pedersen and his group in Århus, have been tried out, but did not fit the data sufficiently well as the chosen model. The first trial was based on the model proposed by Wiener et al. [173, 174] and further developed by Pabst et al. [175] with an electron density profile as in equation 8.8 and introduced in chapter 8.1.2. For this model a good set of starting parameters are required as the sign and position of the phases, i.e. to calculate the "raw" electron density profile, which can be obtained by a Fourier synthesis of the different orders of reflection in an x-ray scattering experiment. This "raw" electron density profile is then fitted with the electron density profile as described in eq. 8.8. This model is based on the model by Pabst et al. [175] mixed with the deconvolution model using step functions developed by Glatter [194, 195]. This has the advantage to avoid any assumptions on the starting values for the coefficients of the step functions. So no a priori information is needed, except its symmetry, for instance lamellar in our case.

In the used model the distance of the first peak agrees well with the expected hydrocarbon chain length of pure EYL bilayers. It is furthermore consistent with other studies on and with other phospholipids with a similar amount of hydrocarbon chains. This indicates that the model is appropriate. However, a physical reason for the second hump in the electron density profile could not be found. One hypothesis has been outlined: bile salt sits in the membrane and pushes the phospholipid headgroups out. This hypothesis is consistent with the fact, that the bilayer width increases for a more soluble bile salt (NaTC), which is reported to have a lower binding strength to the membrane. The change of bile salt, was the only parameter, which affected the electron density profile significantly. In contrast temperature and salt concentration seem to have no impact on the structures formed in the "viscous" phase. This was unexpected prior to

the measurement.

Various scenarios are consistent with the results obtained by SAXS study: Lamellar stacking, open vesicles with perforation, extended bilayer sheets with holes, disordered bilayer in a network, micelles growing on the surface of the bilayer structures. Now these scenarios are discussed in turn.

In Leng *et al.* [60] a lamellar stacking was predicted to occur during the micelle-to-vesicle transition under specific conditions. This kinetic model describes an initial rapid formation of disklike intermediate micelles, a growth of these micelles by coalescence and the closure of the micelles to form vesicles. It was furthermore suggested that at high salt concentrations, where the van der Waals attraction between parallel discs dominates over electrostatic repulsion, the vesicle closing process becomes slower than stacking of large disklike micelles. By increasing the salt concentration c_s the disklike micelles can grow bigger before the event of closure or stay unclosed. For a big enough line tension the closure to vesicles could happen more easily and happens for low salt concentration as it was found in numerous studies [46, 160, 196, 44] and also observed for c_s $\leq$300 mM in the SANS experiments (chapter 7). At higher salt concentration the event of closure could still happen, but the radii after a further growth might result in large vesicles, as remarked earlier, larger than the length scale observed in our SANS experiments.
Without closure, this could lead to the formation of lamellar phase instead of vesicles [60]. In the SANS experiments at high salt concentration ($c_s = 1000$ mM), the typical features of the micelle-to-vesicle transition are lost while large objects seem to be present in the "two-phase" region. Therefore the analysis of the SAXS data was performed for infinitely extended bilayer structures with cross-sectional profile. In the SAXS experiments of the "viscous" phase at high c_s, the typical scattering pattern for a stacked lamellar phase, where various diffraction peaks would appear, was not observed. Although an unilamellar extended sheet with cross-sectional profile is fitted, this does not mean, that there is no lattice order at all. A few stacked lamellar sheets would still not give ordered Bragg peaks, which would allow to "see" a well-developed structure factor.

The lamellar phase is a very common form of self-aggregation especially for long-tailed amphiphiles [1]. In the Luzzati description, i.e. the classical picture of stacked bilayers, these bilayers are undisrupted and contain solvent in between the individual bilayers (in section 8.1). This idea gets progressively revised since strongly undulated bilayers and bilayers with defects are found. Nowadays defective or perforated lamellar structures have attracted a growing interest and were observed in cryo-TEM studies [192, 197].
Previously it was neglected that membranes could spontaneously form holes, but Betterton

and Brenner [198] show this in a simple model of a charged membrane. It was motivated by stable holes in human red blood cell ghosts [199, 200], where the size of holes depends on the salt concentration of the surrounding solvent [200]. Furthermore is was observed that the vesiculation process is often preceeded by the stable holes in the membrane [200].

If at higher ionic strength c_s the membranes that grow upon coalescence close to form large vesicles outside the length scale observed with SANS, then one could imagine a scenario where holes are formed. Upon dilution, the growth of the disclike micelles by bile salt removal is initiated, but at higher c_s this is less pronounced. Vesicles could form as for low salt concentration, i.e. below c_s =250 mM, but might be non-equilibrium structures, since bile salt monomers or micelles from bulk could bind initially symmetrically, later also asymmetrically to the vesicles. It is known, that above a critical bile salt content, the stress on membranes are high due to the asymmetric binding [191] of the bile salt to the outer bilayer and very low rates of transbilayer movement (known as flip-flop rates) [201]. Together this could lead to the formation of transient holes, even for bilayers in an aggregate rich samples.
Next to the hydrophobic and hydrophilic reasons for aggregation and membrane reconstitution, there is also the influence due to the electrostatic repulsion on the bilayer. With increased bile salt content in the bilayer, especially at the edges, membranes favours the creation and maybe expansion of holes, despite the cost of energy due to unfavorable hydrocarbon/water interface. Another factor is the line tension, which is the energy per unit length of the rim of the membrane. The hole costs energy, since the edge of the membrane is exposed. The adsorption of bile salt on the rim by increasing the ionic strength, results in a reduced line tension and in a increase in closure time [59]. Closure becomes energetically unfavourable [198] when the Debye screening length κ_D of the electron screening "cloud" around the membrane is lower than the size of the hole.
In this scenario more and more bile salt monomers need to share increasingly less lipids. In Schubert *et al* [193] it is pictured that high bile salt which is sitting on the membrane surface suddenly folds over into the vesicles in a solubilsation process during which bilayer holes are transiently formed.

Another, although non-equilibrium structures have been found for bile salt/EYL systems in the cryo-TEM study of Walter *et al.* [192], where micelles grow out of the surface of the bilayer structures and vesicles, which also might be a possibility, maybe even as an equilibrated structure.

The nature of the "viscous" phase or the structures existing in the "two-phase" region cannot be unambiguously answered with the data obtained here. One can only hypothesise as done. With a combination of further scattering experiment and imaging methods some questions on

the structural changes of the mixed aggregates at higher salt concentration, which were started in this, thesis might be resolved. Imaging methods have been already applied to lipid-detergent mixtures. In the following, these methods will be closely compared to the results obtained in the previous two chapters to strengthen the hypothesis made.

8.4 Conclusion

It was found that the structure of the "viscous" phase throughout the two-phase region is independent of the salt concentration, dilution and temperature (in the range observed). This has been modeled by infinitely extended bilayer sheets with a cross-sectional electron density profile.

Speculations about the nature of the "viscous" phase have been made where at high salt concentration a rapid growth process of intermediate disklike structures leads to the formation as bilayer sheets or maybe large vesicles

Chapter 9

How do All These Measurements come Together?

Several different techniques, microcalorimetry, light, x-ray and neutron scattering, have been used to investigate the phase behaviour and structural changes of the bile salt/EYL system under increasing salt concentration. But what greater picture underlies the results obtained in each of the studies?

Starting from the microcalorimetry (chapter 6): The solubilisation line obtained to determine the phase boundaries of the c_s=100 mM line yielded exactly the same result as a previous study (as it can be seen in table 6.7), where the micellar size upon dilution was measured and the phase boundary between the micelles and micelle/vesicle coexistence was obtained [61]. As expected in the solubilisation process, i.e. vesicle-to-micelle transition and in the reverse direction of diluting the mixed aggregates to induce a transition from micelles to vesicles, the phase boundary was found to be the same.

Also the recalculation of the solubilisation phase diagram for various ionic strength back into the dilution d versus ionic strength c_s illustration, which is generally used in the phase diagram investigated in dilution-dependent scattering experiments, a good agreement between prior measurement especially at lower ionic strength was found.

The composition of the aggregates in various regime of the phase diagram was quantified, especially the increase of bile salt molecules with increasing salt concentration. These values of R_e at the saturation and solubilisation line as determined by calorimetry, were used for the contrast $\Delta\rho$ of SANS data fitting with the appropriate model (chapter 7) or for the bulk density ϱ_D to compare the fitted results of the molar mass to the calculated molar mass from volume and bulk density of the aggregate. The comparison clearly shows that the calculation and the

analysis of the SANS data is consistent with respect to the composition of the aggregates. Furthermore from the composition of the aggregates the surface potential is calculated, from which the electrostatic energy Ψ was deduced as a function of the salt concentration. This measured result also agrees very well to the electrostatic energy calculated for the composition of aggregates in the framework of a kinetic model [59].
The compositions where macroscopically two phases were observed coincides with the appearance of large structures in the SANS measurement, although only the "non-viscous" phase was investigated (fig. 7.13). The SANS results are consistent with light scattering experiments. A further comparison of the light scattering results with previous light scattering experiments, where a pronounced growth with increasing salt concentration was observed when a sample from the "two-phase" region was measured [59], showed a good agreement (figure 7.12).

The "viscous" phase, which is aggregate rich, was investigated with the x-ray scattering experiments. The results of the solubilisation studies quantified the increasing number of bile salt molecules in the mixed aggregates by increasing the salt concentration, which resulted in increasing curvature, increasing flexibility of the membrane, decrease of line tension, increasing charge density, increasing surface potential. In a kinetic "picture" of the micelle-to-vesicle transition [59] increasing of c_s yields a further growth of the disklike micelles due to the screening, and the reduced line tension leads to an increase of the closure time. If closure would happen, then these vesicles would be larger than those previously observed. And if closure does not happen, this would result in bilayer sheets. This is consistent with the SANS results, which showed that the size is outside the lengthscale of the measured q-range.

This increased amount of bile salt and its possible consequences consistently fits to the analysis performed on the x-ray scattering data of an infinitely extended bilayer sheet. In the discussion of the last chapter some possible structures existing in the "viscous" phase have been introduced. A way to obtain further information on the nature of the structures would be by using imaging techniques, which have already been widely applied on similar mixed systems of lipids with detergents. Also pictures were taken that show multilamellar aggregates, open vesicles with perforation, extended bilayer sheets with holes and disordered bilayers in a network, all in equilibrium. Also unstable structures as micelles growing on the surface of the bilayer structures were observed under non-equilibrium conditions.

Vesicles with holes were also found for EYL mixed with the bile salt cholate in 100 mM NaCl solution and neutral pH by Walter *et al.* [192] in cryo-TEM pictures of a non-equilibrium system. Although the reverse process, the solubilisation of vesicles was observed, it was shown that detergent addition altered the diameter of the vesicles from (400-600) Å to (300-800) Å.

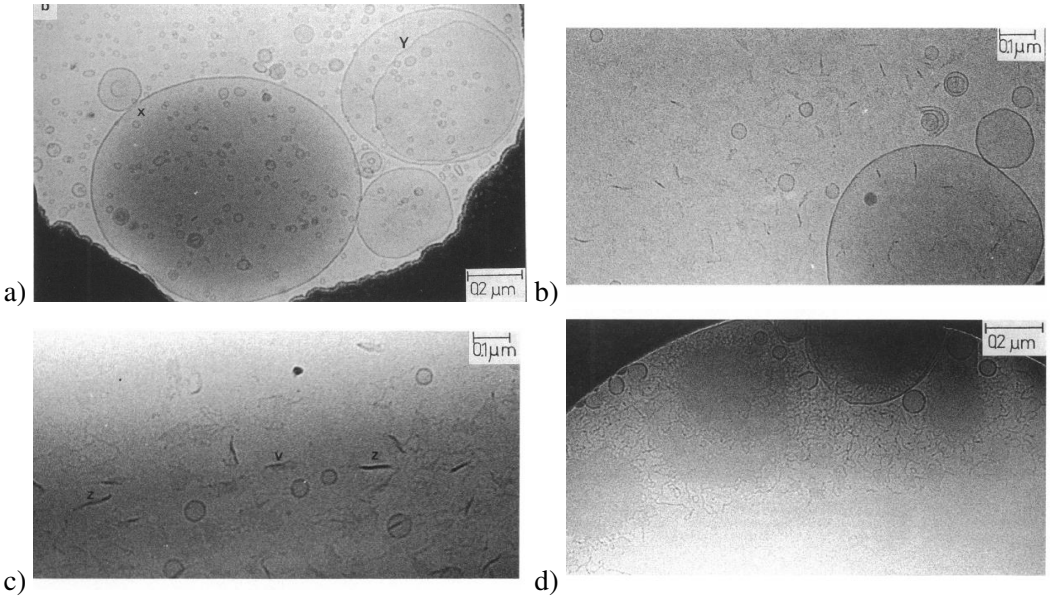

Figure 9.1: Cryo TEM picture of a mixture of EYL (9 mM) and cholate (6 mM) that was prepared by adding chlolate to sonicated lipid vesicles. Some exceptionally large vesicles coexist with smaller vesicles similar to those observed. The vesicle at x appears to be open and the bilayer at Y is rippled in such a way as to indicate that the normal bilayer structure is perturbed. (b) Large vesicles coexist with short dense projections and en face views of pieces of bilayer. Some of the vesicles appear to have openings (6 mM cholate, 9 mM EYL). (c) Vesicles and patches of bilayer seen on edge indicated by z and en face. The structure at v appears to be a twisted piece of bilayer as indicated by a linear electron-dense region appearing to unfurl into a piece of bilayer. The projections emerging from the patches appear to be the origin of cylindrical mixed micelles (7.25 mM cholate, 9 mM EYL). (d) Large patches of membrane with many cylindrical mixed micelles emerging from the edges simultaneously (6.5 mM cholate, 9 mM EYL) All from ref. [192].

Only little more addition of cholate changed the morphology completely, i.e. the small sized vesicles coexisted with large, open or perforated vesicles, which afterwards relaxed to sheets (figure 9.1 a). In b) dense linear projections of single lipid bilayers and long flexible cylinder structures coexisted with open vesicles in a wide range of cholate concentration [192]. In c) it is shown, that these dense structures are patches of bilayer membrane (labeled Z) compared to the oblique view (labeled V) of the same structure. With even higher detergent concentration, cylindrical mixed micelles start to grow out of the outer bilayer surface of the perforated vesicle or bilayer sheet (see figure 9.1 d) especially from the edges, where it is presumed, that the bile salt stabilises the rims by a higher concentration than in the central part of the aggregate [43, 60], before disintegrating into mixed micelles from a network of bilayer sheets. This happens in a very narrow “tongue” in the phase diagram of bile salt concentration versus EYL concentration at physiological conditions, i.e. lower electrolyte concentration.

Although the preparation of the mixed EYL/bile salt sample in this study [192] differs from our preparation method and obviously a reverse way has been gone, i.e. the vesicle-to-micelle transition, after a first pore formation at the vesicular bilayer, membrane patches, i.e. parts of the vesicular bilayer, have been found. This corresponds well to our model of extended lamellar sheets, since lamellar sheets are nothing but bilayers, where the cross-sectional length is much smaller then the extension [192] and is thus in accordance with the proposed model. The limit in the phase diagram, where open vesicles and bilayer sheets coexist with mixed micelles, is very narrow in the study of Walter *et al.* [192]. But by increasing the salt concentration, decreasing the electrostatic repulsion, more bile salt is in the aggregates as found in the microcalorimetry studies. More detergent concentration, i.e. cholate concentration, increases the curvature of the aggregate. After the solubilisation into micelles by further increasing the cholate concentration which can be seen in [192], the micelles become more flexible and can bend in three dimension. This can also be seen in the fitting of the SANS data of c_s=1000 mM, where the Kuhn length decreased with increasing salt concentration from 400 Å down to 50 Å. The proposed lamellar stacking in Leng *et al.* [60] gives way to flexible lamellar sheets.

If we compare the sizes of the vesicles observed in [192], they correspond well with the results of chapter 7. The radii in the purely vesicular region ranged between 120-250 Å, which corresponds well to the diameter of 300-800Å of the vesicles found at c_s=300 mM (which is similarly sized again as the system is under physiological condition). Just at the boundary, the narrow "tongue", the size increased up to 750 Å [192]. Vesicular structures much bigger then 1000 Å are not in the experimental window of the SANS experiment. At higher salt concentration only large structures coexist with the fitted wormlike micelles. This corresponds well with the result of [192], where also little wormlike micelles coexist with the huge perforated vesicle structure or bilayer sheets. It was also observed that wormlike micelles grow out of bilayer structures.

An EYL system with a alkyl sulfate detergent with varying chain length ($C_{10}SO_4^-$, $C_{12}SO_4^-$ and $C_{14}SO_4^-$) has been investigated [202]. The samples were equilibrated for 6 to 7 days prior to the measurement. Intermediate structures are referred as the aggregates formed during the vesicle-to-micelle transition. For short chained surfactants as $C_{10}SO_4^-$ a coexistence between vesicles composed of normal lamellar (L_α) phase and thread-like micelles were observed whereas during solubilisation of $C_{12}SO_4^-$ and $C_{14}SO_4^-$ presumably vesicles, open sheets, composed of what appears to be holey bilayers coexisted (figure 9.2) (a) and (b)). After 7 days the closed, vesicle like structures of fig. 9.2 (b) are broken into small fragments with time, but still with the characteristic holey appearance [202]. For the $C_{14}SO_4^-$ chained surfactant a similar transition is observed as it can be seen in fig. 9.2 (d) and (e). First open and holey vesicles (d) and by

further addition of surfactant flat fragments composed of a perforated or holey lamellar phase (e) with the occasional appearance of some extremely long cylindrical micelles. It is interesting to note that the intermediate structures in this system have been found at physiological salt concentration, i.e. 150 mM, but by lowering down the salt concentration, the holey lamellar phase was no longer observed in the higher chained surfactants [202].

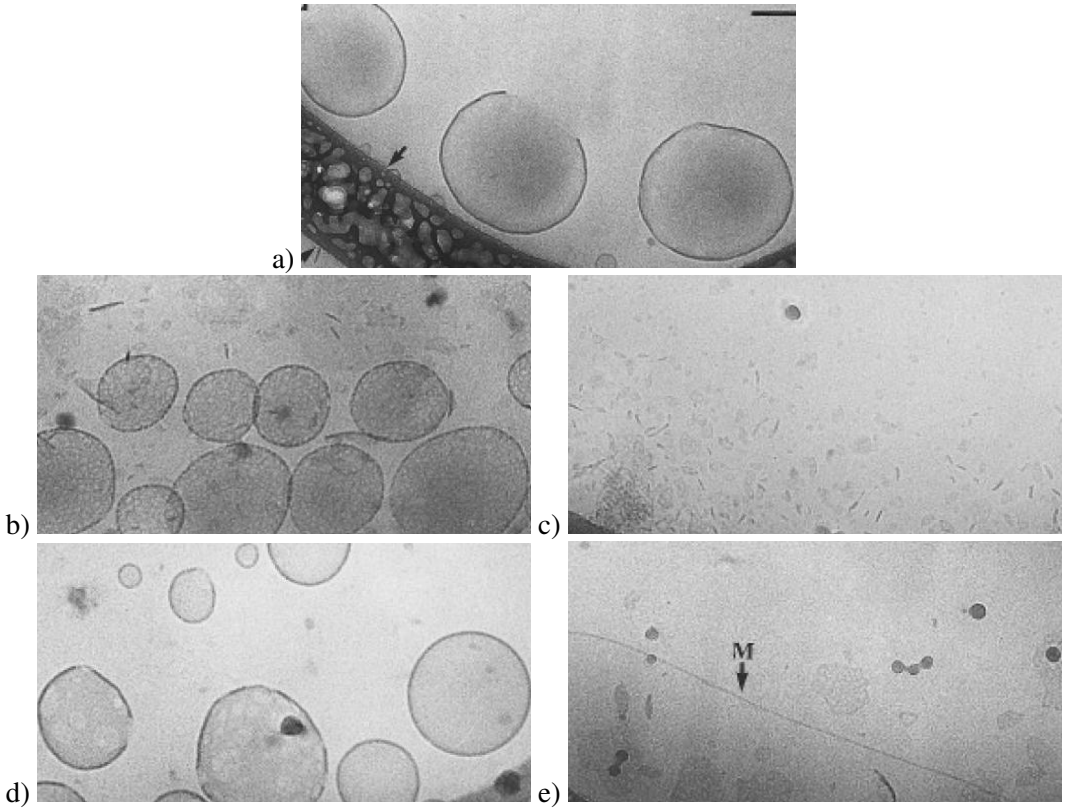

Figure 9.2: Cryo TEM picture of a mixture of EYL and alkyl sulfate surfactants in buffer containing 150 mM NaCl. (a) [$C_{14}SO_4^-$]/[EYL] = 4.5, 7 days after preparation (b) Further intermediate structure formed during the vesicle-to-micelle transition of $C_{12}SO_4^-$ with [$C_{12}SO_4^-$]/[EYL]=4.0, 24 h after preparation; (c) [$C_{12}SO_4^-$]/[EYL]=4.0, 7 days after preparation. (d) [$C_{14}SO_4^-$]/[EYL]=5.0; (e) [$C_{14}SO_4^-$]/[EYL]= 7.0. All from ref. [202]. Bar=100nm.

Although bile salt with its more or less nonexistent tail is difficult to compare with alkyl sulfate surfactants, it has been clearly shown that geometrical packing constraints and salt concentration are very important. Maybe detergents with higher curvature can induce this type of intermediate structures only at higher salt concentration. Unfortunately salt concentration above 150 mM were not studied in [202]. In many other cryo-TEM studies the aggregational structure in systems containing lipid vesicles and a number of surfactants have been observed, such as the octyl glucoside and octaethylene glycol-n-dodecyl monoether [197], $C_{12}E_8$ [203]

and the ones previously mentioned. In these systems the transition has been observed to proceed through a region of coexistence between open vesicles and/or lamellar sheets and long thread-like cylindrical micelles.

As we propose the holey or perforated bilayer structures for bile salt/lipid systems, Ollivon et al. [35] proposed this scenario for the micelle-to-vesicle transition in EYL-octyl glucoside mixtures. As here, they had a bulk phase separation of a lower viscous phase in H_2O and higher non-viscous phase. They suggested a solubilisation scheme, that vesicles of this system initially swell, then open and break into long sheets. During this breakage the sheets are supposed to have large holes, then they transform into micelles. Later this scheme was visualised by cryo-TEM studies, for the solubilisation process, where of non-equilibrated, intermediate structures were investigated [197].

Chapter 10

Summary and Outlook

In this last chapter the main results of this thesis will be summarised and suggestions for future experiments given. The thesis was focused on the study of EYL/bile salt systems in aqueous solutions at higher salt concentration to tie in with the well-known phase behaviour of this mixed system under physiological conditions (150 mM NaCl concentration, neutral pH)[41, 54]. Whereas the phase boundaries are well-known, there is still ongoing debate about the structural changes and the composition of the aggregates.

10.1 Summary

Numerous studies have been performed on the important biological model system of a lipid aggregating together with bile salts, but still a lot of questions are unresolved. Nature is still many steps ahead. The body produces giant unilamellar vesicles by a mixture of lipids with bile salts, which cannot be reproduced in the laboratories. The transitional process leading from micelles to vesicles and the details of the aggregational composition need to be understood in order to find the right pathway to achieve for instance giant unilamellar vesicles of EYL/bile salt system. Introducing higher salt concentration to the dilution dependent transitional pathways of this system, changes the generated structures completely from those observed under physiological conditions. This is the main focus of this thesis.

In the beginning, we wanted to observe the pathways of the transition process with a controlled knowledge of the bile salt concentration in bulk and in the aggregate. The electrochemical studies showed us, that at some point the bile salt control might be possible, since it is proposed that the outer layer of a (PNMP/bile salt) film can release the bile salt anions, which were incorporated during film formation. But for the follow-up experiments to investigate the micelle-to-vesicle transition, as aimed at this study, this was not sufficient. The produced polymer film could only be used once and unfortunately had no long-term stability to be able

to prepare various films in order to use them for subsequent experiments.

The rest of the thesis deals with the influence of the higher salt concentration for the phase diagram of the EYL/bile salt mixtures and the structure of the aggregates in the various phases as already stated. The initial observation was a phase separation of the sample into a “viscous” and a “non-viscous” phase starting at an ionic strength of about 300 mM NaCl concentration and higher and over a broad range of dilutions for the NaTCDC/EYL system. The NaTC/EYL lecithin had a observable phase separation from 1200 mM to 1900 mM NaCl concentration. The main system of this study are NaTCDC/EYL mixtures, where either the whole sample was investigated in the microcalorimetry studies, the mostly “non-viscous” sample in the SANS and LS studies and the ”viscous” precipitate was investigated in the SAXS measurements.

With ITC two types of experiments were performed, a demicellisation of NaTCDC aggregates to measure the influence of increasing the salt concentration on the *cmc* and a solubilisation experiment of the mixed system to obtain the phase boundaries. The *cmc* decreases with increasing salt concentration, since the energy barrier of the electrostatic repulsion of bile salt anions decreases. The same can be observed in the mixed system of the same bile salt with EYL. With increasing ionic strength the aggregates are able to incorporate more bile salt. The solubilisation boundary at physiological condition fitted very well to previous results [61].

By recalculating the solubilisation phase diagram for various salt concentration back into the dilution d versus salt concentration c_s representation, good agreement between prior measurement at lower salt concentration was found, although the reverse process by detergent solubilisation was measured. In the last chapter the complementarity of the microcalorimetry and scattering results were discussed. Although no evident conclusion could be given on the nature of the structures in the “two-phase” region, extended bilayers or even huge vesicles might exist, which would bring us closer to the giant unilamellar structures observed in nature.

In the last chapter a discussion of the results of the last three experimental techniques have been given, which can be summarised by:

- In both “viscous” and “non-viscous” phases the appearance of large aggregates can be observed in the “two-phase” region. To the SANS data (chapter 7) a structure could not be fitted, since they were larger than the observed length-scale.
- The investigations using SAXS of the “viscous” phase showed that the structures do not vary much within the “two-phase” region. All data ware by a model of extended bilayer sheets (chapter 8.3 and 9), but further investigations are needed to support the model, which will be discussed in the next chapter.

- Outside the "two-phase" region, the known micelle-to-vesicle transition could be observed upon dilution, but with increasing salt concentration c_s the coexistence phase, where vesicles coexist with micellar aggregates, seems to be in a broader range of dilutions, which could be seen by the microcalorimetry experiments (figure 6.14) too, although with a high error in the measurements, and with the SANS experiments (section 7.2).

10.2 Outlook

There are various ways to continue the research on this interesting biological model system. Although it was not attempted in this thesis, but a deeper understanding of the self-assembly of bile salt or bile salt mixture on their own, might help to understand the nature of the aggregational behaviour of mixed systems. Bile salt is an unusual amphiphile due to its molecular architecture and all the possible properties arising from that. Bile salt forms gels at higher ionic strength.

Lamellar structures formed by lipids alone have been studies extensively and helped us to understand the mixed system of bile salt/lecithin. But unfortunately little is known about the micellisation behaviour of bile salt alone. For instance, about the proposed two stage aggregation, its micellar aggregation numbers and especially the structures of bile salt micelles plus the nature of the driving forces of the aggregation process (hydrogen bonding or hydrophobic interactions). (See Chapter 1.2).

Especially the intermediate structures formed might differ to classical head-tail detergents, since it has been observed with cryo-TEM that the alkyl chain length has a strong influences on the structures formed during the micelle-to-vesicle transition [202]. Short alkyl chain surfactants mixed with EYL formed open or closed vesicles coexisting with cylindrical micelles and end up in cylindrical micelle networks, whereas longer chained surfactant form holey lamellar structures before decomposing into mixed micellar structures.

Although, a bile salt exchanging film was not found suitable for the experiments aimed in the framework of the thesis, nevertheless a (PNMP/bile salt) film with an inner and an the outer layer was found, where the outer film is able to eject anions. The research in the field of microarray electrodes evolved very fast in the last decade. Microarrays with a high surface area could be designed, which can release a sufficient number of bile salt anions out of the outer layer of a (PNMP/bile salt) film.

Also the QCM technique, which was used to simultaneously measure with the electrochemical

methods, could be used on its own. The QCM used for the thesis was not sensitive enough to perform the experiment, which was planned in the framework of this thesis, but not tried out. Bile salt concentrations in medical laboratories are still measured with HPLC methods, which is time consuming. A sensing device with a fast response to bile salt concentration might be the answer. And instead of bile salt anion concentration control, a sensing could be attempted using the QCM technique. Since the dilution dependent transition of our bile salt/EYL system is based on the removal of bile salt from the aggregates into the bulk solution, this concentration change could be sensed with a fast enough responding device. Chance *et. al.* [204] built a novel chemical sensor for bile acids. A sensitive QCM crystal is coated with cholestyramine resin, which is known to bind to bile acids. Cholestyramine is used in pharmaceutical drugs to decrease the cholesterol concentration in the metabolism, since it binds to bile salt, which then does not get reabsorbed in the enterohepatic cycle. It is claimed, that the cholestyramine resin coated piezoelectric crystal has a detection limit in water in the range of 0.2-9 nmol and can be reused up to 400 times. If a similar sensor would work as claimed, it would be an ideal experimental method to observe the bile salt concentration change in bulk during the dilution steps.

Only one molar ratio of EYL/bile salt mixtures was used in the microcalorimetry studies. This was one of the reasons, why the error bar for the boundary at higher salt concentrations was relatively high, since the sample was already close to saturation or even solubilisation boundary. But this problem can be overcome by starting with various molar ratios of the mixed aggregates. The microcalorimetry study performed here gives an optimal starting point for a more detailed determination of the phase boundaries at higher salt concentration.

To tie the SANS study with the SAXS study in this thesis, further neutron scattering experiments were performed at PSI after finishing the experimental work on this thesis. SANS measurements have been performed on the viscous phase only. The measurement is not analysed, yet. But similar scattering curves were observed for aggregates forming vesicles and lamellar sheets [205, 206], which would support our proposed network structure.

Especially, the proposed coexistence structures in the “two-phase” region open an entirely new direction for research. Especially a combined scattering study with direct observation (imaging) methods such as cryo-TEM, would validate our results obtained by scattering experiments.

List of Figures

List of Tables

Bibliography

[1] J. Israelachvili. *Intermolecular and Surface Forces*. Academic Press volume 2nd edition, 1992.

[2] F. Reiss-Husson and V. Luzzati. The structure of the micellar solutions of some amphiphilic compounds in pure water as determined by absolute small-angle x-ray scattering techniques. *J. Phys. Chem.*, 68, 1964.

[3] D.F. Evans and H. Wennerstrom. *The Colloidal Domain*. VCH, 1994.

[4] D. Andelman; M.M. Kozlov and W. Helfrich. Phase transitions between vesicles and micelles driven by competing curvatures. *Europhys. Lett.*, 25:231–236, 1994.

[5] W. Kaenzig; P. Schurtenberger and N. Mazer. Static and dynamic light scattering studies of micellar growth and interaction in bile salt solutions. *J. Phys. Chem.*, 87:308–315, 1983.

[6] N. Mazer; R. F. Kwasnick; M. C. Carey and G. B. Benedek. Quasielastic light-scattering of aqueous biliary lipid systems: Size, shape and thermodynamics of bile salt micelles. *Biochemisty*, 18:3064–3075, 1979.

[7] J. P. Kratohvil; W. P. Hsu and D. I Kwok. How large are the micelles of di-α-hydroxy bile salts at the critical micellization concentration in aqueous electrolyte solutions? results for sodium taurodeoxycholate and deoxycholate. *Langmuir*, 2:256–258, 1986.

[8] K. Fontell. Micellar behaviour in solutions of bile acid salts. *Kolloid Z. Z. Polym.*, 244:253–257, 1971.

[9] J. P. Kratohvil; W. P. Hsu and D. I Kwok. Size of bile salt micelles: Techniques, problems and results. *Hepatology*, 4:85S–97S, 1984.

[10] M. C. Carey; D. M. Small and C. M. Bliss. Lipid digestion and absorption. *Annu. Rev. Physiol.*, 45:651–668, 1983.

[11] M. Janich; J. Lange; H. Graener and R. Neubert. Extended light scattering investigations on dihydroxy bile salt micelles in low-salt aqueous solutions. *J. Phys. Chem. B*, 102:5957–5962, 1998.

[12] D.M. Small. The physical chemistry of cholanic acids. bile acids- chemistry, physiology and metabolism. *Plenum Press*, page Chapter 8, 1973.

[13] A. Jover; F. Meijide; E. R. N*úñ*ez and J. V. Tato. Aggregation number for sodium deoxycholate from steady-state and time-resolved fluorescence. *Langmuir*, 13(161-164), 1997.

[14] M.C. Carey and D.M. Small. Micellar properties of dihydroxy and trihydroxy bile salts: effects of counterion and temperature. *J. Colloid Interf. Sci.*, 31:382–396, 1969.

[15] N. Mazer; R. F. Kwasnick; M. C. Carey and G. B. Benedek. *Quasielastic light scattering spectroscopic studies of aqueous bile salt, bile salt-lecithin and bile salt-lecithin-cholesterol solutions*, volume 1. Plenum Press NY, 1977.

[16] W. C. Duane. Taurocholate- and taurochenodeoxycholate-lecithin micelles: The equilibrium of bile salt between aqueous phase and micelle. *Biochem. Biophys. Research Comm.*, 74:223–229, 1977.

[17] M.C. Carey N.A. Mazer and G.B. Benedek. *Quasielastic Light Scattering Studies of Model Bile Systems*, volume Lasers in Biology and Medicine. Plenum Publishing, New York,, 1980.

[18] P. Ekwall; A. Sten and A. Norman. Some differences between solubilization in bile salt and paraffin chain salt solutions. *Acta. Chem. Skand*, 10:681–704, 1956.

[19] A. Coello; F. Meijide; E. R. N*úñ*ez and J. V. Tato. Aggregation behaviour of bile salt in aqueous solutions. *J. of Pharm. Sci.*, 85(1-14), 1996.

[20] N. Funasaki; S. Hada and S. Neya. Self-association patterns of sodium taurocholate and taurodeoxycholate as studied by frontal derivative chomatography. *J. Phys. Chem. B.*, 103:169–172, 1999.

[21] K. Matsuoka; M. Suzuki; C. Honda; K. Endo and Y. Moroi. Micellization of conjugated chemodeoxy- and ursodeoxycholates and solubilisation of cholesterol into micelles: comparison with other four conjugated bile salts species. *Chem. and Phys. of. Lipids*, 139:1–10, 2006.

[22] D. Kritchevsky and P.P Nair. *The Bile Acids- Chemistry, Physiology and Metabolism*, volume 1, chapter Chemistry of bile acids, pages 1–9. Plenum Press NY, 1971.

[23] H. Matsuoka; J.P. Kratohvil and N. Ise. Small-angle x-ray scattering from solutions of bile salts: sodium taurodeoxycholate in aqeous electrolyter solutions. *J. Colloid Interfe Sci.*, 118:387–396, 1987.

[24] D. M. Small. Size and structure of bile salt micelles: influence of structure, concentration, counterion concentration, ph and temperature. *Adv. Chem. Ser. B.*, 84:31–42, 1968.

[25] D. M. Small; S. A. Penkett and D. Chapman. Studies on simple and mixed bile salt micelles by nuclear magnetic resonance spectroscopy. *Biochim. Biophys. Acta*, 176:178–189, 1969.

[26] C. Tanford. *The Hydrophobic Effect: Formation of Micelles and Biological Membranes*. Krieger and Malabar Publishing Group, 1991.

[27] M. C. Carey; J.-C. Montet; M. C. Phillips; M. J. Armstrong and N. A. Mazer. Thermodynamic and molecular basis of dissimilar cholesterol-solubilizing capacities by micellar solutions of bile salts: Cases of sodium chenodeoxycholate and sodium ursodeoxycholate and their glycine and taurine conjugates. *Biochemistry*, 20:3637–3648, 1981.

[28] H. Kawamura; Y. Murata; T. Yamaguchi; H. Igimi; Mitsuri Tanaka; G. Sugihara and J.P. Kratohil. Spin-label studies of bile salt micelles. *J. Phys. Chem.*, 93:3321–3326, 1989.

[29] A. Coello, F. Meijide, E. Rodriguez Nunez, and J. Vazquez Tato. Aggregation behavior of sodium cholate in aqueous solution. *Journal of Physical Chemistry*, 97(39):10186–10191, 1993.

[30] E. Bottari; A. A. D'Archivio; M. R. Festa; L. Galantini and E. Giglio. Structure and mixture of taurocholate micellar aggregates. *Langmuir*, 15:2996–2998, 1999.

[31] J. M. Seddon and R. H. Templar. *Polymorphism of lipid-water systems.*, chapter Chapter 3, pages 97–160. North-Holland Amsterdam, 1995.

[32] B. A. Cornell; J. Middlehurst; F. Separovic. Molecular packing and stability within highly curved phospholipid bilayers. *Biochim. and Biophys. Acta*, 598:405–410, 1980.

[33] A. F Hofmann and D. M. Small. Detergent properties of bile salts: Correlation with physiological function. *Annu. Rev. Physiol.*, 18:333–376, 1967.

[34] D. M. Small. Phase equilibria and structure of dry and hydrated egg lecithin. *J.Lipid Res.*, 8:551–557, 1967.

[35] M. Ollivon; O. Eidelman; R. Blumental and A. Walter. Micelle-vesicle transition of egg phosphatidylcholine and octyl glucose. *Biochemistry*, 27:1695–1703, 1988.

[36] C. Huang and J. T. Mason. Geometric packing constraints in egg phosphatidylcholine vesicles. *Proc. Natl. Acad. Sci., USA*, 75:308310, 1978.

[37] L. Arleth; R. B. Bauer; L. H. Ogendal; S. U. Egelhaaf; P. Schurtenberger and J. S. Pederson. Growth behaviour of mixed wormlike micelles a small-angle scattering study of the lecithin-bile salt system. *Langmuir*, 19:4096–1409, 2003.

[38] D. M. Small. Physicochemical studies of cholesterol gallstone formation. *Gastroentrology*, 52:1687–1690, 1967.

[39] D. M. Small; M. C. Bourges and D. G. Dervichian. The biophysics of lipid associations 1. the ternary systems lecithin-bile salt-water. *Biochim. and Biophys. Acta*, pages 563–580, 1966.

[40] N. Mazer; M. C. Carey; R. F. Kwasnick and G. B. Benedek. Quasielastic light-scattering of micelle formation and cholesterol precipitations in model bile solutions. *Hepatology*, 4:143–150, 1979.

[41] S. U. Egelhaaf and P. Schurtenberger. Shape transformations in the lecithin-bile system: from cylinders to vesicles. *J. Phys. Chem.*, 98:8560–8573, 1994.

[42] P.R. Hjelm; P. Thiyagaragan; H. Alkan. A small-angle neutron scattering study of the effect of dilution on particle morphology in mixture of glycocholate and lecithin. *J. Appl. Cryst.*, 21:858–863, 1988.

[43] P.R. Hjelm; P. Thiyagaragan; D. S. Sivia; P. Lindner; H. Alkan and D. Schwahn. Small-angle neutron scattering from aqueous mixed colloids of lecithin and bile salt. *Prog. Poly. Sci.*, 81:225–231, 1990.

[44] P.R. Hjelm; P. Thiyagaragan; H. Alkan-Onyüksel. Organization of phosphatidylcholine and bile salt in rodlike mixed micelles. *J. Phys. Chem.*, 96:8653–8661, 1992.

[45] J. S. Pederson; S. U. Egelhaaf and P. Schurtenberger. Formation of polymerlike mixed micelles and vesicles in lecithin-bile salt solutions. a small-angle neutron scattering study. *J. Phys. Chem*, 99:1299–1305, 1995.

[46] M. A. Long; E. W. Kaler and S. P. Lee. Structural characterization of the micelle-vesicle-transition in lecithin-bile salt solutions. *Biophys. J.*, 67:1733–1742, 1994.

[47] J. Ulmius; G. Lindblom; H. Wennerstrom; L.B. Johannson; K. Fontell; O. Soderman and G. Arvidson. Molecular organization in the liquid crystalline phases of lecithin-sodium cholate-water systems studied by nuclear magnetic resonance. *Biochemistry.*, 21:1553–1560, 1982.

[48] J. W. Nichols and J. Ozarowski. Sizing of lecithin-bile salr mixed micelles by size-exclusion high-performance liquid chomotography. *Biochemistry*, 29:4600–4606, 1990.

[49] G. B. Benedek D. E. Cohen; R. A. Chamberlain; G. M. Thurston. Cylindrical 'worm-like' micelles in bile salt-lecithin solutions: implications for the earliest events in bile formation. *Falk Symposium*, 58:147–150, 1991.

[50] A.L. Koch. Primeval cells: possible energy-generating and cell-division mechanisms. *J. Mol. Evol.*, 21 (3):270277, 1984.

[51] D. D. Lasic. *Applications of liposomes; Structure and Dynamics of Membranes*, volume , chapter 10, pages 419–519. North-Holland, 1995.

[52] M. Keller; A. Kerth; and A. Blume. Thermodynamics of lipid membrane solubilization by sodium dodecyl sulfate. *Biochim. Biophys. Acta*, 178:1326, 1997.

[53] J. Lasch. Interaction of detergents with lipid vesicles. *Biochim. Biophys. Acta*, 1241:269–292, 1995.

[54] Y. Roth; E.Opatowski; M.M. Kozlov and D. Lichtenberg. Phase behaviour of dilute aqueous solutions of lipid surfactant mixtures: effect of finite size of micelles. *Langmuir*, 16:2052–2061, 2000.

[55] D. Lichtenberg; R.J. Robson and E.A. Dennis. Solubilization of phospholipids by detergents: Structural and kinetic aspects. *Biochim. Biophys. Acta*, 737:285–304, 1983.

[56] D. Lichtenberg. Characterization of the solubilization of lipid bilayers by surfactants. *Biochim and Biophy. Acta*, 821:470–478, 1985.

[57] D. Fattal; D. Andelman and A. Ben-Shaul. The vesicle-micelle transition in mixed lipid-surfactant systems: A molecular model. *Langmuir*, 11:1154–1161, 1995.

[58] E.Opatowski; M.M.Kozlov and D. Lichtenberg. The heat of transfer of lipid and surfactant from vesicles into micelles in mixtures of phospholipid and surfactant. *Biophy. J*, 73:1448–1457, 1997.

[59] J. Leng; S. U. Egelhaaf and M. E. Cates. Kinetics of the micelle-to-vesicle transition aqueous lecithin-bile salt mixtures. *Biophys. J.*, 85:1624–1646, 2003.

[60] J. Leng; S. U. Egelhaaf and M. E. Cates. Kinetics pathway of spontaneous vesicle formation. *Europhys. Lett.*, 59:311–317, 2002.

[61] A. Salonen. *Mixed Micelle System: Equilibrium and Kinetics*. PhD thesis, University of Edinburg; School of Physics, 2005.

[62] S. U. Egelhaaf; J. Leng; A. Salonen; P. Schurtenberger and M. Cates. Pathway of vesicle formation. *Self Assembly*, 82:422–2807, 2003.

[63] K. M. Kale; E. L. Cussier and D. F. Evans. Charecterization of micellar solutions using surfactant ion electrodes. *J. Phys. Chem.*

[64] K. Ryu; J. M. Lowery; E. L. Cussier and D. F. Evans. Studie of model bile solutions using surfactant ion electrodes. *J. Phys. Chem.*, 87:5015–5019, 1983.

[65] P. Brown; M. A. Thomason; D. M. Painter; D.M Bloor; D. G. Hall H. Gharibi; N. Takisawa and E. Wyn-Jones. Analysis of the fast relaxation times for micelle kinetics taking into account new emf data. *J. Chem. Soc., Faraday Trans.*, 87:707–710, 1991.

[66] H. Gharibi and A. A. Rafati. Electrochemical and kinetic studies of micellization of sodium tetradecyl sulfate in the presence of poly(vinylpyrrolidone). *Langmuir*, 14:2191–2196, 1998.

[67] D. Bloor; J. Gray; J. Hughes and G. J. T. Tiddy. Surfactant specifiv electrode measurements of mesophases. electrode and x-ray measurements of hexadecyltrimethylammonium bromide/hexadecanol gel (l_β) dispersions show large, nonequilibrium dissolution effects. *Langmuir*, 17:6127–6131, 2001.

[68] W. John Albery. Molecular recognition and molecular sensors. *Langmuir*, 158:55–72, 1991.

[69] W. J. Albery; R. B. Lennox; E. Magner; G. Rao; D. Armstrong; R. H Dowling; G. M. Murphy. An amperometric enzyme electrode for bile acids. *Anal. Chim. Acta.*, 281:655–661, 1993.

[70] Hiroshi Shiigi; Daisuke Kijima; Yukata Ikegena; Kenji Hori; Sotishi Fukazawa; Tsutomei Nagaoka. Molecular recognition for bile acids using a molecularly imprinted overoxidized polypyrrole film. *J. of Electrochem. Soc.*, 152:H129–H134, July 2005.

[71] Hiroshi Shiigi; Kentaro Okumura; Daisuke Kijima; Bhavana Deore; Usha Sree and Tsutomei Nagaoka. An overoxidised polypyrrole/dodecylsulfonate micelle composite film for amperometric serotonin sensing. *J. of Electrochem. Soc*, 150:H119–H123, 2003.

[72] Q. Pei and O. Ingamas. Electrochemical applications of the bending beam method. 2. electroshrinking and slow relaxation in polypyrrole. *J. Phys. Chem.*, 1993:6034–6041, 1993.

[73] M. Zhou; M. Pagels; B. Geschke and J. Heinze. Electropolymerization of pyrrole and electrochemical study of polypyrrole. 5. controlled electrochemical synthesis and solid-state transition of well-defined polypyrrole variants. *J. Phys. Chem. B*, 106:10065–10073, 2002.

[74] Qingji Xie; Susumu Kuwubata and Hiroshi Yoneyama. Eqcm studies on polypyrrole in aqueous solutions. *J. Electranal. Chem.*, 420:219–225, 1997.

[75] E. M. Peters and J. D. Van Dyke. Copolymers of pyrrole and bithiophene by oxidative electropolymerization. *J Polymer Science Part A: Polym. Chem.*, 29:1379–1385, 1991.

[76] H. Shirakawa; E. J. Louis; A. G. MacDiarmid; C. K. Chiang and A. J. heeger. Synthesis of electrically conducting organic polymers: halogen derivatives of polyacetylene, (ch)x. *J. Chem. Soc.: Chem. Comm.*, pages 578 – 580, 1977.

[77] A. G. MacDiarmid A. J. Heeger and H. Shirakawa. The nobel price in chemistry 2000: Conductive polymers.

[78] Atkins. *Physical Chemsitry*. Oxford University Press, 6th edition, 1998.

[79] A. F. Diaz; A. Martinez; K.K Kanzawa and M. Salmon. Electrochemistry of some substituted pyrroles. *J. Electroanal. Chem.*, 130:181, 1980.

[80] E. M. Genies and A. F. Diaz. Electrochemistry of some substituted pyrroles. *J. Electroanal. Chem.*, 149:101, 1983.

[81] R.J. Waltman and J Bargon. Electrically conducting polymers: a review of the electropolymerization reaction, of the effects of chemical structure on polymer film properties, and of applications towards technology. *Can. J. Chem.*, 64:76, 1985.

[82] G.M. Spinks G.G. Wallace M.R. Gandhi, P. Murray. Mechanism of electromechanical actuation in polypyrrole. *Syn. Met.*, 73:247–256, 1995.

[83] Q. Pei and R. Quian. Protonation and deprotonation of polypyrrole chain in aqueous solutions. *Syn. Met.*, 45:35–48, 1991.

[84] J. Unsworth; P.C. Innis; B. A. Lunn; Z. Jin and G. P. Norton. The influence of electrolyte ph on the surface morphology of polypyrrole. *Synth. Met.*, 53:59–69, 1992.

[85] J. Ouyang and Y. Li. Anion dominated electrochemical process of poly(n-methylpyrrole). *J. Appl. Poly. Sci.*, 61:1487–1491, 1996.

[86] R. M. Mammone and M. Binder. *Polym. Comm.*, 32:140, 1990.

[87] A.F. Diaz; J. I. Castilloa; J.A. Logana and W.-Y Lee. Electrochemistry of conducting polypyrrole films. *J. Electroanal. Chem.*, 129:115, 1981.

[88] A. Merz; R. Schwartz and R. Schropp. 3,4-dimethoxypyrrol; monomer synthesis and conducting polymer formation. *Adv. Mater.*, 6:402, 1992.

[89] J.J. Kim; T. Ameniya; D. A. Tryk; K. Hashimoto and A. Fujishima. Charge transport of processes in electrochemically deposited poly(pyrrole) and poly(n-methylpyrrole) thin films. *J. Electroanal. Chem.*, 416:113–119, 1996.

[90] K. Hyodo and M. Omae. Colorimetric study of the electrochromic properties of a conducting polymer. *J. Electroanal. Chem.*, 292:93–102, 1990.

[91] A. J. Bard and L. R. Faulkner. *Electrochemical Methods-Fundamentals and Applications*. John Wiley and Sons (New York), 1980.

[92] G.Z. Sauberbrey. Use of quartz vibrator for weighting thin film on a microbalance. *Z. Phys.*, 155:206–222, 1959.

[93] C.-S. Lu and O. Lewis. Investigation of film-thickness determination by oscillating quartz resonators with large mass load. *J. Appl. Phys.*, 43:4385–4390, 1972.

[94] A. Kanzawa and J. G. Gordon. Frequency of a quartz microbalance in contact with liquid. *Anal. Chem.*, 57:1770, 1985.

[95] http://www.ecochemie.nl/.

[96] http://www.maxtekinc.com.

[97] S. Basak; K. Rajeshwar and M. Kaneko. Ion binding by poly(pyrrole-co-[3-(pyrrole-1-yl)propanesulfonate])thin films. *Anal. Chem.*, 62:1407–1413, 1990.

[98] C.S.C. Bose; S. Basak; K. Rajeshwar. Electrochemistry of poly(pyrrole chloride)films: A study of polymerisation efficiency, ion transport during redox and doping level assay by eqcm, ph, and ion-selectivity measurements. *J. Phys. Chem.*, 62:1407–1413, 1992.

[99] C.S.C. Bose; S. Basak and K. Rajeshwar. Elyectrochemisty of polypyrole chloride films: A study of polymerization efficiency, ion transport ion-selective electrode measurements. *J. Phys. Chem.*, 9899-9906:1992, 96.

[100] Peter G. Pickup Xiaoming Ren. Ion transport in polypyrrole and a polypyrrole/polyanion composite. *J. Phys. Chem.*, 97:5356–5362, 1993.

[101] C. Weidlich; K.-M. Mangold and K. Juttner. Eqcm study of the ion exchange behaviour of polypyrrole with different counterions in different electrolytes. *Electrochimica Acta*, 50:1547–1552, 2005.

[102] Juhyuon Kwak Hochun Lee, Haesik Yang. Mass transport behavior of polypyrrole and poly(n-methylpyrrole) films in acetonitrile solutions. *J. of Electroanal. Chem.*, 468:104–109, 1999.

[103] W. Paik; I. H. Yeo; H. Suh; Y. Kim and E. Song. Ion transport in conducting polymers doped with electroactive anions examined by eqcm. *Electrochimica Acta*, 450:3833–3840, 2000.

[104] H.Yang and J. Kwak. Mass transport investigated with the electrochemical and electrogravimetric impedance techniques. 2. anion and water transport in pmpy and ppy films. *J. Phys. Chem. B*, 101:4656–4661, 1997.

[105] H. Yang and J. Kwak. Mass transport investigated with the electrochemical and electrogravimetric impedance techniques. 1. water transport in ppy/cupts films. *Journal of Physical Chemistry B*, 101.

[106] P. Garidel; A. Hildebrand; R. Neubert and A. Blume. Thermodynamic characterization of bile salt aggregation as a function of temperature and ionic strength using isothermal titration calorimetry. *Langmuir*, 16:5267–5375, 2000.

[107] H. Heerklotz; H. Binder; G. Lantzsch; G. Klose and A. Blume. Lipid/detergent interaction thermodynamics as a function of molecular shape. *J. Phys. Chem.*, 101:639–645, 1997.

[108] A. Hildebrand; R. Neubert; P. Garidel; and A. Blume. Bile salt induced solubilization of synthetic phophatidylcholine vesicles studied by isothermal titration calorimetry. *J. Colloid and Interface Sci.*, 18:2836–2847, 2002.

[109] A. Hildebrand; K. Beyer; R. Neubert; P. Garidel; and A. Blume. Solubilization of negatively charged dppc/dppg liposomes by bile salts. *J. Colloid and Interface Sci.*, 279:559–571, 2004.

[110] S. Keller; H. Heerklotz; N. Jahnke and A. Blume. Thermodynamics of lipid membrane solubilization by sodium dodecyl sulfate. *Biophys. Journal*, 101:639–645, 1997.

[111] A. Hildebrand; K. Beyer; R. Neubert; P. Garidel; and A. Blume. Thermodynamics of demicellisation of mixed micelles composed of sodium oleate and bile salts. *Langmuir*, 2004.

[112] C.M. Cooper, A. ; Johnsson. *Introduction to microcalorimetry and biomolecular energetics: Methods in Molecular Biology*, volume 22. Marcel Dekker - New York, 1994.

[113] www.microcalorimetry.com.

[114] MicroCal Inc., Northhampton, MA, USA. *Microcal ITC unit - User's Manual*.

[115] O. Glatter and O. Kratky. *Small Angle X-ray scattering*. Academic Press, London, 1982.

[116] P. Lindner and T. Zemb. *Neutrons, X-rays and Light: Scattering Methods Applied to Soft Condensed Matter*. Academic Press, London, 2002.

[117] V. F. Sears. Thermal-netron scattering lengths and cross-sections for condenser matter research. Technical report, Report AECL-8490 Chalk River Laboratories, Ontaro, 1984.

[118] J. S. Pederson; D. Posselt and K. Mortensen. *J. Appl. Cryst*, 23:321–333, 1990.

[119] M. Kerker. *The scattering of Light and other electromagnetic radiation*. Academic Press, New York, 1959.

[120] B. J. Berne and R. Pecora. *Dynamic Light Scattering*. Wiley, NY, 1976.

[121] D. E. Koppel. Analysis of macromolecular polydispersity in intensity correlation spectroscopy: The method of cumulants. *J. Chem. Phys.*, 57:4814–4820, 1972.

[122] S. W. Prowencer. Contin: A general purpose constrained regularization program for inverting noisy linear algebraic and integral equations. *Comput. Phys. Commun.*, 27:229–242, 1982.

[123] R. T. C. Ju; C. W. Frank and A. P. Gast. Contin analysis of colloidal aggregates. *Langmuir*, 8:2165 – 2171, 1992.

[124] J. S. Pederson. A flux- and background-optimized version of the nanostar small-angle x-ray scattering camera for solution scattering. *J. of Appl. Crystallogr.*, 37:369, 2004.

[125] S. U. Egelhaaf R. E. Ghosh and A. R. Rennie. *A computing Guide for Small-Angle Scattering Experiments*. Institut Max von Laue and Paul Langevin, 2006.

[126] G. C. Kresheck and W. A. Hargraves. Thermodynamic titration studies of the effect of head group, chain length, solvent and temperature on the thermodynamics of micelle formation. *J. Colloid Interf. Sci.*, 48:481–493, 1974.

[127] R. P. Majhi and S. P. Moulik. Energetics of micellization: Reassessment by a high-sensitivity titration microcalorimeter. *Langmuir*, 14:3986, 1998.

[128] P. L. Privalov and S. J. Gill. The hydrophobic effect: A repraisal. *Pure Appl. Chem.*, 61:1097–1104, 1961.

[129] S. Paula; W. S$\ddot{u}$s; J. Tuchtenhagen and A. Blume. Thermodynamics of micelle formation as a function of temperature: A high sensitivity titration calorimetry study. *J. Phys. Chem.*, 99:11742–11751, 1995.

[130] E. Fisicaro; C. Compari and A. Braibanti. Entropy/enthalpy compensation: Hydrophobic effect, micelles and protein complexes. *PCCP*, 6:4156–4166, 2004.

[131] B. Kronberg; M. Costas and R. Silveston. Thermodynamics of the hydrophobic effect in surfactant solutions - micellization and adsorption. *Pure Appl. Chem.*, 67(6):897–902, 1995.

[132] N. Funasaki; M. Nomura; S. Ishikawa and S. Neya. Hydrophobic self-association of sodium taurochenodeoxycholate and tauroursodeoxycholate. *J. Phys. Chem. B.*, 104:7745–7751, 2000.

[133] P. Garidel; A. Hildebrand. Thermodynamic properties of association colloids. *J. Therm. Anal. Cal.*, 82:483–489, 2005.

[134] A. Roda; A. F. Hofmann and K. J. Mysel. Bile salt structure in aqueous solutions. *J. Biol. Chem.*, 258:6362–6371, 1983.

[135] W. Spivak; C. Morrison; D. Devinuto and W. Yuey. Spectrophotometric determination of the critical micellar concentration of bile salts using bilirubin monoglucuronide as a micellar probe. *Biochem. J*, 252:275–281, 1988.

[136] P. Mukerjee and P. Cardinal. Solubilization as a method for studying self-association: Solubility of napthalene in the bile salt sodium cholate and the complex pattern of its aggregation. *J. Pharm. Sci.*, 65:882886, 1976.

[137] G. Sugihara; K. Yamakawa; Y. Murata and M. Tanaka. Effects of ph, pna, and temperature on micelle formation and solubilization of cholesterol in aqueous solutions of bile salts. *J. Phys. Chem.*, 86:2784, 1982.

[138] M. Corrin and W. Harkins. The effect of salts in the critical concentration for the fromation of micelles in colloidal electrolytes. *J. Am. Chem. Soc.*, 69:1947, 1947.

[139] R. Kakehashi; T. Takeda and H. Maeda. Effects of micellar charge density on the coefficient of the corrin-harkins relation. *J. Col. Interf. Sci.*, 253:238–240, 2002.

[140] H. Maeda; Y. Kanakubo; M. Miyahara, R. Kakehashi; V. Garamus, and J. S. Pedersen. Effects of protonation on tetradecyldimethylamine oxide micelles. *J. Phys. Chem B*, 104:6174–6180, 2000.

[141] H. Maeda. Some thoughts regarding theoretcal aspects of the corrin-harkins relation and the micellisation product of ionic micelles. *J. Col. Interf. Sci.*, 241:18–25, 2001.

[142] H. Maeda. A thermodynamic analysis of charged mixed micelles in water. *J. Phys. Chem B*, 109:15933–15940, 2005.

[143] R. Palepu; D. G. Hall and E. Wyn-Jones. The use of ion-selective electrodes to determine the effective degree of micelle dissociation in tetracylpyridium bromide solutions. *J. Chem. Soc Faraday Trans.*, 86(9):1535–1538, 1990.

[144] D. F. Evans; D. J. Mitchell and B. W. Ninham. Ion binding and dressed micelles. *J. Phys. Chem.*, 88:6344–6348, 1984.

[145] D. G. Hall. Thermodynamics if solutions of polyelectrolytes, ionic surfactants and other charged colloidal systems. *J. Chem. Soc. Faraday Trans. I*, 77:1121–1156, 1981.

[146] John G. Kirkwood and Frank P. Buff. The statistical mechanical theory of solutions. i. *The Journal of Chemical Physics*, 19(6):774–777, 1951.

[147] R. Ninomiya; K. Matsuoka and Y. Moroi. Micelle formation of sodium chenodeoxycholate and solubilisation into the micelles: comparison with unconjugated bile salts. *Biochim. Biophys. Acta*, 1643:116–125, 2003.

[148] J. Ulmius B. Lindman; N. Kamenka; H. Fabrw and T. Wieloch. Aggregation behavior of bile salts in aqueous solution. *J. of Col. Interf.*, 73:556, 1980.

[149] B. Lindman; M. C. Kamenka; N. Kamenka; R. Rymden and P. Stilbs. Micelle formation of anionic and cationic surfactants from fourier transform hydrogen-i and lithium-7 nuclear magnetic resonance and tracer self-diffusion studies. *J. Chem. Phys.*, 88:5048, 1984.

[150] P. R. Mahji and A. Blume. Temperature-induced micelle-vesicle transition in dmpc-sds and dmpc-dtab mixtures studied by calorimetry and dynamic light scattering. *J. Phys. Chem. B*, 106:10753–10763, 2002.

[151] H. Heerklotz; H. Binder; G. Lantzsch; G. Klose and A. Blume. Thermodynamic characterisation of dilute aqueous lipid/detergent mixtures of popc and $c_{12}eo_8$ by means of itc. *J. Phys. Chem.*, 100:6764–6774, 1996.

[152] F. Ollila and J. P. Slotte. A thermodynamic study of bile salt interactions with phosphatidylcholine and spingomyelin unilamellar vesicles. *Langmuir*, 17:2835–2840, 2001.

[153] M. S. Johnson F. Ollila; O. T. Pentikainen; S. Forss and J. P. Slotte. Characterisation of bile salt/cyclodextrin interactions using itc. *Langmuir*, 17:2835–2840, 2001.

[154] P. Garidel; A. Hildebrand; K. Knauf and A. Blume. Membranolytic activity of bile salts: Influence of biological membrane properties and composition. *Molecules*, 12:2292–2326, 2007.

[155] W. Kaenzig; P. Schurtenberger and N. Mazer. Micelle to vesicle transition in aqueous solutions of bile salt and lecithin. *J. Phys. Chem.*, 8:1042–1049, 1985.

[156] H. Heerklotz; H. Binder; G. Lantzsch; G. Klose and A. J. Blume. Lipid/detergent interaction thermodynamics as a function of molecular shape. *Chem. Phys. Lett.*, 235:517–, 1995.

[157] W. C. Duane. The intermicellar bile salt concentration in equilibrium with the mixed-micelles of human bile. *Biochimica et Biophysica Acta*, 398:275–286, 1975.

[158] E. Kucinka and J. Seelig. Interaction of melittin with phosphatidylcholine membranes. binding isotherm and lipid headgroup. *Biochemistry*, 28:4216–4221, 1989.

[159] A. Seelig; P. R. Allegrini and J. Seelig. Partitioning of local anesthetics into membranes: surface charge effects monitored by the phospholipid head-group. *Biochim. Biophys. Acta*, 939:267–276, 1988.

[160] M. A. Long; E. W. Kaler; S. P. Lee and G. D. Wignall. Characterization of lecithin taurodeoxycholate mixed micelles using small-angle neuton scattering and static and dynamic light scattering. *J. Phys. Chem.*, 98:4402–4410, 1994.

[161] L. Arleth; M. Bergstrom and J. S. Pederson. A small-angle scattering study of the growth behaviour, flexibility and intermicellar interactions of wormlike sds micelles in nabr aqueous solutions. *Langmuir*, 18:5343–5353, 2002.

[162] T. Shimada; M. Doi and K. Okano. Concentration fluctuations of stiff polymers. i. static structure factor. *J. Chem. Phys.*, 88:2815–2821, 1988.

[163] J. S. Pederson and P. Schurtenberger. Static properties of polysterene in semidilute solutions: A comparison of monte carlo simulation and small angle neutron scattering. *Europhys. Lett*, 45:666–672, 1999.

[164] T. Yoshikawa and H. Yamakawa. Scattering functions of wormlike and helical wormlike chains. *Macromolecules*, 13:1518–1525, 1980.

[165] J. S. Pederson and P. Schurtenberger. Scattering functions of semiflexible polymers with and without excluded volume effects. *Macromolecules*, 29:7602–7612, 1996.

[166] J. S. Pederson and P. Schurtenberger. Static properties of polystrene in semidilute solutions: a comparison of monte carlo simulation and small-angle neutron scattering results. *Europhys. Lett.*, 45 (6), 1999.

[167] K. Schweizer and J. G. Curro. Prism theory of the structure, thermodynamics, and phase transitions of polymer liquids and alloys. *Adv. Polym. Sci*, 116:319–377, 1994.

[168] V.W. Garamus; J. S. Pederson; H. Kawasaki and H. Maeda. Scattering from polymerlike micelles of tdao salt/water solutionsat semidilute concentrations. *J. Phys. Chem*, 99:1299–1305, 1995.

[169] J. S. Pederson. Analysis of small-angle scattering data from colloids and polymer solutions: modeling and least-squares fitting. *Adv. Coll. Int. Sci*, 70:171–210, 1997.

[170] A. Tardieu; V. Luzzati; and F. C. Reman. Structure and polymorphism of the hydrocarbon chains of lipids: a study of lecithin-water phases. *J. Mol. Biol.*, 75:711–733, 1973.

[171] V. Luzzati. *X-ray diffraction studies of lipid-water systems.*, chapter Biological Membranes, pages 71–123. Academic Press, London, 1967.

[172] M. C. Wiener; R. M. Suter and J. F. Nagle. Structure of the fully hydrated gel phase of dipalmitoylphosphatidylcholine. *Biophy. J.*, 55:315–325, 1989.

[173] M. C. Wiener; R. M. Suter and J. F. Nagle. Structure of fluid dioleophosphatidylcholine bilayer determined y joint refinement of x-ray and neutron diffraction data. part ii. *Biophy. J.*, 61:428–433, 1992.

[174] M. C. Wiener; R. M. Suter and J. F. Nagle. Structure of fluid dioleophosphatidylcholine bilayer determined y joint refinement of x-ray and neutron diffraction data. part ii. *Biophy. J.*, 61:434–447, 1992.

[175] G. Pabst; M. Rappolt: H. Amentisch and P. Laggner. Structural information from multilamellar liposomes at full hydration: Full q-range fitting with high quality x-ray data. *Phys. Rev. E*, 62:4000–4009, 2000.

[176] R. Zhang; R. M. Suter and J. F. Nagle. Theory of the structure factor of lipid bilayers. *Phys. Rev. E*, 50(6):5047–5060, 1994.

[177] J. Lemmich; K. Mortensen; J. H. Ipsen; T. Honger; R. Bauer and O. G. Mouritsen. Small-angle neutron scattering from multilamellar lipid bilayers: Theory, model, and experiment. *Phys. Rev. E*, 53:5169–5180, 1996.

[178] A. E. Blaurock. Evidence of bilayer structure and of membrane interactions from x-ray diffraction analysis. *Biochim. Biophys. Acta*, pages 167–207, 1982.

[179] P.G. Gennes. Conjectures sur letat smectique. *J. Phys. France C4*, 30:65–71, 1969.

[180] J. F. Nagle; R. Zhang; S. Tristam-Nagle; W. Sun and H. I. Petrache. X-ray structure determination of fully hydrated l_α phase of dmpc bilayers. *Chem. and Phys. of Lipids*, 95:83–94, 1998.

[181] J. F. Nagle and S. Tristam-Nagle. Structure of lipid bilayers. *Biochim. et Biophys. Acta*, 1469:159–195, 2000.

[182] N. Kucerka; S. Tristam-Nagle and J. F. Nagle. Structure of fully hydrated fluid phase lipid bilayers with monosaturated chains. *J. Membrane Biol.*, 208:193–202, 2005.

[183] F. Nallet; R. Laversanne and D. Roux. Modeling x-ray scattering or neutron scattering spectra of lyotropic lamellar phases: interplay between form and structure factors. *J. Phys. II France*, 3:487–502, 1993.

[184] J. Katsaras N. Kucerka; J.Pencer J. N. Sachs, J. F. Nagle. Curvature effect on the structure of phospholipid bilayers. *Langmuir*, 23:1292–1299, 2007.

[185] Private communications with Jan Skov Pedersen and Dr. Christiano Olivera.

[186] O. Glatter. A new method for the evaluation fo small-angle scattering data. *J. App. Cryst.*, 10:415421, 1977.

[187] J. S. Pederson. Model-independeant determination of the surface scattering-length-density profile from secular reflectivity dat. *J. Appl. Cryst*, 25:129–145, 1992.

[188] E. H. Pape and W. Kreutz. A deconvolution method for evaluating small-angle x-ray scattering from lamellar structures. *J. App. Cryst.*, 11:421429, 1978.

[189] T. J. McIntosh. The effect of cholesterol on the structure of phosphatidylcholine membranes. *Biochimica et Biophys Acta*, 513:43–58, 1978.

[190] T. J. McIntosh; A. D. Magid and S. A. Simon. Cholesterol modifies the short-range repulsive interactions between phosphatidylcholine membranes. *Biochemistry*, 8:17–25, 1989.

[191] R. Schubert and K. H. Schmidt. Structural changes in vesicle membranes and mixed micelles of various lipid compositions after binding of different bile salts. *Biochemistry*, 27:8787–8794, 1988.

[192] A. Walter; K. P. Vinson; A. Kaplun and Y. Talmom. Intermediate structures in the cholate-phoshatidylcholine vesicle-micelle transition. *Biophys. J.*, 60:1315–1325, 1991.

[193] R. Schubert; K. Beyer; H. Wolburg and K. H. Schmidt.

[194] O. Glatter. Convolution square root of band-limited symmetrical functions and its application to small-angle scattering data. *J. App. Cryst.*, 14:101108, 1981.

[195] O. Glatter and B. Hainisch. Improvements in real-space deconvolution of small-angle scattering data. *J. App. Cryst.*, 17:435441, 1984.

[196] S. U. Egelhaaf and P. Schurtenberger. Micelle-to-vesicle transition: A time-resolved structural study. *PRL*, 82:2804–2807, 1999.

[197] K. P. Vinson; Y. Talmom and A. Walter. Intermediate structures in the cholate-phoshatidylcholine vesicle-micelle transition. *Biophys. J.*, 56:669–681, 1989.

[198] M. Betterton and M. Brenner. Electrostatic edge instability of lipid membranes. *Phys. Rev. Lett.*, 82:15981601, 1999.

[199] T. L. Steck; R. S. Weinstein; J. H. Straus and D. F. H. Wallach. Inside-out red cell membrane vesicles: Preparation and puirification. *Science*, 168:255–257, 1970.

[200] M. R. Lieber and T. L. Steck. Inside-out red cell membrane vesicles: Preparation and puirification. *J. Biol. Chem.*, 257:651, 1982.

[201] D.J. Cabral; D.M. Small; H.S. Lilly and J.A. Hamilton. Transbilayer movement of bile acids in model membranes. *Biochemistry*, 26:1801, 1987.

[202] M. Silvander; G. Karlson and K. Edwards. Vesicle solubilization by alkyl sulfate surfactants: A cryo-tem study of the vesicle to micelle transition. *JOURNAL OF COLLOID AND INTERFACE SCIENCE*, 179:104113, 1996.

[203] K. Edwards and M. Almgren. Solubilization of lecithin vesicles by c12e8: structural transitions and temperature effects. *J. Colloid Interface Sci.*, 147:1–, 1991.

[204] J. J. Chance and William C. Purdy. Bile acid measurement using a cholestyramine-coated tsm acoustic wave sensor. *Anal. Chem.*, 68:3104–3111, 1996.

[205] M. Bergström and J. S. Pedersen. Small-angle neutron scattering (sans) study of aggregates formed from aqueous mixtures of sodium dodecyl sulfate (sds) and dodecyltrimethylammonium bromide (dtab). *Langmuir*, 14:3754–3761, 1998.

[206] Magnus Bergström and Jan Skov Pedersen. Small-angle neutron scattering (sans) study of aggregates formed from aqueous mixtures of sodium dodecyl sulfate (sds) and dodecyltrimethylammonium bromide (dtab). *J. Phys. Chem. B*, 103:9888–9897, 1999.